DISS. ETH NO. XXXXX

# IMPACT OF VEGETATION ON URBAN MICROCLIMATE

A thesis submitted to attain the degree of

DOCTOR OF SCIENCES of ETH ZURICH
(Dr. sc. ETH Zurich)

presented by

LENTO MANICKATHAN

Master of Science in Aerospace Engineering,
Delft University of Technology

born on 23.04.1990

citizen of India

accepted on the recommendation of

Prof. Dr. Jan Carmeliet, examiner
Prof. Dr. Bert Blocken, co-examiner
Prof. Dr. Peter Edwards, co-examiner

2019

# ABSTRACT

Vegetation in cities is seen as an effective strategy to combat the growing UHI as it provided natural cooling. Vegetation offers natural cooling primarily by providing shading to urban structures and additionally by extracting heat from the surroundings during the photosynthesis driven transpiration process. However, the effectiveness of transpirative cooling is directly related to the water availability of the plants, and in extreme environmental conditions such as drought, the effectiveness of vegetation can be severely compromised. Furthermore, trees can obstruct ventilation which can have a negative impact on the pollution dispersion characteristics in cities. Therefore, the net impact of vegetation on pedestrian comfort and health in cities is dependent on various conditions and the most effective configuration for UHI mitigation is a non-trivial problem. Thus, an urban microclimate model that can model the airflow, radiation and the water cycle in an integrated approach is necessary for accurately assessing the impact of vegetation in a complex urban environment.

The thesis aims at establishing a more accurate and detailed prediction of the thermal influence of vegetation in an urban environment by simultaneously taking in account of its heat, mass and momentum exchanges and the influence of the water availability. The goal is to provide better guidelines for effective mitigation strategies with vegetation for any given urban, vegetation configuration and environmental conditions. The cooling potential of vegetation such as trees on the microclimate of a street-canyon is studied using a computational fluid dynamics (CFD) model in OpenFOAM. The flow field is numerically modeled by solving the Reynolds-averaged Navier-Stokes equations (RANS) with realizable $k - \varepsilon$ turbulence closure model. The vegetation model is integrated into the CFD solver as a porous medium, providing the necessary source terms for heat, mass and momentum fluxes, with additional closures for turbulence enhancement due to vegetation. A radiation model is developed to model the short-wave and long-wave radiative heat fluxes between the leaf surface and the surrounding. The radiation model enables

to model the impact of the diurnal variation of solar intensity and direction, and the long-wave radiative fluxes between vegetation and nearby urban surfaces. Also, the water cycle driven by the transpiration process is explicitly modeled by coupling with an integrated soil heat and moisture dynamics model. A soil-plant-atmosphere continuum modeling approach is essential as the transpiration rate through the stomata is directly linked to the water availability at the roots of the plant. Therefore, the proposed method helps us understand the response of vegetation during extreme environmental conditions such as drought and provides a more accurate prediction towards the cooling performance of vegetation. The present study investigates the influence of transpirative and shaded cooling due to vegetation on pedestrian comfort inside a street canyon. The influence of various vegetation features such as size, shape, and density is studied to determine the optimal configuration for improving pedestrian comfort and health.

The thesis also employs wind tunnel experiments to provide a deeper understanding of the influence of an isolated tree on the flow. A comparative study of drag force and wake flow field of small model and natural trees shows the distinction between their responses and provide an insight into the challenges of representing trees in urban flow wind tunnel studies with model trees. Furthermore, the microclimate measurement of the small natural plant provide an understanding of the dynamic response of a plant and more a basis for the validation of the numerical model.

# ZUSAMMENFASSUNG

Vegetation in Städten wird als wirksame Strategie zur Bekämpfung des zunehmenden urbanen Hitzeinsel-Effekts (UHI) angesehen, da sie eine natürliche Kühlung bietet. Die Vegetation erzeugt natürliche Kühlung in erster Linie durch Schattenbildung und zusätzlich durch Wärmeentnahme aus der Umgebung durch den Transpirationsprozess während der Photosynthese. Die Wirksamkeit der transpirativen Kühlung hängt jedoch direkt mit der Wasserverfügbarkeit der Pflanzen zusammen. Bei extremen Umweltbedingungen wie Dürre kann die Wirksamkeit der Vegetation stark beeinträchtigt werden. Andererseits können Bäume die Belüftung behindern, was sich negativ auf die Ausbreitungseigenschaften der Luftverschmutzung in Städten auswirken kann. Daher ist der Nettoeffekt der Vegetation auf Fußgängerkomfort und -gesundheit in Städten von verschiedenen Bedingungen abhängig und die effektivste Konfiguration für die UHI-Minderung ein nichttriviales Problem. Daher ist ein Mikroklimamodell für ein Stadtgebiet erforderlich, das den Luftstrom, die Strahlung und den Wasserkreislauf in einem integrierten Ansatz modellieren kann, um die Auswirkungen der Vegetation auf eine komplexe städtische Umgebung genau zu bewerten.

Das Ziel dieser Dissertation ist es, eine genauere und detailliertere Vorhersage des thermischen Einflusses der Vegetation in einer städtischen Umgebung zu ermöglichen, indem gleichzeitig der Austausch von Wärme, Masse und Impuls sowie der Einfluss der Wasserverfügbarkeit berücksichtigt werden. Das Ziel ist es, bessere Richtlinien für effektive Schutzstrategien des lokalen Klimas für jede gegebene Stadt, Vegetationskonfiguration und Umweltbedingungen bereitzustellen. Das Kühlungspotenzial von Vegetation wie Bäumen im Mikroklima eines Street-Canyons wird mit einem numerischen Strömungsmechanikmodell (CFD) in OpenFOAM untersucht. Das Strömungsfeld wird numerisch modelliert, indem die Reynolds-gemittelten Navier-Stokes-Gleichungen (RANS) mit einem "realizable $k-\varepsilon$" Turbulenz modell gelöst. Das Vegetationsmodell ist als poröses Medium in den CFD-Solver integriert und liefert die notwendigen Quellterme für Wärme-, Massen- und Impulsflüsse. Ein Strahlungsmo-

dell wird entwickelt, um die kurz- und langwelligen Strahlungswärmeflüsse zwischen der Blattoberfläche und der Umgebung zu modellieren. Das Strahlungsmodell ermöglicht die Modellierung des Einflusses der tageszeitlichen Variation der Sonnenintensität und -richtung sowie der langwelligen Strahlungsflüsse zwischen Vegetation und nahegelegenen Oberflächen. Der Wasserkreislauf, der durch den Transpirationsprozess angetrieben wird, wird auch explizit durch Kopplung mit einem integrierten Bodenwärme- und Feuchtedynamikmodell modelliert. Ein Modellierungsansatz für die Boden-Pflanzen-Atmosphäre-Kontinuität ist wesentlich, da die Transpirationsrate durch die Stomata direkt mit der Verfügbarkeit von Wasser an den Wurzeln der Pflanze zusammenhängt. Daher hilft das vorgeschlagene Verfahren, die Reaktion der Vegetation unter extremen Umweltbedingungen wie Dürre zu verstehen, und bietet eine genauere Vorhersage hinsichtlich der Kühlleistung der Vegetation. Die vorliegende Studie untersucht den Einfluss von transpirativer und schattierter Kühlung aufgrund von Vegetation auf den Fußgängerkomfort in einem Street-Canyon. Der Einfluss verschiedener Vegetationsmerkmale wie Größe, Form und Dichte wird untersucht, um die optimale Konfiguration zur Verbesserung des Komforts und der Gesundheit von Fußgängern zu bestimmen.

In dieser Arbeit werden auch Windkanalexperimente durchgeführt, um ein tieferes Verständnis des Einflusses eines isolierten Baums auf die Strömung zu vermitteln. Eine vergleichende Studie über das Widerstandsfeld zwischen Zugkraft und Nachlauf von kleinen Modell- und Naturbäumen zeigt den Unterschied ihrer Reaktionen und liefert einen Einblick in die Herausforderungen der Einbeziehung von Bäumen in "Urban Flow"-Windkanalstudien mit Modellbäumen. Darüber hinaus liefert die Mikroklimamessung der kleinen natürlichen Pflanze ein Verständnis der dynamischen Reaktion einer Pflanze und dazu eine Grundlage für die Validierung des numerischen Modells.

# ACKNOWLEDGMENTS

I would like to thank my promoter, Prof. Dr. Jan Carmeliet, for giving me the opportunity to pursue a challenging research topic that called for multiple skill sets. His supervising formed an integral part of my PhD life, helping become a researcher and person that I am now. I would like to also thank Dr. Dominique Derome for her role in my research.

I can't thank enough to my daily (maybe hourly) supervisor, Prof. Dr. Thijs Defraeye. You have my been more than a supervisor, but also a mentor throughout my PhD. Advising me when needed an advice, guiding me when need guidance, . You have both helped me reflect on my weakness and helping me improve them and my strengths.

I would like to thank my company of friends and colleagues who I had to fortune to meet and share intellectually. Dr. Karol Kulasinski, Dr. Aytac Kubilay, Dr. Marcel Vonlanthen, Dr. Georgios Mavromatidis, Dr. Boran Morvaj, Dr. Marc Hohmann, Dr. Marcelo Parada, Dr. Laure Lemrich, Dr. Omid Dorostkar, Dr. Kevin Prawiranto, Christian Kanesan, Giovanni Langella, Dr. Soyoun Son, Dr. Jaebong Lee, Dr. Jonas Allegrini, Dr. Christoph Waibel, Dr. Somil Miglani, Chi Zhang, Mingyang Chen, Gianluca Mussetti, Dr. Andrea Radu. I would like to acknowledge the technical assistance of Roger Vonbank and Beat Margelisch. My gratitude also goes out to Stephan Carl for offering his assistance whenever it was needed the most. I owe special thanks to Martina Koch for her prompt and cheerful administrative assistance.

Finally, I would like to thank my family, Jose, Alphonsa, Linda chechi and Denis chetan. Thank you for your constant support and faith in me.

Lento Manickathan
June 2019

# PUBLICATIONS

## JOURNAL

The following publications are included in parts or in an extended version in this thesis:

1. **Manickathan, L.**, Defraeye, T., Carl, S., Richter, H., Allegrini, J., Derome, D., & Carmeliet, J. (2019). Unveiling dynamic changes in the diurnal microclimate of a Buxus sempervirens with non-intrusive imaging of flow field, leaf temperature, and plant microstructure. *Submitted to Agricultural and Forest Meteorology*. (preprint: https://arxiv.org/abs/1903.02283).

2. **Manickathan, L.**, Defraeye, T., Allegrini, J., Derome, D., & Carmeliet, J. (2018). Comparative study of flow field and drag coefficient of model and small natural trees in a wind tunnel. *Urban Forestry & Urban Greening*, 230–239. http://doi.org/10.1016/j.ufug.2018.09.011.

3. **Manickathan, L.**, Defraeye, T., Allegrini, J., Derome, D., & Carmeliet, J. (2018). Parametric study of the influence of environmental factors and tree properties on the transpirative cooling effect of trees. *Agricultural and Forest Meteorology*, 248, 259–274. http://doi.org/10.1016/j.agrformet.2017.10.014.

## CONFERENCE

1. **Manickathan, L.**, Kubilay, A., Defraeye, T., Allegrini, J., Derome, D., Carmeliet, J.: Integrated vegetation model for studying the cooling potential of trees in urban street canyons. *7th International Building Physics Conference*, Syracuse, NY, USA, September 23 - 26, 2018.

2. **Manickathan, L.**, Kubilay, A., Defraeye, T., Allegrini, J., Derome, D., Carmeliet, J.: Integrated CFD vegetation model with soil-plant-air water dynamics for studying the cooling potential of

vegetation in an urban street canyon. *10th International Conference on Urban Climate/14th Symposium on the Urban Environment*, New York, NY, USA, 6 - 10 August 2018.

3. **Manickathan, L.**, Kubilay, A., Defraeye, T., Allegrini, J., Derome, D., Carmeliet, J.: Conjugate soil-vegetation-air-radiation model for studying the environmental impact of porous media such as vegetation. *Interpore 2018*, New Orleans, LA, USA, May 14 - 17, 2018.

4. **Manickathan, L.**, Kubilay, A., Defraeye, T., Allegrini, J., Derome D., Carmeliet, J.: Influence of vegetation on pedestrian thermal comfort in a street canyon. *1st International Conference on New Horizons in Green Civil Engineering*, Victoria, BC, Canada, April 25 - 27, 2018.

5. **Manickathan, L.**, Defraeye, T., Allegrini, J., Derome, D., Carmeliet, J.: Transpirative cooling potential of vegetation in an urban environment using coupled CFD and leaf energy balance model. *15th Conference of the International Building Performance Simulation Association*, San Francisco, CA, USA, 2017.

6. **Manickathan, L.**, Defraeye, T., Allegrini, J., Derome, D., Carmeliet, J.: Conjugate Vegetation Model for Evaluating Evapotranspirative Cooling in Urban Environment. *97th AMS Annual Meeting*, Seattle, WA, USA, 2017.

7. **Manickathan, L.**, Defraeye, T., Allegrini, J., Derome, D., Carmeliet, J.: Aerodynamic characterization of model vegetation by wind tunnel experiments. *4th International Conference on Countermeasures to Urban Heat Island*, Singapore, 2016.

# NOMENCLATURE

## NOTATIONS

| | |
|---|---|
| $a$, $b$, $f$, $g$, $\sigma$, $\phi$ | scalar |
| $\boldsymbol{a}$, $\boldsymbol{b}$, $\boldsymbol{f}$, $\boldsymbol{g}$, $\bar{\sigma}$, $\bar{\phi}$ | vector |
| $\mathbf{A}$, $\mathbf{B}$, $\mathbf{F}$, $\mathbf{G}$, $\bar{\bar{\sigma}}$, $\bar{\bar{\phi}}$ | tensor |

## LATIN SYMBOLS

| | | |
|---|---|---|
| $a$ | leaf area density | $\mathrm{m^2\,m^{-3}}$ |
| $a_c$ | relative diffusion of water vapor to $CO_2$ (= 1.6) | - |
| $A$ | area | $\mathrm{m^2}$ |
| $A_f$ | frontal area | $\mathrm{m^2}$ |
| $A_g$ | ground area | $\mathrm{m^2}$ |
| $A_l$ | net leaf area | $\mathrm{m^2}$ |
| $A_n$ | assimilation rate | $\mathrm{mol\,m^{-2}\,s^{-1}}$ |
| $A_x$ | xylem cross-sectional area area | $\mathrm{m^2}$ |
| $b$ | Vogel exponent | - |
| $c$ | $CO_2$ concentration | $\mathrm{mol\,mol^{-1}}$ |
| $c_d$ | leaf drag coefficient | - |
| $C_d$ | drag coefficient | - |
| $c_i$ | intercellular $CO_2$ concentration | $\mathrm{mol\,mol^{-1}}$ |
| $c_p$ | specific heat capacity (at constant pressure) | $\mathrm{J\,kg^{-1}\,K^{-1}}$ |
| $c_{pa}$ | specific heat capacity of dry air (= 1006.43) | $\mathrm{J\,kg^{-1}\,K^{-1}}$ |
| $c_{pl}$ | specific heat capacity of liquid (= 4182) | $\mathrm{J\,kg^{-1}\,K^{-1}}$ |
| $c_{pv}$ | specific heat capacity of water vapor (= 1880) | $\mathrm{J\,kg^{-1}\,K^{-1}}$ |

| | | |
|---|---|---|
| $c_a^*$ | reference $CO_2$ concentration | $\mathrm{mol\,mol^{-1}}$ |
| $C$ | aerodynamic resistance coefficient | $\mathrm{s^{0.5}\,m^{-1}}$ |
| $C_F$ | Forchheimer coefficient | - |
| $C_{o,a}$ | oxygen concentration | $\mathrm{mol\,mol^{-1}}$ |
| $C_{mm}$ | moisture capacity | $\mathrm{kg\,m^{-3}\,Pa^{-1}}$ |
| $C_{TT}$ | heat capacity associated to temperature | $\mathrm{J\,m^{-3}\,K}$ |
| $C_{Tp}$ | heat capacity associated to pressure | $\mathrm{J\,m^{-3}\,Pa}$ |
| $D$ | diameter | m |
| $D$ | vapor pressure deficit | kPa |
| $D$ | vapor pressure deficit | $\mathrm{Pa\,Pa^{-1}}$, $\mathrm{mol\ mol^{-1}}$ |
| $D_{va}$ | diffusion coefficient of vapor to dry air | $\mathrm{m^2\,s^{-1}}$ |
| $D_{va,mat}$ | diffusion coefficient of vapor to dry air in solid | $\mathrm{m^2\,s^{-1}}$ |
| $D_{ca}$ | diffusion coefficient of $CO_2$ to dry air | $\mathrm{m^2\,s^{-1}}$ |
| $e$ | internal energy per unit mass | $\mathrm{J\,kg^{-1}}$ |
| $e_m$ | maximum quantum efficiency of the leaf | - |
| $E$ | energy | J |
| $\hat{E}$ | energy per unit mass | $\mathrm{J\,kg^{-1}}$ |
| $E$ | leaf transpiration flux | $\mathrm{kg\,s^{-1}}$ |
| $\boldsymbol{f}$ | body forces | N |
| $f_c$ | $CO_2$ assimilation (photosynthesis) rate | $\mathrm{mol\,m^{-2}\,s^{-1}}$ |
| $f_v$ | transpiration rate | $\mathrm{mol\,m^{-2}\,s^{-1}}$ |
| $F$ | force | N |
| $F_d$ | drag force | N |
| $g$ | gravitational acceleration | $\mathrm{m^2\,s^{-1}}$ |
| $\boldsymbol{g}$ | mass flux | $\mathrm{kg\,m^{-2}\,s^{-1}}$ |
| $\boldsymbol{g}_{c,i}$ | convective mass flux of species $i$ | $\mathrm{kg\,m^{-2}\,s^{-1}}$ |
| $\boldsymbol{g}_{d,i}$ | diffusive mass flux of species $i$ | $\mathrm{kg\,m^{-2}\,s^{-1}}$ |
| $\boldsymbol{g}_l$ | liquid water flux | $\mathrm{kg\,m^{-2}\,s^{-1}}$ |
| $\boldsymbol{g}_v$ | water vapor flux | $\mathrm{kg\,m^{-2}\,s^{-1}}$ |
| $g_{c,leaf}$ | $CO_2$ vapor mass flux | $\mathrm{kg\,m^{-2}\,s^{-1}}$ |
| $g_{v,leaf}$ | water vapor mass flux | $\mathrm{kg\,m^{-2}\,s^{-1}}$ |

| | | |
|---|---|---|
| $g_{v,root}$ | root water uptake | $kg\,m^{-2}\,s^{-1}$ |
| $G_{v,root}$ | net root water uptake | $kg\,s^{-1}$ |
| $G_{v,xylem}$ | net xylem water flux | $kg\,s^{-1}$ |
| $h$ | specific enthalpy per unit mass | $J\,kg^{-1}$ |
| $h_a$ | specific enthalpy of dry air | $J\,kg^{-1}$ |
| $h_v$ | specific enthalpy of water vapor | $J\,kg^{-1}$ |
| $h_{c,h}$ | convective heat transfer coefficient | $W\,m^{-2}\,K^{-1}$ |
| $h_{c,m}$ | convective mass transfer coefficient | $m\,s^{-1}$ |
| $H$ | height | m |
| $HU$ | Hounsfield units | - |
| $I$ | Turbulence intensity | % |
| $k$ | turbulent kinetic energy | $m^2\,s^{-2}$ |
| $k_b$ | boundary layer conductance | $mol\,m^{-2}\,s^{-1}$ |
| $k_s$ | soil conductance in rhizosphere | $s^{-1}$ |
| $k^*_{sr}$ | effective soil-root system conductance | $s\,m^{-1}$ |
| $k_{st}$ | stomatal conductance to $CO_2$ | $mol\,m^{-2}\,s^{-1}$ |
| $k_{st,v}$ | stomatal conductance to vapor | $mol\,m^{-2}\,s^{-1}$ |
| $k^*_{st}$ | effective stomatal conductance to $CO_2$ | $mol\,m^{-2}\,s^{-1}$ |
| $k^*_{st,v}$ | effective stomatal conductance to vapor | $mol\,m^{-2}\,s^{-1}$ |
| $k_r$ | root system conductance | $s^{-1}$ |
| $k_x$ | xylem conductance | $m\,Pa^{-1}\,s^{-1}$ |
| $k_{x,max}$ | maximum xylem conductance | $m\,Pa^{-1}\,s^{-1}$ |
| $k^*_x$ | effective xylem conductance | $s\,m^{-1}$ |
| $K$ | permeability | $m^2$ |
| $K$ | hydraulic conductivity | $m\,s^{-1}$ |
| $K_{lp}$ | liquid water permeability | s |
| $K_{vp}$ | water vapor permeability | s |
| $K_{vT}$ | water vapor permeability due to temperature | s |
| $K_c$ | Michaelis constant for $CO_2$ | $mol\,mol^{-1}$ |
| $K_{lp}$ | liquid water permeability due to pressure | s |
| $K_o$ | Michaelis constant for $O_2$ | $mol\,mol^{-1}$ |

| | | |
|---|---|---|
| $K_{vp}$ | water vapor permeability due to pressure | s |
| $K_{vT}$ | water vapor permeability due to temperature | s |
| $l$ | length | m |
| $l$ | characteristic leaf size | m |
| $\mathcal{L}$ | Lagrangian | - |
| $L_v$ | latent heat of vaporization for water ($= 2.5 \times 10^6$) | $\mathrm{J\,kg^{-1}}$ |
| $m$ | mass | kg |
| $M$ | molar mass | $\mathrm{kg\,mol^{-1}}$ |
| $M_a$ | molar mass of dry air ($= 0.028\,966$) | $\mathrm{kg\,mol^{-1}}$ |
| $M_v$ | molar mass of water vapor ($= 0.018\,015\,34$) | $\mathrm{kg\,mol^{-1}}$ |
| $n$ | Van Genuchten parameter | - |
| $p_c$ | capillary pressure | Pa |
| $p_l$ | liquid pressure | Pa |
| $p_l$ | gas phase pressure | Pa |
| $p_v$ | partial vapor pressure | Pa |
| $p_{v,i}$ | intercellular vapor pressure | Pa |
| $p_{v,leaf}$ | vapor pressure at leaf surface | Pa |
| $p_{vsat}$ | saturation vapor pressure | Pa |
| $P$ | pressure | Pa |
| Pr | Prandtl number | - |
| $\mathrm{Pr}_t$ | turbulent Prandtl number | - |
| $q$ | specific humidity | $\mathrm{kg\,kg^{-1}}$ |
| $\boldsymbol{q}$ | heat flux | $\mathrm{W\,m^{-2}}$ |
| $\boldsymbol{q}_c$ | conductive heat flux | $\mathrm{W\,m^{-2}}$ |
| $\boldsymbol{q}_d$ | heat flux due to mass diffusion | $\mathrm{W\,m^{-2}}$ |
| $q_{lat,lat}$ | latent heat flux from leaf | $\mathrm{W\,m^{-2}}$ |
| $q_r$ | net radiative heat flux | $\mathrm{W\,m^{-2}}$ |
| $q_{r,sw}$ | short-wave radiative heat flux | $\mathrm{W\,m^{-2}}$ |
| $q_{r,lw}$ | long-wave radiative heat flux | $\mathrm{W\,m^{-2}}$ |

| | | |
|---|---|---|
| $q_{rad,lat}$ | radiative heat flux into leaf | $\mathrm{W\,m^{-2}}$ |
| $q_{sen,lat}$ | sensible heat flux from leaf | $\mathrm{W\,m^{-2}}$ |
| $Q_p$ | flux of incoming PAR | $\mathrm{mol\,m^{-2}\,s^{-1}}$ |
| $r$ | root area density | $\mathrm{m^2\,m^{-3}}$ |
| $r_a$ | aerodynamic resistance | $\mathrm{s\,m^{-1}}$ |
| $r_s$ | stomatal resistance | $\mathrm{s\,m^{-1}}$ |
| $\mathcal{R}$ | universal gas constant (= 8.314 459 8) | $\mathrm{J\,mol^{-1}\,K^{-1}}$ |
| $RAI$ | root area index | $\mathrm{m^2\,m^{-2}}$ |
| Re | Reynolds number | - |
| $RH$ | Relative humidity | % |
| $R_v$ | specific gas constant of dry air (= 287.042) | $\mathrm{J\,kg^{-1}K^{-1}}$ |
| $R_v$ | specific gas constant of water vapor (= 461.524) | $\mathrm{J\,kg^{-1}K^{-1}}$ |
| $s$ | long-term intercellular to ambient $CO_2$ concentration (= 0.7) | - |
| $s_\varepsilon$ | volumetric TDR source | $\mathrm{W\,m^{-3}\,s^{-1}}$ |
| $s_\rho$ | volumetric mass source | $\mathrm{kg\,m^{-3}\,s^{-1}}$ |
| $s_h$ | volumetric energy source | $\mathrm{W\,m^{-3}}$ |
| $s_k$ | volumetric TKE source | $\mathrm{W\,m^{-3}}$ |
| $s_{q,r}$ | volumetric radiative source | $\mathrm{W\,m^{-3}}$ |
| $s_r$ | volumetric root water uptake source | $\mathrm{kg\,m^{-3}\,s^{-1}}$ |
| $s_T$ | volumetric temperature source | $\mathrm{K\,m^{-3}}$ |
| $\boldsymbol{s}_u$ | volumetric momentum source | $\mathrm{N\,m^{-3}}$ |
| $s_w$ | volumetric humidity source | $\mathrm{kg\,kg^{-1}\,s^{-1}}$ |
| $S_l$ | liquid saturation | - |
| $\mathbf{S}$ | Mean strain-rate | $\mathrm{s^{-1}}$ |
| $\mathrm{Sc}_t$ | turbulent Schmidt number | - |
| $t$ | time | s |
| $T$ | temperature | K |
| $T_g$ | ground temperature | K |
| $T_l$ | leaf temperature | K |
| $T_{leaf}$ | leaf temperature | K |

| | | |
|---|---|---|
| $T_L$ | leaf temperature | K |
| $T_{sky}$ | sky temperature | K |
| $TR$ | net hourly transpiration rate | $\mathrm{g\,h^{-1}}$ |
| $\boldsymbol{u}$ | velocity | $\mathrm{m\,s^{-1}}$ |
| $u_*$ | friction velocity | $\mathrm{m\,s^{-1}}$ |
| $U$ | mean wind speed | $\mathrm{m\,s^{-1}}$ |
| $U_{ref}$ | reference velocity | $\mathrm{m\,s^{-1}}$ |
| $UTCI$ | universal thermal climate index | °C |
| $V$ | Volume | $\mathrm{m^3}$ |
| $V_{cmax}$ | maximum carboxylation capacity | $\mathrm{mol\,m^{-2}\,s^{-1}}$ |
| $V_{pore}$ | volume of open pores | $\mathrm{m^3}$ |
| $w$ | moisture content | $\mathrm{kg\,m^{-3}}$ |
| $w_a$ | dry air content | $\mathrm{kg\,m^{-3}}$ |
| $w_{cap}$ | capillary moisture content | $\mathrm{kg\,m^{-3}}$ |
| $w_l$ | liquid water content | $\mathrm{kg\,m^{-3}}$ |
| $w_s$ | solid matrix water content | $\mathrm{kg\,m^{-3}}$ |
| $w_v$ | water vapor content | $\mathrm{kg\,m^{-3}}$ |
| $WUE$ | water use efficiency | - |
| $x_i$ | mass concentration of species $i$ | $\mathrm{kg_i\,kg^{-1}}$ |
| $z$ | vertical height | m |
| $z_0$ | aerodynamic roughness length | m |

## GREEK SYMBOLS

| | | |
|---|---|---|
| $\alpha$ | aerodynamic porosity | - |
| $\alpha^{2D}$ | 2D aerodynamic porosity | - |
| $\alpha_p$ | leaf absorptivity of PAR | - |
| $\beta$ | optical porosity | - |
| $\beta$ | extinction coefficient for short-wave radiation extinction | - |
| $\beta$ | volumetric thermal expansion coefficient | $\mathrm{K^{-1}}$ |
| $\beta_p$ | fraction of MKE converted to TKE | - |

| | | |
|---|---|---|
| $\beta_d$ | fraction of TKE shortcut to TDR | - |
| $\gamma$ | apparent quantum yield | - |
| $\delta_v$ | water vapor diffusion coefficient | s |
| $\varepsilon$ | turbulent kinetic energy dissipation rate | $m^2\,s^{-3}$ |
| $\kappa$ | von Kármán constant ($= 0.41$) | - |
| $\lambda$ | thermal conductivity | $W\,m^{-1}\,K^{-1}$ |
| $\lambda$ | Lagrange multiplier | $mol\,mol^{-1}$ |
| $\lambda$ | second coefficient of viscosity | $N\,s^{-1}\,m^{-2}$ |
| $\mu$ | attenuation coefficient | $m^{-1}$ |
| $\mu_{sw}$ | extinction coefficient for short-wave radiation extinction | - |
| $\mu$ | chemical potential | $J\,mol^{-1}$ |
| $\mu$ | dynamic viscosity | $kg\,m^{-1}\,s^{-1}$ |
| $\nu$ | kinematic viscosity | $m^2\,s^{-1}$ |
| $\nu_t$ | turbulent viscosity | $m^2\,s^{-1}$ |
| $\rho$ | density | $kg\,m^{-3}$ |
| $\rho_a$ | density of air | $kg\,m^{-3}$ |
| $\rho_l$ | density of liquid water ($= 1000$) | $kg\,m^{-3}$ |
| $\rho_s$ | density of solid matrix | $kg\,m^{-3}$ |
| $\sigma_\nu$ | Schmidt number | - |
| $\sigma_{\nu_t}$ | turbulent Schmidt number | - |
| $\bar{\bar{\sigma}}$ | Cauchy stress tensor | $N\,m^{-2}$ |
| $\bar{\bar{\tau}}$ | sgear-stress tensor | $N\,m^{-2}$ |
| $\phi$ | porosity | $m^3\,m^{-3}$ |
| $\phi_o$ | open porosity | $m^3\,m^{-3}$ |
| $\psi$ | shelter parameter | - |
| $\psi$ | water potential | Pa |
| $\psi_g$ | gravitational potential | Pa |
| $\psi_L$ | leaf water potential | Pa |
| $\psi_R$ | root water potential | Pa |
| $\psi_s$ | soil water potential | Pa |
| $\Omega$ | domain | - |

| | | |
|---|---|---|
| $\Omega_a$ | air domain | - |
| $\Omega_s$ | soil domain | - |

### SUBSCRIPTS

| | |
|---|---|
| *eff* | effective |
| *g* | gas |
| *g* | ground |
| *i* | intercellular |
| *l* | liquid (water) |
| *l* | leaf |
| *leaf* | leaf |
| *lw* | long-wave |
| *L* | leaf (net property) |
| *o* | open |
| *pore* | pore |
| *ref* | reference |
| *root* | root (net property) |
| *sat* | saturated |
| *R* | root |
| *s* | solid |
| *s* | soil |
| *sky* | sky |
| *sw* | short-wave |
| *t* | time |
| *v* | vapor |
| *xylem* | xylem |

### ACRONYMS

| | |
|---|---|
| ABL | atmospheric boundary layer |

| | |
|---|---|
| CFD | computational fluid dynamics |
| CHTC | convective heat transfer coefficient |
| CMTC | convective mass transfer coefficient |
| CT | computational tomography |
| DEHS | Di-Ethyl-Hexyl-Sebacat |
| DIG | diagonal-based incomplete Cholesky |
| DNS | direct numerical simulation |
| ETHZ | Eidgenössische Technische Hochschule Zürich |
| FOV | field of view |
| FFT | fast Fourier transformation |
| FVM | finite volume method |
| HPC | high performance computing |
| LAI | leaf area index |
| LAD | leaf area density |
| LDPE | low-density Polyethylene |
| LES | large eddy simulation |
| LHS | left hand side |
| MOE | modulus of elasticity |
| PAR | photosynthetically active radiation |
| PCG | preconditioned conjugate gradient |
| PIV | particle image velocimetry |
| PPM | parts per million |
| RAI | root area index |
| REV | representative elementary volume |

| | |
|---|---|
| RANS | Reynolds-averaged Navier-Stokes |
| RHS | right hand side |
| ROI | region of interest |
| SPIV | stereoscopic particle image velocimetry |
| TDR | turbulent dissipation rate |
| TKE | turbulent kinetic energy |
| UHI | urban heat island |
| UTCI | universal thermal climate index |
| WUE | water use efficiency |

# CONTENTS

# 1

# INTRODUCTION

## 1.1 MOTIVATION

The global population is steadily increasing and migrating from rural areas to urban areas which have resulted in an ever-growing urban population for the past two centuries (Oke et al. 2017). This urbanization and the rise in human activity in cities has resulted in numerous detrimental effects such as increased air temperature, increased building energy consumption, and reduced air quality (Kovats and Hajat 2008; Salmond et al. 2016; Santamouris and Asimakopoulos 2001). The higher air temperature in cities compared to the nearby rural area is defined as an urban heat island (UHI). The UHI has shown to have a negative impact on human comfort and health in cities, e.g., increased heat strokes and infant mortality especially during heat waves (Fouillet et al. 2006). Furthermore, the impact of *climate change*, driven by human activity, on the urban society needs to be addressed as climate change has been seen to further amplify the adverse effects of urbanization. Therefore, the ecology of the urban system should be one of the primary concerns of society (Pachauri et al. 2014). Cities should focus on developing or refining existing strategies to mitigate the growing detrimental effects of UHI. A lack thereof can have not only implication on the comfort and health of the urban populace but also the global climate.

Vegetation provides natural cooling through shading and transpiration. Therefore, it is seen as one of the primary UHI mitigation strategies as it can not only improve the pedestrian comfort and health (Bowler et al. 2010; Gillner et al. 2015; Loughner et al. 2012) but also has shown to improve the well-being of citizens (Donovan and Butry 2010; Kuo and Sullivan 2001). Towards this, it is impera-

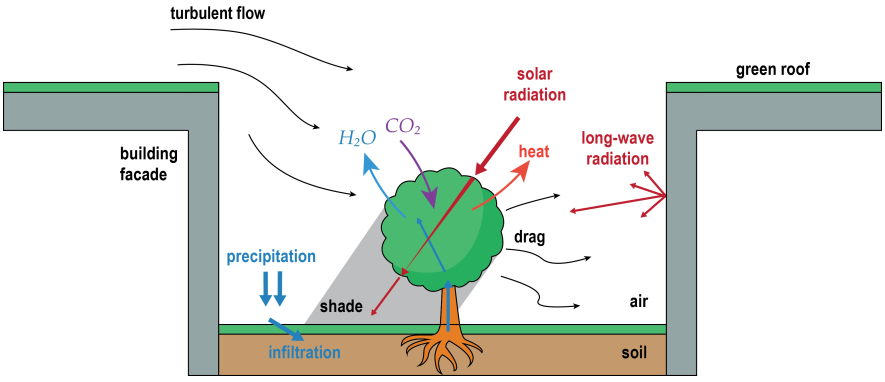


Figure 1.1: Impact of vegetation on urban microclimate.

tive to understand and predict the impact of vegetation on the urban climate and the comfort of the citizens.

However, the cooling provided by vegetation is fundamentally dependent on environmental conditions. This dependency is one of the complexities which makes urban greening strategies a non-trivial problem. Environmental factors such as the climatic conditions (i.e., wind speed, air temperature, and relative humidity), radiative fluxes (i.e., solar radiation and thermal radiation), and the water availability is known to influence the cooling potential of vegetation. Figure 1.1 shows a schematic representation of the various fluxes between a tree and the urban environment. The figure shows that the vegetation interacts with multiple physical processes in an urban microclimate. The plant transpiration is related to the ambient conditions and the solar radiation, resulting in the well-documented transpirative cooling effect (Abtew and Melesse 2012; Farquhar and Roderick 2007; Melesse et al. 2008; Oke et al. 2017). Furthermore, due to the interception of solar radiation by the plant foliage, vegetation provides additional cooling by shading of nearby building elements. However, the moisture transpired by vegetation is also known to depend on water availability. The dependency indicates that soil moisture is an important factor contributing to the cooling potential of vegetation. So, accurate predictions must take into account the hygrothermal characteristics such as air temperature, air relative humidity, and soil moisture.

Thus, there is a need to understand better these complex, coupled, physical processes that contribute to the cooling provided by vege-

tation. We must better quantify the influence of vegetation on the urban energy balance. Therefore, a multi-domain coupled numerical model is to be developed to elucidate the interactions and the feedback loops of vegetation in an urban context. Furthermore, the water cycle driven by the plant transpiration should be modeled to accurately assess the impact of vegetation on urban microclimate, especially the influence on thermal comfort. Moreover, there is a great need for high-resolution experimental data that can reveal the spatial and temporal variability in the plant responses. For example, the leaf temperature is known to be a function of space and the plant transpiration rate is known to vary throughout the day.

## 1.2 OBJECTIVE AND METHODOLOGY

As vegetation is increasingly being sought after as a natural UHI mitigation strategy, accurate predictions tools need to be available. Therefore, the goals of the thesis are:

- to assess the impact of vegetation on the microclimate.
  - *airflow*: to better understand how the sheltering provided by small model trees (typically used in wind tunnel experiments) differs from that of natural trees.
  - *airflow*: to better understand how the seasonal foliar density change affects the sheltering provided by trees.
  - *hygrothermal*: to quantify the change in urban energy balance due to vegetation.
- to quantify the natural cooling provided by vegetation.
  - *hygrothermal*: to quantify the difference between transpirative cooling and cooling due to shading by trees.
  - *hygrothermal*: to quantify the influence of wind speed, air temperature, relative humidity, and solar radiation intensity on the plant cooling potential.
  - *hygrothermal*: to quantify the influence of plant properties (i.e., leaf size, stomatal resistance, tree height) and foliage density on the plant cooling potential.

  - *hygrothermal*: to better understand the diurnal response of the plant and any spatial and temporal variability in plant condition (i.e., leaf temperature, transpiration rate).

- to understand the influence of water stress on natural cooling.
  - *hygrothermal*: to better understand the feedback loop between soil moisture and plant transpiration.
  - *hygrothermal*: to quantify the influence of water availability on the plant cooling potential.

- to quantify the impact of vegetation on pedestrian thermal comfort.
  - *comfort*: to better understand the governing factor related to vegetation that affect the pedestrian thermal comfort.

In this thesis, experimental and numerical approaches are combined to assess the impact of vegetation on the microclimate. Experiments in an atmospheric boundary layer (ABL) wind tunnel are opted to understand the impact of vegetation on the airflow and the (near-wake) microclimate, where the small model and natural trees are employed as scaled models. Measurement techniques such as particle image velocimetry (PIV) and drag force measurement are employed to quantify the modification of airflow due to vegetation. Measurement techniques such as infrared thermography and hygrothermal sensor analysis are used to quantify the change in hygrothermal variables of the microclimate. A numerical assessment of the impact of vegetation on urban microclimate is achieved by integrating a vegetation model into a computation fluid dynamics (CFD) model in OpenFOAM. The developed numerical approach simultaneously resolves turbulence modification, radiation balance, heat and mass fluxes, and the sensitivity to soil moisture. The influence of the water availability on the transpiration rate is modeled using a soil-plant-atmosphere continuum (SPAC) model. Thus, the model is to quantify the cooling potential of vegetation along with its impact on thermal comfort for a pedestrian.

The present thesis hopes to address the impact of vegetation at a microclimate scale. Therefore, the study aims to prove a better estimation of the efficacy of vegetation as a mitigation strategy for improving human health and thermal comfort in cities. Moreover,

the developed numerical model provides a key element missing in the urban microclimate model in the present research group (i.e., Chair of Building Physics). In future, the detailed model can be enable parametric studies on the role of vegetation in the urban environment. Such advanced model will support the design of UHI mitigation strategies by the integration of vegetation in cities.

## 1.3 OUTLINE OF THE THESIS

This thesis is divided into two parts: i) experimental studies (Chapters 3 and 4), and ii) numerical studies (Chapters 5 to 8) of the impact of vegetation on urban microclimate. The thesis is organized as follow:

- *Chapter 2*: The chapter addresses state of the art providing an introduction to urban climate, the influence of vegetation at microclimate scale, and typical experimental approaches and numerical approaches for assessing the impact of vegetation. The goal of the chapter is: i) to provide an overview of relevant researches that are present and are employed for quantifying the impact of vegetation on urban microclimate and ii) to justify the scope of the numerical model that is presented in this thesis.

- *Chapter 3*: This chapter is the first part of the experimental studies, where the impact of vegetation on the airflow is investigated. The aim of the study is the understand how the sheltering provided by small model trees differs from that of small natural trees and subsequently quantify the difference with mature trees. The influence of vegetation on the airflow is studied in an atmospheric boundary layer (ABL) wind tunnel using small model and natural trees. In the study, the turbulent airflow behind the trees is studied using particle image velocimetry (PIV) measurement technique and is linked to the drag force measurements using a load cell. The chapter has been published as: Manickathan, L., Defraeye, T., Allegrini, J., Derome, D., & Carmeliet, J. (2018). "Comparative study of flow field and drag coefficient of model and small natural trees in a wind tunnel". *Urban Forestry & Urban Greening*, 230–239. http://doi.org/10.1016/j.ufug.2018.09.011.

- *Chapter 4*: This chapter is the second part of the experimental studies, where the impact of vegetation on the microclimate is investigated. The influence of vegetation on the microclimate is studied in the wind tunnel using a small *Buxus sempervirens* plant. In the study, the diurnal dynamics of the plant microclimate of a *Buxus sempervirens* is investigated using various high-resolution non-intrusive imaging techniques. The wake flow field is measured using stereoscopic particle image velocimetry (SPIV), the spatiotemporal leaf temperature history is obtained using infrared thermography, and the plant microstructure metrics such as plant porosity, leaf area density (LAD) is obtained through X-ray tomography. This chapter has been submitted as: Manickathan, L., Defraeye, T., Carl, S., Richter, H., Allegrini, J., Derome, D., & Carmeliet, J. (2018). "Unveiling dynamic changes in the diurnal microclimate of a Buxus sempervirens with non-intrusive imaging of flow field, leaf temperature, and plant microstructure". *Submitted to Agricultural and Forest Meteorology*.

- *Chapter 5*: In this chapter the numerical model of assessing the impact of vegetation in urban microclimate is described. The *air* domain solver, the *solid* domain solver, and the *radiation* model is described in detail. Furthermore, the chapter describes the coupling strategy employed to couple these three models with a detailed description of the coupling algorithm. The influence of water availability on transpiration rate is addressed by an advanced stomatal model based on the soil-plant-atmosphere continuum (SPAC) model approach.

- *Chapter 6*: This chapter is the first part of the numerical studies, where the impact of vegetation on the transpirative cooling potential is investigated. The aim of the study is to quantify how much the environmental factors (i.e., wind speed, air temperature, relative humidity, and solar radiation intensity) and tree properties (i.e., leaf size, stomatal resistance, and leaf area density) contribute to the plant cooling performance and the pedestrian comfort. The influence of vegetation on the transpirative cooling is studied using a computational fluid dynamics (CFD) modeling approach, where vegetation is modeled as a porous medium. The full-model described in Chapter 5 is

simplified to focus the study on the leaf energy balance and its influence on the transpirative cooling effect of the air domain. Further simplification is performed to enable a rigorous parametric study by only investigating a stand-alone tree at solar noon and the stomatal model is simplified to depend only on the atmospheric evaporative demand (AED) and solar radiation intensity such that the influence of soil moisture is removed. The chapter has been published as: Manickathan, L., Defraeye, T., Allegrini, J., Derome, D., & Carmeliet, J. (2018). "Parametric study of the influence of environmental factors and tree properties on the transpirative cooling effect of trees". *Agricultural and Forest Meteorology*, 248, 259–274. http://doi.org/10.1016/j.agrformet.2017.10.014.

- *Chapter 7*: This chapter is focuses on comparing the developed numerical in Chapter 6 with the microclimate measurements of Chapter 4. The goal of the chapter is to compare and determine the discrepancy of the numerical model in predicting the airflow and the transpiration cooling of vegetation. The simplified model is used for comparison as the present measurement campaign still lacks the necessary parameters for an accurate calibration of the full-model, such as the plant xylem properties and rhizosphere properties. The present study only focused on the atmospheric changes due to plant transpiration. In future, a multi-domain measurement campaign consisting of measurements of air domain, soil domain, and plant physiology, can enable the assessment of the full model.

- *Chapter 8*: This chapter is the second part of the numerical studies, where the impact of vegetation on the urban microclimate is investigated using the numerical model described in Chapter 5. The impact of vegetation on the urban microclimate consists of a modification of the turbulent urban airflow, the addition of transpirative cooling in the urban area, and the plant shading provided by the foliage. The influence of these phenomena is investigated together with the impact of pedestrian thermal comfort.

- *Chapter 9*: This chapter provides a conclusion and some of the main finding in the thesis. Furthermore, the chapter provides

an overview of the contributions to the research field from the present thesis. Finally, an outlook and possible future research aspects are given.

# 2

# STATE OF THE ART

In this chapter, the role of urban vegetation in the urban climate is discussed. First, a general background of urban climate is given, with an introduction of the urban microclimate and its energy budget. The concept of urban heat island (UHI) and its implication on human comfort is provided after that. An overview of the relevant research on the impact of vegetation i1n urban microclimate is given including experimental and numerical methods. Based on the overview, the relevance of the research is indicated with specific research goals.

## 2.1 AN OVERVIEW OF URBAN CLIMATE

"*Urban climates are a prime example of inadvertent climate modification - the unintended impact of human activity on the atmosphere*" (Oke et al. 2017). In other words, the urban climate describes the modification of the atmosphere due to various components of the urban ecosystem. More specifically, the urban ecosystem modifies the natural environment through five aspects: atmosphere, biosphere, hydrosphere, pedo- and lithosphere, and the built system (Oke et al. 2017). The urban atmosphere describes the influence of urban elements on the atmospheric conditions. The urban biosphere describes the influence of urban vegetation and other biological elements. The urban hydrosphere describes the water movement in the urban area, where the process such as surface run-off is described. The urban pedo- and lithosphere deals with the soil and ground modification in cities. Finally, the built system describes the influence of human-made structures on its environment. Therefore, the net urban climate is a result of these five aspects and the coupling between all

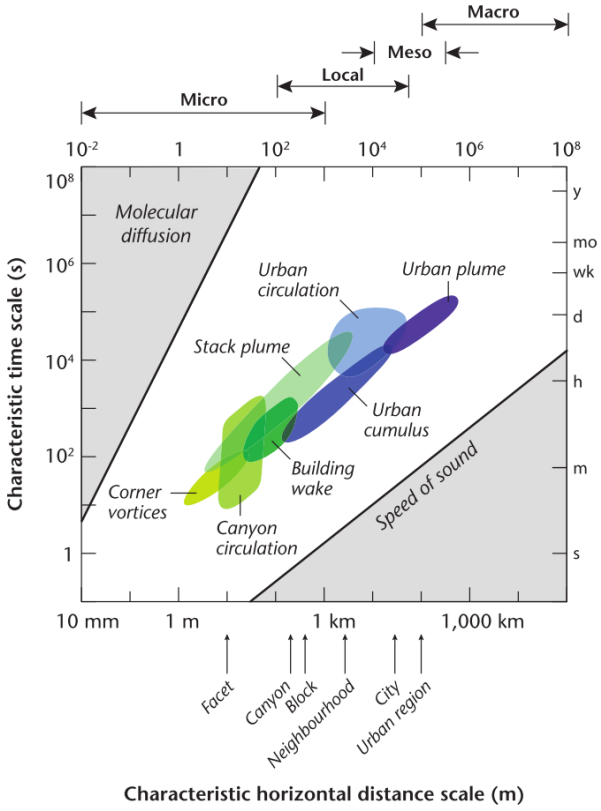


Figure 2.1: Time and length scale of phenomena in urban climate (Oke et al. 2017).

these components is needed to be understood to study the urban climate.

### 2.1.1 *Urban scales*

Due to the complexity of the urban area, in terms of its morphology and the associated climatological phenomena, the topology of the urban elements are typically simplified to various length scales. The urban elements are approximated at four length scales: micro (< km), local (100 m - 100 km), meso (10 - 100 km), and macro ($10^3$-$10^5$ km) scale. Fig. 2.1 shows the characteristic time and length scales in the urban climate (Oke et al. 2017). The microscale resolves nearly all the topological features, resolving urban elements such as facets, individual buildings, and street-canyons. The local scale approximates the features of the microscale and only resolves topological variability between 100 m and up to 100 km such as an urban neighborhood. The local climate zone (LCZ) clustering scheme is used to approximate the microscale urban element features, parameterizing the topology using parameters such as building plan area density $\lambda_b$ (%) (i.e., ratio of plan-view area of building to total surface area), canyon aspect ratio $\lambda_s$ (i.e., ratio of building height to building width) and mean roughness length $z_H$ (m). The mesoscale further approximates the urban topology, only resolving the features between 10 km and 100 km scales. Therefore, modeling the urban climate at microscale means resolving urban elements such as facet (i.e., roofs, walls) and buildings, and the climatic properties associated with them. At microscale, flow phenomena such as *standing vortex*, *corner vortices*, *canyon circulation* and *building wake* are typically present. We are interested in the influence of building morphology on the these flow phenomena along with the *hygrothermal* and *radiative* conditions (e.g. shadowing) around the buildings, as all these parameters have a direct influence on the *pedestrian comfort*. Ergo, urban microclimate models are designed to describe these phenomena. In contrast, urban mesoscale models which deal with length scales $\mathcal{O}(10)$ - $\mathcal{O}(10^2)$ km, are designed to capture phenomena of much larger time and length scales such as *urban heat island*, *urban plumes* and *cloud and precipitation* (Oke et al. 2017). In such models, microclimate phenomena are either neglected or parameterized to ensure their computational tractability.

### 2.1.2 *Urban boundary layer*

The atmospheric boundary layer (ABL) is modified over the city resulting in an urban boundary layer (UBL). The UBL during the day is divided into four distinct regions: urban canopy layer (UCL), roughness sublayer (RSL), inertial sublayer (ISL), and mixing layer (ML) (Oke et al. 2017). Figure 2.2 shows the layout of these layers over a city. The UCL spans from the surface to the average building/tree height in cities. The RSL, consisting of the UCL spans from the ground up to 2-5 times the average height of buildings in cities. The urban microclimate phenomena cannot be neglected at this scale such as the geometry-dependent flow characteristics (i.e., vortices, flow circulation, and building/tree wake) and non-uniformity in the surface fluxes. In other words, the 3D nature of the cities becomes an essential factor in describing the flow and climate characteristics. Therefore, a study of urban climate in this domain requires the consideration of the spatial variability of the city. The ISL, typically between 25 to 250 m is above the RSL and the uppermost layer of the surface layer (SL). At this layer, the flow is only affected by the integral effects of the urban neighborhood, and the spatial variability is less than the RSL. Furthermore, the wind profile is well defined through logarithmic profiles. The ML is above the ISL spanning vertically from 250 up to 2500 m. During the day, due to heating of the urban surfaces, there is strong mixing present in this layer (Oke et al. 2017). The ML is separated from the free atmosphere (FA) (i.e., where the surface influences are negligible) by an entrainment zone (EZ).

### 2.1.3 *Energy balance*

A study on the energy budget in an urban canopy layer can provide an initial understanding of the coupling between various processes in the urban microclimate. The energy budget can be determined by applying the conservation of energy for the UCL. The heat sinks and sources inside the domain are balanced by the fluxes at the boundaries. Figure 2.3 shows a schematic representation of the energy balance applied to the UCL.

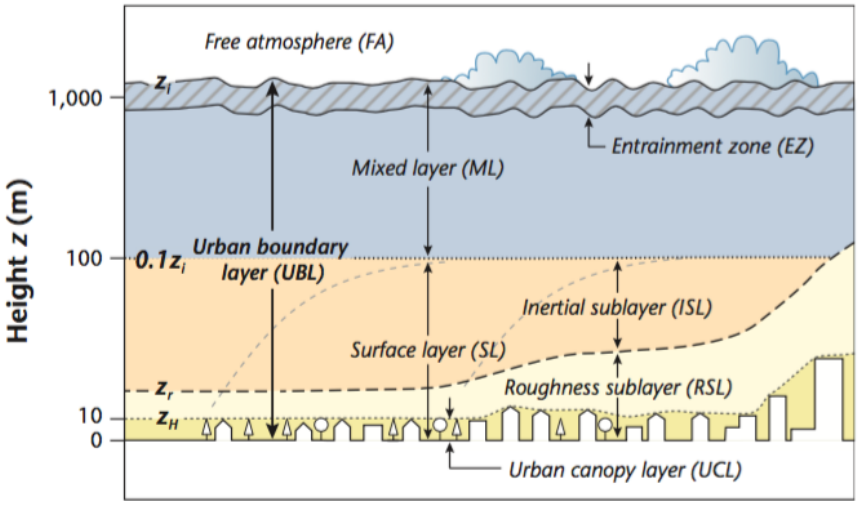


Figure 2.2: Urban boundary layer during the day and divided into 4 distinct regions: urban canopy layer (UCL), roughness sublayer (RSL), inertial sublayer (ISL), and mixing layer (ML) (Oke et al. 2017).

The energy budget is defined as:

$$Q_r + Q_f = Q_s + Q_l + \Delta Q_t + \Delta Q_a \tag{2.1}$$

where $Q_r$ ($\mathrm{W\,m^{-2}}$) is the net radiative heat flux, $Q_f$ ($\mathrm{W\,m^{-2}}$) is the net anthropogenic heat flux, $Q_s$ ($\mathrm{W\,m^{-2}}$) is the sensible heat flux, $Q_l$ ($\mathrm{W\,m^{-2}}$) is latent heat flux, $\Delta Q_t$ ($\mathrm{W\,m^{-2}}$) is the net energy storage change, and $\Delta Q_a$ ($\mathrm{W\,m^{-2}}$) is the net energy advected by the wind into and out of the domain. In this thesis, the influence of vegetation on the energy balance in an urban microclimate is of focus.

### 2.1.4 *Urban heat island*

Cities are known to experience higher temperatures than the surrounding rural areas (Oke 1973; Oke et al. 2017). The presence of unshaded, urban structures with low albedo and high thermal capacity, the lack of natural bodies such as open-water (e.g., ponds, rivers, and lakes), the lack of impervious surfaces (e.g., soil), and

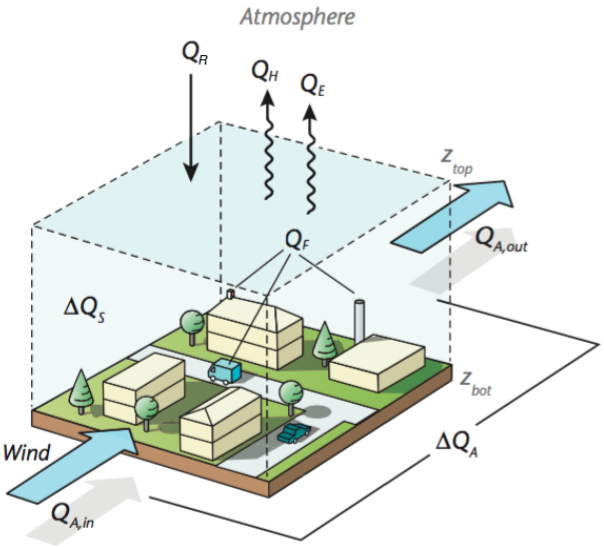


Figure 2.3: The energy balance of an urban canopy layer (UCL) (Oke et al. 2017).

the lack of vegetation fraction is known to result in the UHI (Bowler et al. 2010).

The UHI-intensity is defined as the difference between the urban air temperature $T_{urban}$ and the rural air temperature $T_{rural}$. It provides a measure on warming associated to the presence of the city. Fig. 2.4 shows the daily and seasonal variation of UHI in Basel, Switzerland, where a UHI of up to 1.5 °C is observed during the summer. More specifically, the figure shows $UHI_{UCL}$, i.e., the air temperature difference urban and rural area using a fixed station with temperature sensors at the height of urban canopy layer. The UHI has been shown to have a negative influence on human health and comfort in cities (Kovats and Hajat 2008; Salmond et al. 2016; Santamouris and Asimakopoulos 2001). For examples, increased heat strokes and infant mortality during the heat wave has been observed in the past, such as in August 2003 summer (Fouillet et al. 2006). In future, the UHI effect is expected to grow due to increasing urbanization, which will lead to a predicted urban population of 5 billion by 2030 and 66% of the world's population living in cities by 2050 (Seto et al. 2012; United Nations 2015). Furthermore, the temperatures in urban areas are predicted to further increase due to

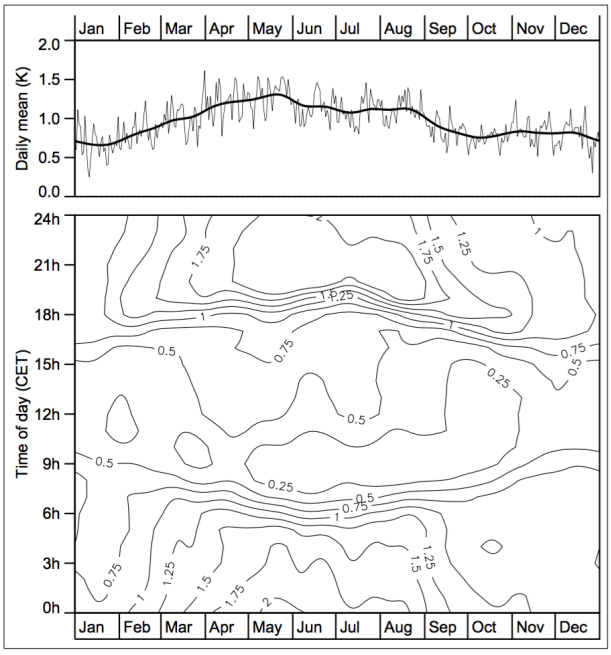


Figure 2.4: Daily and seasonal variation of UHI (K) in Basel, Switzerland (Parlow et al. 2014). The UHI is calculated as the air temperature difference between urban (Basel Spalenring) and rural area (Lange Erlen) obtained from hourly mean values for 1994-2003.

the combined effect of climate change with a projected $2-4$ °C increase in global average surface temperature by 2100 (Pachauri et al. 2014). Thus, the detrimental effects of UHI are not only expected to grow but also is expected to affect more of the global population. Therefore, one of the driving objectives in cities is to mitigate this growing UHI and make cities more resilient and sustainable.

### 2.1.5 *Human comfort*

One of the key aspects of the urban microclimate study is its impact on the urban population (Oke et al. 2017; Saneinejad 2013). The response and the state of the human body to the urban microclimate can be quantified through human physiological modeling. The en-

ergy balance of a human consists of heat flux from the body core to skin and the heat flux between the skin surface and environment:

$$Q_m + Q_w + Q_s + Q_l + Q_t = \Delta Q_s \tag{2.2}$$

where $Q_m$ ($\mathrm{W\,m^{-2}}$) is the heat produced from metabolism, $Q_w$ ($\mathrm{W\,m^{-2}}$) is muscular activity, $Q_s$ ($\mathrm{W\,m^{-2}}$) is sensible heat flux, $Q_l$ ($\mathrm{W\,m^{-2}}$) is latent heat flux, $Q_t$ ($\mathrm{W\,m^{-2}}$) is heat produced from respiration, and $\Delta Q_s$ ($\mathrm{W\,m^{-2}}$) is the rate of energy storage. Various comfort models have been developed to solve the energy balance. The Munich Energy-Balance Model for Individuals (MEMI) solves energy balance with a two-node system solving the heat flux from the skin to the body core and heat fluxes through clothing (Höppe 1999).

A more realistic model is the UTCI-Fiala model that uses a 12 element (head, face, neck, shoulder, thorax, abdomen, upper and lower arm, hands, upper and lower legs, and feet), 187-node model (Blazejczyk et al. 2012; Błazejczyk et al. 2013; Bröde et al. 2012; Fiala et al. 2001; Jendritzky et al. 2012; Lokys et al. 2015). The physiological response can then quantify using various thermal/human comfort indexes such as predicted mean vote (PMV), perceived temperature (PT), OUT-SET*, physiological equivalent temperature (PET), universal thermal climate index (UTCI). The UTCI (°C) is determined as:

$$UTCI = T + f\left(T, T_{mrt}, |\boldsymbol{u}|, RH\right) \tag{2.3}$$

where it is a function of air temperature $T$, the mean radiant temperature $T_{mrt}$, wind speed $|\boldsymbol{u}|$ and relative humidity $RH$ (Blazejczyk et al. 2012; Bröde et al. 2012; Fiala et al. 2001). The mean radiant temperature $T_{mrt}$ is influenced by the long-wave and the short-wave radiation, which is a function of direct solar radiation $q_{r,sw}$ and the solar altitude $\phi$. The mean radiant temperature $T_{mrt}$ (°C) is defined as:

$$T_{mrt} = \left(T_{umrt}^4 + \frac{f_p a_b}{\epsilon_p \sigma} q_{s,dir}\right)^{\frac{1}{4}} \tag{2.4}$$

where $T_{umrt}$ is the mean radiant temperature component belonging to the diffused or reflected part (i.e., from terrestrial source), $f_p$ is projected surface area of the person exposed to the sun, $\alpha_p$ is the albedo, $\epsilon_p$ is the emission coefficient and $q_{s,dir}$ ($\mathrm{W\,m^{-2}}$) is the direct

| PMV | PET | Thermal perception | Grade of physiological stress | Universal Thermal Climate Index (UTCI) (°C) range | Physiological responses |
|---|---|---|---|---|---|
| | | Very cold | Extreme cold stress | < 40 | Decrease in core temperature |
| −3.5 | 4 | | | −27 to −40 | Shivering, average skin temperature will fall below 0°C if exposure is sustained |
| −2.5 | 8 | Cold | Strong cold stress | −13 to −27 | Face temperature < 7°C (numbness), core to skin temperature gradient increases |
| | | Cool | Moderate cold stress | 0 to −13 | Vasoconstriction, exposed skin temperature < 15°C |
| −1.5 | 13 | Slightly cool | Slight cold stress | +9 to 0 | Localized cooling, need for gloves |
| −0.5 | 18 | | | | |
| | | Comfortable | No thermal stress | +9 to +26 | Comfortable, sweat rate < 100 g $h^{-1}$ |
| 0.5 | 23 | | | | |
| 1.5 | 29 | Slightly warm | Slight heat stress | +26 to +32 | Slight heat stress |
| | | Warm | Moderate heat stress | +32 to +38 | Positive change in rate of sweating, and of skin temperature |
| 2.5 | 35 | Hot | Strong heat stress | +32 to +38 | Sweat rate > 200 g $h^{-1}$ |
| 3.5 | 41 | | | +38 to +46 | Small core to skin temperature gradient (< 1 K). Sweat rate increase (> 650 g $h^{-1}$ at limit) |
| | | Very hot | Extreme heat stress | > 46 | Increase in core temperature |

Figure 2.5: Range, relation and physiological response for different parameters of the comfort indexes (Błazejczyk et al. 2013; Matzarakis et al. 1999; Oke et al. 2017).

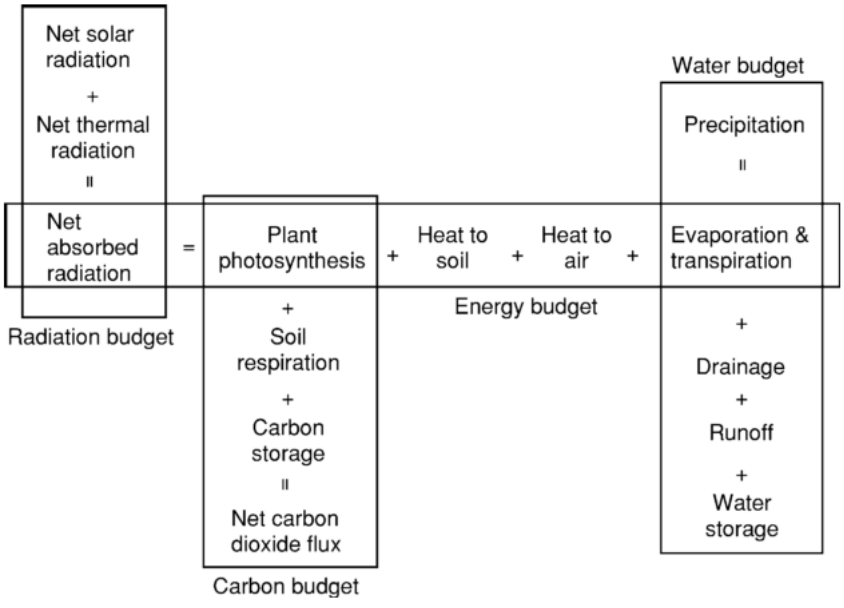


Figure 2.6: Coupling between radiative, energy and water budget (Sławiński and Sobczuk 2011).

solar radiation. The diffused/reflected component of the MRT is defined as:

$$T_{umrt} = \left[ \frac{1}{\sigma} \sum_{i}^{N} \left( q_{r,i} + \frac{a_b}{\epsilon_p} q_{s,i} \right) F_i \right]^{\frac{1}{4}} \tag{2.5}$$

where $q_{r,i}$ (W m$^{-2}$) is the long-wave radiation emitted from surface $i$, $q_{s,i}$ (W m$^{-2}$) is the reflected (assumed to be diffused) short-wave radiation from surface $i$, and $F_i$ is the view-factor between surface $i$ and the person. Figure 2.5 shows the various physiological responses at different values of various thermal indexes. The human body is defined to be in a comfortable state between $9 \geq$ UTCI $\geq 26$ °C. Above this regime, heat stress occurs, where sweating rate and skin temperature starts to increase. The physiological stresses above comfort level are categorized as slight, moderate, strong and extreme heat stresses.

## 2.2 IMPACT OF VEGETATION ON URBAN MICROCLIMATE

Urban greening solutions is seen as an effective tool to mitigate the growing UHI and improve the climate in urban areas (Bowler et al. 2010; Gillner et al. 2015; Loughner et al. 2012). The energy contribution of the latent heat flux from vegetation in urban microclimate cannot be neglected as seen in section 2.1.3. Furthermore, urban vegetation has a direct influence on the aerodynamic, radiative, thermal and moisture properties of the urban microclimate (Oke et al. 1989). Thus, the interaction of urban vegetation with the environment can be seen as the coupling between the radiative, heat and moisture balance, as depicted in Fig. 2.6. Therefore, to accurately assess the impact of urban vegetation on the urban microclimate, these coupled processes must be taken into account.

The influence of plants on the microclimate in an urban environment is of growing interest due to the need of mitigating detrimental effects of urbanization and climate change on urban air temperature (Demuzere et al. 2014; Dimoudi and Nikolopoulou 2003; Matthews et al. 2017; Shashua-Bar and Hoffman 2000; Shashua-Bar et al. 2009; Yu and Hien 2006). Plants modify the climate by intercepting solar radiation and by extracting heat from the environment through transpiration during photosynthesis (Nobel 2009). Furthermore, the plant interferes with the airflow, extracting momentum and enhanc-

ing turbulent mixing (Finnigan et al. 2009; Gromke et al. 2015; Sanz 2003). Due to the present growing need to ensure that cities are resilient and can mitigate the rising temperatures, proposed mitigation strategies are to be properly assessed and such assessment requires an adequate characterization of the effects of vegetation.

Foliage density is known to have an impact on the wind sheltering provided by a plant (Bitog et al. 2011; Bitog et al. 2012; Guan et al. 2003; Manickathan et al. 2018a). The aerodynamic properties of vegetation can be expressed simply through porosity and drag coefficient (Grant and Nickling 1998; Guan et al. 2003; Manickathan et al. 2018a). The porosity and drag coefficient are known to depend on plant species (Cao et al. 2012; Manickathan et al. 2018a; Rudnicki et al. 2004; Vollsinger et al. 2005), age (Dahle and Grabosky 2010) and, for deciduous plants that shed leaves during winter, the parameters have been observed to vary seasonally as well (Dellwik et al. 2019; Hwang et al. 2011; Maass et al. 1995). It is known that plant porosity can have an impact on turbulent mixing (Bai et al. 2012; Hiraoka and Ohashi 2008; Manickathan et al. 2018a; McClure et al. 2017), which is seen to directly impact the thermal and pollutant dispersion characteristics of air flow (Conan et al. 2015; Gromke and Blocken 2015; Gromke and Ruck 2008; Gromke et al. 2008). Plants with high foliage density are seen to have a detrimental effect on pollutant dispersion of below-canopy pollutant sources such as automobiles (Nowak et al. 2006). Nevertheless, a high foliage density is also shown to have a beneficial impact on the pedestrian thermal comfort due to increased shading provided by the plant (Hwang et al. 2011; Morakinyo et al. 2017; Ng et al. 2012). Foliage density is parameterized using the leaf area index (LAI) to describe the net area of leaves and leaf area density ($a$) to describe the foliage distribution within the plant volume. A dense plant canopy can result in a significant amount of solar radiation being absorbed resulting in a high leaf-to-air temperature (Hiraoka 2005; Leuzinger and Körner 2007; Manickathan et al. 2018b). Higher plant transpiration is then required to compensate for the high solar radiation absorption (Manickathan et al. 2018a), and this can result in a lower air temperature under the foliage (Wong et al. 2003). Studies have also revealed that plant transpiration rate varies not just due to atmospheric evaporative demand (AED) (Kichah et al. 2012; Manickathan et al. 2018b; McVicar et al. 2012; Tuzet et al. 2003) but can also dynamically vary

during the day with higher transpiration during morning than in the evening (Huang et al. 2017; Tuzet et al. 2003).

### 2.2.1 *Influence of vegetation on the energy balance*

The energy balance satisfies:

$$\underbrace{\text{energy into leaves}}_{\substack{\text{absorbed radiation}}} - \underbrace{\text{energy out of leaves}}_{\substack{\text{emitted infrared}\\ \text{heat convection}\\ \text{heat conduction}\\ \text{evapotranspiration}}} = \underbrace{\text{energy stored}}_{\substack{\text{metabolism}\\ \text{heat capacity}}} \tag{2.6}$$

Typically, the energy storage is small with respect to heat gain and heat loss. The heat conducted and convected is the sensible heat and the heat loss due to evaporation and transpiration at the leaf surface is known as latent heat. The resulting formulation can be simplified to:

$$q_{rad,leaf} + q_{sen,leaf} + q_{lat,leaf} = 0 \tag{2.7}$$

where $q_{rad,leaf}$ is the net radiative flux ($\mathrm{W\,m^{-2}}$) consisting of absorbed net radiation and the emitted radiation from the leaves. In the context of urban microclimate, the radiative heat flux is divided into two components: the short-wave radiative heat flux $q_s$ ($\mathrm{W\,m^{-2}}$) and the long-wave radiative heat flux $q_r$ ($\mathrm{W\,m^{-2}}$). The short-wave component is also known as the solar radiation as it describes the radiation emitted from the sun, dealing with the portion of electromagnetic spectrum consisting of UV, visible and near-Infrared (NIR) radiation. On the other hand, the long-wave component is known as thermal radiation as it describes the radiation emitted by terrestrial elements such as buildings, vegetation, and clouds. The portion of electromagnetic spectrum it occupies is above 2-5 $\mu$m.

Figure 2.7 shows the spectral distribution associated to the short-wave and long-wave radiative heat fluxes, where it is simply a function of the temperature of the emitting body. The Stefan-Boltzmann law describes the radiative energy flux density $E$ ($\mathrm{W\,m^{-2}}$) of a given body:

$$E = \varepsilon\,\sigma\,T^4 \tag{2.8}$$

where $\varepsilon$ is the emissivity of body, $\sigma = 5.67 \times 10^{-8}\ \mathrm{W\,m^{-2}\,K^{-4}}$ is the Stefan-Boltzmann constant, and $T$ is the surface temperature (K).

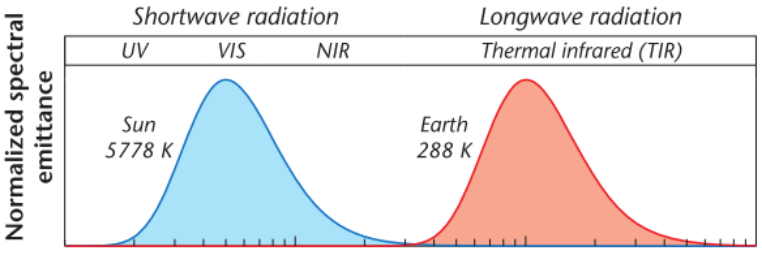


Figure 2.7: Decomposition of the energy spectrum into two distinct parts: short-wave radiation $q_s$ and long-wave radiation $q_r$ (Oke et al. 2017).

Unlike buildings, which are regarded as opaque, vegetation is a semi-transparent medium which transmits radiation depending on the wavelength. Figure 2.8 shows the radiation absorption, transmission, and reflection fraction of a leaf. The leaves are semi-transparent to wavelength in between 0.5 and 2 $\mu$m. However, below and above these wavelengths, the leaves can be considered as an opaque medium absorbing all the radiation. Therefore, vegetation such as trees plays an essential role in the radiative balance in an urban area. Figure 2.9 shows an infrared image indicated the shading effect of a tree on an asphalt street, where a surface temperature drop of up to 15.2 K was observable.

The sensible heat flux $q_{sen}$ (W m$^{-2}$) is directly related to the temperature gradient:

$$q_{sen} = h_{c,h} \left( T_{leaf} - T_a \right) \tag{2.9}$$

where $h_{c,h}$ is the convective heat transfer coefficient (CHTC) (W m$^{-2}$ K$^{-1}$), $T_{leaf}$ (K) is the leaf temperature, and $T_a$ (K) is the air temperature. Therefore, a larger temperature gradient or a larger CHTC results in larger sensible heat flux. Figure 2.10 shows a typical range of leaf and air temperature during day and night. The leaf temperature is dependent on the photosynthetic rate and can either add or extract sensible heat from air depending on the sign of the temperature gradient.

Finally, due to photosynthesis the latent heat flux generated from transpiration also has an impact on the energy balance. The latent heat flux $q_{lat}$ (W m$^{-2}$) from the leaf surface is:

$$q_{lat} = L_v g_{v,leaf} \tag{2.10}$$

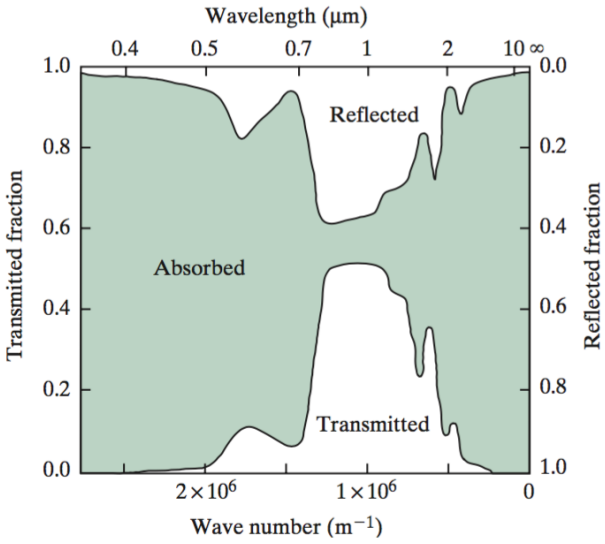


Figure 2.8: Electromagnetic spectrum absorbed, transmitted, and reflected by a leaf (Lambers et al. 2008; Nobel 2009).


Figure 2.9: Infrared image assessing the shading effect of a tree (*Tilia cordata*) on an asphalted streets (Gillner et al. 2015).

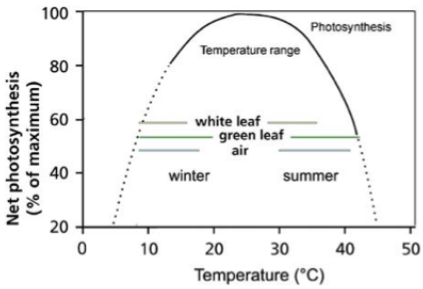


Figure 2.10: Typical daily range of air and leaf temperature of glabrous green winter leaves and pubescent white summer leaves of *Encelia farinosa* (brittlebush) (Lambers et al. 2008).

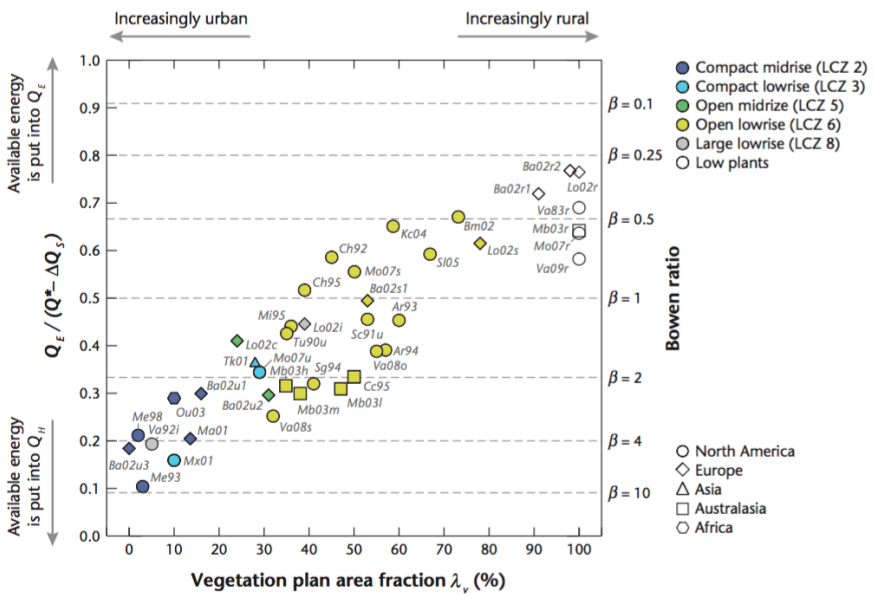


Figure 2.11: Dependency of Bowen ratio $\beta$ to vegetation density for various cities around the world (Oke et al. 2017).

where $L_v = 2.464 \times 10^6\ \mathrm{J\,kg^{-1}}$ (at 15°C) is the latent heat of vaporization and $g_{v,leaf}$ is the net evaporation and transpiration (i.e. evapotranspiration). During condensation, latent heat is released from water vapor in the air resulting in a temperature rise. During evapotranspiration, the opposite happens, where latent heat in the domain is increased, resulting in a temperature drop. Thus, the evapotranspiration rate of an urban area can become an effective strategy to extract the thermal energy from the environment. The resulting mitigation strategy is termed as evapotranspirative cooling (Taha 1997). It has been observed that evapotranspirative cooling can generate oases that are up to $2 - 8$ °C cooler than other urban areas (Oke et al. 1989; Taha et al. 1991). An effective parameter that can give an insight into the cooling effect is the Bowen ratio $\beta$:

$$\beta = \frac{Q_s}{Q_l} \tag{2.11}$$

where it is simply the ratio between sensible and latent heat fluxes. Cities with high Bowen ratio (such as $\beta > 1$) are attributed to having either lower vegetation density or litter open water surfaces and higher density of impervious urban structures. Figure 2.11 shows that there is a linear relationship between the Bowen ratio and vegetation density for various cities around the world. A higher vegetation density results in increased energy conversion to latent heat in the domain. However, it must be noted that the lower Bowen ratio can indicate higher humidity flux in the atmosphere due to increased evapotranspiration which can diminish the thermal comfort.

### 2.2.2 *Transpiration driven water cycle*

The water cycle driven by vegetation is a fundamental aspect of the influence of vegetation in cities. The transpiration driven or the vegetation water cycle is divided into three main aspects: water movement from soil to plant, water movement inside the plant, and finally the water movement from plant to the atmosphere. This process is the essence of the soil-plant-atmosphere continuum model, where the cohesion-tension theory is the mechanism used to describe the water movement (Dixon and Jolly 1895).

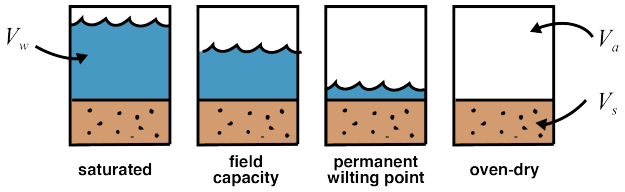


Figure 2.12: Various degrees of soil moisture: $V_w$ is volume of water, $V_a$ is volume of air and $V_s$ is volume of soil.

An important variable used to define the state of water in various domains (e.g., soil, plant, air) is the water potential $\psi$. Water travels from high water potential to low water potential, and so, the transport of water can be determined merely from the water potential gradient. It is formulated as follows:

$$g = k \nabla \psi \tag{2.12}$$

where $g$ is the water flux, $k$ is the conductance, and $\psi$ is the water potential. Therefore, for water to be supplied at the leaf from roots for transpiration, a sufficient gradient is required between the soil water potential and the leaf water potential. As the water demand at the leaves increases, a larger gradient will be required. Following this logic, water stress (i.e., difference between leaf water potential and soil water potential) is minimal before dawn and maximum during midday.

The water stress is magnified as the soil dries. Figure 2.12 shows the various degrees of soil moisture that can exist. The volumetric water (or moisture) content $\theta$ (%) is defined as the ratio of mass of water $V_w$ to the total volume $V$ (i.e. $V = V_w + V_a + V_s$),

$$\theta = \frac{V_w}{V} \tag{2.13}$$

and provides a relative measure of volume of water. Similarly, the soil moisture content $w$ ($\mathrm{kg\,m^{-3}}$) is defined as the ratio of mass of water $m_w$ to the total volume $V$

$$\theta = \frac{m_w}{V} \tag{2.14}$$

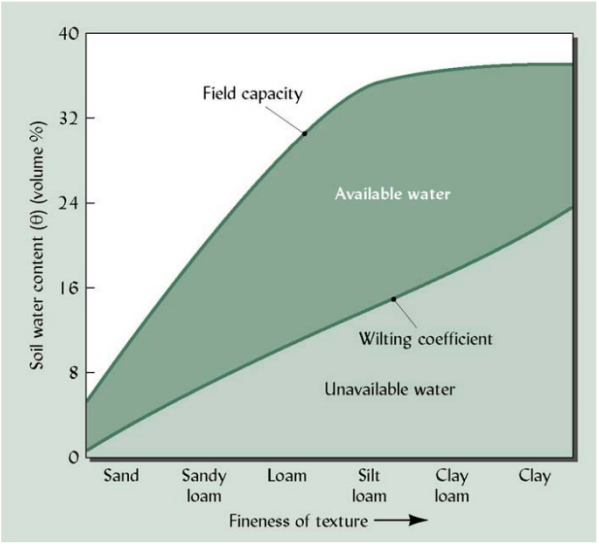


Figure 2.13: Soil water content for various soil types: sand, sandy loam, loam, silty loam, clay loam, and clay (Nobel 2009).

The water content in the soil is maximum at saturated conditions, and as the soil dries, the soil moisture reaches the field capacity. The field capacity is the equilibrium state after an excess amount of water has drained away. As the soil dries further, the soil moisture reaches the permanent wilting point (PWP) or wilting point. Below the wilting point, plants start to wilt (i.e., the plant cells loose turgidity) and can no longer recover from the water stress. Typically, the wilting point is defined to be at a water potential of $\psi = -1.5$ MPa. However, the water content associated with this water potential depends on the soil type. Figure 2.13 shows the regimes of field capacity and wilting point for various soil types.

A larger difference between field capacity and the wilting point indicates a larger availability of water for the plants. We see that sand cannot hold much water and furthermore, it quickly dries towards the wilting point. Whereas, loam and silt loam is seen to have a larger field capacity and buffer of water until it reaches the wilting point. Figure 2.14 shows the typical dependency of the soil water potential $\psi$ to the volumetric soil water content $\theta$ (i.e., ). The optimal zone for a plant is between the field capacity and around 10 orders of magnitude above the wilting point. The figure also shows that

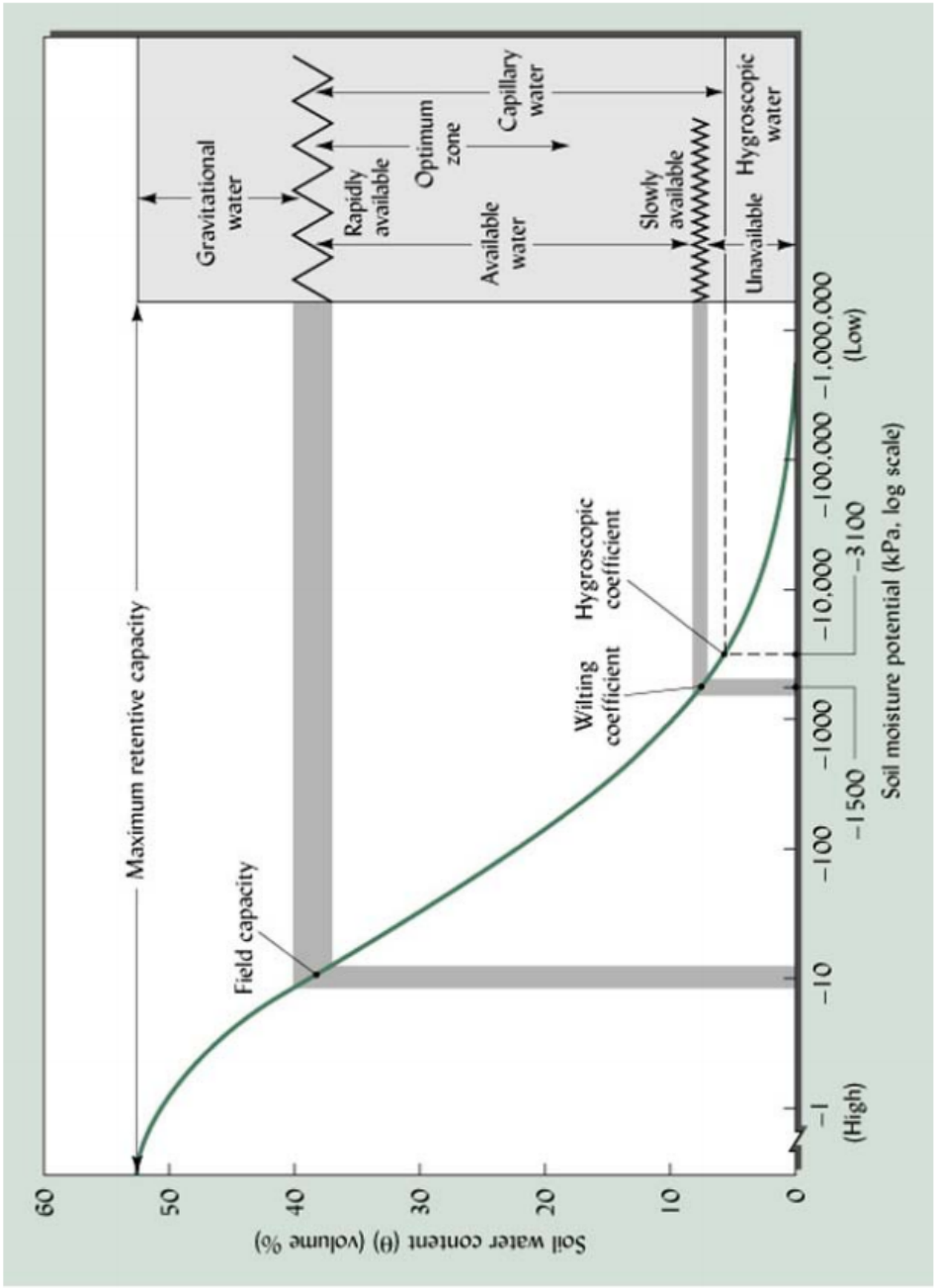


Figure 2.14: A typical relation of soil water potential $\psi$ as a function of soil water content $\theta$ (Nobel 2009).

with high water content, water potential varies less. However, approaching the wilting point, the water potential drops exponentially, indicating a non-linearity in the water stress.

Figure 2.15 shows the diurnal response of soil, root and leaf water potential. We see that once the water potential too low, the onset of leaf wilting can compromise the transpiration driven water cycle and potential the health of the plant. Therefore, plants are more susceptible to lower soil moisture content, and in cities, water availability will become a critical factor, especially during a heat wave, for the survivability of the urban vegetation.

## 2.3 ASSESSING IMPACT OF VEGETATION USING EXPERIMENTAL METHODS

Various experimental approaches have been employed to assess the response of plants to environmental conditions ranging from field measurements (Dellwik et al. 2019; Grant and Nickling 1998; Hagishima et al. 2007; Koizumi et al. 2016; Shashua-Bar and Hoffman 2000; Shashua-Bar et al. 2009; Yuan et al. 2017), greenhouse studies (Fatnassi et al. 2006; Ganguly and Ghosh 2009; Majdoubi et al. 2009; Montero et al. 2001), and wind tunnel experiments (Grace and Russell 1977; Liu et al. 2018; Manickathan et al. 2018a; Miri et al. 2019; Rudnicki et al. 2004; Vollsinger et al. 2005; Yue et al. 2008). Wind tunnel experiments, which provide the most control over the airflow conditions, typically focus on the aerodynamic characteristics such as drag coefficient, porosity, and sheltering effect of plants and neglect the hygrothermal responses of the plant (Grace and Russell 1977; Manickathan et al. 2018a). Therefore, the relationship between porosity heterogeneity and hygrothermal conditions of plants has yet not been experimentally observed and characterized. Moreover, few studies provide a high-resolution temporal and spatial study of the hygrothermal conditions of the plant which can be used for validating numerical models. Thus, there is a need for high-resolution experimental datasets investigating the links between plant morphology, and atmospheric conditions including diurnal variations of the hygrothermal conditions such as air temperature, and relative humidity and how all of these affect plant conditions.

### 2.3.1 *Field measurements*

Field measurements or "*in-situ*" measurements provide the most realistic kind of measurements. There exist various measurement techniques for determining the evaporation or evapotranspiration. A summary of these techniques is provided below:

- *Pan evaporation*: Evaporation rate measured by measuring the change in volume of water in an open pan (Abtew and Melesse 2012; Crowell and Mtundu 2000; Farquhar and Roderick 2007; Finnigan 1979). It is one of the simplest and common technique to measure the water evaporation.

- *Lysimeters*: Lysimeters are used to measure the net evaporation and transpiration from the plant and soil (Abtew and Melesse 2012; Abtew 1996).

- *Eddy correlation*: Measures the vertical wind speed and local humidity at high temporal resolution (German 2000; Shuttleworth 1993). The covariance of these two variables quantifies the water vapor flux, where $u_z'$ is the vertical fluctuating velocity and $w'$ is the fluctuating moisture content of air.

$$G_v = \overline{u_z' w'} \tag{2.15}$$

- *Bowen ratio*: The Bowen ratio dependent on the change in air temperature and vapor pressure provide an estimate for the net evapotranspiration by satisfying the urban energy balance (Abtew and Melesse 2012; Deardorff 1978; Dos Reis and Dias 1998; Thom et al. 1975; Yu and Hien 2006).

$$\mathrm{B} = \frac{Q_s}{Q_l} = \gamma \frac{\Delta T}{\Delta p_v} \tag{2.16}$$

- *Lidar*: Lidar or Light Detection and Ranging method can be used to sample the 3-D profile of water vapor concentration over the surface (Abtew and Melesse 2012; Idso 1977).

- *Remote sensing*: Remote sensing methods such as from a satellite instrument can also provide an estimation of the evapotran-

spiration rate (Abtew and Melesse 2012; Kustas 1990; Melesse et al. 2008; Melesse et al. 2009).

However, a study on the mitigation potential of vegetation using such measurement is usually difficult as it requires a parametric study on the vegetation configuration. Authors have shown the possibility of hygrothermal measurements such as in a scaled street canyon to study the mitigation potential of vegetation such as green roofs or green walls (Djedjig et al. 2015; Malys et al. 2014). Figure 2.16 shows a setup used to measure the microclimate of such green facades. Such reduced-scale studies enable to assess the impact of vegetation on the nearby building where configurations with and without vegetation can be assessed. Various authors have also studied the microclimate of crops in greenhouse (Baille et al. 1994; Boulard and Wang 2002; Fatnassi et al. 2006; Kichah et al. 2012; Montero et al. 2001; Roy 2011). Such studies provide a more controlled setup. The focus of such studies is to access the transpiration rate of plants and the microclimate developed around the plants and not necessarily towards the advancement of novel UHI mitigation strategies.

### 2.3.2 *Wind tunnel measurements*

Similar to greenhouse studies, wind tunnel measurements provide a level of control that is seldom available from field measurements. Atmospheric boundary layer wind tunnel studies focus on trees in an urban setting (Gromke 2011; Gromke and Ruck 2008), measurements of flow past windbreaks (Guan et al. 2003) or in forest canopies (Bai et al. 2013; Conan et al. 2015; Kinnersley et al. 1994), but are limited to the use of small model trees to match the size of building models typically used in these wind tunnel studies. This requirement prohibits the use of a larger mature natural tree. However, it is not known sufficiently to which extent small model trees can substitute such natural trees and whether both types display similar aerodynamic characteristics. There are several difficulties associated to scaling down of large natural trees to smaller model trees. Natural trees vibrate, deform and reconfigure, which all directly influence the drag and the resulting flow field around the tree (Schouveiler and Boudaoud 2006; Tadrist et al. 2014; Vogel 1989).

The mechanical properties of the tree are known not to scale linearly with size, so this fact should be considered when employing model trees to represent their larger counterparts (de Langre 2008). Moreover, predicting the dynamic response of a natural tree itself is a complex task due to the anisotropy in the material properties of the plant (James et al. 2017). The tree trunk wood of natural trees are known to have a radial anisotropy, resulting in a more complex mechanical response compared to isotropic materials (Albrecht et al. 2016). Furthermore, the location of the plant during its growth, for example forest-grown trees versus isolated trees, is known to alter the final form of the canopy architecture (James et al., 2014). Therefore, the plant growth history also plays a vital role in the plant morphology, and will result in a different mechanical response. Moreover, the age of the plant, varying from juvenile sapling to a mature plant, will further influence the mechanical properties of the plant. In this context, various authors have shown that the elastic modulus varies not only with species but also with the maturity of the plant (Dahle and Grabosky 2010; Macdonald and Hubert 2002; Telewski 1995; Watt et al. 2008; Woodrum et al. 2003). It is challenging to capture such allometric and morphological variability of different plants with small model trees. Without adequate care when designing the model trees, the response of model trees will not accurately represent natural trees that are found in an urban environment.

Furthermore, measurement techniques such as Particle Image Velocimetry provide a level of detail of the flow structure that is not possible from field measurements. The downside to wind tunnel measurements is the requirement for scale similarity and requirement for measurement facility. Various authors have successfully studied the flow characteristics of natural vegetation. Cao et al. (2012) compare various shrubby trees including a deciduous, coniferous, and broadleaf evergreen tree. The study investigated the dependency of drag and the overturning moment of various tree species to wind speed. Similarly, wind tunnel measurements are performed for hardwood species (Vollsinger et al. 2005) and conifers (Bitog et al. 2011; Mayhead 1973; Vollsinger et al. 2005). These controlled experiments provide a better understanding of the influence of tree morphology on the drag coefficient. These measurements can be then used to improve existing computational fluid dynamics (CFD) models and accurately assess their impact on the flow (Bitog

et al. 2011). The PIV measurements of the tree wake can provide additional means of quantifying the turbulence modification due to trees in the flow (Lee and Lee 2012; Lee et al. 2014). Furthermore, these studies show additional understanding of sheltering provided by trees. The drag measurement is a useful tool to quantify the sheltering factor of the porous tree (Gromke and Ruck 2008; Guan et al. 2003; Kinnersley et al. 1994). Table 2.1 briefly summarizes previous studies of drag forces on model and natural trees in wind tunnels. The natural trees are categorized into two types: hardwood and coniferous species. In these studies, the drag measurements are performed under airflow varying between 4 and 20 $\mathrm{m\,s^{-1}}$. The main limitation of wind tunnel measurements is the height of the wind tunnel, as it restricts the maximum size of the measured trees. Nevertheless, these controlled experiments provide an improved understanding of the influence of tree morphology on the drag coefficient. They can improve the computational fluid dynamics (CFD) modeling of vegetation and respective model calibration, and thereby enable a more accurate assessment of the impact of vegetation on the environment (Bitog et al. 2011; Bitog et al. 2012). Additionally, wind tunnels enable non-intrusive flow measurements of the tree wake using particle image velocimetry (PIV). Such PIV measurements of the wake allow quantifying the impact on turbulence and the degree of sheltering provided by trees (Lee and Lee 2012; Lee et al. 2014).

Turbulent momentum exchange of vegetation with the environment was also investigated experimentally, such as in wind tunnels. In these studies, the flow field around the vegetation is typically correlated to its drag coefficient. Gromke and Ruck (2008) investigated the flow around small model trees of various porosity and material, as shown in Figure 2.17. They used Laser Doppler Velocimetry (LDV) to perform a spectral analysis of the velocity, enabling to correlate the drag coefficient to the TKE dissipation. Investigations for natural, flexible trees were performed by Rudnicki et al. (2004) and Vollsinger et al. (2005), where the effects of pruning and streamlining are quantified using drag coefficient measurements. Cao et al. (2012) employed a similar approach and investigated the impact of volumetric density on various deciduous, coniferous, and broadleaf evergreen trees (Figure 2.18). However, a detailed experimental study on the influence of natural vegetation on the flow using detailed flow field measurements nor a study of combining vegetation and a built

Table 2.1: Summary of previous studies measuring the drag coefficient of model and natural trees in wind tunnel.

| Tree type | Species | $H$ (m) | $U$ (m s$^{-1}$) | References |
|---|---|---|---|---|
| model | wood-wool | 0.115 | 5.5 – 13.5 | Gromke and Ruck (2008) |
| model | sisal-fibre | 0.115 | 5.5 – 13.5 | |
| coniferous | emerald cedar[a] | 0.98 | 5 – 15 | Cao et al. (2012) |
| hardwood | rose of sharon[b] | 1.24 | 5 – 15 | |
| coniferous | western redcedar[c] | 1.95 | 4 – 20 | Vollsinger et al. (2005) |
| coniferous | western hemlock[d] | 1.95 | 4 – 20 | |
| coniferous | lodgepole pine[e] | 1.95 | 4 – 20 | |
| hardwood | red adler[f] | 1.95 | 4 – 20 | Vollsinger et al. (2005) |
| hardwood | trembling aspen[g] | 1.95 | 4 – 20 | |

Scientific names: [a]*Thuja occidentalis Smaragd*, [b]*Hibiscus syriacus*, [c]*Thuja plicatas*, [d]*Tsuga heterophylla*, [e]*Pinus contorta*, [f]*Alnus rubra*, [g]*Populus tremuloides*

environment is not available in the literature. The evolution of the turbulent flow field within the vegetation is difficult to measure in a wind tunnel using imaging techniques such as PIV as the flow inside is occluded by the foliage from the camera. However, the knowledge on the relation between turbulent production and dissipation within the vegetation is an essential determinant for the exchange processes of vegetation and the airflow. The simplest representation of trees is a porous fence. Various authors in the past have studies the flow past a thin porous fence: (Conan et al. 2015; Dong et al. 2010; Gandemer 1979; Hagen and Skidmore 1971; Perera 1981). The model construction approach has also been extended to study flow past 3D dense vegetation and to study the flow through vegetation canopy (Conan et al. 2015; Poggi et al. 2004). Figure 2.19 shows a typical construction of vegetation canopy for wind tunnel studies. Such studies enable to understand passive scalar transport modification such as pollution dispersion due to vegetation (Gromke 2011; Gromke et al. 2008). A more advanced model constructions have also been employed where fractal type porous structures are made to mimic the tree structure (McClure et al. 2017). Authors have also modeled a resolved tree canopy using fractal dimensioning (Bai and Katz 2014; Bai et al. 2012).

## 2.4 ASSESSING IMPACT OF VEGETATION USING NUMERICAL METHODS

The global influence of vegetation on the local climate has been assessed by using urban microclimate models (Bruse and Fleer 1998; Robitu et al. 2006). There are two distinct classes of modeling the flow past vegetation: resolved approaches (Endalew et al. 2006; Endalew et al. 2009) and unresolved approaches using porous media approaches (Gromke et al. 2015; Katul et al. 2004; Kenjereš and ter Kuile 2013; Sanz 2003). In the resolved type of numerical methods, the elements of vegetation are directly resolved, where the Dirichlet and Neumann boundary conditions are directly prescribed. When employing a porous media approach, vegetation is simplified to representative volume elements, defined through the leaf area density $a$ ( or $LAD$) ($\mathrm{m}^2\,\mathrm{m}^{-3}$):

$$a = \frac{A_{leaf}}{V} \tag{2.17}$$

defined as the ratio between one-side leaf surface area $A_{leaf}$ in a given volume.

### 2.4.1 *Integral energy budget models*

There exist various approaches to model evapotranspiration $E$ (Abtew and Melesse 2012):

- *Temperature-based methods*: The evapotranspiration is determined empirically from air temperature.

$$E = f(T) \tag{2.18}$$

- *Radiation-based methods*: The evapotranspiration is determined from an empirical relation from downward short-wave radiation.

$$E = f(Q_{r,sw}) \qquad \text{or} \qquad E = f(T, Q_{r,sw}) \tag{2.19}$$

- *Energy balance methods or Penman-Monteith method*: The evapotranspiration is determined from the urban energy balance, taking in account of the momentum transfer, mass transfer, heat storage, and heat conduction:

$$E = \frac{1}{\lambda} \frac{\Delta \left(Q_{r,net} - Q_c\right) + \rho c_p k_a \left(p_v - p_d\right)}{\Delta + \gamma \left(1 + \frac{k_a}{k_c}\right)} \tag{2.20}$$

  where $k_c$ is the canopy conductance.

In literature, several approaches have been used to model the heat and mass exchange of vegetation with the air. The big-leaf approach treats the whole canopy as a single leaf to determine the exchanges between vegetation and environment (Penman and Schofield 1951; Sellers et al. 1996; Shuttleworth and Wallace 1985). A dual-big-leaf approach can differentiate sunlit and shaded leaves, providing an improvement to the big-leaf model (Dai et al. 2004). As an extension to these models, a multi-layer model segments the vegetation into layers, introducing a vertical heterogeneity concerning evapotranspiration in the vegetation (Leuning et al. 1998; Wang and Jarvis 1990). These vertical energy budget models are used as simple rep-

resentations of vegetation in urban microclimate models (Dolman 1993; Krayenhoff et al. 2014; Ryder et al. 2014).

Salim et al. (2015) showed that numerical models should take into account the influence of trees without gross averaging approaches or surface parameterization and instead at least employ explicit approaches such as representing trees by porous media. This is especially important when wind flow patterns are the driving factors of the microclimate. Furthermore, parameters such as wind direction and foliage density and its interaction with urban configuration can be studied. Therefore, computational fluid dynamics models are seen as a better approach to achieve this goal. Such explicit methods allow to take into account parameters such as wind direction, and foliage density distribution. To represent trees as a porous medium, their drag coefficient is required and is typically assumed to be constant and independent of wind speed, and dependent only on tree species (Wilson and Shaw 1977).

### 2.4.2 *Computational fluid dynamics model*

*Turbulent momentum exchange*

To represent trees as a porous medium, their drag coefficient is required, which is typically assumed to be constant, independent of wind speed and tree species (Wilson and Shaw 1977). The porous media formulation of vegetation is obtained from the filtered Navier-Stokes where the filter is the representative volume element (REV). The filtered Navier-Stokes equations used for porous media formulation of vegetation has two additional terms:

$$-\frac{1}{\rho}\langle\nabla p''\rangle + \nu\langle\nabla^2 \boldsymbol{u}''\rangle \tag{2.21}$$

where the first term is the contribution due to pressure $p$ and the second term is the viscous contribution of the plant at velocity $u$. The problem is closed using Darcy-Forcheimer type force equation:

$$F_d = a_1 U^2 + a_2 U \tag{2.22}$$

and typically, the viscous drag is assumed to be negligible compared to the form drag (Raupach and Thom 1981; Sanz 2003). So, the effect

of vegetation on momentum is described by the following expression:

$$\boldsymbol{f} = c_d a \boldsymbol{u} |\boldsymbol{u}| \tag{2.23}$$

where $a_1 = c_d\, a$, $c_d$ is the leaf drag coefficient (-) and $a$ is defined as leaf area density ($m^2\, m^{-3}$) defining a spatially varying vegetation density. During the simulation, the drag coefficient and leaf area density are usually fixed. However, de Langre et al. (2012) shows that flexible tree foliage undergoes reconfiguration, particularly at high wind speeds as the leaves and branches reorient themselves along the wind direction. Such reconfiguration influences the flow through trees and the resulting drag coefficient. Similar findings are made during in-situ measurements of mature trees (Grant and Nickling 1998; Kane and Smiley 2006; Koizumi et al. 2016). Turbulent momentum exchange of vegetation with the environment employing Computational Fluid Dynamics (CFD) was initially investigated for canopy flow, mainly using the Reynolds-Averaged Navier Stokes approach (RANS). Wilson and Shaw (1977) developed a one-dimensional mathematical model for turbulent airflow around vegetation canopies with closure for mean momentum, turbulent kinetic energy (TKE) and turbulent dissipation rate (TDR). Liu et al. (1996) determined source/sink terms for a two-dimensional $k - \varepsilon$ model, thereby modeling vegetation as a porous media. They investigated the eddy diffusivity past a forest edge and discussed the accuracy and limitation of employing the two equation closure model. Liang et al. (2006) improved the $k - \varepsilon$ closure model for vegetation with additional terms and investigated 3D flow past a small forest immersed in atmospheric boundary layer flow. Regarding the urban environment, Kenjereš and ter Kuile (2013) assessed the turbulent flows in urban areas with vegetation using a $k - \varepsilon$ turbulence closure. Bruse and Fleer (1998), Robitu et al. (2006) and Gromke and Blocken (2015) also employed the $k - \varepsilon$ turbulence closure or a modified $k - \varepsilon$ model for urban studies. Such RANS approaches are usually employed to investigate the turbulent momentum exchanges between three-dimensional heterogeneous vegetation and the environment. Some authors have also employed large-eddy turbulence modeling approach (LES) for the canopy flows (Lopes et al. 2013; Maruyama 2008; Moonen et al. 2013; Shaw and Schumann 1992). These approaches enable instantaneous realizations of the turbulent

velocity and scalar fields. The benefit of such model is that the turbulence closure due to vegetation requires less empirical formulation (Hiraoka 2011; Lopes et al. 2013). However, the downside is the high computational cost comparing to RANS models. Therefore, RANS approaches are preferred (specifically $k - \varepsilon$ derivatives) as they enable higher number of simulation of various design cases of interest. Moreover, larger parametric studies can enable the analysis and optimization of urban mitigation strategies.

*Heat, mass and radiative exchanges*

To describe the real three-dimensional heterogeneity of heat and mass transport in vegetation, a more complex model is required. Dauzat et al. (2001) employed a virtual plant model to incorporate a detailed representation of plant geometry. The transpiration of the foliage was calculated for individual leaves. Sinoquet et al. (2001) coupled the energy balance of the leaves with a radiative transfer model. The authors introduced a coupled radiation absorption, transpiration, and photosynthesis (RATP) model where the vegetation was modeled as a turbid medium. Hiraoka (2005) considered the budget of heat, moisture, and carbon dioxide within a 3D vegetation model coupling a turbulence model with a diffusion approximated Ross's radiation transfer model and a stomatal conductance model developed by Collatz et al. (1991). These various studies show there exist various modeling approaches to determine the heat, mass, and radiative fluxes from vegetation. However, to accurately predict the effectiveness of vegetation, a fully coupled model including radiation such as developed by Hiraoka (2005) is required. The complex radiation model enables to determine the shading below the crown and thereby the cooling due to shading. The downside of the such complex radiation model is the computation cost associated to the ray tracing. Bailey et al. (2014) showed that the computational expense of ray tracing in the RAPT model can be reduced using parallelization in GPU hardware. Other studies such as studies on the response of vegetation inside a greenhouse show that radiation absorption within vegetation can be assumed to follow a vertical function (Kichah et al. 2012; Majdoubi et al. 2009). The model describes the radiation within vegetation as a function of the short-wave and long-wave component reaching the canopy. This approach enables

a fast and simple coupling of radiation with a turbulent flow field calculation of the vegetation and the environment making them effective for exhaustive parametric studies.

Increasingly, authors have started to apply CFD methods to study the performance of vegetation in cities for real situations where spatial distributions are of interests (Buccolieri et al. 2018; Gromke et al. 2015; Yoshida et al. 2006). Studies such as the cooling effect of parks have been studied using CFD models (Toparlar et al. 2018), green areas (Honjo and Takakura 1990; Ng et al. 2012) and green roofs (Alexandri and Jones 2008). However, typically, the cooling power of vegetation is parameterized as a function of LAD with a fixed or simplified volumetric cooling power $P_c$ ($\mathrm{W\,m^{-3}}$). Furthermore, the radiative exchanges between vegetation and the environment are either neglected or grossly simplified, where phenomena such as 3D tree shadowing dynamics are not taken into account.

### 2.4.3 *Soil-plant-atmosphere continuum*

In the presence of vegetation, water travels through the plant from the roots in the soil to the leaves exposed in the atmospheres. The resulting soil-plant-atmosphere pathway describes the transpiration driven water cycle modification. The theory used to describe the movement of water through the plant is the cohesion-tension theory by Dixon and Jolly (1895). The transpiration at the leaves creates a tension in the xylem and creates an upwards driving force on water at the roots. Figure 2.20 shows a schematic representation of the transpiration driven potential gradient. Bruse and Fleer (1998) coupled a vegetation model with a soil model to capture the water availability and investigate the response of the trees in urban configurations. Tuzet et al. (2003) investigated the coupling between the exchange of moisture from vegetation to the atmosphere, and the water availability at the roots. The model show the feasibility of coupling the stomatal conductance, photosynthesis, and leaf energy balance with a soil-plant-atmosphere water transport continuum model. Furthermore, the resulting plant transpiration is directly linked with the soil moisture content.

*Root water uptake*

An important aspect of the soil-plant-atmosphere continuum model is the root water uptake. Similar to the representing leaves in the air domain as porous media, the roots are typically represented in the soil as a sink in the water transport model. The root uptake is commonly modeled as a bulk sink term (Hopmans and Bristow 2002; Vrugt et al. 2001), where the net root water uptake is given as:

$$G_{root} = G_{leaf} \tag{2.24}$$

More recently, authors have employed a spatially varying root uptake model to study the influence of non-uniform soil moisture and dynamics such as hydraulic redistribution (Huang et al. 2017; Lai and Katul 2000; Manoli et al. 2014a; Manoli et al. 2014b; Volpe et al. 2013). However, the focus of these studies is on the hydrological phenomena of the soil and less on the atmospheric changes due to the plant transpiration. Therefore, there is a lack of understanding of how the water availability and the resulting dynamics have an influence on the climate above the ground.

## 2.5 NEED FOR FURTHER RESEARCH

The present thesis aims to address the main research need as found based on the literature review. The main gap is the lack of an integrated numerical model that can simultaneously answer the following questions:

- How does vegetation modify the urban heat, mass, momentum, and radiative fluxes at an urban microscale?
- What is the influence of environmental and plant condition on the natural cooling (transpirative and shadowing) provided by vegetation?
- How does the water stress affect the cooling provided by vegetation?
- What is the influence of vegetation on pedestrian thermal comfort?

There is a need for a rigorous approach that can predict the impact of transpiration from vegetation in an urban microclimate and directly assess the impact of vegetation on urban thermal comfort. Such a model can help study the cooling potential of vegetation and its potential mitigation factor. For this, a three-dimensional computational fluid dynamics (CFD) model of heterogeneous, porous vegetation needs to be developed, which calculates the turbulent momentum, heat, and mass exchanges of vegetation with the urban environment. Furthermore, as the important factor that drives the transpiration rate is the water availability at the root zone, a soil-plant continuum model is implemented to capture the full water transport cycle. This enables to investigate the water cycle between the atmosphere to the soil and then back to the environment via the vegetation. More importantly, the influence of water stress on the urban microclimate and its implication on thermal comfort can be addressed. Thus, the developed modeling framework aims to investigate the response of vegetation in an urban environment for various climate conditions, built and vegetation parameters.

## 2.6 CONCLUSION

The present chapter, reviewing the state of the art, provided a brief background and introduction to the urban climate discussing various urban climate scales, energy balances and the influence of vegetation at the microclimate scale. A brief study of various experimental techniques showed that wind tunnels experiments provide a level of control on the air flow condition that is not possible with field measurements. However, the cost is that smaller plants have to be used to ensure a minimal blockage effect inside the tunnel. In this thesis, wind tunnel measurements with small natural and model trees will be investigated to experimentally assess the impact of the plant on airflow and other microclimatic parameters such as air temperature and relative humidity. For an effective assessment, the experimental studies will be divided into two campaigns. The first part will investigate the impact of vegetation on the airflow. The aim will be to understand how the sheltering provided by small model trees differs from that of small natural trees and subsequently quantify the difference with mature trees. The second measurement campaign will assess the impact of vegetation on the

microclimate through the use of a small *Buxus sempervirens* plant. The literature review showed high-resolution measurement is possible with non-intrusive imaging techniques such as particle image velocimetry (PIV). Therefore, the flow field velocity statistics will be measured using stereoscopic particle image velocimetry (SPIV). A brief study of various numerical techniques showed that CFD methods are optimal at assessing the urban microclimate flow. Furthermore, we see that there is a need for an integrated approach that couples the conditions of the atmosphere with soil properties to determine the impact of water availability on the transpirative cooling potential of trees. So, a coupled model is to be developed to assess the hygrothermal impact of vegetation on the urban microclimate. The soil-plant-atmosphere continuum (SPAC) model will be used to link the plant transpiration with the soil moisture. The present thesis aims at assessing the impact of vegetation on the urban microclimate by understanding the influence of vegetation on turbulent urban airflow, the influence of transpiration on hygrothermal conditions, the influence of plant shading on the urban climate, and finally, the net effect on the pedestrian thermal comfort.

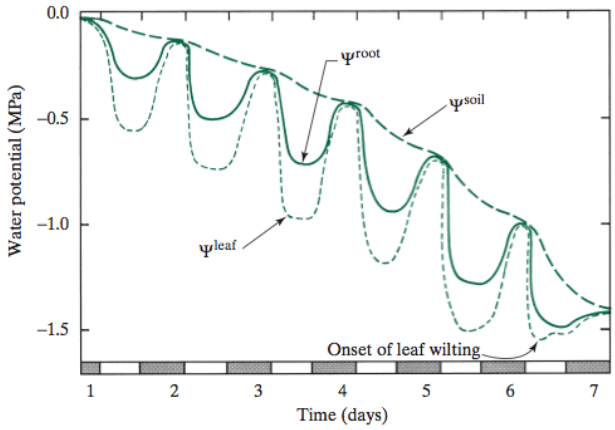


Figure 2.15: Schematic representation of diurnal change in soil, root, and leaf water potential (Nobel 2009).

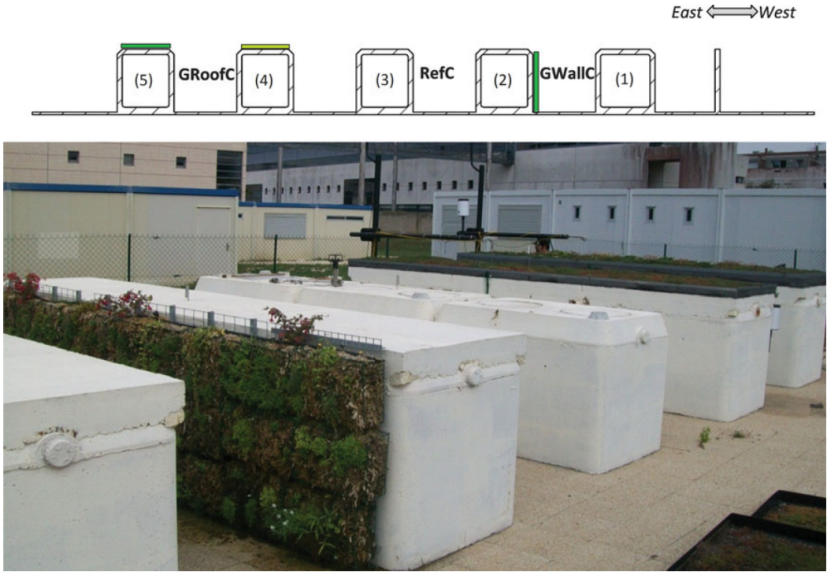


Figure 2.16: Microclimate study of green roofs and green walls in model street canyons (Djedjig et al. 2015)

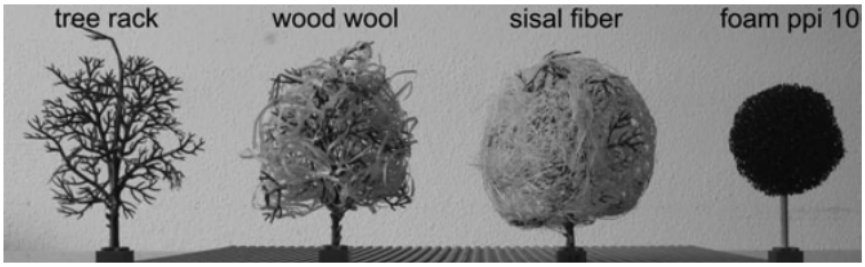


Figure 2.17: Different types of model trees used in wind tunnel studies (Gromke and Ruck 2008).

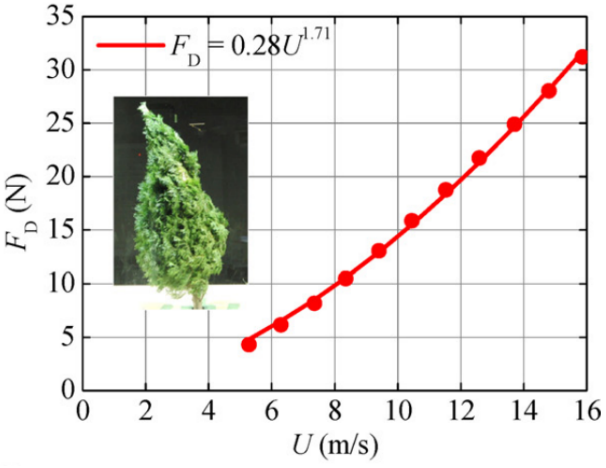


Figure 2.18: Drag measurement study of small trees in windtunnel (Cao et al. 2012).

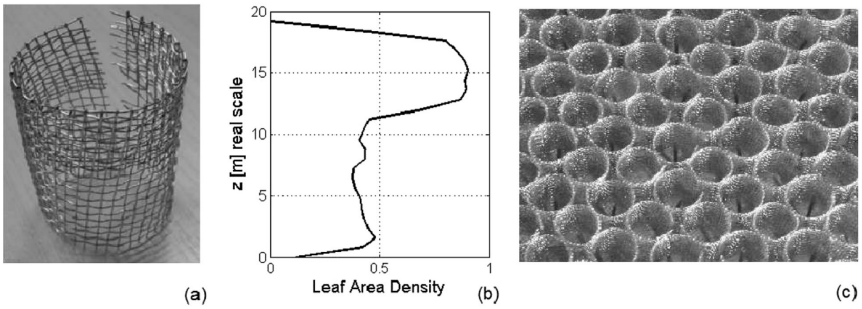


Figure 2.19: Wind tunnel model of a vegetation canopy from wire mesh (Conan et al. 2015): **(a)** a picture of single mesh ring, **(b)** the vertical distribution of leaf area density $a$ of the single mesh ring and **(c)** an arrangement of multiple mesh rings to to model vegetation canopy flow.

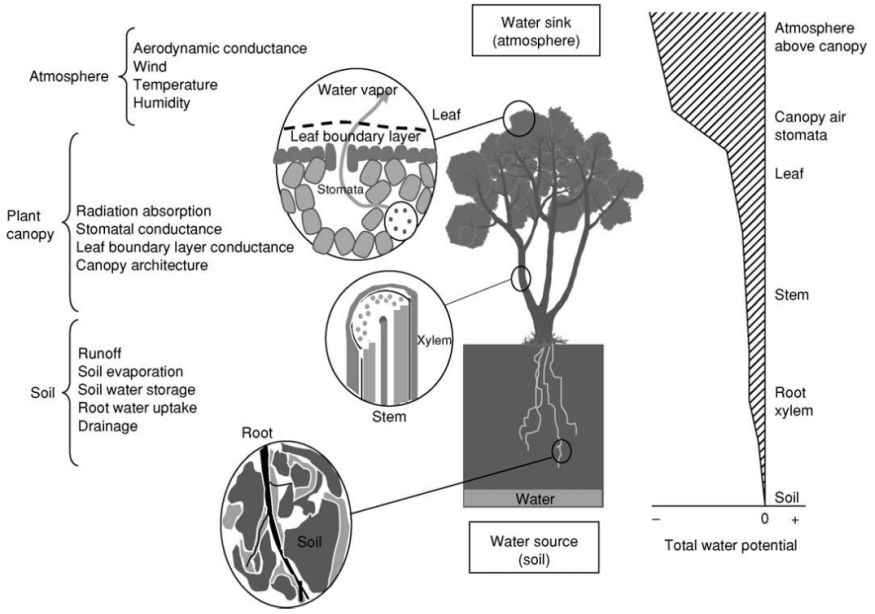


Figure 2.20: Water movement in plant due to transpiration at the leaf surface (Sławiński and Sobczuk 2011).

# 3

# EXPERIMENTAL STUDY OF THE IMPACT OF VEGETATION ON THE AIRFLOW

This chapter has been published as: Manickathan, L., Defraeye, T., Allegrini, J., Derome, D., & Carmeliet, J. (2018). "Comparative study of flow field and drag coefficient of model and small natural trees in a wind tunnel". *Urban Forestry & Urban Greening*, 230–239. http://doi.org/10.1016/j.ufug.2018.09.011.

## 3.1 INTRODUCTION

This chapter focuses on assessing the impact of vegetation on the airflow from experimental observation. The hygrothermal influence of vegetation such as the impact of plant transpiration on the atmosphere experimentally is studied in the next chapter, Chapter 4. In this chapter, we focus on the aerodynamic influence of plant foliage on the airflow. More specifically, we investigate how the drag coefficient, plant porosity, and foliage flexibility influence the wake velocity statistics. The objective of the present chapter is to obtain insight into the aerodynamic influence of vegetation.

Typically, the influence of trees in urban areas is assessed using urban microclimate models. These models rely on wind tunnel experiments using small-scale tree models to verify and validate their predictions of the flow field. However, it is not known sufficiently to which extent small model trees used in wind tunnel studies can recreate the behavior of large trees found in cities. In the present study, the drag coefficient and the turbulent flow downstream of model trees are compared with the ones of natural trees of a sim-

ilar size to determine whether both types of tree provide similar aerodynamic characteristics. Therefore, measurements of the drag force and the flow field, using particle image velocimetry, are performed. The aerodynamic characteristics of the small trees are compared with the ones measured on larger mature trees from previous studies. The present chapter shows that the drag coefficients of model and natural trees are similar only if both types have a similar aerodynamic porosity and if the model tree can undergo an aerodynamic reconfiguration similar to that of a natural tree. Such reconfiguration implies the reorientation of the branches and leaves due to wind. A study on the influence of seasonal foliar density variation shows that the foliage configuration plays a critical role on the drag coefficient and the flow field. A defoliated tree, such as a deciduous tree in winter, is shown to have a substantially lower drag coefficient and a negligible influence on the flow.

## 3.2 MODEL AND NATURAL TREES

A range of model and natural trees with different heights and porosities is used in the present study to answer question regarding whether model trees behave similarly to natural trees. Table 3.1 lists the specification of the model and natural trees used for drag and PIV measurements. It tabulates the tree type, tree height $H$, frontal area $A$, optical porosity $\beta$ and aerodynamic porosity $\alpha$. The aerodynamic porosity $\alpha$ is determined directly from the optical porosity $\beta$ using an empirically fitted relationship:

$$\alpha = \beta^{0.4} \tag{3.1}$$

where the exponent is obtained from a wind tunnel drag study of realistic tree-like windbreak models (Guan et al. 2003). The study shows that this formulation provides a good estimate for 3D tree models and has been applied by others to estimate the aerodynamic porosity for individual trees (Bitog et al. 2011; Lee et al. 2014; Rosenfeld et al. 2010).

Fig. 3.1 shows the thresholded frontal view of the model and natural trees used during the experiment. The thresholded images are used for the calculation of optical porosity and the resulting aerodynamic porosity. The optical porosity is defined as the ratio of white

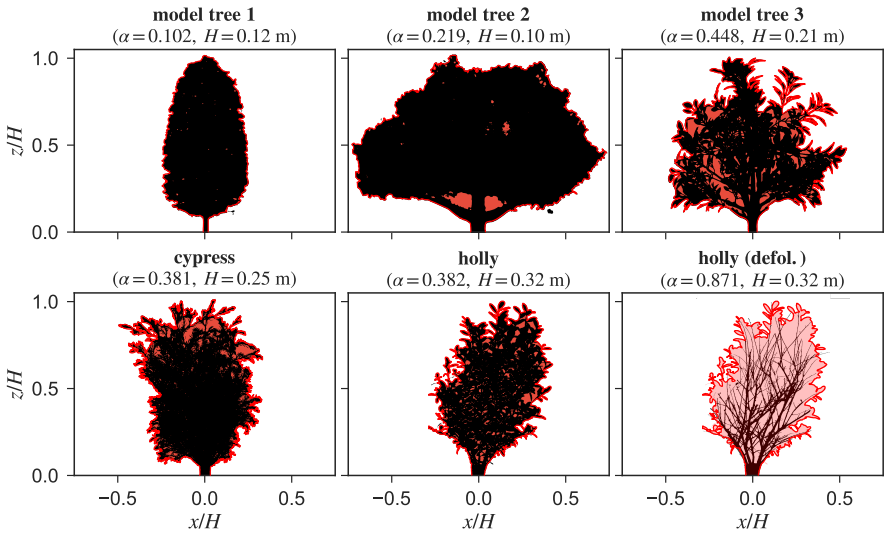


Figure 3.1: Frontal thresholded images of model and natural trees at rest: **(a)** model tree 1, **(b)** model tree 2, **(c)** model tree 3, **(d)** cypress, **(e)** holly and **(f)** holly (defoliated). The red region indicates the frontal area of the tree. The frontal area of holly is used as a reference for both foliated and defoliated holly.

area to the total area within the silhouette of the tree, which is delineated in red on Fig. 3.1. To note is that this silhouette area is considered as the frontal area of the tree $A$ used in Eq. (3.1) and also required for calculating the drag coefficient $C_d$ (further explained in Section 3.3.1). The drag measurements are performed for all the trees listed in the table and PIV measurements are performed for a selected number of trees (two model and two natural trees as indicated in Table 3.1. These trees are chosen based on their distinct differences in morphology and porosity. Model trees 1 and 2 are small model trees made of polymeric materials with different porosity and shape. These are H0 scale (i.e. 1:87, a standardized scaled typically used for rail transport modeling) broad-leaf model trees. Model tree 3 is a larger model, with individual polymeric thin leaves mimicking those of a natural tree. The model trees are commercially available and have been designed to capture the geometrical characteristics of the natural trees. Such scaled models are commonly used in wind-tunnel studies of urban microclimate research, to represent the impact of trees on the airflow field around scaled model buildings (Gromke and Ruck 2007; Gromke and Ruck 2018; Gromke et al. 2008; Guan et al. 2003; Meroney 1968). Note however that designing trees to match the mechanical properties of the actual trees of interest would be most realistic. The design of model trees that have the mechanical properties of the natural trees such as moment of elasticity (MOE) or the bending stiffness requires careful attention. In the past, various types of materials such as plastic-simulated boughs (Meroney 1968), Nylon-66 stems with low-density Polyethylene (LDPE) branches (Stacey et al. 1994) have been used to provide flexibility to the tree models. Tree models with crowns made of wood-wool, sisal fiber or porous foam on a stiff trunk (Gromke and Ruck 2008) have also been designed to provide appropriate porosity and drag coefficient. Even though rigid model trees can be deemed appropriate to capture the static response, the dynamic response of the natural trees is not captured due to their rigidity. Therefore, one of the objectives of the study is to see to which extent the flexible model trees, such as H0 scale trees, can provide more accurate airflow fields for wind tunnel studies, due to their flexibility.

The natural trees used in the present study are divided into two categories: hardwood and coniferous species. Generically, hardwood species have broad-like leaves whereas coniferous trees have

Table 3.1: Specifications of the model and natural trees used for drag and PIV measurements. The trees used for PIV measurements are indicated with an asterisk (*).

| Name | Tree type | $H$ (m) | $A$ (cm$^2$) | $\beta$ | $\alpha$ [(1)] |
|---|---|---|---|---|---|
| model tree 1 (*) | model | 0.12 | 48 | 0.003 | 0.102 |
| model tree 2 | model | 0.1 | 82 | 0.022 | 0.219 |
| model tree 3 (*) | model | 0.21 | 240 | 0.134 | 0.448 |
| cypress[a] (*) | coniferous | 0.25 | 297 | 0.09 | 0.381 |
| holly[b] (*) | hardwood | 0.32 | 411 | 0.09 | 0.382 |
| holly[b] (defol.) (*) | hardwood | 0.32 | 411 | 0.708 | 0.871 |

(1) Guan et al. (2003)

Scientific names: [a]*Chamaecyparis pisifera*, [b]*Ilex crenata*

needle-like leaves. In the present study, smaller young (juvenile) trees are used with a maximum height of 32 cm, although a typical mature holly is known to grow up to 3 to 5 m and a mature cypress to 35 to 50 tall. The impact of seasonal foliar density variation is studied by defoliating the holly and subsequently performing drag and flow measurements.

The wind tunnel experiments are performed in the ETHZ / Empa Atmospheric Boundary Layer (ABL) wind tunnel. It is a closed circuit Göttingen type wind tunnel with a test section cross-section of 1.9 m (width) by 1.3 m (height). The wind tunnel can provide wind speeds ranging from 0.5 to 25 m s$^{-1}$. Fig. 3.2 shows the setup used for combined measurement of drag force and the flow field behind the trees. The origin of the $x$, $y$, $z$ coordinate system is located at the bottom-center of the tree foliage. The corresponding instantaneous velocity components of the velocity vector $\boldsymbol{u}$ are $u$, $v$, and $w$, oriented along the streamwise, spanwise and vertical directions, respectively. The mean and fluctuating velocities of the velocity vector $\boldsymbol{u}$ are defined $\overline{\boldsymbol{u}}$ and $\boldsymbol{u}'$, with the overbar denoting an ensemble average. The tree is mounted on the pole-load cell configuration, away from the wind tunnel floor. The trees are mounted in this fashion to reduce the influence of the wind tunnel boundary layer, the load cell and the traverse system at the measurement region. Fig. 3.3 shows the

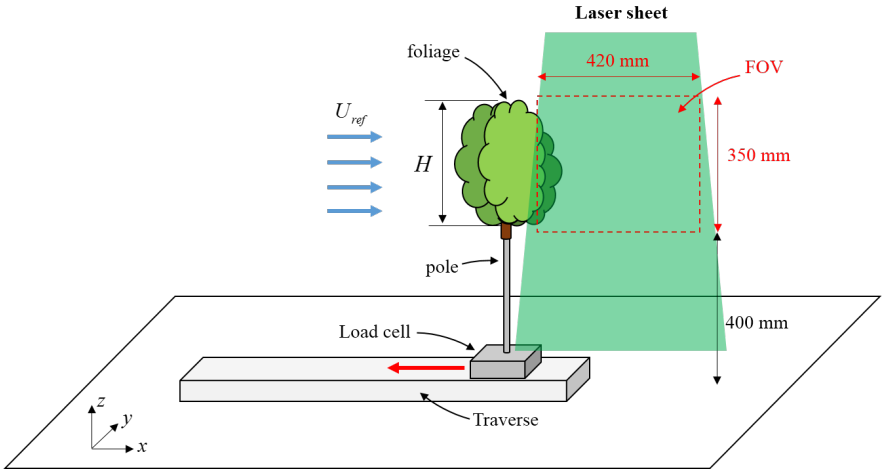


Figure 3.2: Wind tunnel setup for combined drag force and PIV measurements. The model trees or natural trees are positioned on a rigid stainless steel pole connected to the load cell. The trees are traversed 3 times in the upstream direction by 300 mm, indicated by the red arrow.

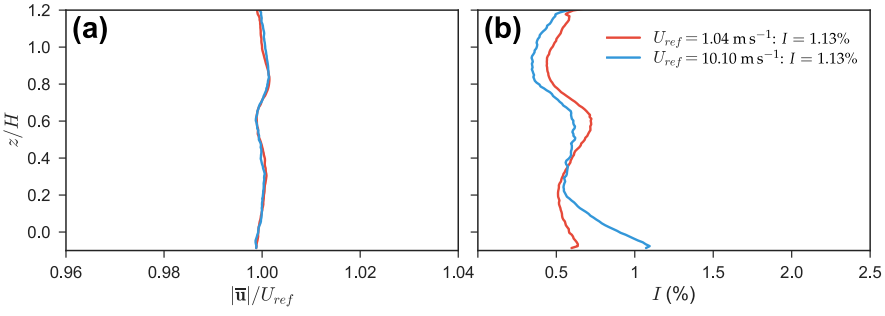


Figure 3.3: Profile at the location $x = 0$ m without trees: **(a)** normalized mean velocity magnitude $|\overline{u}|/U_{ref}$ and **(b)** turbulence intensity $I$ (%).

normalized mean velocity and the turbulence intensity for two wind speeds of $U_{ref} = 1$ and 10 m s$^{-1}$. Fig. 3.3a displays a nearly-uniform approach flow wind profile, with a maximum deflection from the mean value less than $5 \times 10^{-3}$ m s$^{-1}$ (0.5%). Furthermore, the measurement was performed for a low upstream turbulence with an average turbulence intensity of $I = 0.4\%$ (Fig. 3.3b). A nearly-uniform wind profile with a low turbulence level is used instead of an atmospheric boundary layer (ABL) to ensure that all trees, which have varying heights, are subjected to the similar velocity profile. However, it must be note that such profile is strictly used to ensure accurate cross-comparison and does not represent the real flow condition in an urban environment.

## 3.3 MEASUREMENT SETUP

### 3.3.1 *Load cell*

The force acting on the trees is measured using a Transmetra K3D120-50N 3-axis load cell with a precision of $\pm 0.5 \times 10^{-2}$ N. The mean load acting on the tree is determined by averaging over approximately one minute. As the measurement time series is acquired at 2.5 Hz, the samples are uncorrelated and a sufficiently large sample series is measured. The influence of wind speed on drag coefficient is studied by measuring at six different wind speeds $U_{ref} = 3, 5, 7, 10,$ 15 and 20 m s$^{-1}$. A minimum wind speed of 3 m s$^{-1}$ is required due to the resolution of the load cell. The maximum measurement error of 25% is found for the smallest model trees at the lowest wind speed due the precision of $\pm 0.5 \times 10^{-2}$ N and the averaged measured drag force of $2 \times 10^{-2}$ N. However, with increasing tree size and/or increasing wind speed, the error in the measured drag force quickly reduces to less than 5%. The drag coefficient $C_d$ of the trees for a given reference wind speed $U_{ref}$ (m s$^{-1}$) is given as:

$$C_d = \frac{2F}{\rho U_{ref}^2 A} \tag{3.2}$$

where $F$ (N) is the measured drag force in the direction of the wind speed, $\rho$ (kg m$^{-3}$) air density and $A$ (m$^2$) projected frontal area (Grant and Nickling 1998; Guan et al. 2003; Mayhead 1973). As men-

tioned above, the projected frontal area is calculated directly from the thresholded images of the trees at rest Fig. 3.1. The frontal area of foliated holly is used as the reference frontal area for the defoliated configuration. This is to ensure that the defoliation of the plant results in an increase in the aerodynamic porosity. If the frontal area is also altered, it can inversely compensate the increase in aerodynamic porosity due to defoliation. The characteristics of the trees are tabulated in Table 3.1.

### 3.3.2 *Particle image velocimetry*

The flow field downstream of the trees is measured using particle image velocimetry (PIV). Fig. 3.2 depicts the PIV set-up for measuring the $x-z$ plane at $y = 0$ m (defined as the middle of the tree trunk). The PIV set-up consists of a $2560 \times 2160$ pixel (5.6 MP) s-CMOS HiSense Zyla camera which images the 1 $\mu$m Di-Ethyl-Hexyl-Sebacat (DEHS) tracer particles, dispersed in the airflow. The particles are illuminated by a 200 mJ/pulse (at 15 Hz) Nd-YAG Litron laser. The field of view (FOV), which the camera set-up provides, is $420 \times 350$ mm$^2$. To image the entire recirculation zone of the trees, the tree set-up is traversed 3 times in the upstream direction by 300 mm, as indicated by the red arrow in Fig. 3.2. The result is three FOVs with an overlap of 120 mm that are then stitched together to provide a larger resolved FOV of $1020 \times 350$ mm$^2$. The velocity vectors are calculated using an iterative cross-correlation algorithm of the Dantec DynamicStudio software and the interrogation windows are automatically deformed based on local particle density and velocity gradients. The final interrogation area is 32 px$^2$ with 50% overlap. The velocity vector outliers are removed using the normalized median test (Westerweel and Scarano, 2005). For each measurement case, around 200 samples of statistically independent vector maps are obtained to ensure proper turbulence statistics. The amount of flow field images that are taken ensures a confidence level of 95% and leads to the estimation that the maximum free-stream normalized turbulence intensity $I = 40\%$ in the wake of the trees. During the experiment, the turbulence intensity for all trees is checked not to exceed this upper bound. The sampling rate is based on the largest time-scale determined from the tree height $H$ and the reference wind speed $U_{ref}$. For smaller trees ($H = 0.1$ m) and larger trees

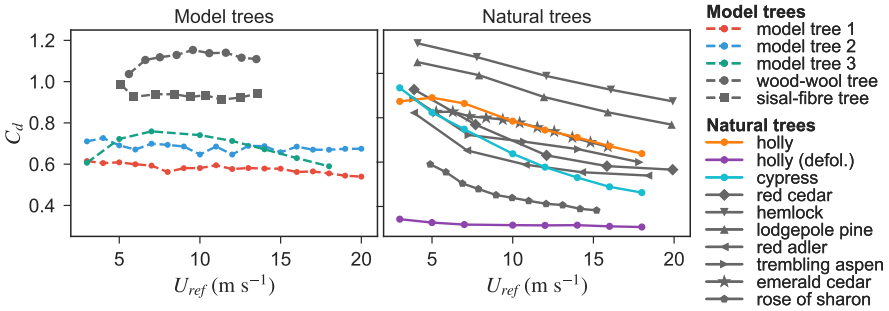


Figure 3.4: Drag coefficient $C_d$ vs. wind speed $U_{ref}$ for various model trees (dashed lines) and natural trees (solid lines). The trees of the present study (colored lines) are compared with previous studies results (black lines) as listed in Table 2.1.

($H = 0.3$ m), at $U_{ref} = 1$ m s$^{-1}$, a sampling rate below 5 Hz and 1 Hz is required, respectively.

The PIV measurements were performed for two wind speeds, $U_{ref} =$ 1 and 10 m s$^{-1}$, providing a comparison for low and high wind speeds. The measurements are performed for two model trees and two natural trees (indicated in Table 3.1) as shown in Fig. 3.1.

## 3.4 DRAG COEFFICIENT OF MODEL AND NATURAL TREES

The drag coefficient is determined using the approach described in Section 3.3.1. Fig. 3.4 shows the drag coefficient of model (dashed colored lines) and natural trees (solid colored lines) as a function of wind speed. Results from previous studies (black lines), as listed in Table 2.1, are added for comparison. The drag coefficients of the model and natural trees are presented with two graphs for readability. The first observation is that, for a given wind speed, there is a large spread in the drag coefficient ranging from 0.25 to 1.25. This variability of the drag coefficient is further investigated in Section 3.4.1, looking at the role of porosity.

With increasing wind speed, the drag coefficients of model trees 1 and 2 are observed to remain nearly constant, with drag coefficients of around $C_d = 0.58$ and $C_d = 0.68$, respectively. This constant relationship is also observed for the model wood-wool tree with $C_d = 1.12$ and sisal-fibre tree with $C_d = 0.94$, studied by Gromke and

Ruck (2008). Therefore, drag coefficients of these model trees appear to be independent of wind speed. In contrast, the drag coefficients of all natural trees, and of model tree 3, decrease with wind speed. This dependent behavior can be attributed to the difference in the rigidity of the trees. Due to the higher rigidity of most model trees, they do not undergo a reconfiguration under wind and maintain a constant drag coefficient. In contrast, with the flexible branches and leaves of the natural trees and of model 3, reconfiguration occurs at higher wind speeds, causing a decay of the drag coefficient. Furthermore, the natural trees used in the present study are juvenile indicating a lower moment of elasticity (MOE) (Macdonald and Hubert 2002; Telewski 1995; Watt et al. 2008). The reduced MOE and the high foliage density further increases the plant bending at high wind speed. This is especially apparent for the cypress (the juvenile conifer plant), as observed from Fig. 3.4. However, when the tree has no leaves, the reconfiguration of the leaves is no longer present, as seen for the defoliated holly. Therefore, leaves play a critical role in the bending and reconfiguration of the tree. Incorporating the differences in MOE, due to age and the varying foliage density due to season, will lead to more appropriate tree models for wind tunnel measurements. To further understand the influence of reconfiguration, the relationship of drag force with wind speed is investigated in Section 3.4.2.

### 3.4.1 *Influence of porosity on drag coefficient*

Fig. 3.4 shows that, for a given wind speed, the drag coefficient of model and natural trees can range from 0.25 and 1.25. This spread in drag coefficient is also apparent in past studies (Bitog et al. 2011; Dong et al. 2007; Guan et al. 2003; Hagen and Skidmore 1971; Rudnicki et al. 2004; Vollsinger et al. 2005; Wilson 1985). The spread in drag coefficient of windbreaks and trees is related to the aerodynamic porosity. Using the empirical relation (Eq. (3.1)), the drag coefficients of model and natural trees at two Reynolds number are plotted versus aerodynamic porosity, as displayed in Fig. 3.5. The lower Reynolds number corresponds to $U_{ref} = 3.0$ to 9.6 $\mathrm{m\,s^{-1}}$ and the higher Reynolds number corresponds to $U_{ref} = 6.1$ to 19.4 $\mathrm{m\,s^{-1}}$, dependent on the given height of the trees Table 3.1. The graph also includes the results from the studies cited above. A large spread in

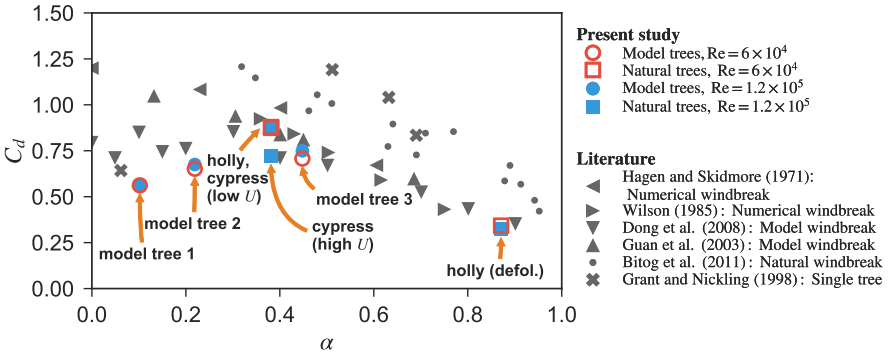


Figure 3.5: Drag coefficient $C_d$ vs. aerodynamic porosity $\alpha$ for various model trees (model tree 1, model tree 2, model tree 3) and natural trees (holly, cypress, defoliated holly) at two Reynolds number $\mathrm{Re} = 6 \times 10^4$ and $\mathrm{Re} = 1.2 \times 10^5$.

the drag coefficient is seen for a given porosity, depending on the tree type. We should consider that the method of calculating the aerodynamic porosity varies across these studies. Some studies rely on optical porosity (Dong et al. 2008; Guan et al. 2003; Hagen and Skidmore 1971; Wilson 1985), others on volumetric porosity (Grant and Nickling 1998) and some determine porosity directly from measuring the bleed flow intensity (Bitog et al. 2011).

In every study (except Hagen and Skidmore (1971)), the drag coefficient initially increases at low aerodynamic porosity ($\alpha < 0.3$) and decreases at higher aerodynamic porosity ($\alpha > 0.3$). Dong et al. (2007) find $\alpha = 0.3$ to be a critical porosity. Below the critical porosity, the airflow goes primarily around the tree with little bleed flow through the tree, creating a recirculation zone behind the tree. Above the critical porosity, the bleed flow becomes dominant and, with increasing porosity, the drag exerted by the tree reduces. However, at the critical porosity, a combination of recirculation and bleed flow is present and this additional bleed flow through the foliage seems to result in a larger drag. Therefore, a tree that has this critical porosity, extracts the most momentum from the flow. A similar finding has also been obtained from windbreak studies (Dong et al. 2008; Hagen and Skidmore 1971; Lee and Kim 1999). Finally, the Reynolds number does not have a significant impact on the drag coefficients for most of our measurements, with a variation of about $\pm 4\%$. The cypress of $\alpha = 0.381$ has a lower drag coefficient at higher

Reynolds numbers, due to the reconfiguration at high wind speeds, as discussed in Section 3.4.2. Therefore, if the Reynolds number is varied without varying the wind speed, such as by varying the tree height, the Reynolds number will have a weak influence on the drag coefficient. The apparent variation in drag coefficient is manifested only from the reconfiguration of the foliage when the wind speed is high.

### 3.4.2 *Influence of plant reconfiguration on drag coefficient*

To study the influence of leaf and branch reconfiguration on the drag coefficient, the drag force-wind speed relationship is examined. The drag force of a tree that reconfigures follows the relationship:

$$F \propto U^{2+b} \tag{3.3}$$

where $b$ is called the Vogel exponent, where $b < 0$. Its magnitude quantifies the decay of the drag coefficient with wind speed (de Langre 2008; Vogel 1989). The Vogel exponent is more negative for trees that strongly reconfigure. de Langre (2008) mentions that it is not uncommon to find values of $b = -1$, indicating that the drag force can be linearly dependent on the wind speed. In the present study, we determine the Vogel exponent of the model and natural trees, which have different reconfiguration behavior at high wind speeds, and compare these values with ones of larger trees from previous studies.

The Vogel exponent of trees from present study and literature are tabulated in Table 3.3. The Vogel exponent is determined using a non-linear regression analysis of the modified drag equation (Eq. (3.3)). The study confirms that foliated natural trees undergo reconfiguration as mentioned above and seen in Fig. 3.4. For natural trees, the Vogel exponent is shown to range from $-0.18$ to $-0.51$. The study also shows that smaller natural trees reconfigure more strongly than larger natural trees possibly due to their thinner branches which can have a lower mechanical stiffness. This is especially apparent for cypress with a Vogel exponent of $b = -0.51$. In contrast, the Vogel exponent of the defoliated holly is $-0.05$, showing a lack of reconfiguration as observed in Fig. 3.4. The study high-

Table 3.3: The Vogel exponent $b$ of model and natural trees.

| *Present study* | | *Literature* | |
|---|---|---|---|
| Name | $b$ | Name | $b$ |
| | | *Model trees* | |
| model tree 1 | $-0.12$ | wood-wool tree[a] | $-0.02$ |
| model tree 2 | 0 | sisal-fiber tree[a] | 0 |
| model tree 3 | $-0.33$ | | |
| | | *Natural trees* | |
| holly | $-0.33$ | red cedar[b] | $-0.25$ |
| holly (defol.) | $-0.05$ | hemlock[b] | $-0.23$ |
| cypress | $-0.51$ | lodgepole pine[b] | $-0.28$ |
| | | red adler[c] | $-0.18$ |
| | | trembling aspen[c] | $-0.26$ |

[a]Gromke and Ruck (2008), [b]Rudnicki et al. (2004), [c]Vollsinger et al. (2005)

lights the influence of leaves in reconfiguration and how reconfiguration dynamically affects the drag coefficient.

Model trees, in general, show less reconfiguration and, as consequence, the Vogel exponent is less negative except for model tree 3. The model tree 3 has a Vogel exponent $b = -0.33$, so equal to that of holly, due to its similar reconfiguration characteristic, and displays as a result a decaying drag coefficient as shown in Fig. 3.4. In contrast, rigid model trees, such as model tree 2 do not behave similarly to the way natural trees do.

## 3.5 IMPACT ON MEAN WIND SPEED

The normalized mean velocity magnitude $\overline{\boldsymbol{u}}/U_{ref}$ provides a first indication of the influence of trees on the airflow. The wind speed is normalized by the reference wind speed $U_{ref}$, determined at the location of the tree before its placement. To allow comparison, all trees are subjected to a similar uniform velocity profile, as explained above. Fig. 3.6 compares the normalized mean wind speed of model

and natural trees at two distinct wind speeds, i.e. at low, $U_{ref} = 1$, and high, $U_{ref} = 10\ \mathrm{m\,s^{-1}}$, wind speeds. The figure shows that the wake flow field differs from tree to tree and varies with wind speed. This behavior is directly related to the variation in the aerodynamic porosity with wind speed, which is evaluated as follows. The aerodynamic porosity of the measured 2D-PIV plane is directly determined from the ratio of the bleed wind speed and the upstream wind speed (Guan et al. 2003):

$$\alpha^{2D} = \frac{\int_0^H |\overline{\boldsymbol{u}}|\,\mathrm{d}z}{U_{ref}\,H} \tag{3.4}$$

measured at $x/H = 0.7$. This location is chosen as it is the closest point to the tree where the measured wake velocity distribution of all the trees is available. Ideally, the bleed flow behind the tree should be measured as close to the tree as possible. The measured 2D-plane aerodynamic porosity is indicated in Fig. 3.6 and represents the effect of the porosity at the measured plane, whereas $\alpha$ is the empirically-determined aerodynamic porosity of the entire tree. Furthermore, the measured 2D-plane aerodynamic porosity is dependent on the wind speed and therefore takes into account the influence of reconfiguration.

Fig. 3.6a-b shows model tree 1 with a strong recirculation, as shown by the appearance of closed streamlines. The 2D-plane aerodynamic porosity of model tree 1 is shown to be substantially lower than that of model tree 3 and of holly. The cypress tree shows a similar wake flow field due to its low porosity. An increase in wind speed results in bending of both the model tree 1 and the cypress. However, the reconfiguration of the trees has a dissimilar effect, where the 2D-plane porosity of model tree 1 increases with wind speed while that of the cypress tree is reduced. This occurs because, unlike model tree 1, the cypress tree has flexible foliage and higher wind speed results in the foliage of the cypress tree to reconfigure into a smaller clump, resulting in a stronger blockage. In contrast, the model tree 3 shows strong bleed flow due to its higher aerodynamic porosity. Furthermore, the bleed flow increases with wind speed, as indicated by the increase of both 2D-plane aerodynamic porosity by 0.115 and wind speeds in the wake. The holly

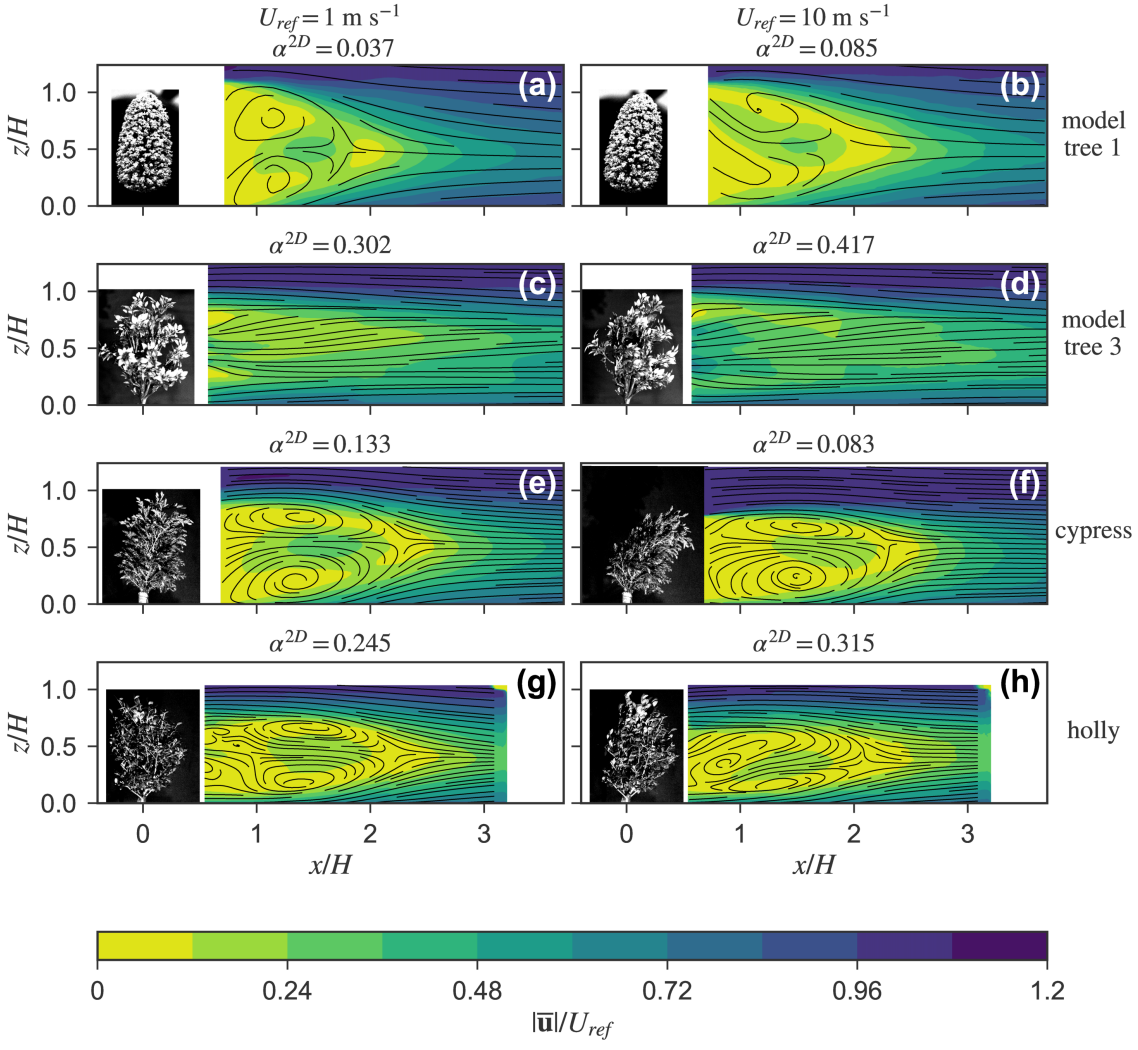


Figure 3.6: Normalized mean velocity magnitude $|\overline{u}|/U_{ref}$ of **(a)(b)** model tree 1, **(c)(d)** model tree 3, **(e)(f)** cypress, **(g)(h)** holly. The comparison is done for two wind speeds: **(a)(c)(e)(g)** $U_{ref} = 1\,\mathrm{m\,s^{-1}}$ and **(b)(d)(f)(h)** $U_{ref} = 10\,\mathrm{m\,s^{-1}}$.

only shows bleed flow where it has a higher porosity, i.e. in its top part. Below, due to the higher foliage density of holly, strong recirculation is evident. In all cases, the impact of reconfiguration is evident, showing an altered wake structure and changing aerodynamic porosity at higher wind speeds. The comparison highlights the implication of reconfiguration on the wake. This change is also reflected in the drag coefficient measurements as seen in Fig. 3.4.

## 3.6 IMPACT ON TURBULENCE INTENSITY

The influence of trees on the fluctuating component of the wind is studied by quantifying the change in local turbulence intensity $I$, defined as

$$I = \frac{\sqrt{2/3\,k}}{|\overline{\boldsymbol{u}}|} \tag{3.5}$$

where $|\overline{\boldsymbol{u}}|$ is the mean local wind speed and

$$k = \frac{1}{2}\mathrm{tr}\left(\overline{\boldsymbol{u}'\boldsymbol{u}'}\right) \tag{3.6}$$

and we approximated lateral variance with the assumption that

$$\overline{v'v'} = \frac{1}{2}\left(\overline{u'u'} + \overline{w'w'}\right) \tag{3.7}$$

The turbulence intensity measures the ratio of the fluctuating velocity to the local mean velocity. Fig. 3.7 shows the turbulence intensity for the model and natural trees at low and high wind speeds. The comparison of the results for model and natural trees shows that the turbulence intensity distribution of model tree 1 resembles the most that of natural trees. Due to the much higher bleed flow of model tree 3, as observed in Fig. 3.6, the turbulence intensity rise in the wake is much lower, with an average local turbulence intensity of less than 20%.

Comparing low to high wind speeds shows how reconfiguration due to bending of the trees influences the turbulence in the wake. Model tree 1 (Fig. 3.7b) and cypress tree (Fig. 3.7f) bend at high wind speeds, as reflected in a weak change in the turbulence intensity distribution. Only in the near vicinity of the trees, a noticeable change is observed, showing a reduction in the size of the high tur-

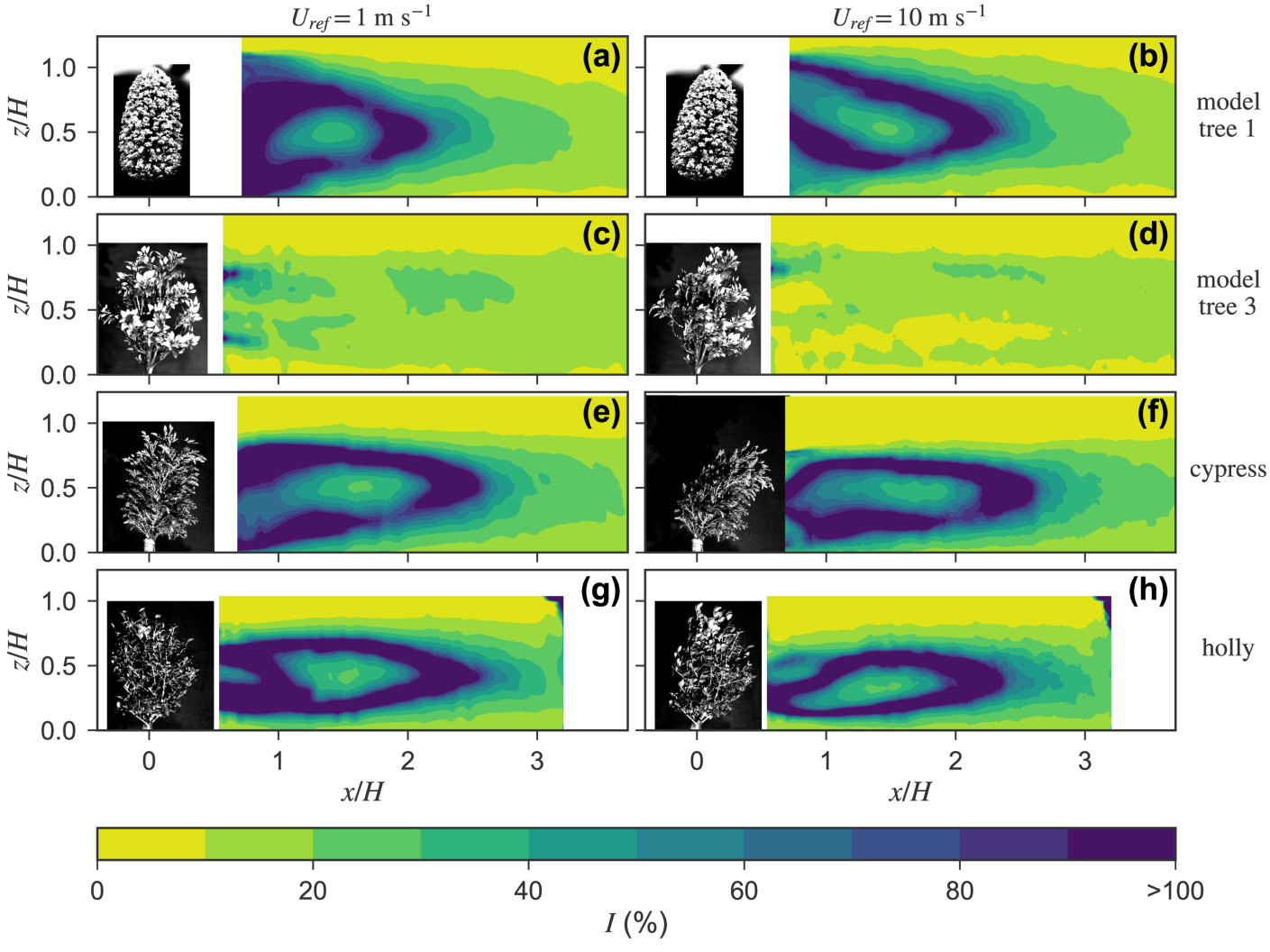


Figure 3.7: Turbulence intensity $I = \sqrt{2/3k}/\overline{u}$ (%) of **(a)(b)** model tree 1, **(c)(d)** model tree 3, **(e)(f)** cypress and **(g)(h)** holly. The comparison is done for two wind speeds: **(a)(c)(e)(g)** $U_{ref} = 1$ m s$^{-1}$ and **(b)(d)(f)(h)** $U_{ref} = 10$ m s$^{-1}$.

bulence intensity region. The influence of reconfiguration due to streamlining of the branches and leaves on the turbulence intensity is observable for model tree 3 and the hardwood holly tree. In the case of model tree 3, the turbulence intensity is seen to reduce, as a result of the increase in aerodynamic porosity of $\Delta\alpha^{2D} = 0.115$, as observed in Fig. 3.6d. In the case of holly tree, the turbulence intensity is only found to increase at the near-wake region ($x/H < 1$), with an increase in aerodynamic porosity of only $\Delta\alpha^{2D} = 0.07$. Therefore, the influence of reconfiguration on the turbulence intensity is strongly influenced by the nature of reconfiguration and varies from species to species.

## 3.7 IMPACT ON SHELTERING EFFECT

The sheltering provided by the trees is known to be related to the shape, porosity and flexibility of the tree. It can be assessed by determining the shelter parameter $\psi$, given as (Gandemer 1979):

$$\psi = \frac{U_{ref} + \sqrt{\frac{2}{3}k_{ref}}}{|\overline{u}| + \sqrt{\frac{2}{3}k}} \tag{3.8}$$

The shelter parameter takes in account the mean velocity and its fluctuating component, thereby quantifying the net reduction in wind speed. Similar formulations of the shelter effect are found in previous studies (Lee and Lee 2012; Lee et al. 2014; McClure et al. 2017; Packwood 2000; Perera 1981; Santiago et al. 2007). The shelter parameter provides a distinction between regions of high sheltering ($\psi \gg 1$) and no sheltering ($\psi \approx 0$).

Fig. 3.8 compares the shelter parameter of four trees at $U_{ref} = 1$ and 10 $\mathrm{m\,s^{-1}}$. Generally, the highest sheltering is provided at the near-wake region ($x/H < 1$), showing highest intensity of $\psi$ . Increasing the wind speed only results in a slight change in the shelter parameter for most trees, except for cypress which shows a substantial increase in sheltering. Model tree 3 shows a decrease in sheltering. Model tree 3 shows that, due to the increased bleed flow caused by streamlining of branches and leaves, the sheltering is slightly reduced. The shelter parameter varies with the change in aerodynamic

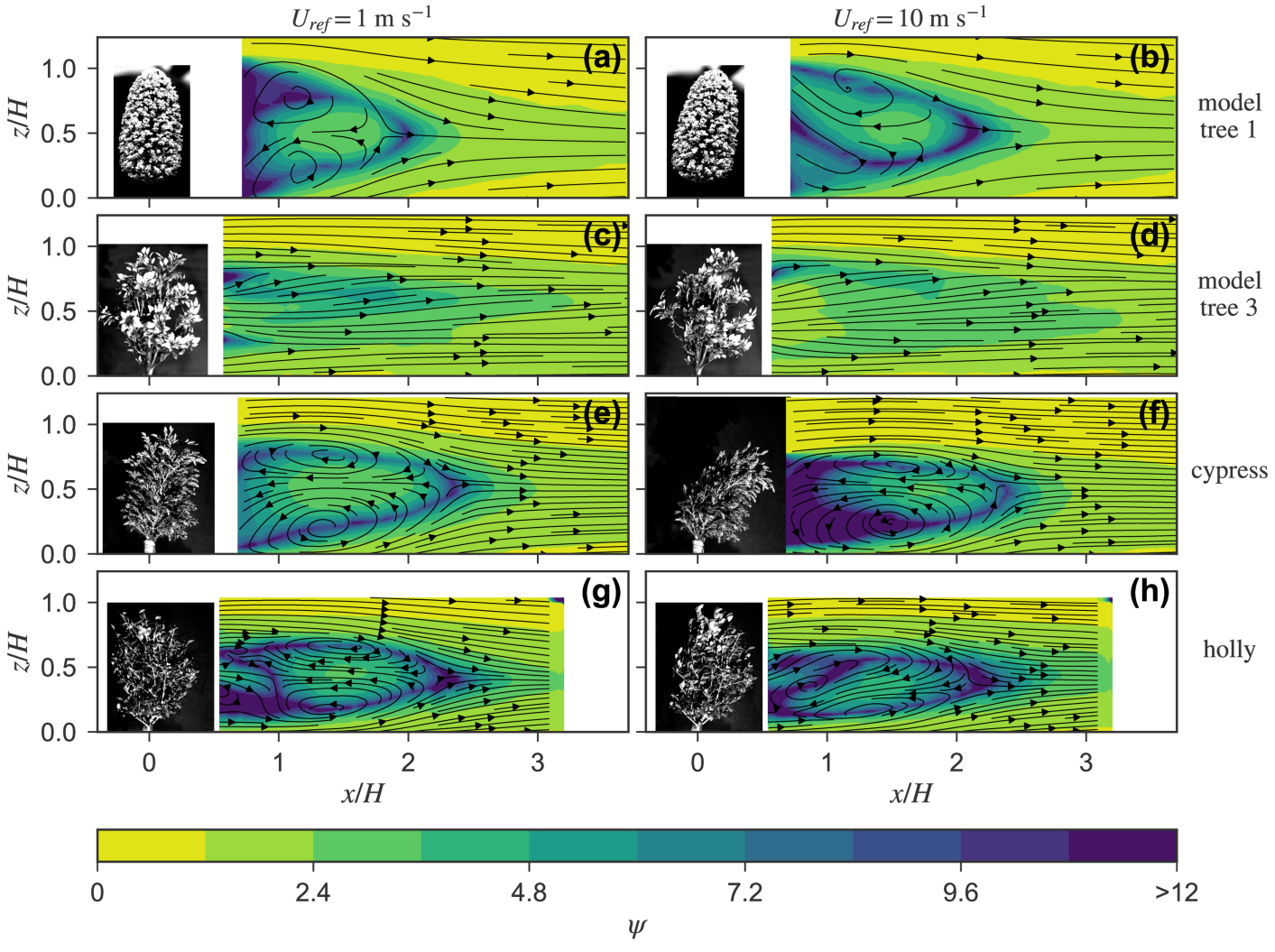


Figure 3.8: Shelter parameter $\psi$ of **(a)(b)** model tree 1, **(c)(d)** model tree 3, **(e)(f)** cypress and **(g)(h)** holly. The comparison is done for two wind speeds: **(a)(c)(e)(g)** $U_{ref} = 1$ m s$^{-1}$ and **(b)(d)(f)(h)** $U_{ref} = 10$ m s$^{-1}$.

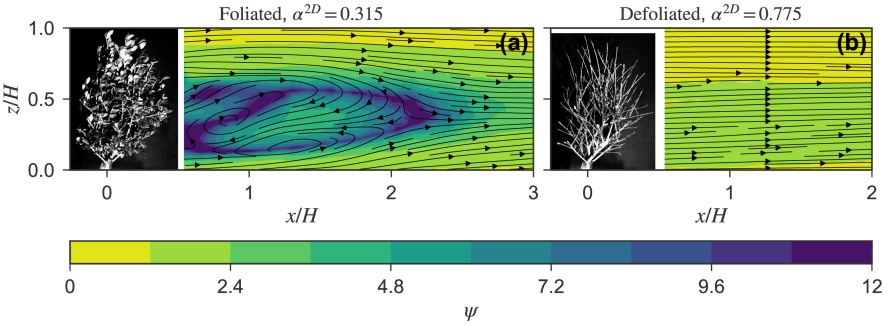


Figure 3.9: Shelter parameter $\psi$ of **(a)** foliated holly and **(b)** defoliated holly at $U_{ref} = 10\ \mathrm{m\,s^{-1}}$.

porosity. Thus, the reconfiguration of the tree has a direct influence on the sheltering provided by the tree.

## 3.8 INFLUENCE OF SEASONAL FOLIAR DENSITY VARIATION

The seasonal foliar density variation evidently affects the flow field with deciduous trees as they which shed their leaves during winter. This influence of the seasonal change of tree foliage on the flow field is illustrated here by comparing the same holly in foliated and defoliated states. Fig. 3.9 shows the shelter parameter and streamlines of holly with and without leaves at a high wind speed ($U_{ref} = 10\ \mathrm{m\,s^{-1}}$). In leafless configuration (Fig. 3.9b), the tree has a negligible influence on the flow whereas the foliated holly shows strong sheltering and recirculation in the wake (Fig. 3.9a). This variation is also quantified by the substantial increase in the 2D-plane aerodynamic porosity $\alpha^{2D}$ from 0.315 to 0.775 and results in a substantial drop of drag coefficient of the tree (Fig. 3.4). The measurement shows that the drag coefficient of defoliated holly is significantly lower than that of the foliated configuration.

Extrapolating from these results, deciduous trees can be assumed to have a negligible impact on the airflow during winter seasons. Therefore, to accurately model the impact of vegetation, urban microclimate models should be able to take in account this annual variation of aerodynamic porosity and the resulting change in turbulence statistics of the tree wake.

## 3.9 CONCLUSION

The present study compares the aerodynamic performance of model trees and natural trees using drag force measurements and PIV (Particle Image Velocimetry) measurements. The drag force measurements show that the behavior of natural trees can be approximated by model trees only if they have a similar aerodynamic porosity and if they are capable of reconfiguring at high wind speeds. The PIV measurements showed that model tree 1, which has a low porosity, had a wake structure similar to the one of the natural cypress tree. Model tree 3, with foliage consisting of individual polymeric thin leaves, reconfigures in a way similar to that of natural hardwood tree. It is evident that the model tree 3 has a much higher aerodynamic porosity than the natural tree resulting in a dominant bleed flow. In contrast, model tree 1 and the natural trees indicated strong recirculation due to their lower aerodynamic porosity.

The influence of foliage reconfiguration where the branches and the leaves deform due to airflow is evident in both the drag-velocity measurements and also from PIV measurements of the wake region. Due to reconfiguration, the drag coefficient decays at high wind speeds. The natural trees and the model tree 3 with artificial leaves show reconfiguration and a linear drag-force-wind speed relationship. A study on the Vogel exponent identifies the strength of the reconfiguration and shows that small young natural trees reconfigure to a larger extent than larger mature trees do (see Table 3.3). Therefore, future studies should focus on directly quantifying foliage deformation and its correlation to the resulting flow field.

In addition to reconfiguration, the aerodynamic porosity of the trees plays a critical role in their drag behavior, as reflected by the drag coefficient. In contrast, the Reynolds number only has an influence on the drag coefficient of the trees due to the influence of wind speed on reconfiguration. From the PIV measurements, it is apparent that the aerodynamic porosity, as determined from the optical porosity, does not reflect the aerodynamic porosity of the measured 2D-PIV plane. The 2D-plane aerodynamic porosity is shown to be dependent on the wind speed as the reconfiguration of the foliage directly influences the aerodynamic porosity. Due to reconfiguration, the turbulence intensity and shelter parameter are shown to be dependent on the wind speed.

The study of seasonal foliar density variation by comparing the holly in foliated and defoliated state shows that, during winter seasons, the influence of deciduous trees on the flow can be assumed to be negligible. Therefore, neglecting deciduous trees during winter in urban microclimate models can be a valid assumption and an advantage towards computational efficiency. In contrast, coniferous trees and evergreen hardwood trees that do not shed leaves and instead maintain their foliage density, annually, still provide sheltering during winter seasons and therefore their influences must be taken into account over all seasons.

In conclusion, towards the design, development or use of model trees for wind tunnel studies, the aerodynamic porosity and the drag coefficient are seen as vital parameters that should be matched to those of the natural trees of interest. When studying the influence of reconfiguration of the plant on the flow field, the Vogel exponent of the model tree is the recommended parameter to compare to the natural tree. Finally, if the objective of the wind tunnel experiment is to study the sheltering characteristics of the plant, the shelter parameter is the one to focus on. However, this requires a direct measurement of the wake flow field using more advanced techniques, such as PIV or hot-wire measurements, which might not be easily available.

# 4

# EXPERIMENTAL STUDY OF THE IMPACT OF VEGETATION ON THE MICROCLIMATE

This chapter has been submitted as: Manickathan, L., Defraeye, T., Carl, S., Richter, H., Allegrini, J., Derome, D., & Carmeliet, J. (2019). "Unveiling dynamic changes in the diurnal microclimate of a Buxus sempervirens with non-intrusive imaging of flow field, leaf temperature, and plant microstructure". *Submitted to Agricultural and Forest Meteorology*. (preprint: https://arxiv.org/abs/1903.02283).

## 4.1 INTRODUCTION

This chapter focuses on assessing the impact of vegetation on the microclimate through experimental investigation. The aim of the chapter is to quantify the influence of wind and radiation on the diurnal response of the plant. The influence of vegetation on the microclimate is studied in the wind tunnel using a small *Buxus sempervirens* plant. In the study, the diurnal dynamics of the plant microclimate of a *Buxus sempervirens* are investigated using various high-resolution non-intrusive imaging techniques. The wake flow field is measured using stereoscopic particle image velocimetry (SPIV), the spatiotemporal leaf temperature history is obtained using infrared thermography, and the plant microstructure metrics such as plant porosity, leaf area density (LAD) is obtained through X-ray tomography. We find that the wake velocity statistics are not directly linked with the distribution of the porosity but depend mainly on the geometry of the plant foliage which generates the shear flow. The interaction between the shear regions and the

upstream boundary layer profile is seen to have a dominant effect on the wake turbulent kinetic energy distribution. Furthermore, the leaf area density distribution has a direct impact on the short-wave radiative heat flux absorption inside the foliage where 50% of the radiation is calculated to be absorbed in the top 20% of the foliage. This localized radiation absorption increases the leaf and air temperature substantially, but locally. Furthermore, a comparison of the diurnal variation in the leaf temperature and the net plant transpiration rate enabled us to quantify the diurnal hysteresis resulting from the stomatal response lag. The day of this plant is seen to comprise of four distinct stages of climatic conditions: *no-cooling*, *high-cooling*, *equilibrium*, and *decaying-cooling* stages. The present chapter shows the need for a soil-plant-atmosphere continuum modeling approach to take into account the water availability. With such a modeling approach, the plant transpiration is linked with the soil moisture content. The high-resolution measurement dataset obtained from this chapter is used to compare a simplified version of the fully-coupled numerical model (see Chapter 5) in Chapter 7. The simplified model is used for comparison as the present measurement campaign still lacks the necessary parameters for an accurate calibration of the full-model, such as the plant xylem properties and rhizosphere properties. The present study only focused on the atmospheric changes due to the plant transpiration. In the future, a multi-domain measurement campaign consisting of measurements of air domain, soil domain, and plant physiology, can enable the validation of the full model.

The goal of the study is to experimentally quantify the influence of plant foliage geometry and environmental conditions such as wind speed and solar radiation on the transpirative cooling performance of a plant (Buxus sempervirens) inside a wind tunnel in an integrated approach. This is achieved by using multiple non-intrusive imaging techniques, thus measuring the plant foliage density with X-ray tomography, the wake flow field using stereoscopic particle image velocimetry (SPIV), the plant leaf temperature with infrared thermography and the hygrothermal conditions inside the foliage using various humidity and temperature sensors. The advantage of X-ray tomography to determine the plant porosity is that it is a non-intrusive approach of determining the plant structure, thus the plant can undergo a series of additional experiments. This approach

is inspired from the field of building physics where, for example, the determination of the microstructural morphology of building materials such as asphalt (Lal 2016; Lal et al. 2017) or materials such as cotton textiles (Parada et al. 2017) is used to link the material configuration to its wetting and drying behavior. Thus, the approach allows us to quantify the impact of the plant foliage morphology on the wake flow characteristics, the hygrothermal conditions such as air temperature and relative humidity inside the plant foliage, the solar radiation penetration through the foliage and, finally, on the spatial distribution of the leaf temperature.

The study aims to answer the questions of how plant cooling varies spatially and temporally under variations of environmental conditions such as wind speed and solar radiation and whether a typical diurnal response of the plant could be defined. Moreover, the experiment provides a high-resolution dataset for future modeling validation studies. Given that this investigation is performed in a wind tunnel, we study the diurnal microclimate of a small plant. As we need to ensure low blockage ratio in the wind tunnel, it is not feasible to put a mature tree in the wind tunnel. For example, the size of the plant, the flexibility of the branches and foliage, etc. can have an influence on the plant aerodynamic responses (de Langre 2008; Manickathan et al. 2018a).

## 4.2 MATERIALS AND METHODS

### 4.2.1 *Materials*

The measurement campaign was performed for a small Buxus plant (Buxus sempervirens) in a wind tunnel as shown in Fig. 4.1. The plant foliage has a dimension $20 \times 20 \times 21$ cm$^3$ ($x \times y \times z$, i.e., streamwise, spanwise and vertical) as shown in Fig. Fig. 4.1b. The plant was placed in a pot, sealed using putty sealant to ensure water was lost only through leaf transpiration (Fig. 4.1c). The water loss due to transpiration was periodically compensated by adding fertilized water (1% (vol.) NPK 7-4-6 Buxus fertilizer). Prior to the experiment, the plant was periodically irrigated and exposed for one week to artificial sunlight with a 12-hour day-night cycle, where day is assumed to be a fixed-intensity photoperiod. The artificial sunlight was provided using an Osram Ultra-Vitalux 300 W solar simulator

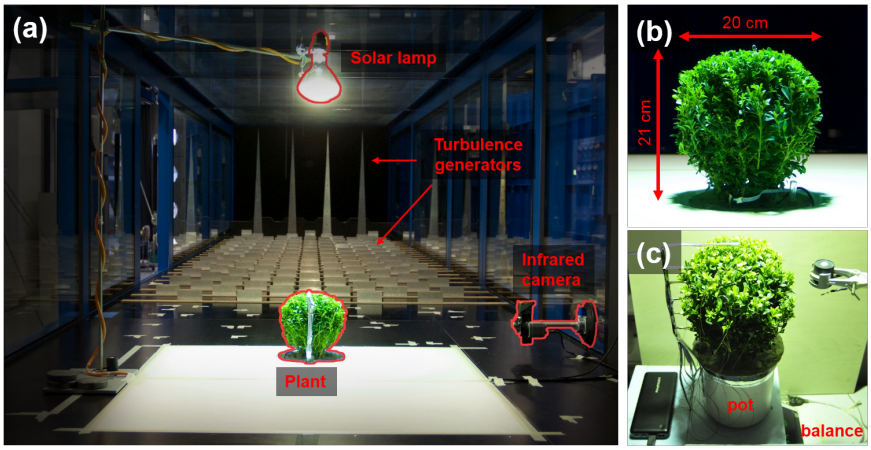


Figure 4.1: Wind tunnel setting for combined microclimate, SPIV, and infrared thermography measurements: **(a)** Photo of plant installed in the tunnel, **(b)** A close-up frontal view (windward) of the plant with dimensions, **(c)** Photo of pre-experiment plant acclimation setup.

bulb, generating 13.6 W of UVA and 3.0 W of UVB. The bulb was placed 60 cm above the plant to provide 100 $\mathrm{W\,m^{-2}}$ plant-canopy incident short-wave radiation. Furthermore, the growth of the plant foliage was periodically trimmed to maintain the desired plant geometry as shown in Fig. 4.1. The detailed measurement of the plant morphology including geometry, porosity distribution, leaf size distribution, and total leaf area, was obtained using a high-resolution X-ray tomography measurement, as explained below.

### 4.2.2 *Experimental setup and procedure*

The experimental campaign was divided into three stages: *offline* plant morphology measurement, pre-experimental controlled acclimatization setup, and the wind tunnel experiment. The *offline* measurement aimed to determine the plant morphological properties such as leaf area, porosity and porosity distribution using high-resolution X-ray imaging Section 4.2.3. The aim of the pre-experiment control setup was to acclimatize the plant to the wind tunnel boundary condition of solar radiation diurnal cycle. Furthermore, the sensors required for measuring the air and leaf temperature and air rela-

tive humidity within the foliage are mounted at this stage. Finally, the wind tunnel experiment aims at documenting the environmental conditions of the plant subjected to moderate wind. Thus, the flow field downstream of the plant, the hygrothermal microclimate inside the plant, the net transpiration rate and the plant foliage thermal profiles are measured.

### 4.2.3 *X-ray imaging*

A high-resolution computed tomography (X-ray CT) of the plant is acquired to determine the foliage morphology, the foliage porosity distribution and the net leaf area. The advantage of such an approach is that it is a non-intrusive approach where the same plant can be further investigated (Lal et al. 2017; Patera et al. 2018). The measurement is performed at the Diagnostic Imaging Research Unit (DIRU) at the Vetsuisse Faculty, University of Zurich, using a Philips Brilliance CT 16-slice scanner, shown in Fig. 4.2, designed for medical imaging with an acquisition period of 39 seconds. The CT slices have a resolution of $0.318 \times 0.318$ mm$^2$ pixel with a slice thickness of 0.4 mm. The 12-bit image intensity data and the associated data of the measurement are stored in DICOM file format. The plant properties such as net leaf area are obtained from the 3D dataset after image processing, consisting of image enhancement, image segmentation, and classification.

#### *X-ray computed tomography*

The attenuation coefficient indicates the absorption of the biological material to X-ray radiation, indicating the variability in the biological composition of the sample. The reconstructed tomographic data provides the 3D distribution of X-ray attenuation by the sample. The Hounsfield scaling normalizes the X-ray attenuation coefficient $\mu$ with that of the air $\mu_{air}$ and distilled water $\mu_{water}$ at standard atmospheric conditions, where the Hounsfield units of air and water are $HU_{air} = -1000$ and $HU_{water} = 0$, respectively:

$$HU = 1000 \times \frac{\mu - \mu_{water}}{\mu_{water} - \mu_{air}} \tag{4.1}$$

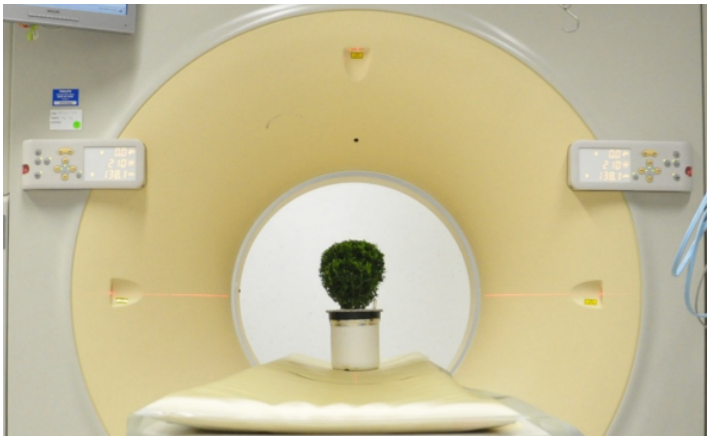

Figure 4.2: X-ray imaging setup of the plant specimen at Diagnostic Imaging Research Unit (DIRU) at the UZH. The specimen is imaged with Philips Brilliance CT 16-slice scanner, a medical imaging device.

HU can be used to extract the biological properties of the plant as the scaling can be a means for fast and simple categorization of biological matter with different water quantity.

*Image segmentation*

Fig. 4.3a shows a side-view of the CT-scan, whereas Fig. 4.3b shows a single image slice at the middle of the plant. Fig. 4.3c shows the histogram distribution of the single image slice. A preliminary observation of the images is that air, leaf, and branch show distinct attenuation coefficients for which a manual thresholding of the histogram is performed. Based on the histogram, a simple segmentation assigns air, leaves, and branches. The pixels are assigned as for air ($-1000$ to 900), leaves ($-900$ to $-700$), branches ($-700$ to 200), and anything beyond as foreign material. The bounds are determined with the help of $k$-means clustering method assuming a tri-modal distribution (i.e., $k = 3$) of the histogram. The histogram of X-ray CT scan (Fig. 4.4c) shows that this assumption is not valid as a clear differentiation between each mode is not visible. However, this histography-based segmentation serves as a base case for the more advanced segmentation algorithm. Fig. 4.4a shows the original dataset before the classification into air,leaves and brnaches.

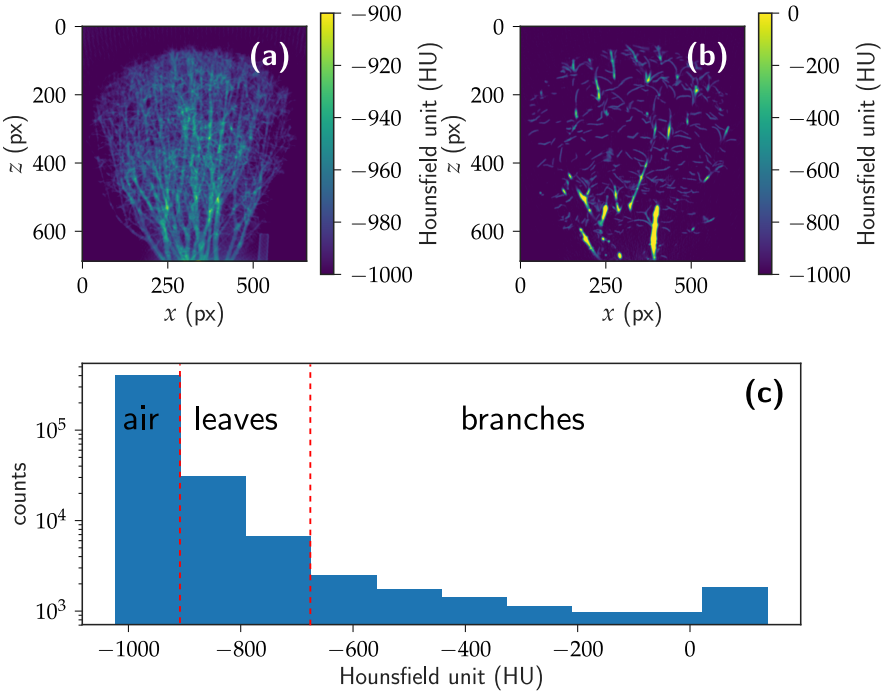


Figure 4.3: Raw image obtained from x-ray CT-scan: **(a)** the side view of CT-Scan, **(b)** a single image slice at the middle of the plant, **(c)** Histogram of **(b)**. The plant attenuation is represented in Hounsfield units (HU) where $-1000$ corresponds to air and 0 corresponds to pure water. The image slice resolution is $\Delta x = \Delta z = 0.318$ mm with a slice thickness of $\Delta y = 0.4$ mm.

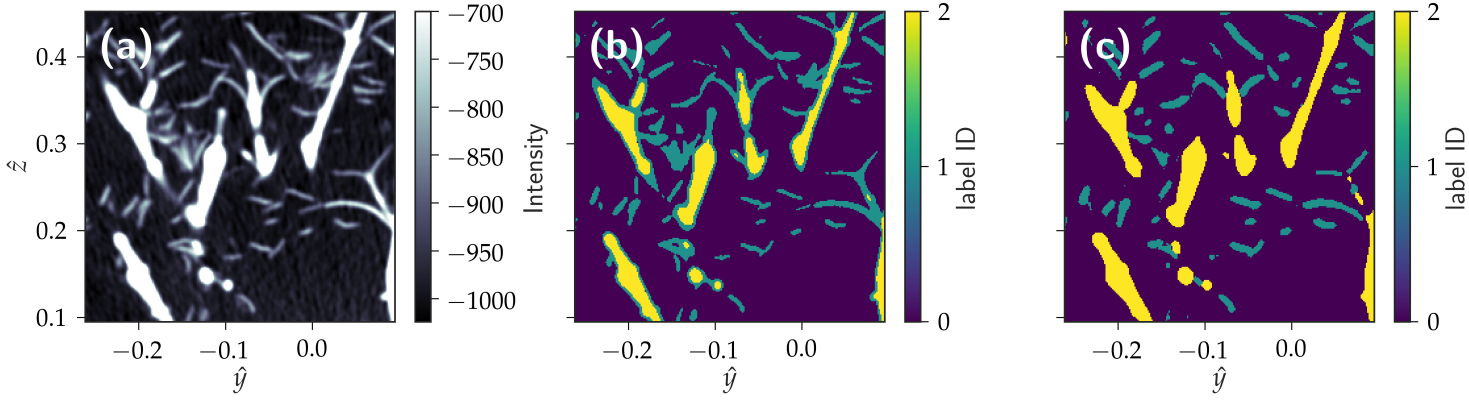


Figure 4.4: Segmentation of the X-ray CT scan: **(a)** slice of original X-ray CT dataset, **(b)** segmentation using user-defined histogram threshold and **(c)** segmentation using Trainable WEKA Segmentation and additional morphological operation (opening + closing). Only a sub-region of an image slice is shown for clarity. The segmented pixels are labeled as air (0, purple), leaf (1, blue) and branch (2, yellow).

Fig. 4.4b shows the histogram-based classification labels. A first observation shows a reasonable classification of the dataset except at boundaries of the branches, due to lower attenuation at the boundaries of the objects.

Therefore, a more advanced approach, the Trainable Weka Segmentation (TWS) (Arganda-Carreras et al. 2017) and additional binary morphological operations are used for classification of the three components of the tree. The TWS segmentation employs an implementation of fast random forest ensemble classification algorithm in the Fiji application (Schindelin et al. 2012) using 200 decision trees with 2 random features from user selection. A larger selection of edge-enhancement filters is used to reduce the over-estimation of the leaves at the boundary. The training procedure consisted of providing an initially labeled training dataset, trained using the classifier, visually validating the classification, and improving the user-provided labeled training dataset for improved classification. Finally, small remaining leaf pixels at the boundary of the branches were removed using additional morphological operations (*opening + closing* (Haralick et al. 1987)) using the python library, `scikit-image` (van der Walt et al. 2014). Fig. 4.4c shows the resulting segmentation using the decision tree classification and morphological operation. The Fig. 4.4c shows a better classification of the plant elements than Fig. 4.4b. From this processed dataset, the plant surface mesh for branches and leaves can be generated to obtain metrics such as net leaf surface area.

### 4.2.4 *Wind tunnel setup*

The measurement setup is an integrated measurement approach for simultaneously measuring multiple microclimate parameters. The climate measurements consisted of the measurement of the air relative humidity, air temperature, the net plant transpiration, and the flow velocity. The measurements were performed inside the ETHZ / Empa Atmospheric Boundary Layer (ABL) wind tunnel, a closed-circuit Göttingen type wind tunnel with a test section cross-section of $1.9 \times 1.3$ m$^2$ ($W \times H$). The blockage ratio (i.e., the frontal area of the plant to wind tunnel cross-section) of the plant is determined to be 1.7%. Fig. 4.1a shows the wind tunnel setup that is employed to ensure minimal disturbances from measurement instruments. Dur-

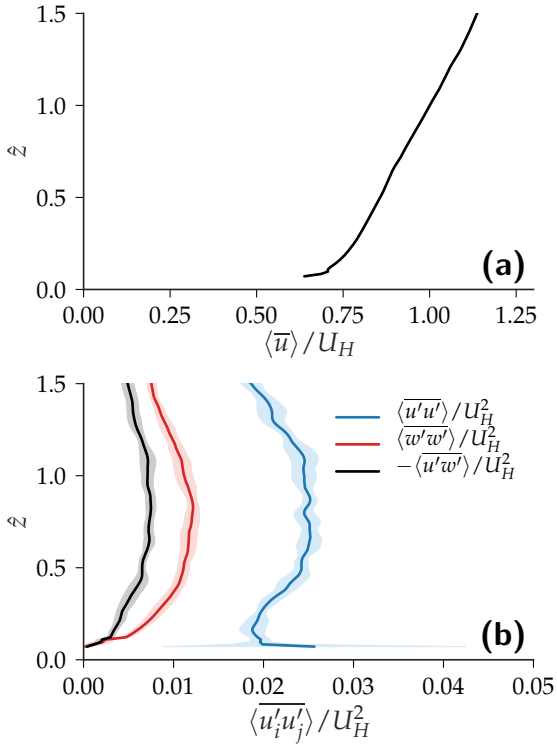


Figure 4.5: Vertical profiles of incoming **(a)** normalized mean streamwise velocity $\langle\overline{u}\rangle / U_H$ and **(b)** normalized Reynolds stresses $\langle\overline{u_i'u_j'}/U_H^2\rangle$. The normalized vertical height $\hat{z} = z/H$. The canopy velocity at $H = 210$ mm is $U_H = 0.77\ \mathrm{m\,s^{-1}}$ (Tsalicoglou et al. 2018).

ing the microclimate measurement, the diurnal variations of the air temperature and relative humidity at different heights were recorded using RH/T (i.e., combined relative humidity and temperature measurement) sensors. In addition, the leaf temperature was measured using infrared thermography. The net transpiration rate from the plant was measured using a mass balance positioned below the wind tunnel floor through an access panel, ensuring that the disturbance of the air flow is affected by the presence of the plant only (Fig. 4.1b). The airflow leeward of the plant was measured using stereoscopic particle image velocimetry (SPIV).

*Microclimate boundary conditions*

A parametric study on the steady-state and dynamic response of the plant exposed to four environmental conditions was performed: two wind tunnel set wind speeds, 0 and 1 $\mathrm{m\,s^{-2}}$, and two plant-canopy incident solar radiation levels, 0 and 100 $\mathrm{W\,m^{-2}}$. A 100 $\mathrm{W\,m^{-2}}$ was seen to be a safe regime for the small buxus plant as a much higher solar radiation intensity was seen to wilt the plant-canopy leaves. The air temperature and the relative humidity inside the wind tunnel were 21 °C and 25% RH, where the condition was coarsely regulated by the HVAC system of the wind tunnel facility.

Fig. 4.5 shows the vertical profiles of the mean upstream streamwise velocity and the Reynolds stresses measured in the empty tunnel at the future position of the plant. At plant canopy height, $H = 210$ mm, the measured mean velocity is $U_H = 0.77\ \mathrm{m\,s^{-1}}$ for the wind speed of $U_{ref} = 1\ \mathrm{m\,s^{-1}}$ (i.e., the set wind tunnel wind speed). The wind tunnel flow was modified using turbulence generators, as shown in Fig. 4.1a, to generate an appropriate ABL profile typically found in an urban context (Tsalicoglou et al. 2018). However, a detailed consideration of the scaling of velocity profile with the tree height was not performed. The profile was chosen to simply mimic the wind profile of an urban area. Fig. 4.5 shows the mean velocity and variance of velocity profiles that is typical for an ABL, with a turbulent intensity $I = \sqrt{2/3\,k}/U_{ref} = 12.1\%$. This turbulence intensity thus exposed the plant foliage to air flow characteristics of an urban boundary profile.

*SPIV setup*

A stereoscopic particle image velocimetry (SPIV) setup was used to measure the time-averaged 3D wake structure of the plant. To reconstruct the full 3D wake of the plant, the SPIV setup is traversed eight times vertically from 60 mm from the ground upwards to 270 mm, at 30 mm intervals, to produce eight SPIV planes, as depicted in Fig. 4.6a. The time-averaged measurements of each plane are then combined to generate a 3D velocity field of the plant wake flow and its associated turbulence statistics.

The SPIV measurement setup consists of two $2560 \times 2160$ pixel s-CMOS HiSense Zyla camera and a 200 $\mathrm{mJ\,pulse^{-1}}$ (at 15 Hz) Nd-YAG Litron laser which is traversed together using a high-precision

system. The two cameras are placed at 38° and 0° normal to the imaging plane. The wind tunnel is seeded with 1 $\mu$m Di-Ethyl-Hexyl-Sebacat (DEHS) tracer particles and the velocity vectors are calculated using an iterative cross-correlation algorithm of Dantec DynamicStudio with final interrogation area of $32 \times 32$ px$^2$ and 50% overlap. The field of view (FOV) of a SPIV plane is $438 \times 559$ mm$^2$ and provides 69 015 PIV vectors per plane with an in-plane resolution of 2.5 mm, whereas the plane-to-plane resolution is 30 mm. To obtain statistically relevant turbulence characteristics, 5000 images are obtained at 15 Hz. Furthermore, to ensure low optical inferences during the SPIV measurement, the hygrothermal measurement devices, thermal imaging devices, and the solar lamp had to be removed. The two distinct setups for airflow measurement and hygrothermal measurement are shown in Fig. 4.6a and Fig. 4.6b, respectively. Furthermore, we assume that the influence of removed devices is minimal for low wind speeds, such as in our case.

*Microclimate and net transpiration rate measurement*

The hygrothermal microclimate conditions within the foliage at various wind and radiation conditions are investigated separately from the flow field measurements, as clarified in Fig. 4.6. Fig. 4.6b shows the setup used to measure the hygrothermal microclimate of the plant. The solar simulator is placed above the plant providing 100 W m$^{-2}$ of incident short-wave radiation at the plant canopy ($H$ = 210 mm). The solar simulator is controlled using a time switch that provides 12-hour periods of 0 and 100 W m$^{-2}$ radiation in alternance, imposing a simplified diurnal solar cycle. A fixed radiation intensity was imposed to obtain the steady-state response on the plant. In future, a time-dependent intensity profile such as sine profile can be investigated. The net plant transpiration is measured using a Mettler PM6100 mass balance placed below the wind tunnel floor in the instrument bay along with the plant pot and water reservoir and the data acquisition system, to minimize their inferences on the flow field. The mass balance has a maximum capacity of 6.1 kg with an accuracy of ($\pm$0.1 g). Simultaneously, the vertical relative humidity and temperature profiles inside the plant are measured using Sensirion SHT35 sensors, as indicated in Fig. 4.6b. Seven SHT sensors are placed as follows: five sensors are directly

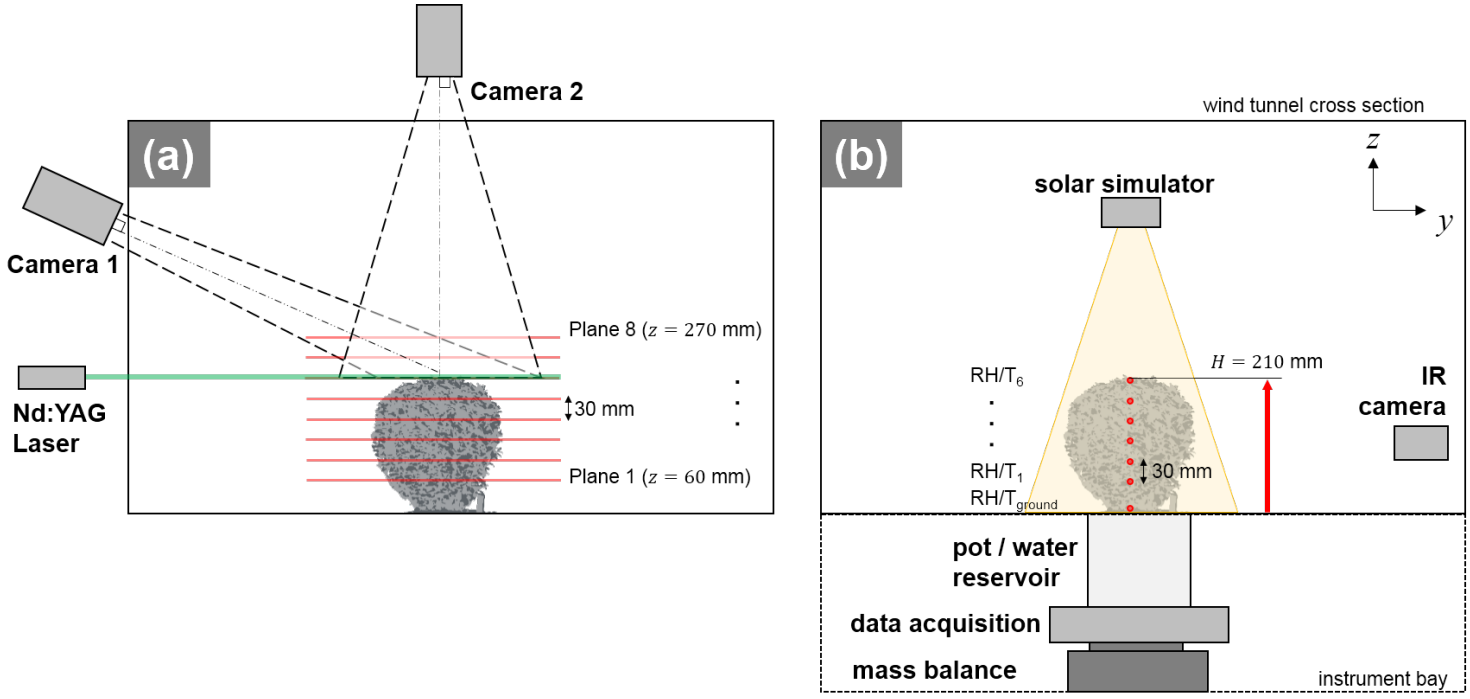


Figure 4.6: Schematic cross section representations of wind tunnel setups used to measure the airflow and hygrothermal microclimate of the plant: **(a)** SPIV setup for multi-plane time-averaged measured velocity consisting of eight horizontal planes, $z = [60, 90, 120, 150, 180, 210, 240, 270]$ mm, **(b)** microclimate measurement setup consisting of IR camera and SHT sensors inside the wind tunnel, mass balance and other data acquisition system below the wind tunnel through an access panel. We note the presence of the solar simulator in the second setup. The two distinct setups are required to attain non-interfered optical measurements of the SPIV.

inside the foliage with a vertical offset of 30 mm starting below the plant canopy (i.e., $z = [60, 90, 120, 150, 180]$ mm), one sensor is at plant canopy (i.e., $z = 210$ mm), and one sensor is below the plant foliage near the ground (i.e. $z = 0$ mm), to measure the shaded conditions. An additional sensor is placed directly downstream of the plant at the height of plant canopy (i.e., $z = 210$ mm). The eight SHT sensors have an accuracy of $\pm 1.5\%$ RH (between 0 and 80% RH) and $\pm 0.1$ °C (between 20 and 60 °C). All the sensors for the plant are connected and powered by the wireless data acquisition system directly below the plant pot, such system is necessary to not hinder the mass balance measurement of water loss due to transpiration. The wireless data acquisition system consists of an Arduino Micro and a 20 100 mAh powerbank providing the necessary power for a multi-day measurement period. The Arduino Micro serves not only as an analog-to-digital signal converter but also as a telemetry device for sending the acquired data to the data logger away from the measurement setup. The data is acquired at a 30-second interval.

*Infrared imaging*

Infrared (IR) thermography is performed to obtain a high-resolution spatial and temporal data of the foliage temperature when exposed to varying environmental conditions. The feasibility of employing infrared thermography to obtain leaf temperature variability has been demonstrated in the past (Jones 1999; Merlot et al. 2002). IR imaging system is employed to measure the outer plant foliage temperature simultaneously with the hygrothermal and net transpiration rate measured for two different wind conditions throughout the diurnal radiation cycle. The IR imaging system consists of the Optris PI 640 IR camera with a $640 \times 480$ px$^2$ sensor, a spectral response between 7.5 and 13 $\mu$m and is set to measure $-20$ to 100 °C with an accuracy of $\pm 2$ °C (Allegrini 2018; Tsalicoglou et al. 2018). A 33° lens is used providing an effective FOV of $223 \times 211$ mm$^2$. The IR measurement is performed at a frequency of 1 frame minute$^{-1}$ throughout the diurnal cycle. A PT100 (platinum resistance thermometer) sensor is placed in FOV of the IR image for calibration (Allegrini 2018).

## 4.3 RESULTS AND DISCUSSION

### 4.3.1 *X-ray tomography: A non-destructive approach to obtain plant traits*

*Plant porosity distribution*

Fig. 4.7a shows the average porosity for representative elementary volumes (REV) of voxel sizes ranging from 5 to 100 $px^3$. To calculate the spatial distribution of plant porosity, a sufficiently large REV has to be chosen to ensure that variability in the plant microstructure is taken into account. However, if the REV is too large, it sacrifices the resolution of the porosity distribution. If the REV size is 100 $px^3$, the resulting porosity is $\langle \phi \rangle_{xyz} = 90\%$. However, the downside of such a large REV size is that it has scarified the spatial resolution of porosity distribution. Therefore, in our case, an REV size of 30 $px^3$ was seen to be optimal, providing sufficient accuracy and resolution, with a calculated average plant porosity of $\langle \phi \rangle_{xyz} = 88\%$. Fig. 4.7a also shows the average porosity obtained from both *weka* segmentation and the *histogram* segmentation methodology as described in Section 4.2.3. We see that both approaches follow the same profile with minor differences. This result indicates that both approaches accurately differentiates air space and biological material. However, in Section 4.2.3, it was seen that the *weka* method provides a better classification of leaf and branches, as visible in Fig. 4.4. So, to obtain key parameters such as leaf surface area, the *weka* method is opted.

Fig. 4.7b shows three vertical distributions of plant porosity. In conjunction with the plant porosity based on the X-ray CT (black line), the optical and aerodynamic porosity of the plant (with respect to the incident airflow direction in the wind tunnel) are investigated. The optical and aerodynamic porosity are typical measures used in the wind tunnel studies to estimate the aerodynamic contribution of the plant porosity (Grant and Nickling 1998; Guan et al. 2003; Manickathan et al. 2018a). The optical porosity $\beta$ and the aerodynamic porosity $\alpha$ can be related as follows:

$$\alpha = \beta^{0.4} \tag{4.2}$$

empirically derived from wind tunnel measurements (Guan et al. 2003). The optical porosity is obtained from a 2D optical image of

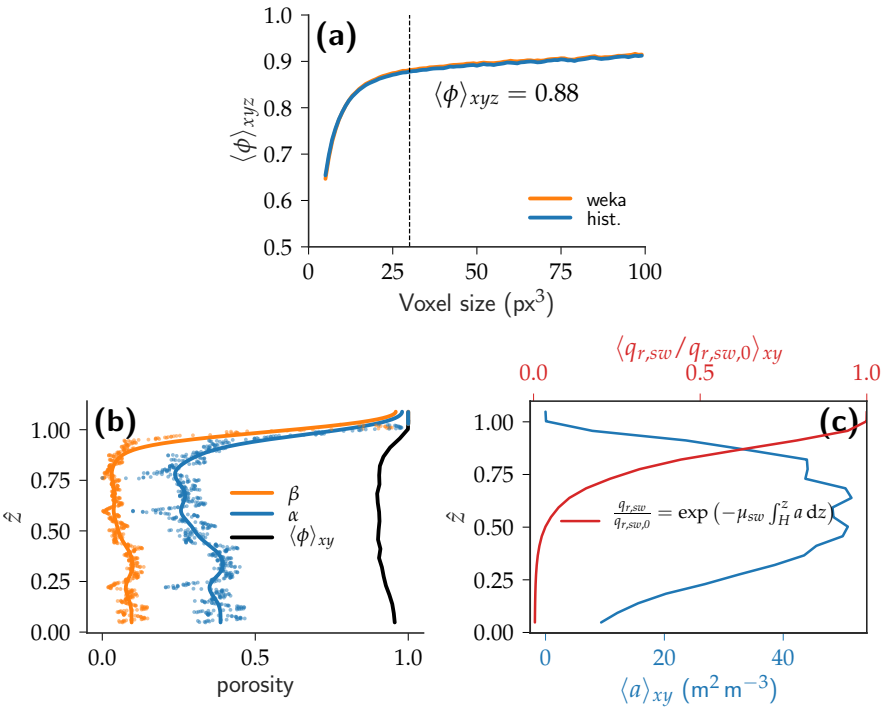


Figure 4.7: **(a)** Average plant porosity $\langle\phi\rangle_{xyz}$ with respect to voxel size (px$^3$) as a base for determining the REV for calculating porosity distribution, **(b)** Three vertical porosity distributions: optical $\beta$, aerodynamic $\alpha$ and true porosity $\langle\phi\rangle_{xy}$, and **(c)** leaf area density $\langle a\rangle_{xy}$ (m$^2$ m$^{-3}$) (blue) and normalized short-wave radiative flux $q_{r,sw}$ profile (red) inside vegetation determined using Beer-Lambert law extinction coefficient of short-wave radiation $\mu_{sw} = 0.78$ (Manickathan et al. 2018b).

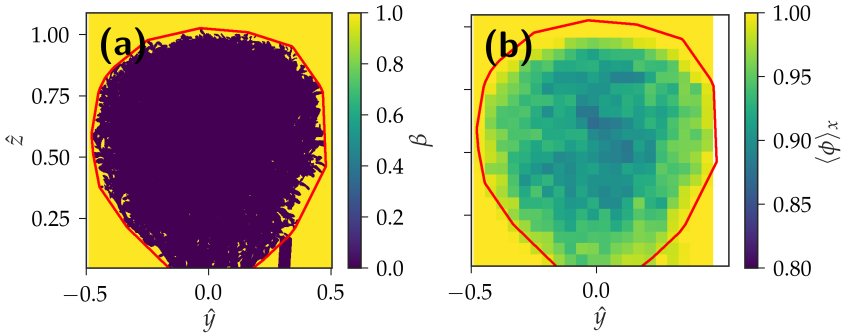


Figure 4.8: Porosity distributions of the plant: **(a)** The optical porosity $\beta$ with plant element and airspace indexed as 0 and 1, respectively and **(b)** streamwise-averaged plant porosity $\langle\phi\rangle_x$.

the tree perpendicular to the incident flow direction (Fig. 4.8a) and is defined as the ratio of empty pixels (without plant elements) to the total number of pixels within the silhouette of the plant, shown in Fig. 4.8. A convex hull is used to define the silhouette of the plant. Furthermore, the streamwise-averaged plant porosity $\langle\phi\rangle_x$ (Fig. 4.8b) is investigated to quantify how much the plant that is blocking the flow field at a given location. It indicates clearly that the highest blockage is found near the top half of the plant (i.e., $\hat{z} = 0.75$). Such location of high plant foliage density can lead to high solar radiative absorptions and a resulting high transpiration rate, a hypothesis that will be studied by measuring the air temperature and relative humidity, showing the regions of high transpiration. The plant foliage density is seen to reduce towards to the edges gradually and at these regions, a lower blockage might be present with a higher bleed flow, which can provide internal ventilation, increasing the convective dominated processes such as sensible and latent heat fluxes (Manickathan et al. 2018b).

The horizontal-averaged ($x - y$ plane) porosity distribution is shown and compared in Fig. 4.7b. Comparing optical, aerodynamic and real 3D-based porosity (i.e., the plant porosity), we see that the real 3D-based porosity of the plant is substantially higher than the optical and the aerodynamic porosities. This indicates that the aerodynamic porosity usually used in various studies (Bitog et al. 2011; Guan et al. 2003; Manickathan et al. 2018a), does not reflect the true

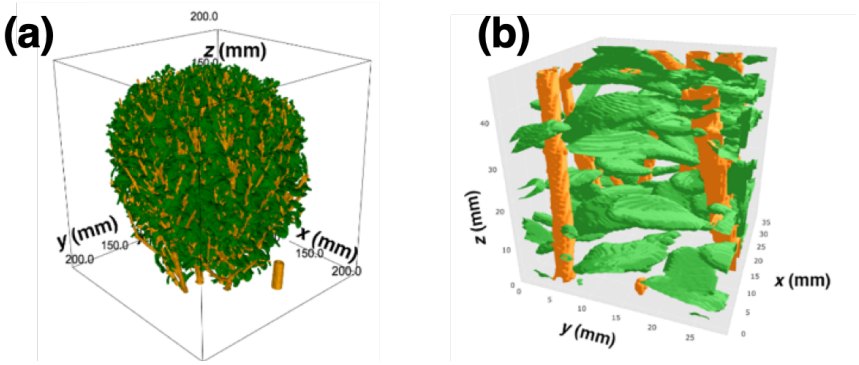


Figure 4.9: Surface geometry of the plant, where leaves (green) and branches (orange) are differentiated: **(a)** complete plant surface, **(b)** sub-volume inside the plant foliage.

plant porosity. However, it is still uncertain as to which porosity provides the best description of the impact of the tree on the flow field such as the wake velocity deficit and the turbulent kinetic energy profile. Therefore, the influence of true plane porosity $\phi$ and the aerodynamic porosity $\alpha$ on the wake velocity statistics is investigated in Section 4.3.2.

*Plant surface mesh and total leaf area*

In addition to the porosity distribution of the plant, the total leaf area, leaf area index and leaf area density are important parameters for understanding and modeling the influence of vegetation (Manickathan et al. 2018b). The plant parameters are obtained from X-ray tomography, and the surface of the plant components is generated from the volumetric data of the plant X-ray CT. Fig. 4.9a shows the leaf and branch surface colored as green and orange, respectively. Fig. 4.9b shows an internal sub-volume of the plant for clarity. The surface geometry is generated using a marching-cube algorithm implemented in `scikit-image` (van der Walt et al. 2014).

The total leaf surface area is determined by integrating the mesh surface and is calculated to be $A_l = 0.75$ m$^2$. A metric of plant trait commonly used to quantify the amount of leaves is the leaf area index (LAI). The leaf area is defined as the ratio of one-sided leaf area to the plant ground cover area $A_g$. The one-sided leaf area is simply assumed to be half the total measured leaf area, and the plant

ground cover area is derived from the X-ray CT dataset. The plant ground cover was determined to be $A_g = 0.031$ m$^2$, and a resulting leaf area index of $LAI = 12.14$ m$^2$ m$^{-2}$ is measured. Therefore, the plant is seen to have a high LAI because it is a shrub species that is commonly used as hedgerows or shelterbelts.

The (one-sided) leaf area density $a$ (m$^2$ m$^{-3}$) (or also known by LAD) is a key parameter that is used to represent vegetation as a porous medium in a numerical models (de Langre 2008; Gross 1987; Manickathan et al. 2018b). It is related to the net leaf surface area (two-sided) $A_l$ and the plant porosity $\phi$, given as:

$$a = \frac{1}{2} A_l \frac{1-\phi}{\int 1-\phi \, \mathrm{d}V} \tag{4.3}$$

Fig. 4.7c shows the vertical distribution of the horizontally-averaged (i.e., streamwise $x$ and spanwise-averaged $y$) leaf area density $\langle a \rangle_{xy}$ (m$^2$ m$^{-3}$). The leaf area density $a$ has a peak value of $\langle a \rangle_{xy} \approx 50$ m$^2$ m$^{-3}$ where the porosity is at lowest and approaches zero at the top and bottom regions of the foliage as $\phi \to 1$. An important aspect of the a distribution is its influence on the solar radiation attenuation within the foliage. The extinction of solar radiation within the foliage due is typically modeled using a simple Beer-Lambert law and can be assumed to depend only on the a distribution and the extinction coefficient of the short-wave radiation $\mu_{sw}$ (Manickathan et al. 2018b) and a detailed description is provided in Section 5.3. Fig. 4.7c also shows the vertical distribution of normalized short-wave radiative flux $\langle q_{r,sw} \rangle_{xy}$ determined from Beer-Lambert law. We see that nearly 50% of the above-canopy solar radiation intensity $q_{r,sw,o}$ is absorbed within just the top 20% of the plant foliage and a further 30% within the next 10% of the foliage. Therefore, most of the solar radiation is seen to be absorbed within the top layer of the plant indicating that the influence of solar radiation will be present at this region (Manickathan et al. 2018b). To investigate this further, the influence of measured leaf area density distribution on the hygrothermal climate variables ($T$, $T_l$, $RH$) inside the foliage is investigated in Section 4.3.3.

### 4.3.2 *3D wake flow characterization by SPIV*

The 3D wake flow field is studied using stereoscopic particle image velocimetry (SPIV). The study aims to understand the influence of the porous plant microstructure on the wake flow characteristics. Therefore, the mean velocity and the turbulence kinetic energy (TKE) of the plant wake is studied and compared with the porosity distribution. The setup of the PIV system is detailed in Section 4.2.4, measuring eight horizontal planes behind the plant at vertical heights of $z = [60, 90, 120, 150, 180, 210, 240, 270]$ mm, heights normalized below to the height of the plant.

*Normalized mean velocity magnitude*

The time-averaged mean velocity of the plant wake is studied first to understand how the plant porosity influences the flow. Fig. 4.10 shows the normalized mean velocity magnitude $|\overline{\boldsymbol{u}}|/U_H$ where $U_H = 0.77\,\mathrm{m\,s^{-1}}$. The coordinate system is normalized with the tree height of $H = 210$ mm, where $\hat{x}_i = x_i/H$ for $x_i = \{x, y, z\}$. This mean velocity distribution shows a prevailing recirculating flow for $\hat{z} \leq 0.71$, whereas above $\hat{z} > 0.71$, the streamlines indicate a bleed flow with $\phi \to 1$ (Fig. 4.8b). To further link the flow field to the climate, the influence of the flow conditions on the hygrothermal microclimate inside the plant will be investigated in Section 4.3.3.

*Turbulent kinetic energy*

An important impact of trees on the airflow is the modification of the turbulent kinetic energy (TKE). In literature, several studies emphasize the role of vegetation in turbulence enhancement for urban flows, which can drastically influence the pollution dispersion and thermal characteristics (Amorim et al. 2013; Gromke et al. 2008; Poggi et al. 2004). The internal structure of the plant is known to affect the budget of TKE directly. In addition to the well-known Richardson-Kolmogorov energy cascade from mean kinetic energy (MKE) to TKE (Pope 2000), the plant is known to *produce* and *dissipate* the TKE due to the additional shortcut in energy transfer from MKE to TKE and the shortcut from TKE to turbulent dissipation rate (TDR) (Finnigan 2000; Wilson and Shaw 1977). This is due to

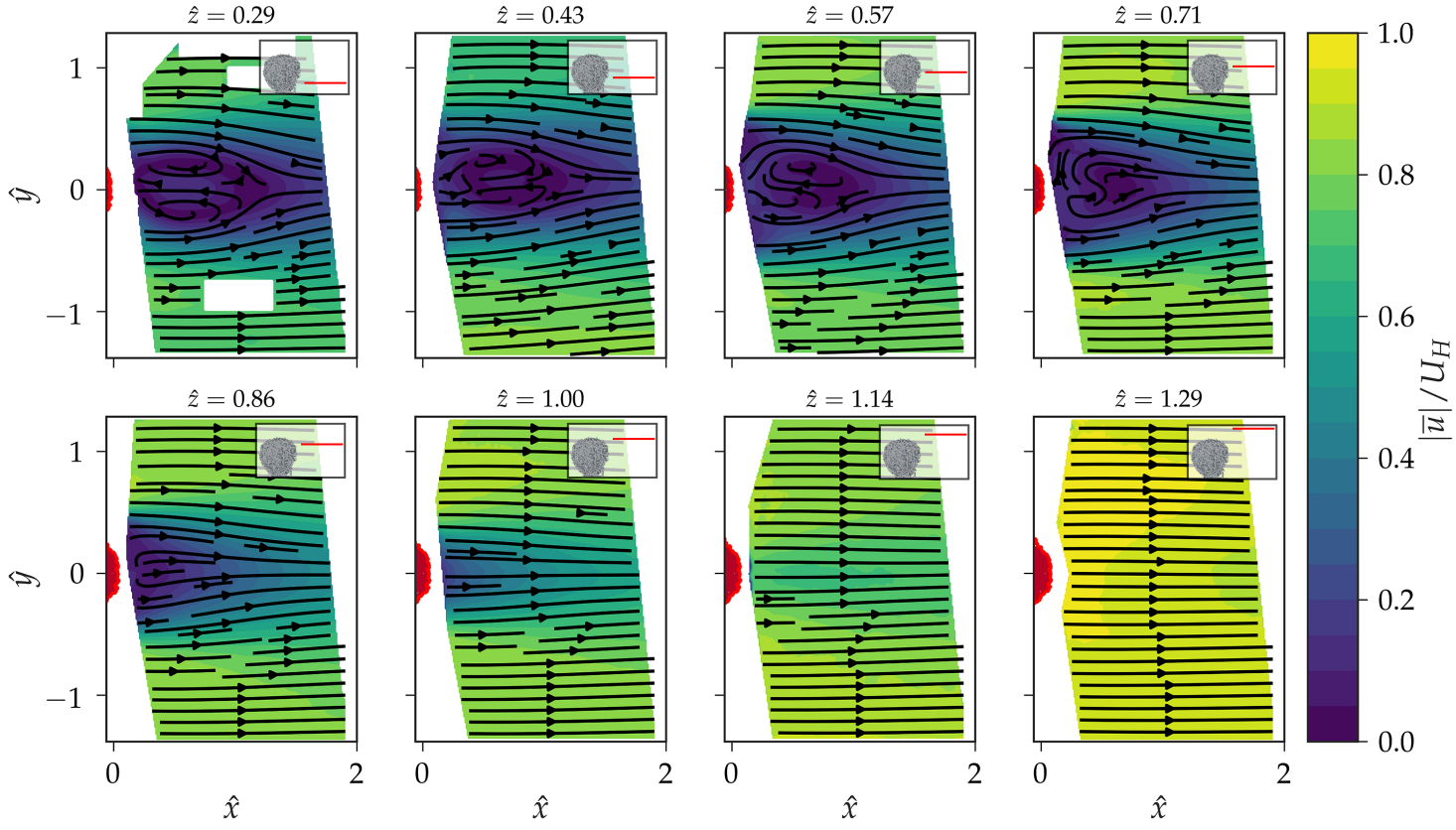


Figure 4.10: Normalized mean velocity magnitude $|\overline{\boldsymbol{u}}|/U_H$ at 8 horizontal planes, $\hat{z} = [0.29, 0.43, 0.57, 0.71, 0.86, 1.0, 1.14, 1.29]$ where the red shaded area indicates the location of the tree. The horizontal plane location is indicated by the red line in the in the sub-box.

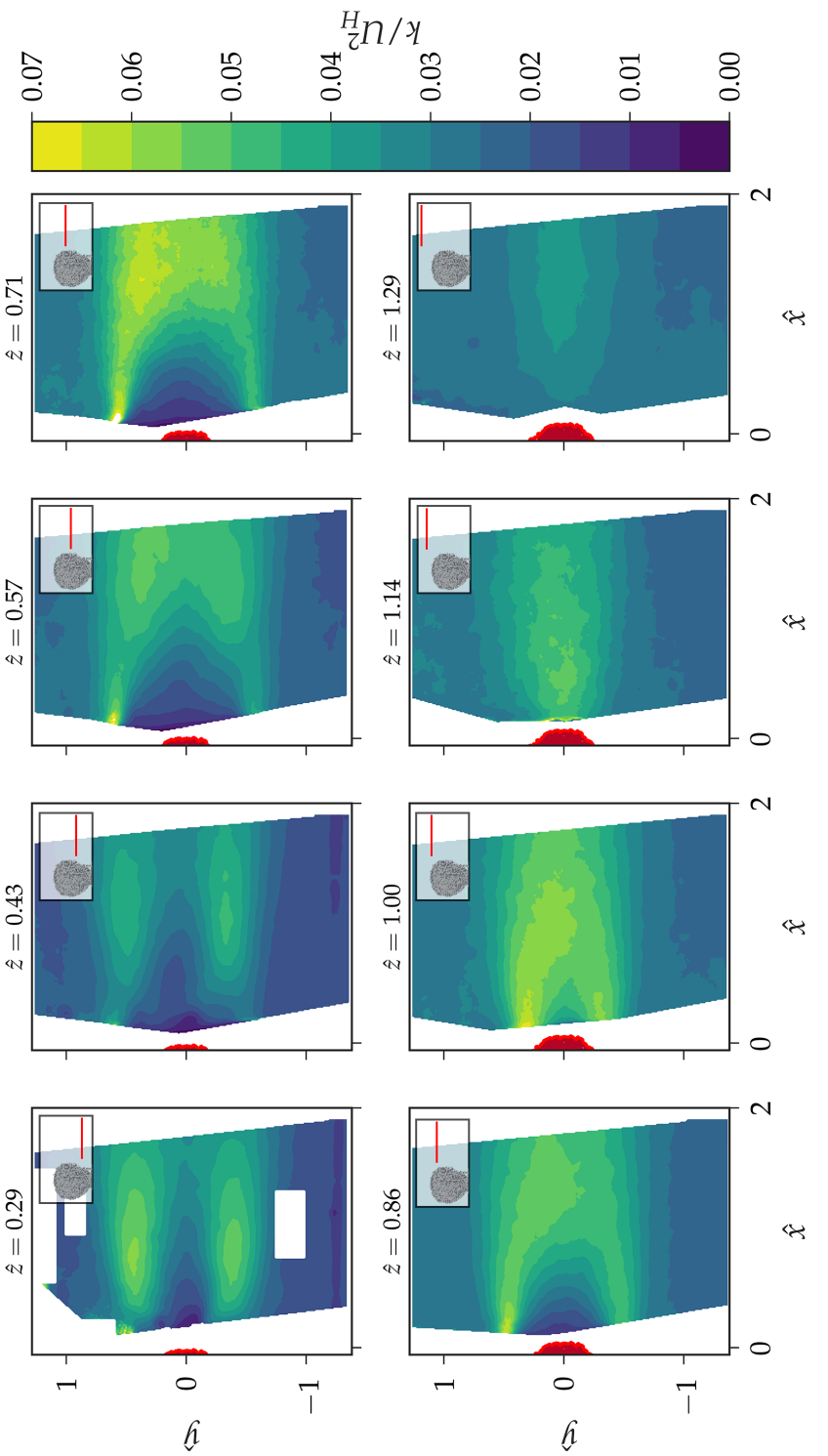


Figure 4.11: Normalized turbulent kinetic energy $k/U_H^2$ at 8 horizontal planes, $\hat{z} = [0.29, 0.43, 0.57, 0.71, 0.86, 1.0, 1.14, 1.29]$ where the red shaded area indicates the location of the tree. The horizontal plane location is indicated by the red line in the in the sub-box.

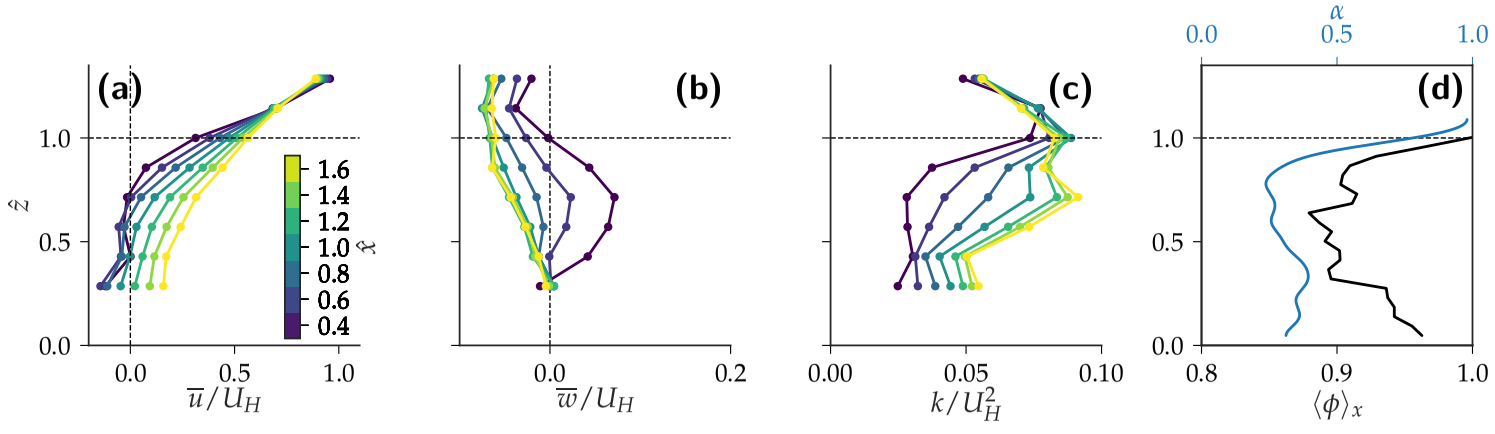


Figure 4.12: Mean vertical profiles at 7 streamwise positions $\hat{x}$ at center-line of the plant $\hat{y} = 0$: **(a)** streamwise velocity $\overline{u}/U_H$ **(b)** vertical velocity $\overline{w}/U_H$, **(c)** turbulent kinetic energy $k/U_H^2$, and **(d)** streamwise-averaged porosity $\langle\phi\rangle_x$ and aerodynamic porosity $\alpha$.

the plant components interacting with the flow creating strong velocity gradients generating the TKE and the leaves act at turbulence suppressors, increasing the dissipation rate (Kenjereš and ter Kuile 2013). The spatial variability in the turbulent kinetic energy (TKE) of the plant wake is investigated to understand the turbulence modification and link this effect to the plant porosity distribution. Fig. 4.11 shows the normalized turbulent kinetic $k/U_H^2$ for the 8 horizontal planes. Trivially, the TKE is low above the tree ($\hat{z} > 1$) and directly behind the plant (near $\hat{x} = 0$, $\hat{y} = 0$ mm), where the air speeds are low. In contrast, the TKE is high at the shear zones between high-speed and low-speed zones. Comparing different planes, we see that the TKE profile is high near the ground ($\hat{z} = 0.29$) and near the plant canopy ($\hat{z} = 1$). This again is attributed to the high shear flows generated from the boundaries of the plant foliage that is present at these two vertical levels.

*Linking flow field to plant porosity*

To better study the influence of plant porosity on the wake flow, the centerline flow statistics and the plant porosity are compared. Fig. 4.12 shows the vertical profiles of the center-line velocity at $\hat{y} = 0$ for 7 streamwise positions, $\hat{x} = [0.4, 0.6, 0.8, 1.0, 1.2, 1.4, 1.6]$. The vertical profiles consist of streamwise velocity $\overline{u}/U_H$, the vertical velocity $\overline{w}/U_H$, and the turbulent kinetic energy $k/U_H^2$. Furthermore, to determine the relation between plant porosity distribution and wake flow field, the vertical streamwise-averaged porosity distributio $\langle\phi\rangle_x$ and aerodynamic porosity $\alpha$, obtained from Fig. 4.8b, is also plotted. We see that both the porosity distributions are only weakly linked to the streamwise velocity $\overline{u}/U_H$. This is observable at $\hat{z} > 0.7$, as porosity approaches $\phi \to 1$, the streamwise velocity increases as well. In contrast, there is no apparent link between the vertical velocity $\overline{w}/U_H$ or turbulent kinetic energy $k/U_H^2$. Instead, we see that wake velocity deficit is governed by how the upstream wind profile is modified by the shear zones generated the outer geometry of the plant. This is because the ABL inflow condition has a more dominant influence on the wake profile and the resulting shear-layer and recirculation zone (as indicated by the negative streamwise velocity at $\hat{z} < 0.5$ and $\hat{x} < 0.8$). Therefore, in the present study, we do not observe a direct link between the spatial distribution of the aero-

dynamic porosity $\alpha$ nor the spatial distribution of the plant porosity $\phi$ with the wake flow statistics. Instead, it is found to be dependent more on the total porosity of the plant and the geometry of the plant foliage. As $\phi \to 1$, the velocity deficit decreases too. An insight of the influence of total plant porosity on the wake velocity statistics is presented in Section 7.3.1, where the plant drag is adjusted by varying the drag coefficient instead of the porosity as scaling the drag coefficient is equivalent to scaling the net porosity (see Eq. (5.13)). We observe that reducing the plant drag, the wake velocity deficit is indeed reduced. Similarly, as plant drag reduces, the TKE is also reduced.

### 4.3.3 *Diurnal hygrothermal behavior of the plant*

A thorough understanding of the plant morphology from Section 4.3.1 and the resulting flow characteristics in Section 4.3.2 enables us to link plant porosity to the wake flow characteristics. In this section, we investigate the link between plant morphology and the hygrothermal parameters such as air temperature and relative humidity. First, the diurnal response of the plant and its daytime and nighttime averages are investigated. Thereafter, the dynamic characteristics during the transition between day and night are investigated.

#### *Influence of environment on diurnal response*

The diurnal behavior of the plant is investigated for two distinctly different boundary conditions: no-wind condition and wind condition with $U_{ref} = 1\ \mathrm{m\,s^{-1}}$. Fig. 4.13 shows the diurnal variation of the water mass loss $m$ (g) throughout the day and night and the resulting the transpiration rate $TR$ ($\mathrm{g\,h^{-1}}$), defined as:

$$TR = \frac{\mathrm{d}m}{\mathrm{d}t} \tag{4.4}$$

measuring the hourly change in mass due to transpiration. We observe that, during the night regardless of the wind condition, a constant transpiration rate of 2.5 $\mathrm{g\,h^{-1}}$ exists. This transpiration rate, in the absence of solar radiation, is therefore associated to the water loss due to dark respiration (Farquhar et al. 1980; Lambers et al.

2008; Launiainen et al. 2015). At dawn, a strong increase in transpiration rate is observable. Furthermore, at this time, the wind speed plays an important role: with the wind, a peak transpiration rate of 15 $g\,h^{-1}$ is observed whereas, without wind, the transpiration rate peaks only at 10 $g\,h^{-1}$. As the day progresses, the stomatal regulation is seen to compensate for the influence of wind, resulting in similar transpiration rate with an average transpiration rate of 9 $g\,h^{-1}$. The decay in the daytime transpiration after dawn has also been observed previously (Javaux et al. 2013; Tuzet et al. 2003). Thus, we see that the day is composed of four unique stages: "*no-cooling*" stage, "*high-cooling*" stage, "*equilibrium*" stage, and finally "*decaying-cooling*" stage. The no-cooling period is present at the initial stages of dawn where the leaves absorb solar radiation and the stomatal response has not been prevalent to provide an adequate transpiration rate. Thereafter, there is period of high transpiration (*HC*) and eventually arrives at an pseudo-equilibrium transpiration rate (*EQ*). Towards the end of the day, the transpiration rate remains decaying (referred to as *DC* or *decayed-cooling*). This decaying transpiration phenomenon is most likely attributed to the reduced rhizosphere soil moisture content. The reduced soil moisture content eventually reduces the stomatal conductance, resulting in the decayed transpiration rate that we observe. However, at night, the soil moisture equilibrates as the root water uptake is drastically diminished to only 2.5 $g\,h^{-1}$.

The influence of the varying transpiration rate is further investigated by studying the hygrothermal microclimate variables, air temperature $T$ (°C) and relative humidity $RH$ (%) inside the plant foliage. The setup of the hygrothermal sensors was detailed in section Section 4.2.4. Fig. 4.14 shows the diurnal variation of the air temperature and relative humidity inside the tree at various heights, with $T_1$ at the bottom of foliage and $T_6$ at the plant canopy ($\hat{z} = 1$). The configuration is such that probes 1 to 5 are directly inside the plant foliage with 30 mm offset. Furthermore, the ambient condition (*air*) and the ground condition below the plant (*ground*) is compared to study the influence of plant shading. Fig. 4.14 shows that, in the *no-wind* condition, there is a quantifiable drop over height in the air temperature and a substantial increase in the relative humidity, with peak $RH = 75\%$ during day time. During the night, the vertical variability in the environmental conditions within the foliage is smaller

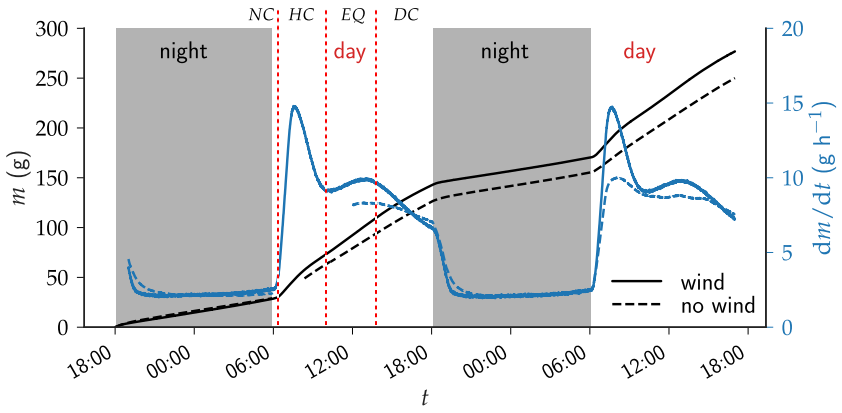


Figure 4.13: Diurnal variation of mass loss $m$ (g) and the resulting transpiration rate $TR = \mathrm{d}m/\mathrm{d}t$ (g $\mathrm{h}^{-1}$) for two wind conditions: *no wind* and *with wind* ($U_{ref} = 1$ $\mathrm{m\,s}^{-1}$). Note: A part of no-wind data is missing (between 06 : 00 to 12 : 00) due to a fault in data acquisition.

but still noticeable. All the sensors inside the plant foliage show lower temperatures compared to ambient temperature, both during day and night. However, the sensor at plant canopy height ($\hat{z} = 1$), shows that the air temperature is noticeably higher than the ambient condition. This indicates that the plant canopy region is strongly influenced by the absorption of solar radiation, leading to higher leaf temperature and thereby heating up the air. Similar observation of such positive leaf-to-air temperature due to high solar radiation absorption have also been observed numerically (Manickathan et al. 2018b). However, in the shadow of the plant, we see that air temperature is lower than in the sunlight region. We must note that the soil is sealed so that water loss is simply due to transpiration of the leaves. Therefore, the cooling by the ground is attributed to the plant shading only resulting in less energy storage and leading to lower air temperatures.

The impact of transpiration, i.e., local cool oasis, diminishes strongly when the wind is present. The increased ventilation of the plant foliage due to the wind is seen to reduce the cool oasis formed by the transpirative cooling indicated by the higher air temperature compared to the no wind conditions especially in the lower zone of the tree. This ventilation by wind also leads to lower relative humidity

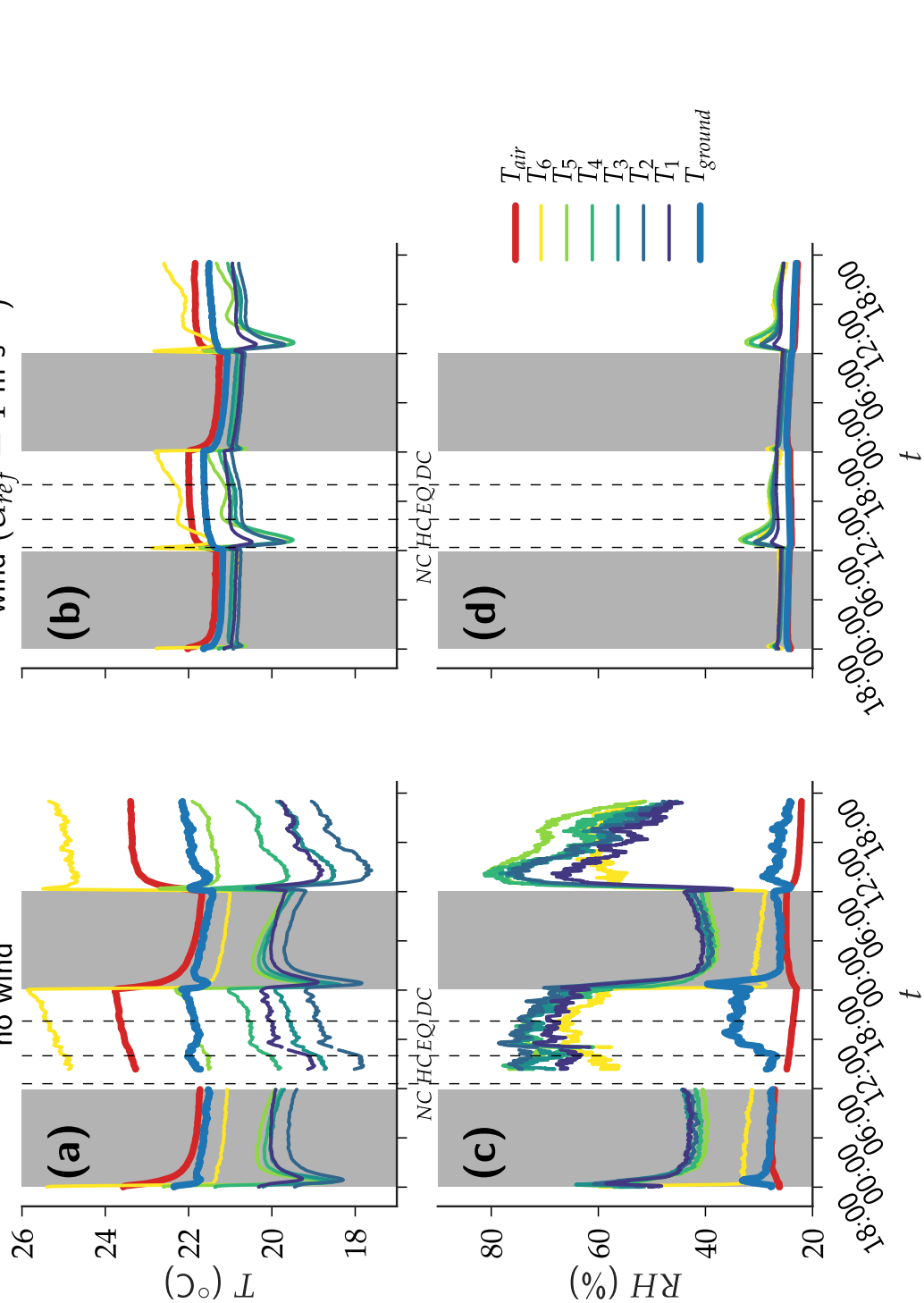


Figure 4.14: Diurnal variation of air temperature $T$ (°C) and relative humidity $RH$ (%) inside the tree at varying heights for two wind conditions: **(a)(b)** *no wind* and **(c)(d)** *wind* ($U_{ref} = 1$ m s$^{-1}$).

values in the tree. Fig. 4.13 shows that the influence of wind on transpiration rate is, however, more complex. When the relative humidity reduces, the vapor pressure deficit (VPD) is known to rise (Manickathan et al. 2018b). Thus, at dawn, due to the high atmospheric evaporative demand (AED) (such as when VPD is low or high radiation intensity), the transpiration rate is substantially higher than in the *no-wind* case. This observation is in line with the theory that transpiration scales with atmospheric evaporative demand (McVicar et al. 2012). At dawn, when the stomatal resistance is low (or stomatal conductance is high), the Penman-Monteith equation predicts an increasing transpiration rate with increasing wind speed (Idso 1977; Nobel 2009). However, as the day progresses, the transpiration rate is seen to equilibrate down to the *no-wind* condition level. This is the result of the influence of wind speed on the leaf water use efficiency (WUE, i.e., carbon uptake rate for a given transpiration rate), resulting in a decreasing transpiration rate (Dixon and Grace 1983; Nobel 2009; Schymanski and Or 2016). As the day progresses, due to the high sensible heat flux providing efficient convective cooling to the leaves, it improves the plant's ability to conserve water, reducing the stomatal conductance (Idso 1977). Thus, even though there is higher wind speed and an equivalently higher AED, the transpiration rate is seen to be similar to that of the *no-wind* condition.

*Day versus night comparison of plant response*

The average daily response of the plant and its influence on the climate are studied to understand the cooling provided by the plant. Fig. 4.15(a-d) shows the median air temperature at various heights for the case *no-wind* Fig. 4.15(a-b) and *wind* Fig. 4.15(c-d), respectively. Furthermore, the figure differentiates the daytime (i.e., 08:00 to 16:00) and nighttime (i.e., 20:00 to 04:00) median air temperature (i.e., a temporal-averaging window size of 8 hours). The daytime and nighttime period were shortened to focus on the period that is nearly steady-state. The figure shows that the air temperature change is largest during the day. However, more interesting, the figure shows that, in the presence of wind, the air temperature inside the tree is more homogenized, whereas, without wind, a large vertical variability is observed. We see that the vertical profile of temperature and relative humidity is correlated with the leaf area

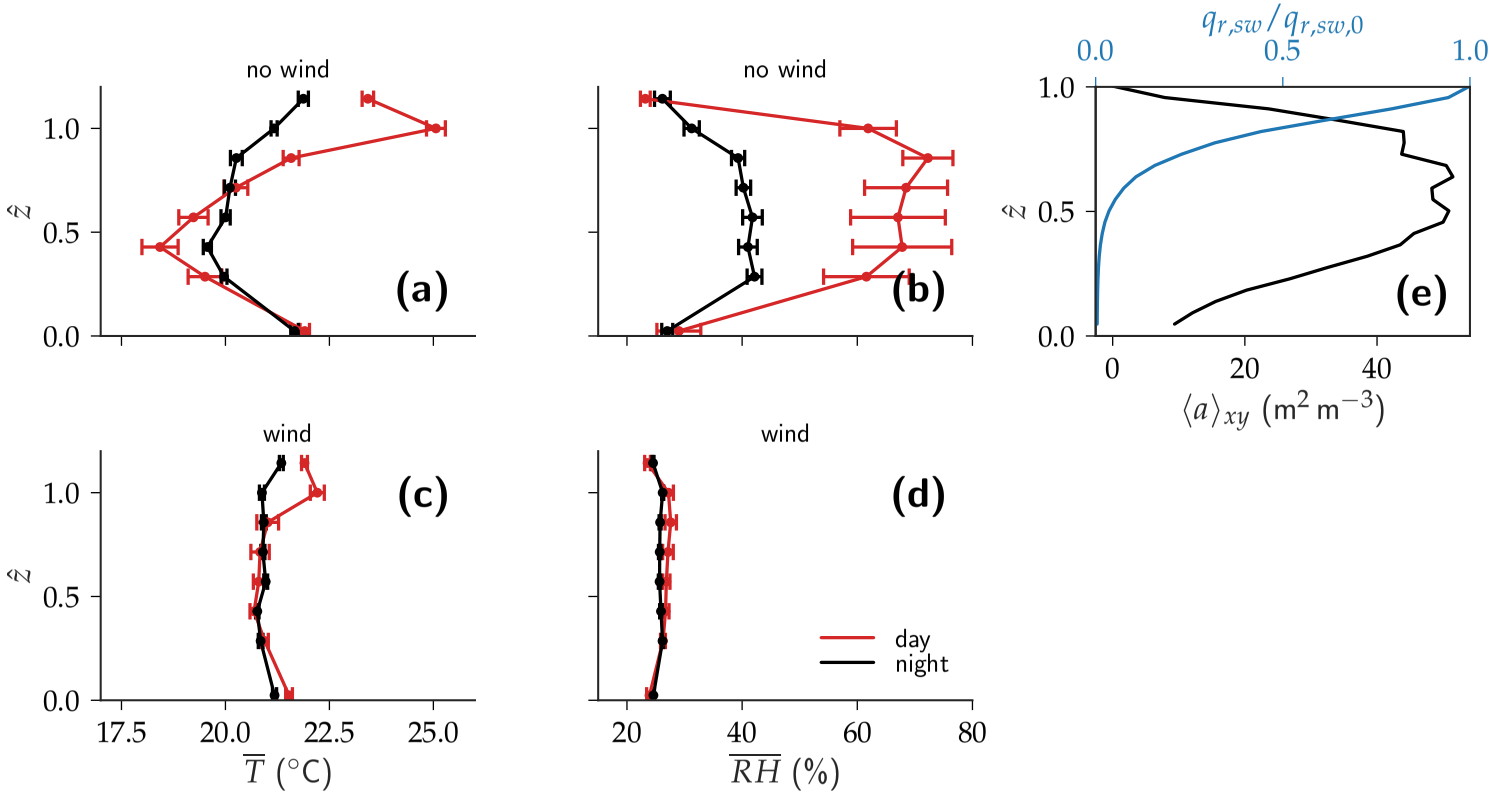


Figure 4.15: Mean vertical distribution of day (08:00 - 16:00) (red) and night (20:00 – 04:00) (black) **(a)(c)** air temperature $T$ (°C) and (**(b)(d)** relative humidity $RH$ (%) inside the tree for two wind conditions: **(a)(b)** *no wind* and **(c)(d)** with *wind* ($U_{ref} = 1$ m s$^{-1}$); and (e) horizontal-averaged vertical distribution of leaf area density$\langle a \rangle_{xy}$ (m$^2$ m$^{-3}$) and normalized short-wave radiation intensity $\langle q_{r,sw}/q_{r,swm,o} \rangle_{xy}$.

density $\langle a \rangle_{xy}$, where large air temperature change and humidity change is observed at regions of high leaf area density. Furthermore, the air temperature is seen to be related to the solar radiative heat flux $\langle q_{r,sw} \rangle_{xy}$ gradient, especially during *no-wind* condition, shown in Fig. 4.15e. At region on high change is solar radiation intensity, a stark increase in air temperature is observed, indicating high solar radiation absorption. The most significant cooling, i.e., providing the largest drop in air temperature, is present for the *no-wind* condition during the day for heights between $0.29 \leq \hat{z} \leq 0.57$. Moreover, at these regions, we also observe a large increase in the relative humidity. We see that relative humidity is high where leaf area density is high. At regions of high LAD, there is a higher transpiration rate resulting in a higher transpirative cooling. Moreover, the enhanced effect of transpirative cooling and the generation of the local cool zone is seen to be only prevalent when the wind is low.

High air temperature is observed at the plant canopy region and is the result of high solar radiation absorption at this layer, as indicated by the solar radiative heat flux profile (Fig. 4.15e) As most of the solar radiation is absorbed in the plant canopy (i.e., top 20% of the foliage), it can result in a large increase in leaf temperature (i.e., $T = 25\ ^{\circ}\mathrm{C}$) and thereby a strong increase in the air temperature (Manickathan et al. 2018b). Such gradient in radiation absorption results in the observed air temperature spike at plant canopy as indicated by probe 6 ($\hat{z} = 1$). In contrast, for probes 1 to 5 ($\hat{z} = [0.29, 0.44, 0.57, 0.71, 0.86]$) that are within the foliage, which are at regions of low solar radiation intensity, significantly lower air temperature is observed.

To investigate the variation in leaf temperature and its link to transpiration and solar radiation, the leaf temperature at the exterior of the plant is measured through infrared thermography. Fig. 4.16 shows the diurnal variation of leaf surface temperature for *wind* and *no-wind* condition. The thermography shows that, during the *wind* condition, the spatial variability in leaf temperature is minimal, especially during the night. Therefore, the convective cooling of the leaves homogenizes the vertical variability in the leaf temperature. This is especially evident when observing the *no-wind* condition. During the *no-wind* condition, the vertical variation in leaf temperature shows a high plant-canopy leaf temperature and a cool in-foliage leaf temperature, especially at the lower regions.

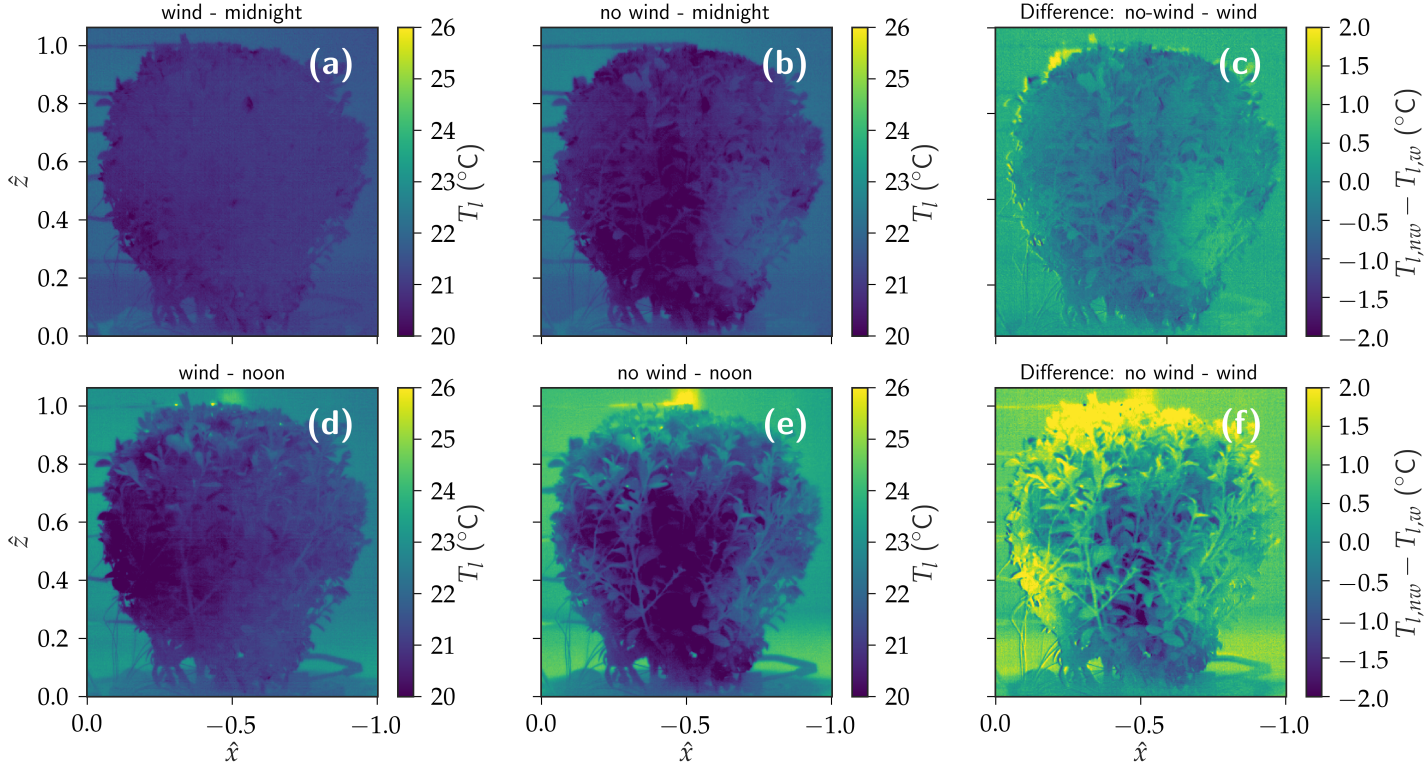


Figure 4.16: Diurnal variation of leaf surface temperature $T_l$ (°C) at **(a)(b)(c)** nighttime (midnight) (**(d)(e)(f)** and midday (noon). The difference between *wind* and *no wind* condition is compared for **(c)** night and **(f)** day.

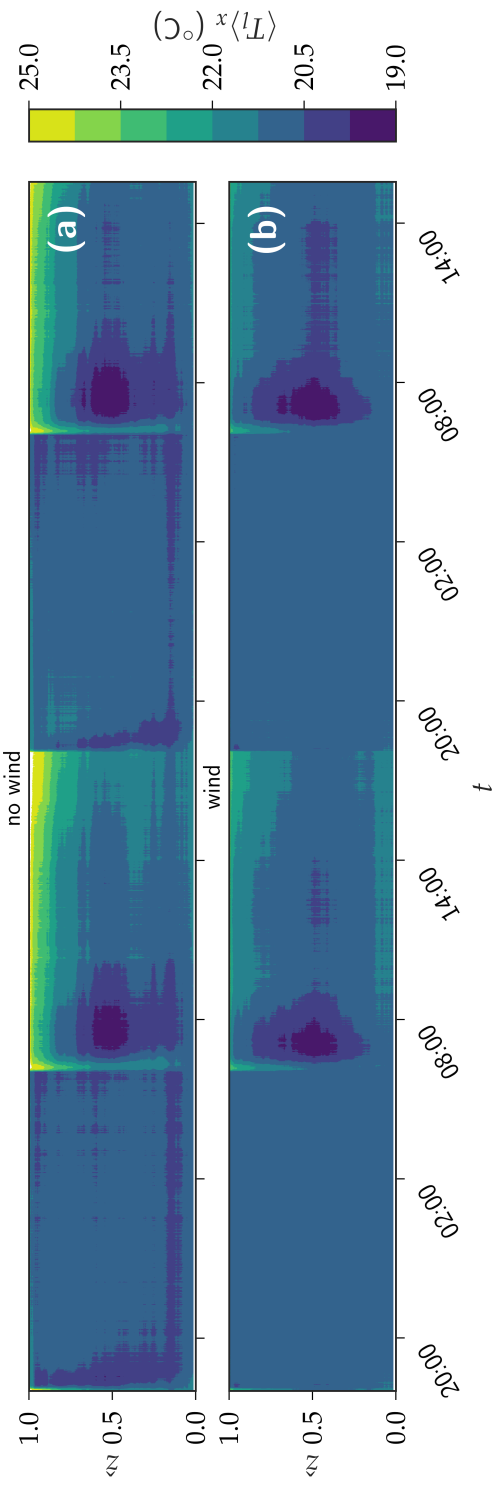


Figure 4.17: Streamwise-averaged spatiotemporal variability of leaf temperature $\langle T_l \rangle_x$ (°C) comparing **(a)** *no wind* and **(b)** *wind* condition. The averaging operator is performed with the pixels belonging to the foliage.

This observation reflects the hygrothermal measurements inside the foliage (Fig. 4.15(a-d)), and the vertical distribution of the solar radiative heat flux (Fig. 4.15e). Where solar radiation intensity is high, there is a large increase in the leaf temperature. So, we see that solar radiation is largest contributor to the leaf temperature rise. At night (Fig. 4.16a and Fig. 4.16b), the spatial variability is negligible. Although, the wind is seen to reduce the leaf temperature due to increased convective heat transfer, as indicated by Fig. 4.16c and Fig. 4.16f.

During the transition between day and night, a faster and a stronger variability is observed, influenced by the abrupt change in the environmental condition. Fig. 4.17 shows the spatiotemporal variability of streamwise-averaged leaf temperature $\langle T_l \rangle_x$ for *no-wind* and *wind* conditions. The figure shows the vertical variability in leaf temperature over the progression of the day. The streamwise averaging is only performed on the pixels with foliage. We see that, as observed with the internal hygrothermal microclimate of the plant (Fig. 4.15), the variability is only prevalent during the daytime. Furthermore, the *no-wind* condition shows stronger temporal and spatial change than the *wind* condition. We see that, during the *wind* condition, the enhanced convective cooling provided by the wind reduces the high leaf temperature at the plant-canopy where the solar radiation penetrates. Furthermore, we observe that the strongest cooling is observed in the middle regions of the plant foliage around dawn with $T_l \approx 19$ °C. This indicates that leaf transpiration is also present at parts of foliage where solar radiation is lower. As the day progress, however, we see a diminishing cooling effect from the plant, indicated by the rising foliage temperature. To better understand this temporal variation between the two wind conditions, we investigate the net spatially-averaged leaf temperature history. It must be noted that the leaf temperature that is measured using the infrared imaging is simply the outer plant foliage temperature. The leaf temperature inside the plant foliage is known to be different and closer to the air temperature (Manickathan et al. 2018b). The air temperature inside the plant foliage is seen to be lower and more uniform as indicated from the hygrothermal measurement, as shown in Fig. 4.15.

Fig. 4.18 shows the diurnal evolution of the net spatial-averaged leaf temperature $\langle T_l \rangle_{xz}$ (i.e., average pixel-value of all pixels belonging to plant foliage shown in Fig. 4.16) comparing *wind* and *no-wind*

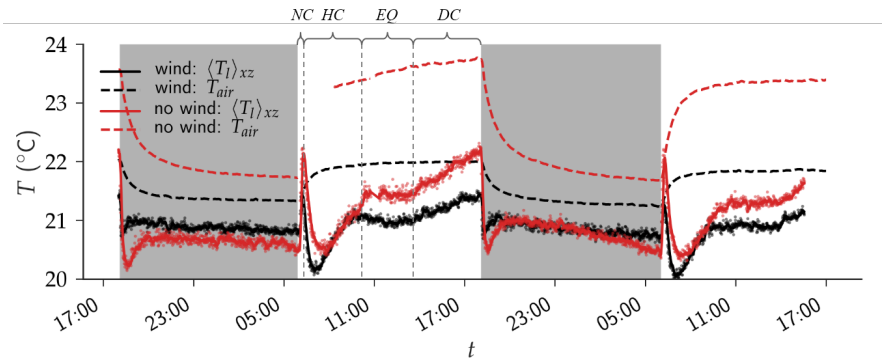


Figure 4.18: Diurnal variation of spatially-averaged leaf temperature $\langle T_l \rangle$ (°C) for *wind* and *no-wind* conditions. The dashed-line indicates the ambient air temperature $T_{air}$ (as shown in Fig. 4.14) measured at $\hat{z} = 1$. The day is comprised of four stages: *no-cooling* (NC), *high-cooling* (HC), *equilibrium* (EQ), and *decaying-cooling* (DC) stages.

conditions. We notice that the *wind* condition and *no-wind* condition responses are very similar with the *no-wind* condition being more amplified. At *no-cooling* stage, due to the delayed response of the plant results in the high overshoot of leaf temperature, which is compensated and corrected by the plant thereafter. However, we see that, during the *high-cooling* stage, the transpiration rate spikes, as evident from plant transpiration rate measurement, Fig. 4.13, resulting in the drastic cooling measured. By midday, the stomatal response equilibrates the necessary transpiration rate and we observe a quasi-steady leaf temperature and transpiration rate (Fig. 4.13) and in-foliage air temperature (Fig. 4.14). Furthermore, the equilibrium leaf temperature of plant foliage during the *no-wind* condition is higher than for the *wind* condition. This is the result of the overall higher plant canopy temperature due to the reduced convective heat transfer. As the day progresses, the leaf temperature transitions to the fourth stage (i.e., *decaying-cooling* stage) with a slow increase in the leaf temperature. The observation correlates with the measured plant transpiration rate, Fig. 4.13, where an equally decaying transpiration rate is observable.

Fig. 4.19 shows a diurnal cycle of the net leaf temperature versus plant transpiration rate hysteresis showing hysteresis: i.e., a de-

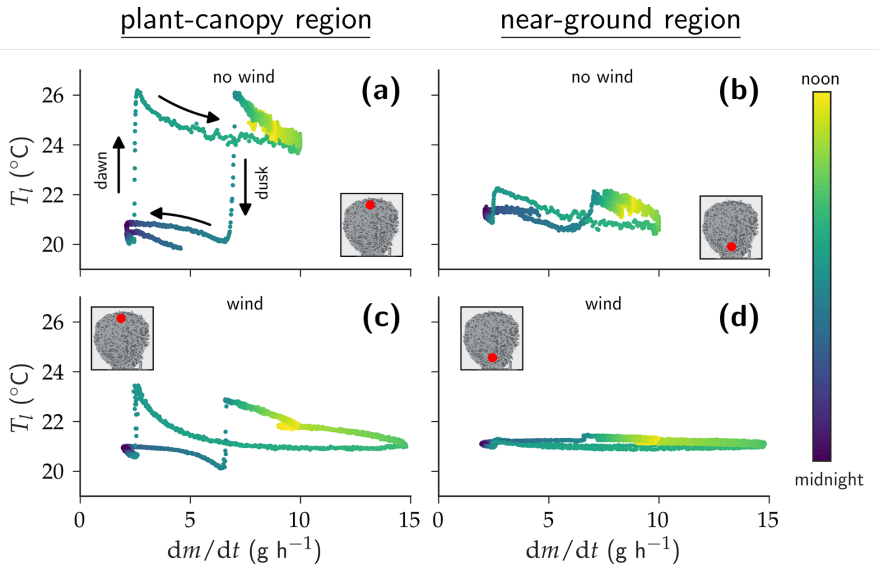


Figure 4.19: Diurnal variation of $TR = dm/dt$ (g h$^{-1}$) and leaf temperature for two wind conditions: **(a)(b)** *no-wind* and **(c)(d)** *wind* condition ($U_{ref} = 1$ m s$^{-1}$). The leaf temperatures are obtained from **(a)(c)** plant canopy region and **(b)(d)** near the ground region of the foliage. The red point on the plant indicates the location where the leaf temperature sensor was located.

layed response resulting in a temporal cyclic pattern. Fig. 4.19a and Fig. 4.19c shows the hysteresis of plant transpiration rate with respect to plant canopy region leaf temperature for *no-wind* and *wind* condition, respectively. Whereas, Fig. 4.19b and Fig. 4.19d shows the hysteresis with respect to ground-region leaf temperature. We see that the hysteresis magnitude at the bottom is less amplified in contrast to the plant canopy leaf temperature. Furthermore, we observe that leaf temperature rises rapidity at the start of the day due to the absorption of solar radiation. After a delay, the transpiration helps to cool the leaves and reaches a quasi-equilibrium between transpiration rate and leaf temperature. In the absence of solar radiation (i.e., after dusk), the leaf temperature quickly decreases. However, we observe that the transpiration rate is not reduced at the same rate. Only after a delayed time-period, does the transpiration rate reduce, resulting in a slight increase in leaf temperature and reaching

the night-time equilibrium state. This diurnal circular cyclic pattern of leaf temperature and transpiration rate, instead of simple linear variation, is observable due to delay in the stomatal response. The hysteresis occurs because the stomatal conductance is not just dependent on the atmospheric evaporative demand (AED) such as light, temperature, and humidity, but also depends on the water transport within the xylem. The root water uptake and the resulting water transport through the plant are known to have a delayed response due to the capacitance on the sub-elements in the plant leaf-xylem-root system. The hysteresis due to the mismatch in transpiration demand and the root water uptake has been well documented in the past (Dauzat et al. 2001; Williams and Rastetter 1996). An essential consequence of this dynamic plant response is that it is impossible to correctly parameterize vegetation in urban climate models without explicit modeling the water transport within the plant. Therefore, a higher-fidelity model that can model the dynamic water transport in the plant system is required to capture such hysteresis patterns (Huang et al. 2017; Manzoni et al. 2011). Furthermore, a simpler model might not be able to predict such rapid changes in leaf temperature when the environmental conditions abruptly change. For example, solar radiation might rapidly change due to changes in cloud cover or the changes in solar shading from nearby buildings, and rapid changes in AED due to changes in wind speed (such as gusts).

## 4.4 CONCLUSION

The goal of the present study was to unveil the diurnal changes in plant microclimate using multiple non-intrusive imaging techniques such as stereoscopic particle image velocimetry (SPIV) for the flow field, infrared thermography for the leaf temperature and X-ray tomography for the plant microstructure. The present study aimed at answering the following questions: What are the spatial and temporal variability of the plant performance due to environmental conditions such as wind speed and solar radiation? What is the diurnal response of the plant?

The high-resolution measurement of the plant porosity through X-ray tomography enabled us to find that the aerodynamic and optical porosities typically used in the wind tunnel studies do not reflect the

true porosity distribution of the plant. Moreover, the paper presents a novel approach of determining the leaf area density directly from X-ray tomography. The advantage of this non-intrusive approach of determining the plant microstructure enabled us to perform series of additional experiments, enabling us to directly quantify the impact of plant foliage morphology on the wake flow characteristics, the hygrothermal conditions such as air temperature and relative humidity inside the plant foliage, the solar radiation penetration inside the foliage and, finally, its impact on the spatial distribution of the leaf temperature. The SPIV measurement of the wake flow field helped us to find that at regions where porosity $\phi \rightarrow 1$, a strong bleed flow is observable, indicated by the mean velocity component. However, in contrast, there was no apparent link between the distribution of the plant porosity and the turbulent kinetic energy (TKE). The TKE intensity was seen to be governed by the net plant porosity and the outer geometry of the plant foliage that generates the shear-layer and how it interacts with the upstream boundary layer profile. A parameteric study on the plant drag forces in Section 7.3.1 equivalent to a change in net porosity showed that the wake TKE intensity is negatively correlated with the plant porosity. For high plant porosity (i.e., very low plant drag), the TKE is minimally affected in the wake.

The hygrothermal measurement at multiple vertical locations within the plant foliage enabled us to find that the local cool zone generated by transpirative cooling quickly diminished when the wind is present. The diurnal measurement of the transpiration rate showed that the water use efficiency (WUE) changes during the day indicated by the decaying transpiration rate. Furthermore, the high-resolution infrared thermography measuring the spatial and temporal changes in the leaf temperature revealed further dynamic variability during the day. A comparison of the diurnal variation in the leaf temperature and the net plant transpiration rate enabled us to quantify the diurnal hysteresis resulting from the stomatal response lag. The plant day is seen to comprise of four unique stages *no-cooling* (i.e., the stage when stomata has not responded to the increase in solar radiation), *high-cooling* (i.e., when stomatal response tries to compensate for increased leaf temperature), *equilibrium* (i.e., when stomatal response and leaf temperature equilibrates) and *decaying-cooling* stage (i.e., when the transpiration rate starts to

weaken). Such plant responses are difficult to parameterize and simplify for urban climate-vegetation models without explicitly modeling the water transport within the plant. The challenge of such complex dynamics is that simplified models might not be able to predict rapid changes in leaf temperature due to the sudden change in atmospheric evaporative demand (AED) resulting from a sudden change in solar radiation (e.g. due to a sudden change in cloud cover) or sudden change in wind speed (e.g. due to gust). Therefore, higher-fidelity models of plant responses should take into account such dynamics that arise from water availability and the stomatal response delay, to accurately assess the transpirative cooling potential of vegetation. Therefore, in Chapter 5, we develop such numerical model that can be used to study to the impact of vegetation on urban microclimate (Chapter 8). The sensitivity of plant transpiration to the water availability is modeled using a soil-plant-atmosphere continuum modeling approach (Section 5.5). A further contribution of the present chapter is to provide high-resolution multivariate measurement dataset for development and validation towards such advanced numerical methods. In Chapter 7, the experimental dataset is used to compare the developed CFD model, albeit using a simpler version of the full-model. Due to complexity of the fully-coupled model, the present measurement campaign still lacks necessary inputs for the model calibration.

# 5

# MODELING THE IMPACT OF VEGETATION ON URBAN MICROCLIMATE

## 5.1 INTRODUCTION

In this chapter, the numerical method for modeling vegetation inside an urban area is described. The numerical model consists of air domain model (Section 5.2), solid domain model (Section 5.4) and the radiation model (Section 5.6). Fig. 5.1 shows the coupling between these three models and the parameters that are communicated between them. A detailed description of the coupling algorithm is provided in Section 5.7.

The *air* domain model describes the transport of moist air through vegetation (i.e., velocity, enthalpy, moisture content, and $CO_2$ concentration). Furthermore, with the air domain, the *leaf energy balance* (LEB) model is solved to determine the heat and mass fluxes, which provides the necessary source and sink terms for solving the moist airflow. A summary of the leaf energy balance and the coupling between the air domain is provided in Section 5.2. The *solid* domain model described the coupled heat and mass transport (i.e., solid temperature, and solid moisture content) in all urban materials (i.e., soil, pavement, and building facades). Furthermore, in the soil region which consists of vegetation roots, the *soil-plant-atmosphere continuum* (SPAC) is solved to determine the leaf water potential (see Section 5.5) and the root water uptake, which provides the necessary sink term in soil region. A detailed description of the solid domain, SPAC model, and the coupling between them is provided in Sections 5.4, 5.5 and 5.7, respectively. The final ingredient is the *radiation* model which calculates the short-wave and long-wave radiative exchanges in the urban street canyon including the impact

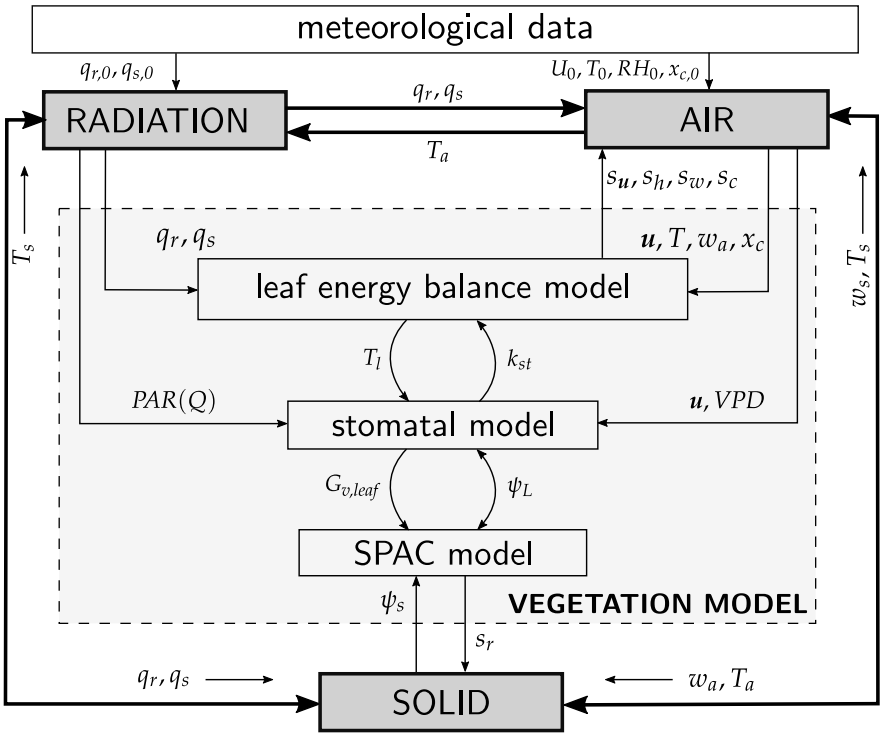


Figure 5.1: Coupling of the *vegetation* model with *air* domain solver, *solid* domain solver, and the *radiation* model. The parameters and the arrow indicate the transfer of information to couple the models.

of vegetation. A detailed description of the radiation model is given in Section 5.6.

## 5.2 AIR DOMAIN: TRANSPORT OF MOIST AIR

The simplified vegetation model is described in Chapter 6, introduction the governing equation for moist flow through vegetation. The vegetation model, consisting of the "*leaf energy balance*" (LEB) model, provides the necessary source (or sink) terms for heat, mass and momentum exchanges between vegetation and air as described in Section 6.2. For the reader, a detailed derivation of the thermodynamics of the moist air is given in Appendix A and a detailed derivation of the governing equation of moist flow is given in Appendix B. In this

section, we summarize the pseudo-compressible form of the governing equation for moist flow through vegetation where the buoyancy force is directly obtained from the density field.

*Conservation of species*

The governing equation consists of conservation of mass, momentum, energy, and species. The conservation equations are given in differential form in a Cartesian coordinate system described by the triplet $\boldsymbol{x} = (x, y, z)$. In our study, the species of interest are water vapor (subscript $v$) and carbon-dioxide ($CO_2$) (subscript $c$). The conservation of species $i$ is given as:

$$\frac{\partial \rho x_i}{\partial t} + \nabla \cdot (\rho x_i \boldsymbol{u}) = -\nabla \cdot \boldsymbol{g}_{d,i} + s_i \tag{5.1}$$

where $x_i$ is the concentration of species $i$, $\boldsymbol{u} = (u, v, w)$ is the fluid velocity, $\boldsymbol{g}_{d,i}$ is the diffusive mass flux of the species, and $s_i$ is the source term. We assume that moist air is composed of dry air $a$, water vapor $v$ and carbon-dioxide $c$. The mass fraction of each component is:

$$x_a = \frac{\rho_a}{\rho} \tag{5.2}$$

$$x_v = \frac{\rho_v}{\rho} \tag{5.3}$$

$$x_c = \frac{\rho_c}{\rho} \tag{5.4}$$

and satisfies:

$$x_a + x_v + x_c = 1 \tag{5.5}$$

where $\rho_a$, $\rho_v$, $\rho_c$ are partial density of dry air, water vapor and $CO_2$ ($\mathrm{kg\,m^{-3}}$). However, as $x_c \ll (x_a + x_v)$, we can approximate Eq. (5.5) to:

$$x_a + x_v \approx 1 \tag{5.6}$$

Similarly, total density of gas mixture $\rho$ is given as:

$$\rho \approx \rho_a + \rho_v \tag{5.7}$$

The Fick's law of diffusion is used to describe the diffusive mass flux as a function of concentration gradient of the species:

$$\boldsymbol{g}_{d,i} = -\rho D_{ia} \nabla x_i \tag{5.8}$$

where $D_{ai}$ is the binary diffusion coefficient of species $i$ in air. Thus, substituting mass fractions Eqs. (5.3) and (5.4), and diffusion mass flux Eq. (5.8) into Eq. (5.1), the conservation equation of species become:

$$\frac{\partial \rho w}{\partial t} + \nabla \cdot (\rho w \boldsymbol{u}) = D_{va} \nabla^2 w + s_w \tag{5.9}$$

$$\frac{\partial \rho c}{\partial t} + \nabla \cdot (\rho c \boldsymbol{u}) = D_{ca} \nabla^2 c + s_c \tag{5.10}$$

where $s_w$ and $s_c$ are source of water and $CO_2$, respectively (see Section 5.3). The notations $w \equiv x_v$ ($\mathrm{kg\,kg^{-1}}$) and $c \equiv x_c M_a / M_c$ ($\mathrm{mol\,mol^{-1}}$) are used to conform with past studies (Carmeliet 2005; Defraeye 2011; Kubilay 2014; Saneinejad 2013).

*Conservation of mass*

A detailed derivation of conservation of mass is given in Appendix B.2. The conservation of mass for compressible moist flow is given as:

$$\frac{\partial \rho}{\partial t} + \nabla \cdot (\rho \boldsymbol{u}) = 0 \tag{5.11}$$

where $\rho$ is defined by Eq. (5.7) and as $\mathcal{O}(s_w) \approx 10^{-4}$ (Appendix B). We assume source of water vapor and $CO_2$ is negligible in conservation of mass.

*Conservation of momentum*

A detailed derivation of conservation of momentum is given in Appendix B.3. The conservation of momentum is given as:

$$\frac{\partial \rho \boldsymbol{u}}{\partial t} + \nabla \cdot (\rho \boldsymbol{u}\boldsymbol{u}) = -\nabla p + \mu \nabla^2 \boldsymbol{u} + \rho \boldsymbol{g} + \boldsymbol{s}_u \tag{5.12}$$

where $p$ is the pressure (Pa), $\mu$ the dynamic viscosity ($\mathrm{kg\,m^{-1}\,s^{-1}}$), $\boldsymbol{g}$ the gravitational acceleration ($\mathrm{m\,s^{-2}}$). The source of momentum $\boldsymbol{s}_u$ is:

$$\boldsymbol{s}_u = -\rho\, a\, c_d\, |\boldsymbol{u}|\boldsymbol{u} \tag{5.13}$$

where $a$ is the leaf area density ($\mathrm{m^2\,m^{-3}}$), and $c_d$ is the leaf drag coefficient ($c_d = 0.2$) (Wilson and Shaw 1977) and is typically assumed to be a constant. It is done so in the present study for simplicity, but future studies can investigate the influence of varying drag coefficient. For turbulent flows, the viscous drag can be assumed to be negligible compared to the form drag (Judd et al. 1996; Li et al. 1990; Liu et al. 1996).

*Conservation of energy*

A detailed derivation of conservation of energy is given in Appendix B.4. The conservation of energy is given as:

$$c_p \left( \frac{\partial}{\partial t} (\rho T) + \nabla \cdot (\rho T \boldsymbol{u}) \right) = -\nabla \cdot (\lambda \nabla T) + \underbrace{a\, q_{sen,leaf}}_{s_h} \tag{5.14}$$

where $\rho$ ($\mathrm{kg\,m^{-3}}$) is the density of mixture and $c_p$ ($\mathrm{J\,kg^{-1}\,K^{-1}}$) is the specific heat capacity of the mixture. The source of energy $s_h$ ($\mathrm{W\,m^{-3}}$) for the above equation (i.e., quasi- transport of temperature) is:

$$\boldsymbol{s}_h = a\, q_{sen,leaf} \tag{5.15}$$

assuming that the sensible heat flux is only due to leaf and air thermal conduction (see Appendix B.4 for detailed derivation).

The (specific) enthalpies of dry air $h_a$ (J,$\mathrm{kg^{-1}}$) and water vapor $h_v$ (J,$\mathrm{kg^{-1}}$) are:

$$h_a = c_{pa} \left( T - T_{ref} \right) \tag{5.16}$$

$$h_v = c_{pv} \left( T - T_{ref} \right) + L_v \tag{5.17}$$

where $L_v$ is the latent heat of vaporization. Thus, the total enthalpy of moist air is:

$$h \equiv \sum_i h_i x_i = c_p \left( T - T_{ref} \right) + L_v x_v \tag{5.18}$$

where $c_p = x_a c_{pa} + x_v c_{pv}$ is the specific heat capacity of gas mixture.

*Turbulence modeling*

The Reynolds decomposition splits the instantaneous velocity into mean and fluctuating component:

$$\boldsymbol{u}(\boldsymbol{x}, t) = \overline{\boldsymbol{u}}(\boldsymbol{x}) + \boldsymbol{u}'(\boldsymbol{x}, t). \tag{5.19}$$

Applying this averaging operator to the NS equations, resulting Reynolds-Averaged Navier-Stokes (RANS) equation is given as:

$$\frac{\partial \overline{\rho}}{\partial t} + \nabla \cdot (\overline{\rho}\,\overline{\boldsymbol{u}}) = 0, \tag{5.20}$$

$$\frac{\partial \overline{\rho}\,\overline{\boldsymbol{u}}}{\partial t} + \nabla \cdot (\overline{\rho}\,\overline{\boldsymbol{u}}\,\overline{\boldsymbol{u}}) = -\nabla \overline{p} + \mu \nabla^2 \overline{\boldsymbol{u}} - \nabla \cdot \left(\overline{\rho \boldsymbol{u}' \boldsymbol{u}'}\right) + \rho \boldsymbol{g} + s_u \tag{5.21}$$

where $\overline{\rho \boldsymbol{u}' \boldsymbol{u}'}$ is the Reynolds stress tensor. The Reynolds stresses are modeled using Bousinessq eddy-viscosity assumption:

$$-\overline{\rho \boldsymbol{u}' \boldsymbol{u}'} = \mu_t \left(\nabla u + \nabla u^T\right) - \frac{2}{3}\rho k \boldsymbol{I} \tag{5.22}$$

where:

$$\mu_t = \rho C_\mu \frac{k^2}{\varepsilon} \tag{5.23}$$

In this study, we employ realizable $k - \varepsilon$ equations for determining the eddy-viscosity (Shih et al. 1995). The system of equations is given as:

$$\frac{\partial \rho k}{\partial t} + \nabla \cdot (\rho k \overline{\boldsymbol{u}}) = \nabla \cdot \left[\left(\mu + \frac{\mu_t}{\sigma_k}\right) \nabla k\right] + P_k - \rho \varepsilon + s_k, \tag{5.24}$$

$$\frac{\partial \rho \varepsilon}{\partial t} + \nabla \cdot (\rho \varepsilon \overline{\boldsymbol{u}}) = \nabla \cdot \left[\left(\mu + \frac{\mu_t}{\sigma_\varepsilon}\right) \nabla \varepsilon\right] + \rho C_{1\varepsilon} P_k \frac{\varepsilon}{k} - \rho C_{2\varepsilon} \frac{\varepsilon^2}{k + \sqrt{\nu \varepsilon}} + s_\varepsilon \tag{5.25}$$

where

$$P_k = -\rho \overline{\boldsymbol{u}' \boldsymbol{u}'} : \nabla \overline{\boldsymbol{u}} = 2\mu_t |\mathbf{S}|^2 \tag{5.26}$$

The mean strain-rate $\mathbf{S}$ is defined as

$$\mathbf{S} = \frac{1}{2}\left(\nabla\overline{\boldsymbol{u}} + \nabla\overline{\boldsymbol{u}}^T\right) \tag{5.27}$$

The TKE source $s_k$ ($\mathrm{W\,m^{-3}}$) is given as:

$$s_k = \rho c_d a\left(\beta_p\left|\overline{\boldsymbol{u}}\right|^3 - \beta_d\left|\overline{\boldsymbol{u}}\right| k\right) \tag{5.28}$$

and the TDR source term $s_\varepsilon$ ($\mathrm{W\,m^{-3}\,s^{-1}}$) is given as:

$$s_\varepsilon = \rho c_d a\left(\beta_p C_{4\varepsilon}\left|\overline{\boldsymbol{u}}\right|^3\frac{\varepsilon}{k} - \beta_d C_{5\varepsilon}\left|\overline{\boldsymbol{u}}\right|\varepsilon\right) \tag{5.29}$$

with model constants $C_{4\varepsilon} = 0.9$ and $C_{5\varepsilon} = 0.9$ (Katul et al. 2004; Kenjereš and ter Kuile 2013; Sanz 2003). The constant $\beta_p = 1.0$ is the fraction of mean kinetic energy converted into turbulent kinetic energy and $\beta_d = 5.1$ describes the reduction in TKE and TDR due to vegetation (Sanz 2003). Kenjereš and ter Kuile (2013) compared various RANS model coefficients for vegetation in an urban area and found the coefficients provided by Katul et al. (2004) to be reasonably accurate showing good numerical stability. Therefore, these parameters are used in this thesis.

## 5.3 LEAF ENERGY BALANCE

The heat and mass exchanges between the tree canopy and the air are simulated using a leaf energy model. The heat and mass exchanges between the tree canopy and the air are simulated using a leaf energy balance as shown in Fig. 5.2. We assume a stationary leaf energy balance and that the dynamic thermal storage of heat in leaves can be neglected.

The stationary energy balance is given as:

$$q_{rad,leaf} - q_{lat,leaf} - q_{sen,leaf} = 0 \tag{5.30}$$

where $q_{rad,leaf}$ ($\mathrm{W\,m^{-2}}$) is the radiative flux, $q_{sen,leaf}$ ($\mathrm{W\,m^{-2}}$) is the sensible heat flux and $q_{lat,leaf}$ ($\mathrm{W\,m^{-2}}$) is the latent heat flux (Bruse and Fleer 1998; Dauzat et al. 2001; Hiraoka 2005; Majdoubi et al. 2009). Positive sensible and latent heat fluxes are defined as heat

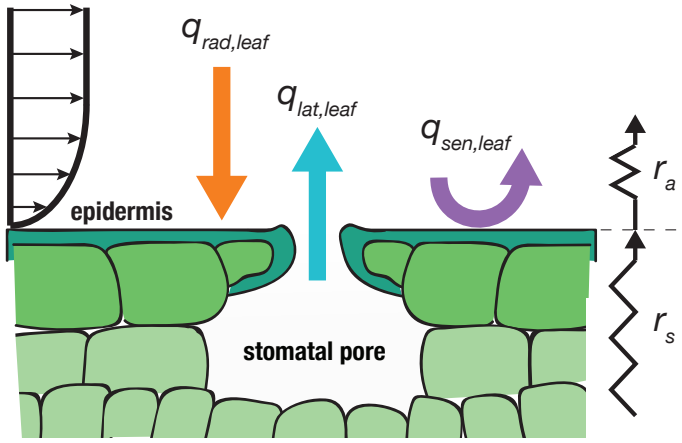


Figure 5.2: Schematic representation of leaf surface with energy balance as given by Eq. (5.30). The radiative flux $q_{rad,leaf}$ absorbed by the leaf is balanced by the sensible $q_{sen,leaf}$ and the latent heat flux $q_{lat,leaf}$ leaving the leaf surface. The stomatal resistance $r_s$ influences the latent heat flux and the aerodynamic resistance $r_a$ influences both the sensible and the latent heat fluxes.

transfer from the leaf into the air. The sensible heat flux due to convective heat transfer from leaf surface to the air is given as:

$$q_{sen,leaf} = h_{c,h}\left(T_{leaf} - T\right) = \frac{2\rho c_p}{r_a}\left(T_{leaf} - T\right) \tag{5.31}$$

where $h_{c,h}$ (W m$^{-2}$ K$^{-1}$] is the convective heat transfer coefficient (CHTC), $T_{leaf}$ (K) is the leaf surface temperature, $T$ (K) is the air temperature and $r_a$ (s m$^{-1}$) is the aerodynamic resistance of the boundary layer around the leaf. A factor 2 is present in the equation as the sensible heat flux occurs on both sides of the leaf. Substituting Eq. (5.31) into Eq. (5.15) gives the source of heat from vegetation in conservation of energy.

The aerodynamic resistance $r_a$ (s m$^{-1}$) is given as (Dauzat et al. 2001; Robitu et al. 2006):

$$r_a = C\left(\frac{l}{|\bar{u}|}\right)^{1/2} \tag{5.32}$$

where $C = 130\ \mathrm{s}^{0.5}\,\mathrm{m}^{-1}$ is the proportionality factor and $l$ (m) is the characteristic leaf size ranging from 0.02 m for conifers and up to 0.5 m for tropical plants (Bruse and Fleer 1998). The latent heat flux from leaf to air due to transpiration is defined as:

$$q_{lat,leaf} = L_v\, g_{v,leaf} \tag{5.33}$$

where $L_v = 2.5 \times 10^6\ \mathrm{J\,kg}^{-1}$ is latent heat of vaporization. The water vapor flux $g_{v,leaf}$ ($\mathrm{kg\,m}^{-2}\,\mathrm{s}^{-1}$) is defined as:

$$g_{v,leaf} = h_{c,m}\left(p_{v,leaf} - p_v\right) = M_w\, k^*_{st,v}\left(\frac{p_{v,i} - p_v}{p}\right) \tag{5.34}$$

where $h_{c,m}$ ($\mathrm{s\,m}^{-1}$) is the convective mass transfer coefficient (CMTC), $M_w = 1.8015 \times 10^{-2}$ ($\mathrm{kg\,mol}^{-1}$) is molar mass of water vapor, $p_{v,i}$ (Pa) is the intercellular vapor pressure, $p_v$ (Pa) is the ambient vapor pressure, $p$ (Pa) is the ambient pressure, and $k^*_{st,v}$ ($\mathrm{mol\,m}^{-2}\,\mathrm{s}^{-1}$) is the effective stomatal conductance of water vapor. A detailed description of the stomatal conductance is given in Section 5.5.4. The energy balance (Eq. (5.30)) is solved once the leaf surface temperature $T_{leaf}$ is known. Combining Eqs. (5.30), (5.31) and (5.33), the leaf temperature is given as:

$$T_{leaf} = T + \frac{q_{rad,leaf} - q_{lat,leaf}}{h_{c,h}} \tag{5.35}$$

where the equation is solved iteratively as $q_{lat,leaf}$ is dependent on the leaf temperature.

So, the source of moisture in the air domain, i.e., Eq. (5.9), is obtained from Eq. (5.34) as:

$$s_w = a\, g_{v,leaf} \tag{5.36}$$

where $s_w$ ($\mathrm{kg\,m}^{-3}\,\mathrm{s}{-}1$) is the moisture source term. In the present study, we assume that there is no condensation or rain on the leaf surface and so evapotranspiration is only due to transpiration through the leaf stomata. Therefore, the vapor pressure at the leaf is the vapour pressure within the leaf stomata which is close to the saturation vapor pressure at the leaf temperature, thereby we can assume

$$p_{v,leaf} \cong p_{vsat,stom}\left(T_{leaf}\right) \tag{5.37}$$

Similarly, the $CO_2$ source in Eq. (5.10) is given as:

$$s_c = a\, g_{c,leaf} \frac{M_a}{M_c} \tag{5.38}$$

where $g_{c,leaf}$ ($\mathrm{kg\,m^{-2}\,s^{-1}}$) is the $CO_2$ flux from the leaf due to photosynthesis and also known as the assimilation rate (i.e., $A_n$). It is defined as:

$$g_{c,leaf} = M_c\, k^*_{st}\, (c_i - c) \tag{5.39}$$

where $k^*_{st}$ ($\mathrm{mol\,m^{-2}\,s^{-1}}$) is the effective stomatal conductance of $CO_2$, $c_i$ is intercellular $CO_2$ ($\mathrm{mol\,mol^{-1}}$) concentration, and $c$ ($\mathrm{mol\,mol^{-1}}$) is the ambient $CO_2$ concentration. A detailed description of assimilation rate is given in Section 5.5.4.

## 5.4 SOLID DOMAIN: COUPLED HEAT AND MOISTURE TRANSPORT

### 5.4.1 *Composition of the porous material*

The building materials and the soil are considered as porous materials consisting of three phases: solid phase (denoted with $s$), liquid phase referring to liquid water ($l$) and the air phase which is split into dry air ($a$) and water vapor $v$ (Carmeliet 2005; Defraeye 2011; Janssen 2002; Saneinejad 2013). The open porosity $\phi_o$ ($\mathrm{m^3\,m^{-3}}$) of the porous material is defined as:

$$\phi_o = \frac{V_{pore}}{V} \tag{5.40}$$

where $V_{pore}$ ($\mathrm{m^3}$) is the volume of open pores and $V$ ($\mathrm{m^3}$) is the total volume of the porous material $\boldsymbol{S}$. The solid material content $w_s$ ($\mathrm{kg\,m^{-3}}$) is defined as:

$$w_s = (1 - \phi_o)\, \rho_s \tag{5.41}$$

where $\rho_s$ ($\mathrm{kg\,m^{-3}}$) is the solid material matrix density. Similarly the dry air $w_a$, water vapor $w_v$, liquid water $w_l$ contents are defined as:

$$w_l = \phi_o S_l \rho_l \tag{5.42}$$

$$w_a = \phi_o \left(1 - S_l\right) \rho_a \tag{5.43}$$

$$w_v = \phi_o \left(1 - S_l\right) \rho_v \tag{5.44}$$

where they are related to the degree of liquid saturation $S_l$ of the porous open pores:

$$S_l = \frac{\phi_{o,l}}{\phi_o} \tag{5.45}$$

with $\phi_{o,l}$ being the amount of liquid water occupied inside the open pores and $\rho_a$, $\rho_l$ being the air and liquid water densities, respectively. The total moisture content $w$ ($\mathrm{kg\,m^{-3}}$) inside the porous material is simply the sum of liquid water and water vapor:

$$w = w_l + w_v \tag{5.46}$$

### 5.4.2 *Water potential*

Water potential is a universal variable to determine the *water status* in any medium (Nobel 2009). In this thesis, we use it to define the water status of multiple domains such as solid porous materials (soil and building facades), plant xylem, and air. The water potential $\psi$ (Pa) describes the chemical potential of water $\mu$ ($\mathrm{J\,mol^{-1}}$) with respect to chemical potential of pure water $\mu^{o,l}$ ($\mathrm{J\,mol^{-1}}$) at the same temperature, standard atmosphere and at zero level:

$$\psi = \frac{\mu - \mu^{o,l}}{V_l^o} \tag{5.47}$$

where $V_l^o = 18.0510^{-3}$ $\mathrm{m^3\,mol^{-1}}$ is the molar volume of pure water in liquid phase. The water potential for pure water at standard atmosphere is $\psi = 0$ Pa. The water tends to move towards a region where $\mu - \mu^{o,l}$ is lower, i.e. in the direction of $-\nabla\psi$. The water potential is related to pressure potential, osmotic potential, matrix potential, and gravitational potential. In our study, we assume that the pressure potential gradient is negligible in the solid and we ignore the influence of osmotic potential $\psi_o$ (Pa) as we assume we have

a non-saline porous material. Therefore, only the matrix potential and gravitation potential influence the water transport:

$$\psi = \underbrace{p_c}_{\psi_c} + \underbrace{\rho_l g z}_{\psi_g} \tag{5.48}$$

where $\psi_c = p_c$ (Pa) is the capillary potential due to capillary pressure, which represents the contribution of the matrix potential, and $\psi_g = \rho_l g h$ (Pa) is the gravitational potential with $g = |\boldsymbol{g}|$ ($\mathrm{m\,s^{-2}}$) where $\boldsymbol{g}$ is the gravitational acceleration. The capillary pressure $p_c$ is defined as the difference between liquid and gas phase pressure, $p_l$ and $p_g$, respectively:

$$p_c = p_l - p_g \tag{5.49}$$

and is related to relative humidity $\phi$ by the Kelvin's law:

$$p_c = \rho_l R_v T \ln(\phi) \tag{5.50}$$

The gravitational potential $\psi_g$ (Pa) is defined as:

$$\psi_g = -\rho \boldsymbol{g} \cdot \boldsymbol{x} = \rho g z \tag{5.51}$$

where $g = |\boldsymbol{g}|$ with $z$ oriented upward. Thus, by taking the capillary and gravitational water potentials into account, the transport of water can be described in building materials and, more importantly, soil region where the plant roots are present.

### 5.4.3 *Coupled transport of heat and mass*

*Conservation of mass*

The conservation of mass in the solid domain is defined as:

$$\frac{\partial w_s}{\partial t} = 0 \tag{5.52}$$

$$\frac{\partial w_a}{\partial t} + \nabla \cdot (w_a \boldsymbol{u}_a) = 0 \tag{5.53}$$

$$\frac{\partial w_l + w_v}{\partial t} + \nabla \cdot (w_l \boldsymbol{u}_l + w_v \boldsymbol{u}_v) = 0 \tag{5.54}$$

assuming that solid matrix does not change, mass of different phases only changes due to evaporation or condensation. Other phenom-

ena such as melting, freezing, sublimation and deposition are neglected. Assuming dry air does not contribute to moisture storage, i.e., $\partial w_a / \partial t = 0$, the conservation of mass simplifies to rate of change of moisture content $w = w_l + w_v$, from Eq. (5.54):

$$\frac{\partial w}{\partial t} = -\nabla \cdot (\boldsymbol{g}_l + \boldsymbol{g}_v) \tag{5.55}$$

where $\boldsymbol{g}_l \equiv w_l \boldsymbol{u}_l$ ($\mathrm{kg\,m^{-2}\,s^{-1}}$) and $\boldsymbol{g}_v \equiv w_v \boldsymbol{u}_v$ ($\mathrm{kg\,m^{-2}\,s^{-1}}$) are defined as the liquid water and water vapor fluxes, respectively. Additionally, the plant transpiration leafs to root uptake leading to a water loss in the soil domain. The contribution of root water uptake due to plant transpiration is introduced through the source term $s_r$ ($\mathrm{kg\,m^{-3}\,s^{-1}}$):

$$\frac{\partial w}{\partial t} = -\nabla \cdot (\boldsymbol{g}_l + \boldsymbol{g}_v) + s_r \tag{5.56}$$

The sink term due to root water uptake is explained in detail later in Section 5.5. In this thesis, the conservation of mass is solved using the $p_c$-form Richards equation, where Eq. (5.56) becomes:

$$\frac{\partial w}{\partial p_c} \frac{\partial p_c}{\partial t} = -\nabla \cdot (\boldsymbol{g}_l + \boldsymbol{g}_v) + s_r \tag{5.57}$$

with $C_{mm} \equiv \partial w / \partial p_c$ ($\mathrm{kg\,m^{-3}\,Pa^{-1}}$) is defined as the moisture capacity. Thus, the change in water content in the porous material is simply due to the liquid and vapor fluxes, and root water uptake (only in soil where root is present). The liquid water flux $\boldsymbol{g}_l$ in porous media is given by:

$$\boldsymbol{g}_l = -K_{lp} \nabla \left( p_c + \rho_l g z \right) \tag{5.58}$$

and assumes the air pressure effects be negligible with respect to capillary and gravitational effects, where $K_{lp}$ (s) is the liquid water permeability. We assume that the liquid water permeability is only due to pressure gradient, and the influence of thermal gradient is neglected (Carmeliet 2005). The water vapor flux in the porous media is given by:

$$\boldsymbol{g}_v = K_{vp} \nabla p_c + K_{vT} \nabla T \tag{5.59}$$

where

$$K_{vp} = -\delta_v \frac{p_v}{\rho_l R_v T} \tag{5.60}$$

is the water vapor permeability (s) due to pressure,

$$K_{vT} = -\delta_v \frac{p_v}{\rho_l R_v T^2} \left(\rho_l L_v - p_c\right) \tag{5.61}$$

is the water vapor permeability (s) due to temperature gradient, and

$$\delta_v = \frac{D_{va,mat}}{R_v T} \tag{5.62}$$

is the water vapor diffusion coefficient (s) where $D_{va,mat}$ ($\mathrm{m^2\,s^{-1}}$) is the binary apparent diffusion coefficient between dry air and water vapor (Carmeliet 2005; Defraeye 2011; Kubilay 2014; Saneinejad 2013). Thus, substituting the fluxes Eqs. (5.58) and (5.59) into Eq. (5.57), the expanded form of conservation of mass is given as:

$$C_{mm} \frac{\partial p_c}{\partial t} = \nabla \cdot \left( K_{lp} \nabla \left(p_c + \rho_l g z\right) + K_{vp} \nabla p_c + K_{vT} \nabla T \right) + s_r \tag{5.63}$$

*Conservation of energy*

The conservation of energy is given as:

$$\frac{\partial h}{\partial t} + \nabla \cdot (h \boldsymbol{u}) = -\nabla \cdot \boldsymbol{q} \tag{5.64}$$

where $h$ ($\mathrm{J\,kg^{-1}}$) is the enthalpy of total solid domain:

$$h = \sum_i w_i h_i = w_s h_s + w_a h_a + w_l h_l + w_v h_v \tag{5.65}$$

and heat conduction $\boldsymbol{q}$ ($\mathrm{W\,m^{-2}}$) is given by Fourier's law as:

$$\boldsymbol{q} = -\lambda \nabla T \tag{5.66}$$

where $T$ (K) is temperature, $\lambda$ ($\mathrm{W\,m^{-1}\,K^{-1}}$) is thermal conductivity.

Substituting Eq. (5.65) into Eq. (5.64) expands to:

$$\frac{\partial}{\partial t} \left(w_s h_s + w_a h_a + w_l h_l + w_v h_v\right) + \nabla \cdot \left(w_a \boldsymbol{g}_a + w_l \boldsymbol{g}_l + w_v \boldsymbol{g}_v\right) = -\nabla \cdot \boldsymbol{q} \tag{5.67}$$

and assuming dry air and water vapor does not contribute to heat storage, i.e., $\partial w_a h_a / \partial t \approx 0$ and $\partial w_v h_v / \partial t \approx 0$, and convection term of dry air is negligible $\nabla \cdot w_a \boldsymbol{g}_a \approx 0$, Eq. (5.67) simplified to:

$$\frac{\partial \left( w_s h_s + w_l h_l \right)}{\partial t} + \nabla \cdot \left( w_l \boldsymbol{g}_l + w_v \boldsymbol{g}_v \right) = -\nabla \cdot \boldsymbol{q} \tag{5.68}$$

The enthalpies of solid $h_s$, liquid water $h_l$ and water vapor $h_v$ are defined as:

$$h_s = c_{ps} \left( T - T_{ref} \right) \tag{5.69}$$
$$h_l = c_{pl} \left( T - T_{ref} \right) \tag{5.70}$$
$$h_v = c_{pv} \left( T - T_{ref} \right) + L_v \tag{5.71}$$

and $L_v$ is the latent heat of vaporization of water. Substituting Eqs. (5.69) to (5.71) into Eq. (5.68), the conservation of energy is given as:

$$\begin{aligned} &\left( c_{ps} w_s + c_{pl} w \right) \frac{\partial T}{\partial t} + \left[ c_{pl} \left( T - T_{ref} \right) \frac{\partial w}{p_c} \right] \frac{\partial p_c}{\partial t} = \\ &- \nabla \cdot \left\{ \boldsymbol{q} + \underbrace{c_{pl} \left( T - T_{ref} \right) \boldsymbol{g}_l}_{\boldsymbol{q}_l} + \underbrace{\left[ c_{pv} \left( T - T_{ref} \right) + L_v \right] \boldsymbol{g}_v}_{\boldsymbol{q}_v} \right\} \end{aligned} \tag{5.72}$$

We defined the thermal capacity terms as:

$$C_{TT} = c_{ps} w_s + c_{pl} w \tag{5.73}$$
$$C_{Tp} = c_{pl} \left( T - T_{ref} \right) \frac{\partial w}{\partial p_c} \tag{5.74}$$

are the thermal capacity terms. Substituting liquid and vapour fluxes, Eqs. (5.58) and (5.59), respectively, thermal capacities Eqs. (5.73)

and (5.74) and heat conduction Eq. (5.66) into conservation of energy equation Eq. (5.72) we get:

$$C_{TT}\frac{\partial T}{\partial t} + C_{Tp}\frac{\partial p_c}{\partial t} = \nabla \cdot \Big( \lambda \nabla T + K_{lp} c_{pl} \left(T - T_{ref}\right) \left(\nabla p_c + \rho_l g z\right) - K_{vp} \Big[ c_{pv} \left(T - T_{ref}\right) + L_v \Big] \nabla p_c - K_{vT} \Big[ c_{pv} \left(T - T_{ref}\right) + L_v \Big] \nabla T \Big) \tag{5.75}$$

where the terms on RHS are heat transport due to conduction, liquid transport, and vapor transport.

### 5.4.4 *Linearized heat and mass transport equation*

In the present study, the conservation of mass and energy is coupled together as a heat and mass model (HAM) according to (Carmeliet 2005; Defraeye 2011; Janssen 2002; Kubilay et al. 2018; Saneinejad 2013). Due to the shape of the water retention curve and the hydraulic conductivity curve, as shown in Fig. 5.3, the Richards equation is highly non-linear. Therefore, the numerical solution of the equation is very sensitive to convergence tolerance and requires linearization techniques to maintain accuracy and computational efficiency. Methods such as fixed-point Picard iterations are used to solve the non-linear equations. More details on the discretization is provided in Janssen (2002), Kubilay et al. (2018), and Liu (2012).

The conservation of mass (i.e., the moisture transport equation), Eq. (5.63), in the linearized form is given as:

$$C_{mm}^{n+1,k}\frac{p_c^{n+1,k+1} - p_c^n}{\Delta t} = \nabla \cdot \Big( K_{lp}^{n+1,k} \nabla \left( p_c^{n+1,k+1} + \rho_l g z \right) + K_{vp}^{n+1,k} \nabla p_c^{n+1,k+1} + K_{vT}^{n+1,k} \nabla T^{n+1,k} \Big) + s_r^{n+1,k+1} \tag{5.76}$$

where the capacity, permeabilities and temperature are determined from the previous Picard iteration ($k$). The subscript ($n$) denotes the global (i.e., outer) time step of $t$ and $k$ denoting the internal Picard

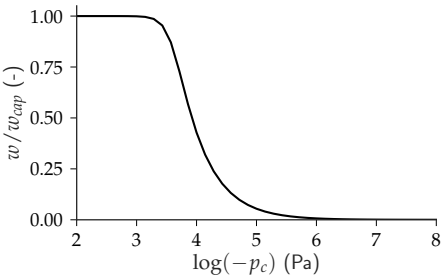


Figure 5.3: Typical non-linear moisture water retention curve for a material which is capillary saturated.

iteration step. When the Picard solution approaches convergence, i.e., $p_c^{n+1,k} \rightarrow p_c^{n+1,k+1}$, $\partial w/\partial p_c$ becomes negligible resulting in larger mass conservation errors. The error is minimized by formulating the Richard's equation in mixed-form (Liu 2012):

$$\begin{aligned} C_{mm}^{n+1,k} \frac{p_c^{n+1,k+1} - p_c^n}{\Delta t} = \nabla \cdot \Big( & K_{lp}^{n+1,k} \nabla \left( p_c^{n+1,k+1} + \rho_l g z \right) \\ & + K_{vp}^{n+1,k} \nabla p_c^{n+1,k+1} \\ & + K_{vT}^{n+1,k} \nabla T^{n+1,k} \Big) \\ & + s_r^{n+1,k+1} - \frac{w^{n+1,k+1} - w^n}{\Delta t} \end{aligned} \tag{5.77}$$

where an additional moisture change term is added.

The linearized form of the heat equation is given as:

$$\begin{aligned} C_{TT}^{n+1,k} \frac{T^{n+1,k+1} - T^n}{\Delta t} = \nabla \cdot \Big( & \lambda \nabla T^{n+1,k+1} \\ & + K_{lp}^{n+1,k} c_{pl} \left( T^{n+1,k+1} - T_{ref} \right) \nabla p_c^{n+1,k+1} \\ & + K_{lp}^{n+1,k} c_{pl} \left( T^{n+1,k+1} - T_{ref} \right) \rho_l g z \\ & - K_{vp}^{n+1,k} \left[ c_{pv} \left( T^{n+1,k+1} - T_{ref} \right) + L_v \right] \nabla p_c^{n+1,k} \\ & - K_{vT}^{n+1,k} \left[ c_{pv} \left( T^{n+1,k+1} - T_{ref} \right) + L_v \right] \nabla T^{n+1,k+1} \Big) \end{aligned} \tag{5.78}$$

where the capillary pressure time derivative term is ignored. The mixed-form the heat equation is given as:

$$\begin{aligned} C_{TT}^{n+1,k}\frac{T^{n+1,k+1}-T^{n}}{\Delta t} = \nabla\cdot\Big(&\lambda\nabla T^{n+1,k+1} \\ &+ K_{lp}^{n+1,k}c_{pl}\left(T^{n+1,k+1}-T_{ref}\right)\nabla p_c^{n+1,k+1} \\ &+ K_{lp}^{n+1,k}c_{pl}\left(T^{n+1,k+1}-T_{ref}\right)\rho_l g z \\ &- K_{vp}^{n+1,k}\Big[c_{pv}\left(T^{n+1,k+1}-T_{ref}\right)+L_v\Big]\nabla p_c^{n+1,k} \\ &- K_{vT}^{n+1,k}\Big[c_{pv}\left(T^{n+1,k+1}-T_{ref}\right)+L_v\Big]\nabla T^{n+1,k+1}\Big) \\ &- \frac{C_{TT}^{n+1}T^{n+1}-C_{TT}^{n}T^{n}}{\Delta t} \end{aligned} \tag{5.79}$$

The system of linear equations is solved by Krylov subspace iteration solver, i.e. preconditioned conjugate gradient (PCG) with diagonal-based incomplete Cholesky (DIG) preconditioning. The convergence criteria for the Picard iteration is user-defined:

$$\left|p_c^{n+1,k+1}-p_c^{n+1,k}\right| \leq \delta p_c \tag{5.80}$$

$$\left|T^{n+1,k+1}-T^{n+1,k}\right| \leq \delta T \tag{5.81}$$

where $\delta p_c = \delta T = 10^{-2}$ (Kubilay et al. 2018).

## 5.5 SOIL-PLANT-ATMOSPHERE CONTINUUM MODEL

The soil-plant-atmosphere continuum (SPAC) model that is integrated into the vegetation model is described in this section, implemented according to the state-of-art techniques: (Farquhar et al. 1980; Idso 1977; Launiainen et al. 2015; Manoli et al. 2014b; Manzoni et al. 2011; Volpe et al. 2013). The root-system of the plants are represented as a network-like structure assuming cooperative strategy among the individual roots and a bulk plant transpiration through the xylem system. We assume no water storage inside the plant and therefore, the water flux from soil to root $G_{v,root}$, from root to leaf through

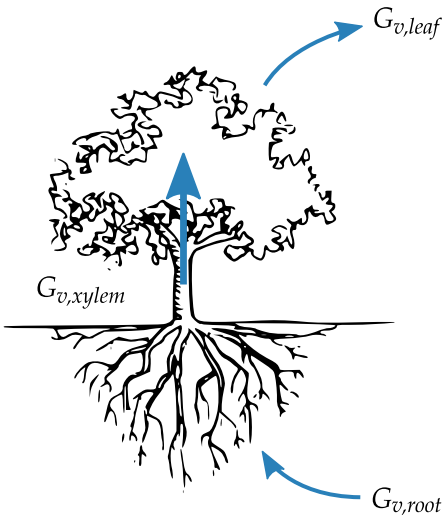


Figure 5.4: Soil-Plant-Atmosphere Continuum: The water balance between plant transpiration and root water uptake, $G_{v,root} = G_{v,xylem} = G_{v,leaf}$.

xylem $G_{v,xylem}$, and from leaf to air $G_{v,leaf}$ is equal, as depicted in Fig. 5.4:

$$G_{v,root} = G_{v,xylem} = G_{v,leaf} \tag{5.82}$$

and so, the atmospheric evaporative demand (AED) is dependent on the water availability near the roots of the plants.

### 5.5.1 *Water transport in soil-root system*

The sink term $s_r$ ($\mathrm{kg\,m^{-3}\,s^{-1}}$) due to root water uptake in soil moisture transport equation (Eq. (5.63)) is simply defined as:

$$s_r = r\, g_{v,root} \tag{5.83}$$

where $r$ ($\mathrm{m^2\,m^{-3}}$) is the root area density and $g_{v,root}$ ($\mathrm{kg\,m^{-2}\,s^{-1}}$) is the root water uptake, i.e., the flux of water from root to soil. It is defined as:

$$g_{v,root} = k^*_{sr}\,(\psi_s - \psi_R) \tag{5.84}$$

where $k^*_{sr}$ ($\mathrm{s\,m^{-1}}$) is effective conductance of the soil-root system (i.e., rhizosphere), $\psi_s$ (Pa) is the soil water potential, and $\psi_R$ (Pa) is the

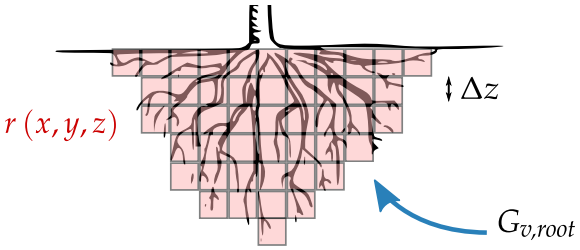


Figure 5.5: Soil-Plant-Atmosphere Continuum: The water transport in soil-root system.

(bulk) root water potential. The effective conductance of the soil-root system (or rhizosphere) $k^*_{sr}$ ($\mathrm{s\,m^{-1}}$) is given as:

$$k^*_{sr} = \frac{1}{|\boldsymbol{g}|} \frac{k_s\, k_r}{k_s + k_r} \tag{5.85}$$

where $\boldsymbol{g}$ ($\mathrm{m\,s^{-2}}$) is the gravitational acceleration, $k_s$ ($\mathrm{s^{-1}}$) is the soil conductance in the root region, and $k_r$ ($\mathrm{s^{-1}}$) is the conductance of the root system. The soil conductance in the root region $k_s$ ($\mathrm{s^{-1}}$) is defined as:

$$k_s = \alpha\, K\, r \tag{5.86}$$

where

$$\alpha = \sqrt{\left(\frac{L}{RAI}\right) \frac{1}{d}} \tag{5.87}$$

$d$ (m) is the root diameter, $L$ (m) is the root-depth height, and $RAI = \int r\, \mathrm{d}z$ is the root area index ($\mathrm{m^2\,m^{-2}}$). The hydraulic conductivity in soil $K$ ($\mathrm{m\,s^{-1}}$) is given as:

$$K = K_{lp}\, |\boldsymbol{g}| \tag{5.88}$$

where $K_{lp}$ (s) being the liquid permeability defined in the Section 5.4.3. Finally, the conductance of the root system $k_r$ ($\mathrm{s^{-1}}$) is given as:

$$k_r = r \frac{\Delta z}{\beta} \tag{5.89}$$

where $\Delta z$ is the vertical height of the root layer mesh and $\beta = 3 \times 10^8$ s.

Thus, the net root water uptake from the soil domain $G_{v,root}$ ($\mathrm{kg\,s^{-1}}$) is given as:

$$G_{v,root} = \int_{\Omega_s} s_r \,\mathrm{d}V = \int_{\Omega_s} r\, g_{v,root} \,\mathrm{d}V \tag{5.90}$$

where $\Omega_s$ denotes the soil domain (note that as $r = 0$ outside root-zone, the integration is essentially only in the root volume).

### 5.5.2 *Water transport in xylem*

The water flux through the plant in xylem layer $g_{v,xylem}$ ($\mathrm{kg\,m^{-2}\,s^{-1}}$) is defined as:

$$g_{v,xylem}(\psi_L) = k_x^* \left(\psi_R - \psi_L\right) \tag{5.91}$$

where $k_x^*$ ($\mathrm{s\,m^{-1}}$) is the effective xylem conductance, $\psi_R$ (Pa) is the (bulk) root water potential, and $\psi_L$ (Pa) is the (bulk) leaf water potential. The net water flux $G_{v,xylem}$ ($\mathrm{kg\,s^{-1}}$) is given as:

$$G_{v,xylem} = \int_{\partial\Omega_{x|s}} g_{v,xylem} \,\mathrm{d}A = g_{v,xylem} A_x \tag{5.92}$$

where $A_x$ ($\mathrm{m^2}$) is the xylem cross-sectional area. The effective xylem conductance $k_x^*$ ($\mathrm{s\,m^{-1}}$) of water is:

$$k_x^* = k_x \,\rho_l \tag{5.93}$$

where plant xylem conductance $k_x$ ($\mathrm{m\,Pa^{-1}\,s^{-1}}$) is modeled using a "*vulnerability curve*" approach. The xylem conductance becomes exponentially smaller with increasing leaf water potential (Volpe et al. 2013). This empirical model is based on plant response of the vulnerability to xylem cavitation and embolism that could occur at very low water potential. The xylem conductance $k_x$ ($\mathrm{m\,Pa^{-1}\,s^{-1}}$) is defined by:

$$k_x = k_{x,max} \exp\left\{-\left(-\frac{\psi_L}{d}\right)^c\right\} \tag{5.94}$$

where $k_{x,max}$ ($\mathrm{m\,Pa^{-1}\,s^{-1}}$) is the maximum xylem conductance, and $c$ and $d$ are fit-coefficients (Volpe et al. 2013).

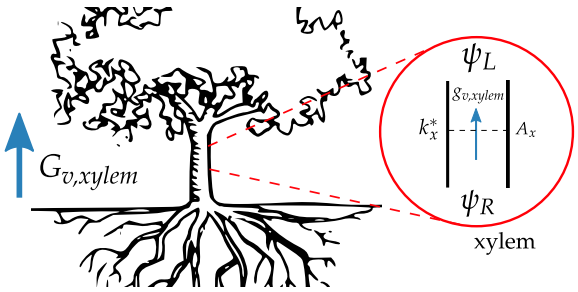


Figure 5.6: Soil-Plant-Atmosphere Continuum: The water transport in plant xylem.

### 5.5.3 *Water transport from leaf to air*

The leaf transpiration rate $g_{v,leaf}$ (kg m$^{-2}$s$^{-1}$) as defined in Section 5.2, Eq. (5.34), and is simply defined as:

$$g_{v,leaf} = M_w \, k^*_{st,v} \left( \frac{p_{v,leaf} - p_v}{p} \right) \tag{5.95}$$

where $p_{v,leaf}$ (Pa) is the vapor pressure at the leaf, $p_v$ (Pa) is the ambient vapor pressure and $p$ (Pa) is ambient pressure. In plant-science community, the leaf transpiration is typically given in molar units ($f_c$ (mol m$^{-2}$ s$^{-1}$)) and is obtained from Eq. (5.95):

$$f_v = g_{v,leaf} / M_w = k^*_{st,v} \left( \frac{p_{v,leaf} - p_v}{p} \right) \tag{5.96}$$

The effective stomatal conductance of water vapor $k^*_{st,v}$ (mol m$^{-2}$ s$^{-1}$) is defined as:

$$k^*_{st,v} = a_c \, k^*_{st} \tag{5.97}$$

where $k^*_{st}$ (mol m$^{-2}$ s$^{-1}$) is the effective stomatal conductance of $CO_2$, and $a_c = 1.6$ is the relative diffusion of water vapor to $CO_2$. The effective stomatal conductance is the sum of stomatal and boundary layer conductance (assumed to be in series):

$$k^*_{st} = \frac{k_{st} \, k_b}{k_{st} + k_b} \tag{5.98}$$

where $k_b$ (mol m$^{-2}$ s$^{-1}$) is the boundary layer conductance (i.e. $g_b$ (in plant-science), or inverse of boundary layer resistance $r_b$, assumed

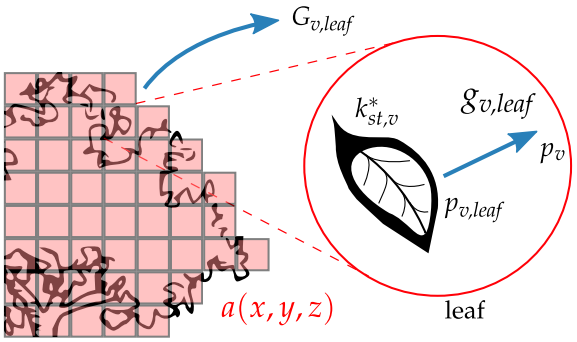


Figure 5.7: Soil-Plant-Atmosphere Continuum: The water transport from leaf to air.

to be equivalent to aerodynamic resistance $r_a$). Eq. (5.98) given in terms of resistances is given as:

$$k^*_{st} = \frac{1}{r_s + r_a} \tag{5.99}$$

where $r_s$ ($\mathrm{s\,m^{-1}}$)is the stomatal resistance.

The net plant transpiration rate $G_{v,leaf}$ ($\mathrm{kg\,s^{-1}}$) is simply the integral of moisture source in the air domain (see Eqs. (5.9) and (5.36)) and is given as:

$$G_{v,leaf} = \int_{\Omega_a} s_w \, \mathrm{d}V = \int_{\Omega_a} a \, g_{v,leaf} \, \mathrm{d}V \tag{5.100}$$

where $a$ ($\mathrm{m^2\,m^{-3}}$) is the leaf area density and $\Omega_a$ denotes the air domain (note that $a = 0$ outside vegetation, the integration is essentially only performed inside the foliage). As the water mass flux to the atmosphere is in equilibrium with the water vapor flux through xylem, i.e., as shown in Eq. (5.82), we can equate Eq. (5.100) to Eq. (5.92):

$$G_{v,leaf} = G_{v,xylem} \tag{5.101}$$

and so:

$$G_{v,leaf} = k^*_x \left(\psi_R - \psi_L\right) A_x \tag{5.102}$$

Therefore, we can determine the root water potential $\psi_R$ as follows:

$$\psi_R = \psi_L + \frac{G_{v,leaf}}{A_x k^*_x} \tag{5.103}$$

and is simply dependent on the leaf water potential $\psi_L$ (Pa), the net plant transpiration rate $G_{v,leaf}$ (kg s$^{-1}$), effective xylem conductance $k_x^*$ (s m$^{-1}$), and the xylem cross-sectional area $A_x$ (m$^2$). Additionally, we can also take in account of the influence of graviational potential change due to height of the plant as follows:

$$\psi_R = \psi_L + \frac{G_{v,leaf}}{A_x k_x^*} + \underbrace{\rho_l g H}_{\psi_g} \tag{5.104}$$

For a plant with a plant canopy height of $H = 10$ m, the additional potential is $\psi_g = 0.1$ MPa and typically is negligible compared to the contribution of leaf water potential.

### 5.5.4 *Stomatal model with water stress sensitivity*

The photosynthetic reaction creates carbohydrate and oxygen from light, water, and $CO_2$. Therefore, the photosynthetic rate $f_c$ (mol m$^{-2}$ s$^{-1}$) defined as the rate of $CO_2$ assimilated by the plant (i.e., denoted also as $A_n$ (in plant-science) or $G_{c,leaf}$ (kg m$^{-2}$) (in building physics)) is directly related to atmospheric condition such as $CO_2$ concentration, availability of light and temperature. The assimilation rate is defined through Fickian diffusion law as: The Fickian diffusion through stomata is given as:

$$f_c = k_{st} (c_a - c_i) \tag{5.105}$$

where $k_{st}$ (mol m$^{-2}$ s$^{-1}$) is the (molar) stomatal conductance to $CO_2$ (note that for now we neglect the boundary layer conductance), $c_i$ (mol mol$^{-1}$) is the intercellular $CO_2$ concentration, and $c_a$ (mol mol$^{-1}$) is the ambient $CO_2$ concentration. During the opening of the stomata, additional moisture is lost by evaporation due to exposure of stomatal cavity to the atmosphere. The transpiration rate $f_v$ (mol m$^{-2}$ s$^{-1}$) (i.e. denoted also as $f_e$ (in plant-science) or $G_{v,leaf}$ (in building physics), and also known as water use) is dependent on the atmospheric humidity and the availability of water for transpiration (Ball et al. 1987; Leuning et al. 1995). It is similarly described, based on Fickian diffusion process:

$$f_v = k_{st,v} \left( \frac{p_{v,i} - p_v}{p} \right) \tag{5.106}$$

where $k_{st,v}$ ($\mathrm{mol\,m^{-2}\,s^{-1}}$) is the (molar) stomatal conductance to water vapor, $p_{v,i}$ (Pa) is the intercellular vapor pressure, $p_v$ (Pa) is the ambient vapor pressure and $p$ (Pa) is the ambient pressure. Furthermore, $p_{v,i} = p_{v,sat}(T_l)$ (Pa) where the intercellular vapor pressure inside the stomatal cavity is assumed to be at saturation at the leaf temperature $T_l$.

So, the stomatal regulatory function is can be modeled through appropriate stomatal conductance. A generally accepted theory of plant response is that the plant regulates the stomatal aperture to optimize the photosynthetic rate for a given transpiration rate. Thus, the function of vegetation can be simplified as just maximizing the photosynthesis (or $CO_2$ assimilation) for a given transpiration rate (water use) (Medlyn et al. 2011) and the water use efficiency (WUE) quantifies the efficiency of the plant of reaching this target:

$$WUE = \frac{f_c}{f_v} \tag{5.107}$$

The *"stomatal optimality model"* reflects the theory of such stomatal behavior (Cowan 1978). The optimal stomatal control is derived from the minimization problem described by the Lagrangian:

$$\mathcal{L}(k_{st}) = f_c - \lambda f_v \tag{5.108}$$

where $\lambda$ ($\mathrm{mol\,mol^{-1}}$) is a Lagrange multiplier and represents the marginal water cost of plant carbon gain (Katul et al. 2010; Manoli et al. 2014b; Medlyn et al. 2011) and $f_c = f_c(k_{st})$ and $f_v = f_v(k_{st})$ are a function of stomatal conductance. Cowan (1978) shows that optimal stomatal behaviour is at the minima of the Lagrangian:

$$\frac{\partial \mathcal{L}}{\partial k_{st}} = 0 \tag{5.109}$$

leading to the following constraint:

$$\lambda = \frac{\partial f_v}{\partial k_{st}} \frac{\partial k_{st}}{\partial f_c} \tag{5.110}$$

or simply:

$$\lambda = \frac{\partial f_v}{\partial f_c} \tag{5.111}$$

Following these constraints, the stomatal conductance $k_{st}$ can be determined, given that problem in the assimilation rate $f_c$ is closed to determine the unknown. To provide a closure for the assimilation rate, the assimilation rate $f_c$ described from the perspective of photochemical reaction model is used. The Farquhar model of photosynthesis describing the biochemical demand function is given as:

$$f_c = \frac{a_1 c_i}{a_2 + s\, c_a} \tag{5.112}$$

where $c_i$ (mol mol$^{-1}$) is the intercellular $CO_2$ concentration, $c_a$ (mol mol$^{-1}$) is the ambient $CO_2$ concentration, and $a_1$ and $a_2$ are parameters dependent on whether photosynthetic reaction rate is limited by light or RuBisCO (Rubilose bisphosphate (RuBP) carboxylase-oxygenase) (Farquhar et al. 1980; Katul et al. 2010), and $s = 0.7$ is the constant representing the long-term intercellular to ambient $CO_2$ concentration ratio (Volpe et al. 2013). A detailed description of calculating $a_1$ and $a_2$ are given in Section 5.5.5.

To solve for the stomatal conductance $k_{st}$, the remaining unknown is the intercellular $CO_2$ concentration $c_i$. We can determine this by equating Fickian $CO_2$ flux (Eq. (5.105)) to the Farquhar biochemical demand (Eq. (5.112)):

$$f_c = \frac{a_1\, c_i}{a_2 + s\, c_a} = k_{st}\,(c_a - c_i) \tag{5.113}$$

and rewriting it for $c_i$, we get:

$$c_i = c_a \frac{a_2 + s\, c_a}{a_1 / k_{st} + a_2 + s\, c_a} \tag{5.114}$$

So, substituting Eq. (5.114) back into the biochemical demand function (Eq. (5.112)), the assimilation rate becomes a closed-problem:

$$f_c = \frac{k_{st}\, a_1\, c_a}{a_1 + k_{st}\,(a_2 + s\, c_a)} \tag{5.115}$$

where only $k_{st}$ is the remaining unknown. Finally, the stomatal conductance $k_{st}$ can be determined by solving Eq. (5.109):

$$\frac{\partial \mathcal{L}}{\partial k_{st}} = \frac{\partial f_c}{\partial k_{st}} - \lambda \frac{\partial f_v}{\partial k_{st}} = 0 \tag{5.116}$$

Substituting Eq. (5.115) and Eq. (5.106) into Eq. (5.116), we have:

$$\frac{\partial}{\partial k_{st}}\left[\left(\frac{k_{st}\, a_1\, c_a}{a_1 + k_{st}\,(a_2 + s\, c_a)}\right) - \lambda\, a_c\, k_{st}\, VPD\right] = 0 \tag{5.117}$$

where $VPD \equiv (p_{v,i} - p_v)\,/\,p$ (mol mol$^{-1}$). Solving Eq. (5.117), we get:

$$\frac{a_1^2\, c_a}{\left[a_1 + k_{st}\,(a_2 + s\, c_a)\right]^2} - \lambda\, a_c\, VPD = 0 \tag{5.118}$$

and rewriting it for $k_{st}$, we obtain:

$$k_{st} = \frac{a_1}{a_2 + s\, c_a}\left(-1 + \sqrt{\frac{c_a}{a_c\, \lambda\, VPD}}\right) \tag{5.119}$$

Additionally, in literature it is known that stomata does not completely close during night allowing for respiration. Therefore, taking this into account:

$$k_{st} = \frac{a_1}{a_2 + s\, c_a}\left(-1 + \sqrt{\frac{c_a}{a_c\, \lambda\, VPD}}\right) + k_{st,n} \tag{5.120}$$

where $k_{st,n}$ (mol m$^{-2}$ s$^{-1}$) is the nocturnal stomatal conductance ($k_{st,n} = 0.018$ mol m$^{-2}$ s$^{-1}$, (Manoli et al. 2014b)).

Thus, we obtain a stomatal model that is a function of the $CO_2$ assimilation (through parameters $a_1$, $a_2$ and $c_a$), atmospheric evaporative demand (AED) (through parameter $VPD$), and the Lagrangian multiplier $\lambda$ which represents the marginal water cost of plant carbon gain. Therefore, $\lambda$ reflects the sensitivity to water availability and is also commonly known as the *marginal water use efficiency*. It is empirically related to the leaf water potential $\lambda = \lambda(\psi_L)$ (Katul et al. 2010; Manoli et al. 2014b) and so, the stomatal response change to water availability is reflected through the change in leaf water potential $\psi_L$. The marginal WUE is determined from experimental measurements of plant photosynthesis, transpiration and stomatal conductance, and solving for the gradient of

$$\lambda\,(\psi_L) = \lambda^*_{max}\frac{c_a}{c^*_a}\exp\left\{-\beta\Big(\langle\psi_L\rangle_{24h} - \psi_{L,max}\Big)^2\right\} \tag{5.121}$$

where $\psi_L$ is assumed to vary slowly such that $\langle\psi_L\rangle_{24h}$ is fixed within the secant iteration, $\lambda^*_{max}$ is the marginal WUE under well-watered

soil condition at reference $CO_2$ concentration $c_a^* = 400$ $\mu$mol mol$^{-1}$ or parts-per-million (ppm), $\beta$ is the plant-specific sensitivity parameter (Huang et al. 2017).

Now that, we have closed the model for determining $k_{st}$ through Eq. (5.119), the intercellular $CO_2$ equation can be further simplified. Substituting Eq. (5.119) into Eq. (5.114), it becomes:

$$c_i = \left(c_a - \sqrt{a_c \, \lambda \, VPD \, c_a}\right) \tag{5.122}$$

meaning that it is only dependent on the ambient $CO_2$ concentration, vapor pressure deficit, and the marginal water use efficiency. Substituting Eq. (5.122) into Eq. (5.115), gives:

$$f_c = \frac{a_1 \, c_a}{a_2 + s \, c_a} \left(1 - \sqrt{a_c \, \lambda \, VPD \, c_a}\right) \tag{5.123}$$

### 5.5.5 *Assimilation rate*

As the photosynthesis can either be *light-limited* or *Rubisco-limited*, the true assimilation rate $f_c$ is given as:

$$f_c = \min\left(f_c^l, f_c^r\right) \tag{5.124}$$

where $f_c^l$ is the assimilation rate limited by light and $f_c^r$ is assimilation rate limited by RuBisCO. Note that it is also possible to incorporate the dark (or night) respiration and in that case $f_c = \min\left(f_c^l, f_c^r\right) - r_d$, but is not modeled in our study.

*Light-limited*

If assimilation is *light-limited*, $a_1$ and $a_2$ is defined as (Katul et al. 2010; Manoli et al. 2014b):

$$a_1 = \underbrace{\alpha_p \, e_m}_{\gamma} \, Q_p \tag{5.125}$$

and

$$a_2 = 2 \, c_p \tag{5.126}$$

where $\alpha_p$ is the leaf absorptivity of photosynthetically active radiation (PAR), $e_m$ is the maximum quantum efficiency of the leaf,

$\gamma = 0.015$ is the apparent quantum yield, $Q_p$ (mol m$^{-2}$ s$^{-1}$) is the flux of incoming PAR, and $c_p$ (mol mol$^{-1}$) is the the $CO_2$ compensation point. The $CO_2$ compensation point is determined as:

$$c_p = \frac{K_c}{2\,K_o} C_{o,a} \frac{k_o}{k_c} \tag{5.127}$$

where $k_c = 2.5$ s$^{-1}$ and $k_o = 0.18 k_c$, and:

$$K_c = K_{c,25} \exp\left\{\gamma_c \left(T_{leaf} - 298.15\right)\right\} \tag{5.128}$$

$$K_o = K_{o,25} \exp\left\{\gamma_o \left(T_{leaf} - 298.15\right)\right\} \tag{5.129}$$

are Michaelis constants for $CO_2$ and $O_2$ inhibition (referenced at 25 °C), and $C_{o,a} = 0.21$ mol mol$^{-1}$ is the oxygen concentration in the atmosphere (Farquhar et al. 1980), with $K_{c,25} = 3 \times 10^{-3}$ mol mol$^{-1}$, and $K_{o,25} = 0.3$ mol mol$^{-1}$. Thus, substituting Eq. (5.127) into Eq. (5.126), and Eqs. (5.125) and (5.126) into Eq. (5.115), we get the light-limited assimilation rate $f_c^l$ as:

$$f_c^l = \frac{\gamma\, Q_p\, c_i}{2\, c_p + s\, c_a} \tag{5.130}$$

*Rubisco-limited*

If the assimilation rate is *Rubisco-limited*, $a_1$ and $a_2$ is defined as (Katul et al. 2010; Manoli et al. 2014b):

$$a_1 = V_{cmax} \tag{5.131}$$

and

$$a_2 = K_c \left(1 + \frac{C_{o,a}}{K_o}\right) \tag{5.132}$$

where $V_{c,max}$ (mol m$^{-2}$ s$^{-1}$) is the maximum carboxylation capacity (referenced at 25 °C). The maximum carboxylation capacity is given as:

$$V_{cmax} = V_{cmax,25} \frac{\exp\left\{0.088\left(T_{leaf} - 298.15\right)\right\}}{1 + \exp\left\{0.29\left(T_{leaf} - 314.15\right)\right\}} \tag{5.133}$$

where $T_{leaf}$ (K) is the leaf temperature, $V_{cmax,25} = 5.9 \times 10^{-5}\,\mathrm{mol\,m^{-2}\,s^{-1}}$, $\gamma_c = 0.074$, and $\gamma_o = 0.015$. Thus, substituting Eqs. (5.131) and (5.132) into Eq. (5.115), the Rubsico-limited assimilation rate is given as:

$$f_c^r = \frac{V_{cmax}\, c_i}{K_c \left(1 + \frac{C_{o,a}}{K_o}\right) + s\, c_a} \tag{5.134}$$

### 5.5.6 *Numerical strategy for solving leaf water potential*

The water transport through the plant from soil to root, from root to xylem, through the xylem, and finally, from leaf stomata to air is a closed-problem once the leaf water potential is known. The leaf water potential is determined from Eq. (5.82):

$$G_{v,leaf}(\psi_L) = G_{v,root}(\psi_L) \tag{5.135}$$

As an optimization problem, it is defined as:

$$\arg\min_{\psi_L} \; \mathcal{G}(\psi_L) = \left| G_{v,leaf} - G_{v,root} \right| \tag{5.136}$$

As this is a non-linear closure problem (Manoli et al. 2014b), a secant method is employed to iteratively converge to the leaf water potential. The $j+1^{\text{th}}$ leaf water potential estimate is determined as:

$$\psi_L^{j+1} = \psi_L^j - G(\psi_L^j) \frac{\psi_L^j - \psi_L^{j-1}}{G\left(\psi_L^j\right) - G\left(\psi_L^{j-1}\right)} \tag{5.137}$$

where the initial estimate of $\psi_L^{j=0} = 0$ MPa and $\psi_L^{j=1} = -10$ MPa and with the additional constraint that $-10 \leq \psi_L \leq 0$ MPa, enforcing that leaf water potential is negative and not larger than $-10$ MPa. The detailed solution strategy for determining for coupling all the models is detailed in next section.

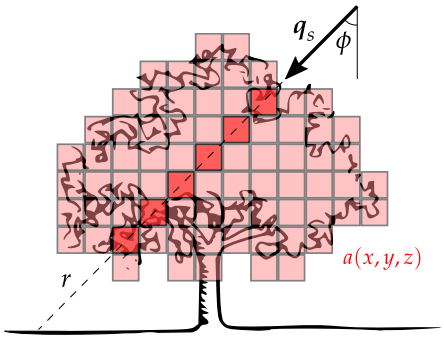


Figure 5.8: A single short-wave radiative flux $q_s$ (W m$^{-2}$) ray decaying inside the plant foliage along the path $r$ as defined by Beer-Lambert law Eq. (5.140). The foliage is discretized using leaf area density $a$ (m$^2$ m$^{-3}$) and integral is performed along the path $r$ for a given ray.

## 5.6 RADIATION MODEL

The radiative heat flux absorbed by the leaf $q_{rad,leaf}$ (W m$^{-3}$) in Eq. (5.30) is defined as:

$$\underbrace{q_{rad,leaf}}_{\text{absorbed by leaf}} = \frac{\overbrace{\nabla \cdot \boldsymbol{q}_s}^{\text{short-wave}} + \overbrace{\nabla \cdot \boldsymbol{q}_r}^{\text{long-wave}}}{a} \tag{5.138}$$

where $\boldsymbol{q}_s$ (W m$^{-2}$) is the short-wave radiative heat flux, and $\boldsymbol{q}_r$ (W m$^{-2}$) is the long-wave radiative heat flux.

The short-wave radiation absorption due to vegetation is split into solar direct and reflected/diffused component (i.e., arriving from nearby surfaces)

$$\nabla \cdot \boldsymbol{q}_s = \nabla \cdot \left( \boldsymbol{q}_{s,dir} + \boldsymbol{q}_{s,dif} \right) \tag{5.139}$$

The Beer-Lambert law describes the radiative extinction of $\boldsymbol{q}_{s,dir}$ directly from the sun along the path $r$ as:

$$\boldsymbol{q}_{s,dir}(r) = \boldsymbol{q}_{s,dir,o} \exp \left\{ -\beta \int a\,(r)\, \mathrm{d}r \right\} \tag{5.140}$$

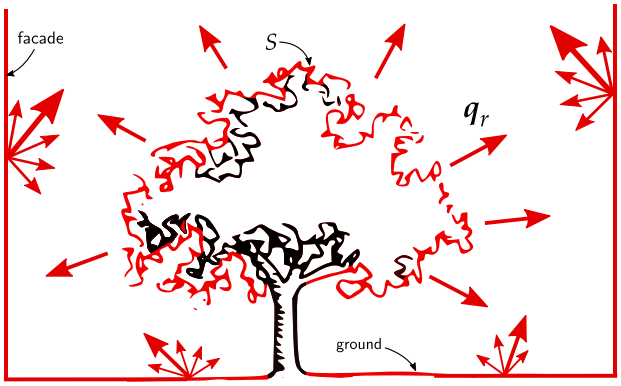


Figure 5.9: Surface flux approximation of long-wave radiative flux $q_r$ (W m$^{-2}$) at the boundary of plant foliage, defined by Eq. (5.143).

where $q_{s,o}$ (W m$^{-2}$) is the short-wave radiative flux above vegetation, and $\beta$ is the extinction coefficient for short-wave radiation. Figure Fig. 5.8 depicts the decay of a single ray along the path $r$ with solar altitude $\phi$. Therefore, to determine the extinction of short-wave radiation within the foliage, the leaf area density $a$ is integrate along the path $r$. The path $r$ depends on the solar altitude $\phi$ at a given time of the day. We assume that direct solar irradiation is composed of parallel beams all with angle of incident $\phi$.

The reflected/diffused short-wave radiation is determined using Gauss theorem simplification. It is assumed that the net reflected/diffused short-wave radiative heat flux absorbed inside the vegetation is equivalent to the short-wave radiative flux at the boundary of the vegetation:

$$\nabla \cdot \boldsymbol{q}_{s,diff} = \frac{\int_{\partial\Omega_{veg}} \boldsymbol{q}_{s,diff} \cdot \hat{\boldsymbol{n}} \, \mathrm{d}S}{\int_{\Omega_{veg}} \mathrm{d}V} \tag{5.141}$$

The vegetation domain is defined as $\Omega_{veg}$, with a boundary $\partial\Omega_{veg}$ and normal vector $\hat{n}$ oriented outward. Similarly, the long-wave radiative heat flux $\boldsymbol{q}_r$ component absorbed by vegetation (in Eq. (5.138)), i.e.:

$$\nabla \cdot \boldsymbol{q}_r \tag{5.142}$$

is also determined using the Gauss theorem simplification, assuming the net long-wave radiative heat flux absorbed inside the vegeta-

tion is equivalent to the long-wave radiative flux at the boundary of the vegetation:

$$\nabla \cdot \boldsymbol{q}_r = \frac{\int_{\partial\Omega_{veg}} \boldsymbol{q}_r \cdot \hat{\boldsymbol{n}} \, \mathrm{d}S}{\int_{\Omega_{veg}} \mathrm{d}V} \tag{5.143}$$

Thus, we assume that the reflected/diffused radiation is uniformly distributed inside the vegetation. However, this assumption might not hold if vegetation is near a high-albedo surface such as a mirror. This is one of the limitations of the present radiation model.

The vegetation model is integrated with the radiative heat transfer model developed by Kubilay et al. (2018) based on the approach detailed in Saneinejad (2013). The model decomposes short-wave (i.e., solar) and long-wave (terrestrial) radiative heat fluxes using a "*radiosity approach*" (or sometimes referred to as view factor model) and treats surfaces as gray and diffuse. The air in the *air* domain is considered to be non-participating such that surface-to-surface (S2S) transfers describe the radiative exchanges within the urban area. The model is modified to incorporate vegetation as a semi-transparent medium which interacts with the short-wave and long-wave radiative heat fluxes and directly affects the leaf energy balance. The radiative exchange between surfaces $i$ and surface $k$ is calculated as:

$$q_{rad,s,k} = (1 - \alpha_k)\, q_{s,dir,k} + \sum_{i=1}^{N} \frac{A_i}{A_k} G_{i,k} \left(\alpha_i q_{s,dir,i} + q_{s,dif,i}\right) \tag{5.144}$$

$$q_{rad,r,k} = \epsilon_k \sigma T_k^5 - \sum_{i=1}^{N} \frac{A_i}{A_k} \epsilon_i \sigma T_i^4 G_{i,k} \tag{5.145}$$

where $Q_{s,k}$ (W) is the short-wave radiative flux for surface $k$, $Q_{r,k}$ short-wave radiative flux for surface $k$, $A$ ($\mathrm{m}^2$) is surface area, $T$ (K) is the surface temperature, $\sigma = 5.67 \times 10^{-8}$ $\mathrm{W\,m^{-2}\,K^{-4}}$ is the Stefan-Boltzmann constant, $\epsilon$ is the emissivity, $\alpha$ is the albedo, $q_{s,dir,k}$ ($\mathrm{W\,m^{-2}}$) is the short-wave radiation directly from the sun arriving at surface $k$, $q_{s,dir,i}$ ($\mathrm{W\,m^{-2}}$) is the direct short-wave radiation reflected from surfaces $i$, $q_{s,dif,i}$ ($\mathrm{W\,m^{-2}}$) is the diffused short-wave radiation from other surfaces and $G$ is the Gebhart factor. The Gebhart factor is calculated using the view factor $F_{i,k}$ between surfaces $i$ and $k$ using:

$$\mathbf{G} = \left(\mathbf{I} - \mathbf{F}\bar{\rho}\right)^{-1} \mathbf{F}\left(1 - \bar{\rho}\right) \tag{5.146}$$

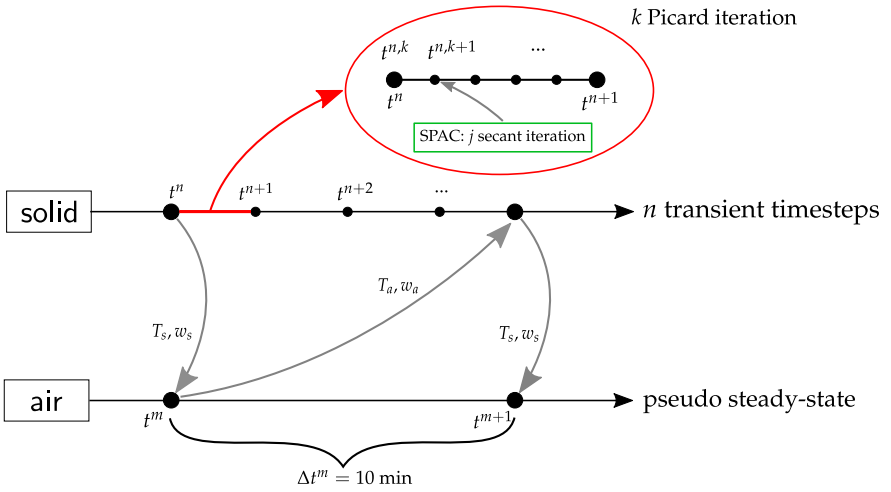


Figure 5.10: Schematic representation of the coupling strategy.

where $\bar{\bar{\rho}}$ is the reflectivity matrix. For more description on the implementation, see (Saneinejad 2013).

## 5.7 COUPLING ALGORITHM

The numerical models for air domain, solid domains (soil, ground, building facade), the radiation model and the vegetation model are implemented into OpenFOAM. Fig. 5.10 shows the schematic representation of the solid and air domain coupling strategy. The solid and air domains are coupled at regular intervals $t^m$ defined as exchange timesteps or air time steps (Kubilay et al. 2018; Saneinejad et al. 2014). The fluxes between air and solid domain consisting of thermal, moisture and radiative transfers are coupled at exchange timesteps, chosen to be an interval of $\Delta t^m = 10$ min.

### 5.7.1 *Air domain*

The air domain is solved using $m$ pseudo steady-state timestep, discretizing the diurnal cycle of a day into 8640 pseudo steady-state timesteps of $\Delta t^m = 10$ min (i.e., 8640 time steps in a 24 hrs). At each $m^{\text{th}}$ step, a steady-state RANS model is solved for the fluid equations: $\rho$, $\boldsymbol{u}$, $h$, $k$, and $\varepsilon$. During the steady-state computation, the *leaf*

*energy balance* (LEB) model is solved to determine the heat and mass fluxes, $q_{sen,leaf}$ and $g_{v,leaf}$, respectively. The algorithm for solving the air domain from $t^m \rightarrow t^{m+1}$ (as shown in Fig. 5.10) is as follows:

1. Update the radiation fields in the air domain using $q_{rad}$ from building surfaces to determine $q_r$ and $q_s$ in the vegetation zone.
2. Solve *leaf energy balance* (LEB) model:
   a) Calculate radiative flux $q_{rad,leaf}$ using Eq. (5.138).
   b) Calculate the stomatal and aerodynamic resistances $r_s$ and $r_a$ using Eq. (5.32) and Eq. (6.7), respectively.
   c) Perform an initial estimate of leaf temperature $T_{leaf} = T$.
   d) Calculate saturated vapor pressure at the leaf surface $p_{vsat,leaf} = f(T_{leaf})$.
   e) Calculate latent heat flux $q_{lat,leaf}$ using Eq. (5.33).
   f) Correct leaf temperature $T_{leaf}$ using Eq. (5.35).
   g) Repeat steps (d) to (f) until the leaf temperature has converged ($\epsilon < 10^{-8}$).
3. Calculate all vegetation source terms $s_\rho$, $\boldsymbol{s}_u$, $s_T$, $s_w$, $s_k$ and $s_\varepsilon$ (see Section 5.2).
4. Solve for the steady-state airflow field for $t^{m+1}$.
5. Repeat steps (2) to (4) until scaled residuals have reached the convergence limit of $\epsilon < 10^{-6}$.

### 5.7.2 *Solid domain*

The solid domain describes the heat and mass transport in urban structures such as building facade, pavement, road and the ground (i.e., soil). Each of these "*sub*" domains consists of $n$ adaptive solid timesteps with $\Delta t^n < \Delta t^m$ as shown in Fig. 5.10 (Janssen 2002; Kubilay et al. 2018). At the beginning of the solid domain iteration, the thermal, moisture and radiative transfers are updated providing the necessary boundary conditions for wall boundaries. For each of $n$ solid timesteps, the linearized heat and mass transport equation are solved using $k$ Picard iterations. In the soil sub-domain only, during each of these $k$ Picard iteration, the soil-plant-atmosphere

continuum (SPAC) model is solved using $j$ secant iterations to determine the root water uptake (Manoli et al. 2014b). The algorithm for solving such soil sub-domain is given as:

1. $k$ Picard iterations solving for the linearized heat and mass transport equations:
   (a) Calculate marginal WUE $\lambda$.
   (b) Calculate stomatal conductance $k_{st}$.
   (c) Calculate assimilation rate $f_c$ and transpiration rate $f_v$.
   (d) Calculate net transpiration rate $G_{v,leaf}$.
   (e) Calculate effective soil-root conductance $k^*_{sr}$.
   (f) $j$ secant iterations solve for leaf water potential $\psi_L$.
      (a) Initial guess of leaf water potential, $\psi_L^{j=0} = 0$ MPa, $\psi_L^{j=1} = -10$ MPa.
      (b) Calculate effective xylem conductance $k^*_x$.
      (c) Calculate root water potential $\psi_R^j$.
      (d) Calculate root uptake $g_{v,root}$ and net root uptake $G_{v,root}$.
      (e) Calculate cost function $\mathcal{G}$.
      (f) Correct leaf water potential using secant method $\psi_L^j \rightarrow \psi_L^{j+1}$.
      (g) Repeat till leaf water potential is converged, $\delta\psi_L \leq \epsilon$.
   (g) Calculate the sink in soil moisture due to root water uptake $s_r$.
   (h) Solve linearized form of heat and mass equation using PCG until $\delta p_c \leq 10^{-2}$ and $\delta T \leq 10^{-2}$, repeating steps before.

2. Use the final surface temperature $T_s^N$ to update $q_{r,lw}$ fluxes at all surfaces.

3. Final surface temperature $T_s^N$ and moisture fluxes $g_v^N$ are boundary conditions for the air domain at the following timestep $t^{m+1}$.

## 5.8 CONCLUSION

In conclusion, the present chapter provided a detailed description of the fully coupled numerical model for modeling the vegetation inside an urban area. The model consists of two domains (air and solid) which are coupled together. The radiation model is modified to take into account radiative exchanges between the plant foliage and the surrounding environment. The radiation model is optimized to predict the shadowing provided by vegetation on building facades throughout the day. To take into account the sensitivity of plant transpiration towards the water availability, the soil-plant-atmosphere continuum modeling approach is utilized to describe the water transport through vegetation. To facilitate the verification and validation of the leaf energy balance and its impacts on the microclimate, a parametric study is performed in Chapter 6 and validated with the experimental study of Chapter 4 in Chapter 7. In Chapter 8, the full model (i.e., the soil moisture dependent transpiration and radiative exchanges between buildings) is used to simulate vegetation in various urban areas. The validation of the fully coupled model is currently out the present scope of the thesis. However, components of the numerical model have been validated in past studies (Kubilay et al. 2018). The coupled heat and moisture transport model (without root water uptake sink) was validated with the moisture uptake experiments on porous stones and HAMSTAD benchmark case.

# 6

# NUMERICAL STUDY OF IMPACT OF VEGETATION ON TRANSPIRATIVE COOLING

This chapter has been published as: Manickathan, L., Defraeye, T., Allegrini, J., Derome, D., & Carmeliet, J. (2018). "Parametric study of the influence of environmental factors and tree properties on the transpirative cooling effect of trees". *Agricultural and Forest Meteorology*, 248, 259–274. http://doi.org/10.1016/j.agrformet.2017.10.014.

## 6.1 INTRODUCTION

This chapter focuses on a numerical study of the impact of vegetation on the transpirative cooling potential. The full-model described in Chapter 5 is simplified to focus the study on the leaf energy balance and its influence on the transpirative cooling effect of the atmosphere. Towards this, the full-model is simplified to a 2D incompressible air flow model with a stand-alone tree (or rows of trees) at solar noon. The thermal influence of the built environment is not considered, and therefore, the long-wave radiation absorption of vegetation is empirically modeled. Finally, the stomatal model is simplified to depend only on the atmospheric evaporative demand (AED) and solar radiation intensity such that the influence of soil moisture is removed. Thus, we assume the water availability does not limit plant transpiration. The numerical model is validated against the numerical and experimental study of impatiens (jewelweed) plants in a greenhouse (Section 6.5). After that, the model is used to study the transpirative cooling effect of trees in Section 6.7. The thermal comfort for a pedestrian is assessed using the Universal

Thermal Climate Index (UTCI) (Fiala et al. 2001). Furthermore, the transpirative cooling is identified by comparing the UTCI at transpiring (when the leaves can transpire) and non-transpiring (when the leaves do not transpire) conditions.

In this chapter, we focus on the cooling effect of a single row of trees at noon with solar altitude at 90° for various environmental factors (wind speed, air temperature, relative humidity and solar radiation intensity) and tree properties (leaf size, stomatal resistance and leaf area density). Furthermore, the influence of tree height and number of tree rows on the cooling effect are studied. The study aims at answering the following key questions: How does the climate influence the transpirative cooling effect of a single row of trees? Which features of the trees improve its cooling performance? Does increasing the size of the vegetated volume consistently improve the cooling of the environment? These findings can then assist in developing specific guidelines for effective UHI mitigation measures. To the author's knowledge, few rigorous studies have been performed to investigate the cooling effect of individual trees.

The Universal Thermal Climate Index (UTCI) around the trees is estimated to determine the impact of transpirative cooling on pedestrian thermal comfort. The study shows that, at low wind speeds, pedestrians would only perceive a local benefit of transpirative cooling. However, vegetation extracts overall more heat from the flow at higher wind speeds. A study on the influence of environmental conditions quantifies to which extent a single row of trees provide maximum cooling during hot and dry conditions. The shading provided by trees improves thermal comfort more that transpirative cooling of a single row of trees. Furthermore, taller trees are more beneficial as the vegetation canopy with high leaf temperatures is further away from the pedestrian level.

## 6.2 INCOMPRESSIBLE MEAN FLOW OF MOIST AIR

In this chapter, we employ the incompressible form of the conservation equations of moist air described in Section 5.2. The buoyancy force is taken into account using the Boussinesq approximation, instead of directly determining the air density variations. The

equations consist of conservation of mass, momentum, temperature, humidity and the turbulence model, respectively:

$$\nabla \cdot \overline{\boldsymbol{u}} = s_\rho, \tag{6.1}$$

$$\frac{\partial \overline{\boldsymbol{u}}}{\partial t} + \overline{\boldsymbol{u}} \cdot \nabla \overline{\boldsymbol{u}} = -\frac{1}{\rho}\nabla \overline{P} + \nabla \cdot \left[2\left(\nu + \nu_t\right)\mathbf{S}\right] - \frac{2}{3}\nabla k - \boldsymbol{g}\beta\left(\overline{T} - \overline{T}_{ref}\right) + \frac{1}{\rho}\boldsymbol{s}_u, \tag{6.2}$$

$$\frac{\partial \overline{T}}{\partial t} + \overline{\boldsymbol{u}} \cdot \nabla \overline{T} = \nabla \cdot \left[\left(\frac{\nu}{\mathrm{Pr}} + \frac{\nu_t}{\mathrm{Pr}_t}\right)\nabla \overline{T}\right] + s_T, \tag{6.3}$$

$$\frac{\partial \overline{w}}{\partial t} + \overline{\boldsymbol{u}} \cdot \nabla \overline{w} = \nabla \cdot \left[\left(\frac{\nu}{\sigma_v} + \frac{\nu_t}{\sigma_{v_t}}\right)\nabla \overline{w}\right] + s_w, \tag{6.4}$$

$$\frac{\partial k}{\partial t} + \overline{\boldsymbol{u}} \cdot \nabla k = \nabla \cdot \left[\left(\nu + \frac{\nu_t}{\sigma_k}\right)\nabla k\right] + P_k - \varepsilon + \frac{1}{\rho}s_k, \tag{6.5}$$

$$\frac{\partial \varepsilon}{\partial t} + \overline{\boldsymbol{u}} \cdot \nabla \varepsilon = \nabla \cdot \left[\left(\nu + \frac{\nu_t}{\sigma_\varepsilon}\right)\nabla \varepsilon\right] + C_{1\varepsilon}P_k\frac{\varepsilon}{k} - C_{2\varepsilon}\frac{\varepsilon^2}{k + \sqrt{\nu\varepsilon}} + \frac{1}{\rho}s_\varepsilon, \tag{6.6}$$

where $\overline{\boldsymbol{u}}$ ($\mathrm{m\,s^{-1}}$) is the mean velocity, $\overline{P}$ (Pa) the mean hydrostatic pressure, $\overline{T}$ (K) the mean air temperature, $\overline{w}$ ($\mathrm{kg\,kg^{-1}}$) the mean humidity ratio (i.e. the ratio of water vapor mass to dry air mass), $k$ ($\mathrm{m^2\,s^{-2}}$) the turbulent kinetic energy (TKE) and $\varepsilon$ ($\mathrm{m^2\,s^{-3}}$) the TKE dissipation rate (TDR).

The environmental constants are the density of air $\rho = 1.225$ ($\mathrm{kg\,m^{-3}}$), the kinematic viscosity of air $\nu = 1.45 \times 10^{-5}$ $\mathrm{m^2\,s^{-1}}$, the gravitational acceleration $\boldsymbol{g} = (0,\ 0,\ -9.81)^T$ $\mathrm{m\,s^{-2}}$, and the thermal expansion coefficient $\beta = 3 \times 10^{-3}$ $\mathrm{K^{-1}}$. The Prandtl number, Schmidt number, turbulent Prandtl number, turbulent Schmidt number are $\mathrm{Pr} = 0.9$, $\sigma_v = 0.9$, $\mathrm{Pr}_t = 0.7$ and $\sigma_{v_t} = 0.7$, respectively. The turbulence model constants are $C_{2\varepsilon} = 1.92$, $\sigma_k = 1.0$ and $\sigma_\varepsilon = 1.2$. The remaining coefficients $C_\mu$ and $C_{1\varepsilon}$ in the porous realizable $k - \varepsilon$ model are determined from velocity gradients and TKE production-dissipation ratio (Shih et al. 1995). Vegetation introduces the source for mass $s_\rho$, momentum $\boldsymbol{s}_u$, temperature $s_T$, humidity ratio $s_w$, TKE $s_k$ and TDR $s_\varepsilon$ in the conservation equations.

## 6.3 SIMPLIFIED STOMATAL MODEL

In the present study, the stomatal resistance is modeled simply as a function of climatic conditions: $q_{r,sw}$ (also $q_{s,dir}$) the short-wave radiative flux in the air and $D \equiv p_{v,sat} - p_v$ (kPa) the vapor pressure deficit in the air (i.e., the difference between the saturation vapor pressure and the vapor pressure of the air). In contrast to the advanced model described in Section 5.5.4, the stomatal model is no longer dependent on the soil moisture and is only dependent on the atmospheric conditions, simplifying the complexity of the model. The stomatal resistance is given as:

$$r_s = r_{s,min} f_1(q_{r,sw}) f_2(D) \tag{6.7}$$

where $r_{s,min}$ (s m$^{-1}$) is the minimal stomatal resistance and

$$f_1 = \frac{a_1 + q_{r,sw}}{a_1 + q_{r,sw}} \tag{6.8}$$

$$f_2 = 1 + a_3 (D - D_0)^2 \tag{6.9}$$

are multiplicative functions describing the stomatal resistance change due to short-wave radiation and vapor pressure deficit in the air, respectively. The constants of the empirical functions are $a_1 = 169$ W m$^{-2}$, $a_2 = 18$ W m$^{-2}$, $a_3 = 0.005$ kPa$^{-2}$ and $D_0 = 1.2$ kPa (Kichah et al. 2012). The minimum stomatal resistance $r_{s,min}$, the resistance when the stomata are fully open, depends on the plant type: e.g. 150 s m$^{-1}$ for impatiens, 200 s m$^{-1}$ for grass, 400 s m$^{-1}$ for gloxinia and deciduous plants (Baille et al. 1994; Bruse and Fleer 1998). It must be noted that various other models exist in literature for the stomatal resistance and an overview is given by Damour et al. (2010). The present model is chosen as it is a simple model which can be used to consider the influence of environmental conditions.

## 6.4 SIMPLIFIED RADIATION EXCHANGE WITH VEGETATION

In this study, we simplify the formulation of radiation within vegetation according to the studies of plants in greenhouses (Boulard and Wang 2002; Fatnassi et al. 2006; Kichah et al. 2012; Majdoubi et al. 2009). We assume the sun is positioned at the solar-noon (i.e.,

directly above the vegetation) and as we deal with a 2D problem, the ray-tracing algorithm described in Section 5.6 can be substantially simplified. Furthermore, the long-wave radiation is empirically modeled as we only investigate a stand-alone tree. Such an approach is ideal for a parametric study on the dominant factors driving the transpirative cooling effect of vegetation.

The short-wave radiative flux $q_{r,sw}$ (or $q_{s,dir}$) within a vegetation volume is determined using Beer-Lambert law:

$$q_{s,dir}(z) \quad \text{or} \quad q_{r,sw}(z) = q_{r,sw,0} \exp\left\{-\beta \int_z^H a\,(z)\,\mathrm{d}z\right\} \tag{6.10}$$

where $q_{r,sw,0}$ (W m$^{-2}$) is the short-wave radiative flux hitting the top of the vegetation and $\beta = 0.78$ is the extinction coefficient for short-wave radiation. Note that the notation of short-wave radiative flux is modified in this chapter. The integral defines the net density of leaves that is present from the top of the vegetation canopy to the height where the short-wave radiative flux is evaluated. The simplification we consider in this study is that the sun is positioned directly above vegetation, i.e. mid-day condition with a solar altitude $\phi = 90°$. A model with varying solar conditions is part of future research. The long-wave radiative flux is modeled empirically, as a function of the downward long-wave radiative flux, i.e. from the sky. It is given by:

$$\nabla \cdot q_r = C_{lw} \frac{q_{r\downarrow}}{H} \tag{6.11}$$

where $C_{lw} = 0.04$ is an empirical constant for quantifying the net absorption of long-wave radiation (Kichah et al. 2012). Using this approach, the thermal emission of the leaves can be empirically modeled. The downward long-wave radiative flux is taken to be the long-wave radiative flux from sky, i.e. $q_{r\downarrow}$ with a sky temperature of $T_{sky} = 15$ °C (Saneinejad et al. 2014).

## 6.5 NUMERICAL MODEL

The vegetation model, described in Sections 6.2 to 6.4, is implemented into the OpenFOAM finite volume solver (Weller et al. 1998). The steady-state velocity field is solved using the SIMPLE pressure-velocity coupling algorithm. A second-order central difference scheme

is used for the gradient operator and a second-order linear upwind differencing scheme for the convective terms. The convergence criterion for the scaled residuals is set to $10^{-8}$ based on sensitivity analysis. The computational domain size and the numerical scheme are chosen based on CFD best practices (Blocken 2015; Franke et al. 2007; Tominaga et al. 2008).

### 6.5.1 *Simulation domain*

The simulation of single row of trees is represented by a 2D porous domain ($x \times z$ axis) consisting of a $1 \times 1$ m$^2$ ($x \times z$ axis) porous vegetation region as shown in Fig. 6.1, while infinitely long in the y-direction, where the source terms (Section 5.2) are non-zero. In this study, we want to focus on the physics behind the transpiration driven phenomena. Therefore, the dimension of the tree does not necessary require to be conform with reality and was simply based on computational efficiency for a rigorous parametric study. The computational domain is $35 \times 11.5$ m$^2$ ($x \times z$ axis) and the mesh resolution is determined by performing a grid sensitivity analysis. The domain is discretized into a regular grid with 40 000 rectangular cuboidal cells. The smallest cell is at the edge of the tree row ($\Delta x = \Delta z = 0.01$ m) and the expansion ratio to the outflow, inlet, ground and top boundaries are 1.05, 1.05, 1.05, and 1.15, respectively.

The environmental factors that are varied for the parametric study are wind speed, ambient air temperature, relative humidity (RH) and solar radiation intensity. The environmental factors are tabulated in Table 6.1. Similarly, the properties of the vegetation are tabulated in Table 6.2 and the parameters that are varied are leaf area density, stomatal resistance, leaf size, tree height and number of tree rows, which are presumed to have an influence on the transpirative cooling effect of vegetation. The upper and lower bounds of the parameters are chosen based on values from literature. The reference tree is chosen to be a densely foliated garden hedgerow in a midday conditions.

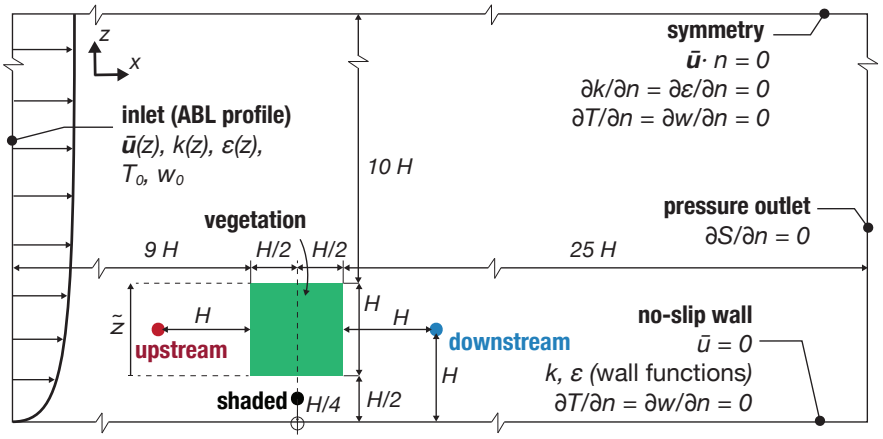


Figure 6.1: Simulation domain of the reference case with $H = 1$ m with description of the domain and the boundary conditions. The porous vegetation region is indicated in green (■) where leaf area density $a = 10\ \mathrm{m^2\,m^{-3}}$ and zero everywhere else. The red point (•) indicate the upstream $(x = -1.5H, y = H)$, blue (•) indicate the downstream $(x = 1.5H, y = H)$, and black (•) indicate the shaded $(x = 0, y = H/4)$ data sampling location.

### 6.5.2 *Boundary conditions*

An atmospheric boundary layer (ABL) profile is prescribed at the inlet (Richards and Hoxey 1993):

$$\overline{u}(z) = \frac{u_*}{\kappa} \ln\left(\frac{z + z_0}{z_0}\right) \tag{6.12}$$

$$k = \frac{{u_*}^2}{\sqrt{C_\mu}} \tag{6.13}$$

$$\varepsilon = \frac{u_*^3}{\kappa\,(z + z_0)} \tag{6.14}$$

where $\overline{u}(z)$ $(\mathrm{m\,s^{-1}})$ is the horizontal inlet velocity at height $z$, $u_*$ $(\mathrm{m\,s^{-1}})$ is the friction velocity, $\kappa = 0.41$ is von Kármán constant, $z_0 = 0.0217$ m is the aerodynamic roughness length and $C_\mu = 0.09$. The inlet boundary conditions for air temperature $T$ and humidity ratio $w$ are for simplicity uniform profiles, $T(z) = T_0$ and $w(z) = w_0$

Table 6.1: Environmental factors varied in the parametric study

| Parameter | Range | Reference |
|---|---|---|
| Solar radiation, $q_{r,sw,0}$ | $[100, 400, 800, 1000]$ | 800 |
| Wind speed, $U_{ref}$ | $[0.1, 0.25, 0.5, 0.75, 1, 2, 3, 5]$ | 1 |
| Air temperature, $T_0$ | $[20, 30]$ | 30 |
| Relative humidity, $RH$ | $[20, 30, 40, 50, 60, 70, 80]$ | 60 |

Table 6.2: Plant properties varied in the parametric study

| Parameter | Range | Reference |
|---|---|---|
| Leaf area density, $a$ | $[1, 3, 5, 7, 10]$ | 10 |
| Min. stomatal resistance, $r_{s,min}$ | $[50, 100, 125, 150, 175, 200, 250, 300]$ | 150 |
| Leaf size, $l$ | $[0.01, 0.05, 0.1, 0.2, 0.3, 0.4]$ | 0.1 |
| Tree height , $H$ | $[1, 2, 3, 5, 10]$ | 1 |
| $\mathcal{N}^{o}$ of tree rows, $n$ | $[1, 2, 5, 10]$ | 1 |

and varied individually during the parametric study as tabulated in Table 6.1.

The ground is modeled using standard wall functions and is considered to be adiabatic. This ensures that the thermal influence of the ground is not present when measuring the cooling effect of vegetation on air. Even though, in reality, the thermal influence of the ground on the air temperature is an important factor, in the present study this simplification was chosen to isolate the influence of transpirative cooling of vegetation. A zero normal gradient boundary condition is applied for the humidity ratio. At the top, a slip velocity boundary condition is used and the temperature and humidity ratio are prescribed a zero normal gradient boundary condition. The outlet of the domain is set to a pressure outlet. The boundary conditions for T and w at outlet are zero normal gradient boundary conditions.

### 6.5.3 *Numerical solution procedure*

In the present study, the following strategy is used for solving the coupled vegetation-air problem:

1. Iteratively solve the energy balance at the leaf surface:
   a) Determine the radiative flux $q_{rad,leaf}$ using Eq. (5.138).
   b) Calculate the stomatal and aerodynamic resistances $r_a$ and $r_s$ using Eq. (5.32) and Eq. (6.7), respectively.
   c) Perform an initial estimate of leaf temperature $T_{leaf} = T$ during the iteration.
   d) Calculate the saturated vapor pressure at the leaf surface $p_{vsat,leaf} = f(T_{leaf})$.
   e) Calculate the latent heat flux $q_{lat,leaf}$ using Eq. (5.33).
   f) Correct the leaf temperature $T_{leaf}$ using Eq. (5.35).
   g) Repeat steps (d) to (f) until the leaf temperature has converged with a convergence criterion of $10^{-8}$.
2. Calculate all vegetation source terms $s_\rho$, $s_u$, $s_T$, $s_w$, $s_k$ and $s_\varepsilon$ (see Section 5.2).
3. Solve for the steady-state flow field, Eqs. (6.1) to (6.6).
4. Repeat steps (1) to (3) until scaled residuals of Eqs. (6.1) to (6.6) have reached the convergence limit of $10^{-8}$.

The algorithm of the vegetation model is implemented as an OpenFOAM C++ library. To satisfy the energy balance problem, the leaf temperature is determined iteratively using Eq. (5.35), with the air temperature as an initial guess for leaf temperature. The energy balance is satisfied once the leaf temperature converges. The numerical model is validated and is used thereafter to investigate the influence of environmental factors and tree properties on the transpirative cooling effect.

## 6.6 VALIDATION OF VEGETATION MODEL

The vegetation model is first validated against the numerical and experiment study of Kichah et al. (2012). The study provides measure-

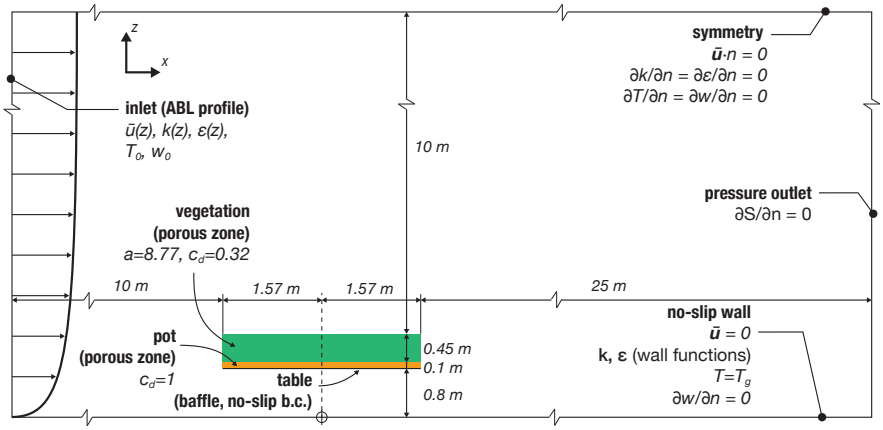


Figure 6.2: Simulation domain and boundary conditions for the validation case Kichah et al. (2012). The impatiens plant in indicated in green (■) and plant pot in orange (■). Both are regions are modeled as porous zone with drag coefficients $c_d = 0.32$ and $c_d = 1$, respectively. The boundary conditions of the simulation are tabulated in Table 6.3 and correspond to 14:00 on June 15$^{\text{th}}$, 2009.

ment and numerical (CFD) results of flow through impatiens (jewelweed) plants in a greenhouse. The study investigates the heat and moisture exchanges between vegetation and the air and provides a comprehensive dataset of the response of vegetation to environmental conditions. The simulation domain is adapted according to the study, where the impatiens plants are placed on a table, Fig. 6.2.

The plants and the pots are both modeled as porous medium with different drag coefficients. The drag coefficient of the plant and pot are $c_d = 0.32$ and $c_d = 1$, respectively. The table is modeled as an internal wall (i.e. baffle) that enforces a standard wall boundary condition. The boundary condition of the ground is $T = T_g$ and standard wall functions are used. The top boundary is a symmetry plane. The outlet is taken to be far enough to ensure zero-normal gradient for all variables and a zero pressure is imposed. The inlet boundary conditions are tabulated in Table 6.3, corresponding to a greenhouse in a sunny day on 15$^{\text{th}}$ July 2009 at 14:00. Based on a mesh sensitivity analysis, (i.e., a grid refinement and solution convergence check), a regular grid discretization is chosen with smallest cells at the edge of the vegetation ($\Delta x = 0.01$ m, $\Delta y = 0.0055$ m) and

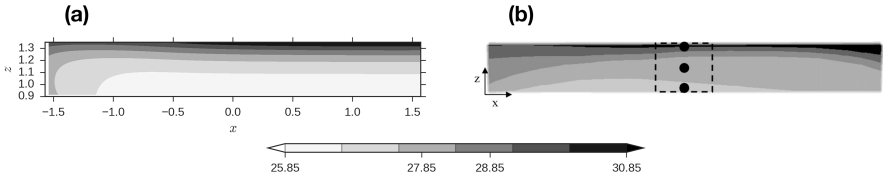


Figure 6.3: Comparison of leaf temperature $T_{leaf}$ (°C) within vegetation ($-1.5 \leq x \leq 1.5$) and ($0.9 \leq z \leq 1.35$): **(a)** present study and **(b)** numerical simulation results from (Kichah et al. 2012). The three dots (*bottom*: $z = 0.9$ m, *middle*: $z = 1.125$ m and *top*: $z = 1.35$ m) indicate the temperature probe positions, Table 6.4.

a total number of cells of 24 000. The grid expansion ratio from the vegetation edges to the outflow, inlet, ground and top boundaries are 1.05, 1.11, 1.13 and 1.15, respectively.

Fig. 6.3 shows the leaf temperature $T_{leaf}$ distribution of the vegetation and is compared with numerical results from the original study (Kichah et al. 2012). We see that the temperature ranges (between 25 °C and 31 °C) are in good agreement. However, the leaf temperature contours are different between the two simulations. The general trend in vertical temperature distribution is in agreement, with peak temperatures appearing close to the top of the vegetation due to radiation absorption. The difference observed between the present model and Kichah et al. (2012) could be due to the use of a turbulence model as the turbulence production and dissipation due to vegetation (Eqs. (11) and (12)) is not done in Kichah et al. (2012). However, it is shown by Sanz (2003) that the influence of vegetation on turbulence has to be modeled to ensure physically accurate turbulence characteristics. Moreover, we employ the porous realizable $k-\varepsilon$ turbulence closure in contrast to the standard porous $k-\varepsilon$ used by Kichah et al. (2012). The porous realizable $k-\varepsilon$ model is chosen as it provides more accurate wake characteristics leeward of a porous medium (Santiago et al. 2007; Shih et al. 1995). The choice of turbulence model is known to have an impact on parameters such as recirculation length (Santiago et al. 2007) and this could result in some difference in the leaf temperature contours.

Furthermore, the validation is performed by comparing the leaf and air temperatures with the numerical and experimental results

from Kichah et al. (2012). The numerical and experimental values of leaf temperature $T_{leaf}$ values are obtained for three positions: "*bottom*" ($x = 0, z = 0.9$), "*middle*" ($x = 0, z = 1.125$) and "*top*" ($x = 0, z = 1.35$). The numerical and experimental values of the air temperature $T_{leaf}$ at position "*middle*" are also compared, as shown in Table 6.4. The comparison shows that the numerical results from the present study are in better agreement with the experiments than the numerical results of Kichah et al. (2012). At the top of the vegetation, the difference between the numerical and experimental results are the highest with $T^{num} - T^{exp} = 1.0$ °C for both the present study and Kichah et al. (2012). The deviation on the top between the predicted and the measured temperatures could be due to the simplification in the leaf distribution. The numerical models assume the leaf area density to be homogeneously distributed, however, in reality, it varies in height. This influences the radiation absorption within vegetation and will impact the heat and mass exchanges. Generally, the leaf temperature trend is seen to be slightly overestimated and the air temperature to be slightly underestimated. However, as the deviation is only within 1.0 °C, we consider the predicted results to be sufficiently accurate.

## 6.7 IMPACT OF ROW OF TREES ON THE MICROCLIMATE

The developed numerical model is first used to understand the impact of a single row of trees (as 2D tree equates to an infinitely long

Table 6.3: Environmental conditions used in Kichah et al. (2012). Data obtained for condition at 14:00 on June 15$^{th}$, 2009.

| Parameter | Value |
|---|---|
| Air temperature, $T_0$ | 32 °C |
| Ground temperature $T_g$ | 24 °C |
| Humidity ratio $w_0$ | 6.21 g kg$^{-1}$ |
| Solar radiation, $q_{r,sw,0}$ | 99 W m$^{-2}$ |
| Long-wave radiation, $q_{r,lw,\downarrow}$ | 522 W m$^{-2}$ |

Table 6.4: Comparison of leaf temperature $T_{leaf}$ at various heights and air temperature $T$ in the middle of vegetation. Experimental and numerical data obtained from (Kichah et al. 2012).

| Parameter | Experimental (Kichah et al. 2012) | Numerical (Kichah et al. 2012) | Present | $T^{num} - T^{exp}$ (Kichah et al. 2012) | $T^{present} - T^{exp}$ |
|---|---|---|---|---|---|
| Leaf temperature $T_{leaf}$ (°C) | | | | | |
| *top* ($z = 1.35$ m) | 29.5 | 30.5 | 30.5 | 1.0 | 1.0 |
| *middle* ($z = 1.125$ m) | 26.7 | 28.0 | 27.0 | 1.3 | 0.3 |
| *bottom* ($z = 0.9$ m) | 26.1 | 27.6 | 26.2 | 1.5 | 0.1 |
| Air temperature $T$ (°C) | | | | | |
| *middle* ($z = 1.125$ m) | 28.11 | 28.5 | 27.9 | −0.4 | −0.2 |

row of trees) on the surrounding microclimate. The transpirative cooling effect of vegetation is determined as the change in the Universal Thermal Climate Index (*UTCI*). Thereafter, a parametric study is performed to determine the impact of different environmental factors, tree properties and vegetation. The simulation domain described in Fig. 6.1 is used as the reference case for the parametric study. The environmental boundary conditions are given in Table 6.1 and the tree properties are tabulated in Table 6.2. To ensure fair comparison in the parametric study, the stomatal resistance is fixed to the minimum stomatal resistance $r_s = r_{s,min}$ and is assumed to be independent of the radiation and humidity levels of the environment. The influence of the stomatal model is investigated separately. As mentioned above, the study assumes that the ground is adiabatic to isolate the influence of transpirative cooling effect of the tree row on the air. To study the impact of a single row of trees on the microclimate, the energy balance at the leaf surface and its implication on the flow field are studied first.

### 6.7.1 *Impact on energy balance at the leaf surface*

The energy balance at the leaf surface is defined by Eq. (5.30), where the absorbed radiative heat flux is converted into latent and sensible heat fluxes. The average radiative flux into the leaf is $\langle q_{rad,leaf} \rangle = 77$ W m$^{-2}$ for the constant and varying stomatal resistance cases. In the case of constant stomatal resistance, $r_s = r_{s,min}$, the average sensible flux is $\langle q_{sen,leaf} \rangle = -50$ W m$^{-2}$ (negative sign indicates cooling of the air) and the average latent heat flux is $\langle q_{lat,leaf} \rangle = 127$ W m$^{-2}$ used to evaporate water. In the case of varying stomatal resistance Eq. (6.7), the average sensible and latent heat fluxes are 9 W m$^{-2}$ and 68 W m$^{-2}$, respectively. To better understand how the radiative heat is converted, the heat flux distribution and the leaf temperature distribution within the foliage are studied. Fig. 6.4 shows the vertical distribution of heat fluxes and temperature along the vertical centre line within the centre of the foliage. Fig. 6.4a shows that the heat fluxes are maximum at the top of the trees, where solar radiation is mostly absorbed due to the high density of vegetation with $a = 10$ m$^2$ m$^{-3}$. A high absorbed radiative heat results in a positive sensible heat flux (indicating heat is leaving the leaf and entering air) leading to an increase of the air temperature, as seen in Fig. 6.4b. The latent

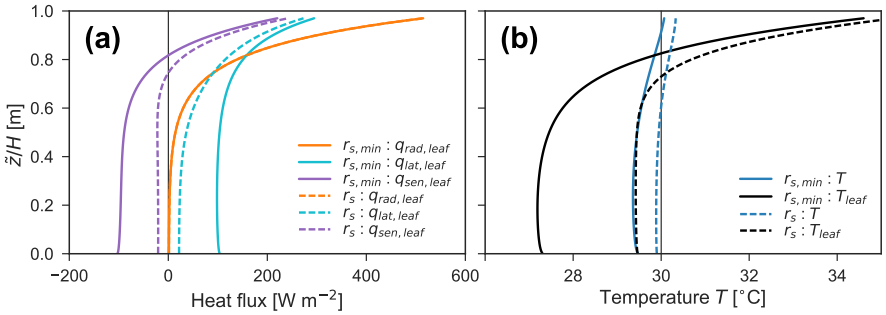


Figure 6.4: Vertical distribution at centre-line of the tree row with height $\tilde{z} = 0$ at bottom of the vegetation volume and $\tilde{z} = 1$ at top of the trees: **(a)** heat fluxes at the leaf surface (Eq. (5.30)) and **(b)** temperature profiles of leaf temperature $T_{leaf}$ (°C) and air temperature $T$ (°C).

heat flux is also positive due to transpiration at the leaf, Eq. (5.33). At lower heights, the radiation decays exponentially given the prior absorption of the short-wave radiation, Eq. (6.10), resulting also in an exponential decay of the latent and sensible heat fluxes. At the bottom of the foliage, the sensible heat flux is negative as the radiation is low but transpiration still occurs, leading to cooling of the air.

In the case of environmentally dependent stomatal resistance, the stomatal resistance is higher than minimum stomatal resistance, when the stomata are fully open. As stomatal resistance is inversely proportional to incident short-wave radiation (Eq. (6.7)), this resistance is low at the top of the trees and high at the bottom of the trees. A higher stomatal resistance means that the CMTC is lower (Eq. (5.34)) and so the water vapor mass flux due to transpiration reduces. The reduced transpiration leads to higher leaf temperature and therefore lower cooling of the air provided by vegetation (Fig. 6.4). With a minimum stomatal resistance, the average air temperature is 29.6 °C. Whereas, with higher stomatal resistances, the transpiration is reduced and the higher leaf temperature results in an average air temperature of 30.0 °C. To further understand the impact of stomatal resistance, the change in flow conditions due to vegetation is studied.

### 6.7.2 *Influence of vegetation on the flow field*

The heat, mass and momentum exchanges between the trees and the air determine the distribution of velocity, temperature and humidity. Furthermore, the turbulence intensity is increased due to the foliage. Fig. 6.5a shows the normalized velocity magnitude $\overline{\boldsymbol{u}}/U_{ref}$, which shows the influence of momentum drag of the trees. The dashed box in the figure indicates the porous region where the source terms for vegetation are present. The figure shows that the wind speed is reduced by 50% behind the tree row. Furthermore, we see that the flow is slightly accelerated below the tree row between the tree bottom and the ground due to the tunneling effect present in below a row of trees. Fig. 6.5b shows the increase in the turbulence intensity (TI) $I = (2/3\,k)/\overline{\boldsymbol{u}}$ due to the trees as it converts the mean kinetic energy into the turbulence kinetic energy. The $I$ inside the porous region is approximately 20% higher than the freestream flow. However, we see that the highest $I$ is observed in the wake region, $I \approx 50\%$, where the mean velocity is lowest and the TKE is high. Therefore, the impact of vegetation on the turbulence characteristics in a microclimate is not negligible.

Fig. 6.5c shows the influence of a single row of trees on the air temperature. We observe that the highest cooling is at the bottom of the trees, where the absorbed radiation is lowest. The temperature is also lower towards the wake of the trees where the velocity is lower. Such "*oasis*" effect of cool temperature region in the vicinity of vegetation has also been observed in various field measurements (Kurn et al. 1994; Taha 1997; Wong et al. 2003) and numerical studies (Dimoudi and Nikolopoulou 2003; Gromke 2011). At the top of the tree foliage, we observe a higher air temperature due to higher absorption solar radiation but the temperature is only marginally higher than the ambient temperature. The air temperature increases because the leaf temperature is higher than the windward air temperature (Fig. 6.4b). Fig. 6.5d shows that the humidity ratio increases and the highest humidity is at the top-downstream region of the trees. The figure shows that maximum transpiration occurs at the top of the trees, since solar radiation absorption is highest at the top of the trees and transpiration is also the process used by the trees to dissipate the absorbed radiative heat. The increase of humidity

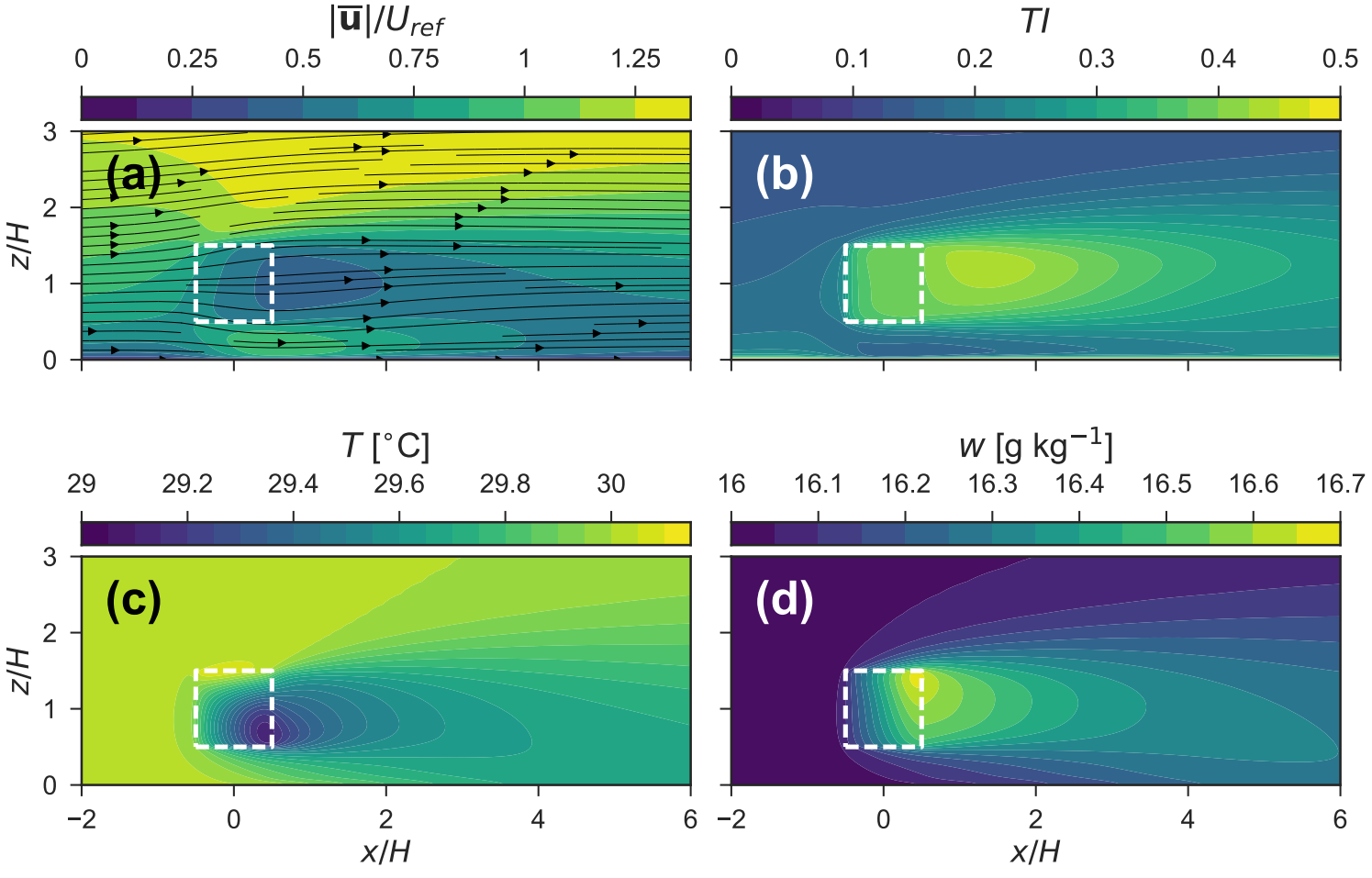


Figure 6.5: Flow field past a single row of trees for the reference case with domain described in Fig. 6.1, with $r_s = r_{s,min}$ and environmental and tree properties tabulated in Tables 6.1 and 6.2, respectively. **(a)** Normalized velocity $\overline{u}/U_{ref}$, **(b)** turbulence intensity $I = (2/3\,k)/\overline{u}$ **(c)** air temperature $T$ (°C) and **(d)** humidity ratio $w$ (g kg$^{-1}$).

ratio towards the downstream region of the trees is due to the wind convecting the humidity towards the leeward side of the trees.

### 6.7.3 *Transpirative cooling effect of a row of trees*

A quantitative analysis of the transpirative cooling effect of a single row of trees and its impact on thermal comfort is possible by investigating the Universal Thermal Comfort Index (UTCI). The comfort index is expressed as an equivalent temperature and is determined from a human thermoregulatory response model coupled with a clothing model (Fiala et al. 2001). The equivalent temperature is dependent on the air temperature, humidity, wind speed and radiation and represents the temperature of a reference environment that would provide the same response for the reference person as it would in the actual environment. It is designed as an outdoor comfort index and is seen to outperform similar other comfort indices such as Perceived Temperature (PT), Physiological Equivalent Temperature (PET) and OUT_SET* (Jendritzky et al. 2012). Furthermore, it can be used as an international standard for all assessments of the outdoor thermal conditions in various fields such as public weather services, public health systems and climate impact research. Therefore, the UTCI is used in this study to provide an indication of the comfort for a pedestrian in vicinity of trees. The UTCI is implemented in the BioKlima 2.6 software package and is calculated as (°C):

$$UTCI = T + f\left(T, T_{mrt}, |\boldsymbol{u}|, RH\right) \tag{6.15}$$

where it is a function of air temperature $T$, the mean radiant temperature $T_{mrt}$, wind speed $|\boldsymbol{u}|$ and relative humidity $RH$. The mean radiant temperature $T_{mrt}$ is influenced by the long-wave and the short-wave radiation, which is a function of direct solar radiation $q_{r,sw}$ and the solar altitude $\phi$. However, in this study we do not take into account the long-wave radiation component in determining the mean radiant temperature. This is one of the limitations in the analysis provided in this chapter. However, as we focus on cross-comparison of the varies cases, we assume the contribution of long-wave radiation between different cases does not vary highly. The main goal of the study is to isolate the influence of transpirative cooling effect on the air and determine the influence of wind

speed, temperature, RH, solar radiation and tree properties on the transpiration rate. By modeling the ground as an adiabatic surface, the soil heat storage could be decoupled from the interaction of transpirative cooling. We remark that, in the present study, diffuse solar radiation and long-wave radiation are not considered in the determination of mean radiant temperature for UTCI. These radiation components will be determined in future analysis for a more accurate assessment of pedestrian comfort, especially in the vicinity of buildings. The UTCI provides an indication of the thermal stress experienced by a pedestrian, as tabulated in Table 6.5. The UTCI values that lie between 18 °C and 26 °C comply as "*thermal comfort zone*" (Marshall 1987). A UTCI value in the range of a moderate heat stress (HS) level can result in sweating for the reference person after 30 minutes, where fatigue is possible after prolonged exposure or physical activity (Blazejczyk et al. 2012; Błazejczyk et al. 2013). A UTCI value in the range of a strong HS level results in an instantaneous change in skin temperature and introduces the risk for sunstroke and muscle cramp after prolonged exposure. A very strong HS level is considered dangerous showing increase in internal body temperature within 30 minutes with high possibility of sunstroke and muscle cramp after prolonged exposure. An extreme HS level is considered highly dangerous with high likeliness of heat stroke.

Fig. 6.6 shows the transpirative cooling effect of a tree row for fixed and varying stomatal resistance conditions. The figure compares transpiring (when stomata are open and transpiration from trees is enabled) and non-transpiring conditions (when stomata are closed and transpiration from trees is disabled). Fig. 6.6a shows the UTCI (°C) distribution during non-transpiring condition. As transpiration does not occur, the UTCI is the same for fixed and varying stomatal resistance. The figure shows that at the upstream region, where the flow is unaffected by the tree ($x/H = -2$ m), the UTCI reduces with height. The decrease of the UTCI with height is caused by the increase of wind speed with height. The figure also shows that the lowest value of the UTCI occurs inside and below the trees as it provides shading from the sun. The UTCI drops from 36 °C to 29 °C. Therefore, the trees have a large influence on the UTCI due to the shadowing effect from the solar radiation. This observation is in good agreement with field measurements of a rooftop garden in Singapore by Wong et al. (2003) where a large reduction in air

Table 6.5: UTCI thermal heat stress categories (Bröde et al. 2012; Oke et al. 2017).

| UTCI (°C) | Thermal stress categories | Physiological responses |
|---|---|---|
| $> 46$ | Extreme heat stress (HS) | Increase in core temperature |
| 38 to 46 | Very strong HS | Small core to skin temperature gradient ($< 1$ K), Sweat rate increase ($> 650\ \mathrm{g\,h^{-1}}$ at limit) |
| 32 to 38 | Strong HS | Sweat rate $> 200\ \mathrm{g\,h^{-1}}$ |
| 26 to 32 | Moderate HS | Increased rate of sweating and skin temperature |
| 9 to 26 | No thermal stress | Comfortable, sweat rate $< 100\ \mathrm{g\,h^{-1}}$ |

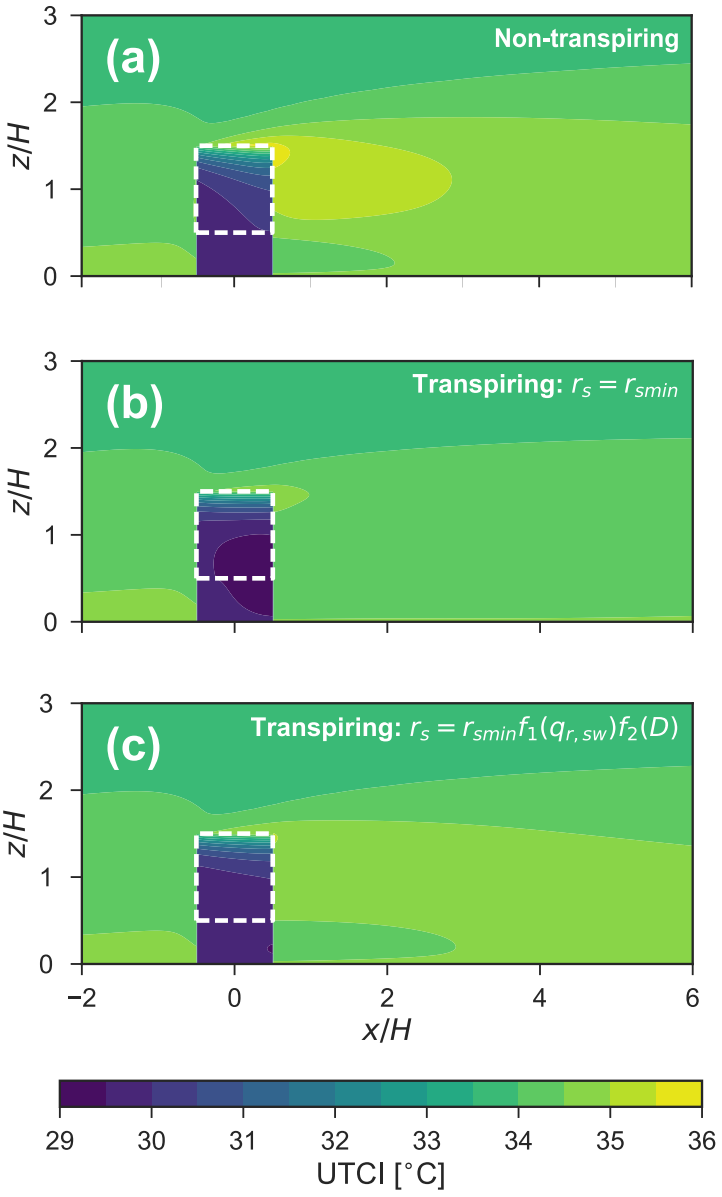


Figure 6.6: Transpirative cooling effect of a single row of trees. The influence of the trees on the Universal Thermal Comfort Index (UTCI) (°C) for **(a)** in non-transpiring condition (NT); in transpiring condition (T) for **(b)** constant stomatal resistance, $r_{s,min}$ and **(c)** for varying stomatal resistance $r_s = r_{s,min} f(q_{r,sw}) f(D)$.

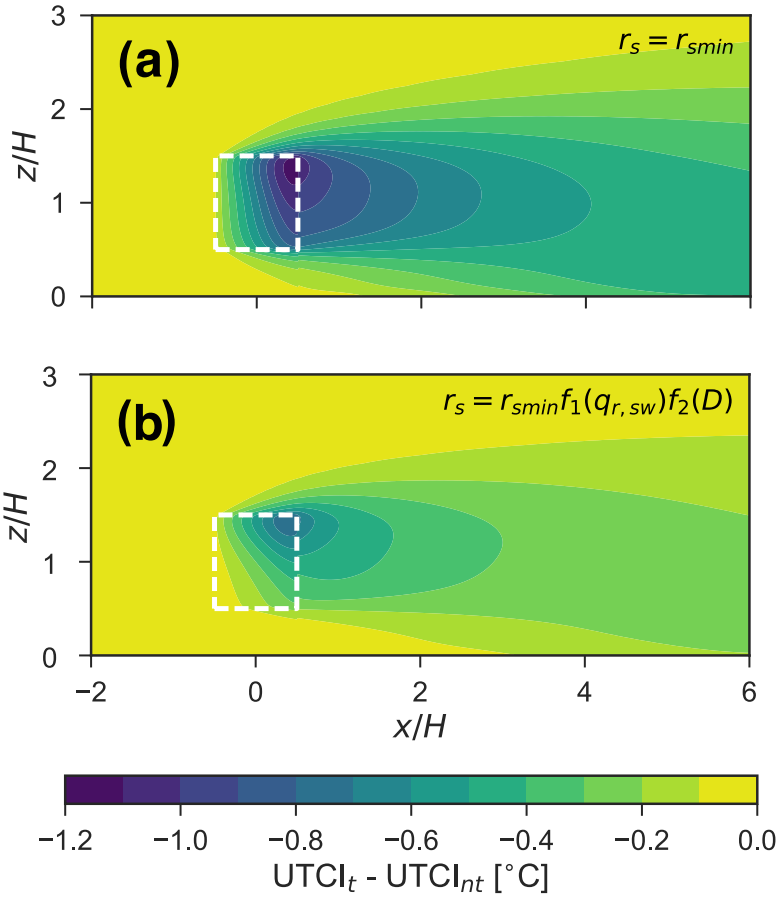


Figure 6.7: UTCI difference between transpiring and non-transpiring conditions, $UTCI_t - UTCI_{nt}$ (°C), for **(a)** constant stomatal resistance and **(b)** varying stomatal resistance.

temperature due to shading is also observed directly below the foliage. In the non-transpiring condition, we see that downstream of the trees, the UTCI increases, especially near the top region of the trees where most solar radiation is absorbed and the air temperature leaving the trees is higher. The absorbed radiation is balanced only with the sensible heat flux. The trees dissipate the energy simply through thermal exchanges leading to an increase in UTCI. Therefore, in an environmental condition such as drought, trees are unable to provide cooling through transpiration. Water availability is a key aspect for trees to form an effective cooling measure in urban areas. This can be challenging for cities as regular irrigation in summer, especially during heat waves, can further exacerbate the water demand and additionally, increase the cost of irrigation.

Fig. 6.6b and Fig. 6.6c show the UTCI during the transpiring condition for fixed and varying stomatal resistances, respectively. We see that, for both cases, transpiration from the trees is beneficial as it reduces the UTCI compared to the non-transpiring condition. Fig. 6.7 shows the difference in UTCI between transpiring and non-transpiring conditions by calculating $UTCI_t - UTCI_{nt}$ (°C). Comparing the fixed and varying stomatal resistance cases, Fig. 6.7a and Fig. 6.7b respectively, we see that the varying stomatal case provides slightly less reduction in UTCI. Referring to the energy balance, and its results on Fig. 6.4, the stomatal resistance is seen to increase towards the bottom of the foliage thereby reducing transpiration and increasing the leaf temperature. The region with the most transpirative cooling is the near-downstream region of the trees. This correlates with the observation of temperature and humidity distribution observed in Fig. 6.5. At higher stomatal resistance, the transpirative cooling is reduced due to the reduced latent heat flux. In the end, we see that the factor most contributing to improve pedestrian comfort is the shadowing provided by the trees, providing much lower UTCI than the transpirative cooling effect.

## 6.8 INFLUENCE OF ENVIRONMENTAL FACTORS

A parametric study is performed on the influence of environmental conditions on the transpirative cooling effect of a single row of trees. The influence of environmental factors, i.e. wind speed $U_{ref}$, air temperature $T$, relative humidity $RH$ and solar radiation $q_{r,sw}$ is

studied by varying them independently Table 6.1. The impact of these environmental factors are determined by studying the energy exchanges at the leaf surface, the air temperature and the UTCI. The air temperature $T$ and the UTCI are evaluated at three distinct locations: *upstream*, *downstream* and in the *shaded* region, as depicted in Fig. 6.1. The upstream region is unaffected by the trees, the downstream region is only affected by the transpiration and, finally, the shaded region shows the influence of shading from sun.

### 6.8.1 *Influence of wind speed*

The wind speed has a direct influence on the convective transfer coefficients at the leaf surface. Due to this, wind speed also has an impact on the cooling effect of the trees. Therefore, the heat exchanges and the resulting cooling of the environment is studied for various wind speeds. The influence of wind speed on the net energy at the leaf is shown in Fig. 6.8a. A negative sensible heat flux indicates that heat is being extracted from the air and, therefore, cooling of the air occurs. The figure shows that the magnitude of the heat fluxes is increasing with wind speed. At high wind speed, the aerodynamic resistance Eq. (5.32) reduces and leads to an increase in CHTC (Eq. (5.31)) and CMTC (Eq. (5.33)). We also observe that, at high wind speeds, the heat fluxes become less sensitive to wind speed. Therefore, it indicates that cooling by the trees becomes less sensitive to wind speed at higher wind speeds due to a power-law like relation of CHTC and wind speed.

[p]

Fig. 6.8b shows the air temperature difference between the inlet and three distinct locations $(T - T_0)$: *upstream*, *downstream* and *shaded*, as depicted in Fig. 6.1. In addition, the air temperature is compared for the transpiring (T) and non-transpiring (NT) conditions, to indicate the influence of transpirative cooling. The upstream region is unaffected by the trees and remains constant for transpiring and non-transpiring conditions. In the shaded region, the transpirative cooling has only a small influence as there is no cold air transported downwards from the trees. For the non-transpiring condition, the air temperature increases slightly at lower wind speeds. For the transpiring condition, the air temperature reduces by 0.4 °C. In the downstream region, the influence of the trees on the air tem-

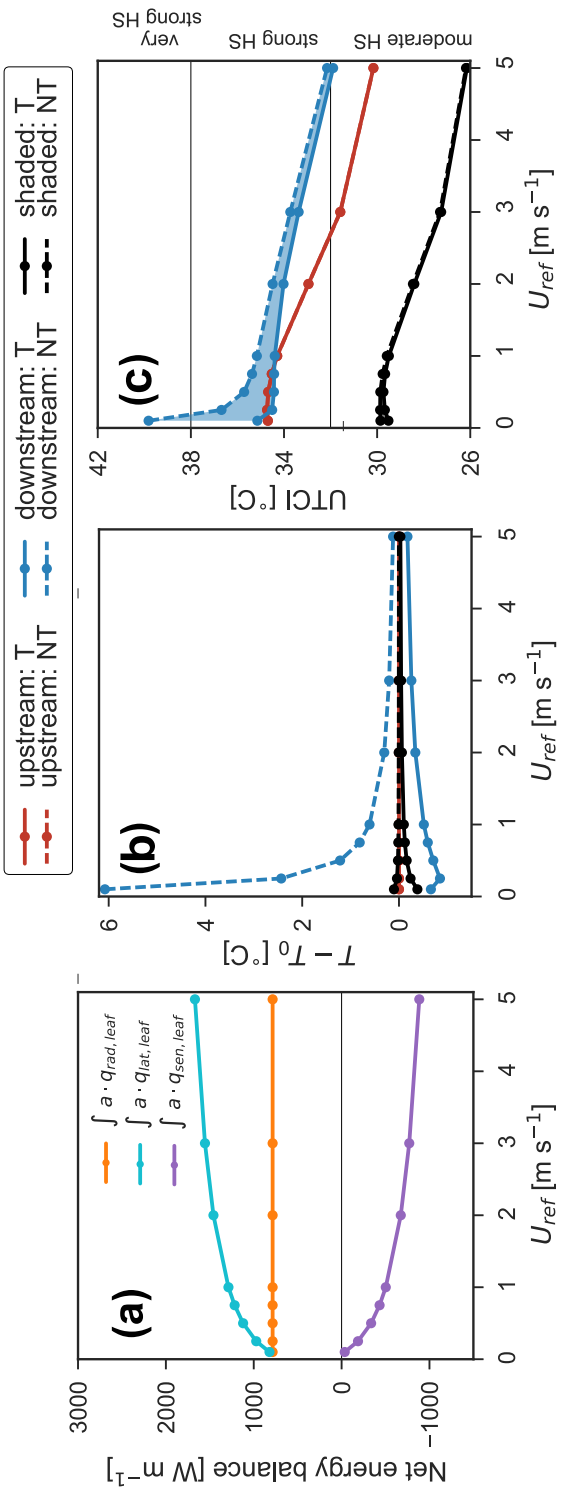


Figure 6.8: Influence of wind speed ($\mathrm{m\,s^{-1}}$) on **(a)** on the net energy balance of radiation, sensible and latent heat fluxes at the trees, $\int a \cdot (q_{rad,leaf} - q_{sen,leaf} - q_{lat,leaf})\ dA = 0$ ($\mathrm{W\,m^{-1}}$), **(b)** on air temperature $T - T_0$ (°C), and **(c)** on *UTCI* (°C). Point measurement of air temperature and *UTCI* at three locations as shown in Fig. 6.1: *upstream* (**red**), *downstream* (**blue**) and *shaded* (**black**) for transpiring (T) (solid, —) and non-transpiring (NT) conditions (dashed, - - -).

perature is clearly visible, with a large increase in air temperature for the non-transpiring condition, up to 6 °C, and a drop in air temperature for the transpiring condition, approximately −0.9 °C at the wind speed of 0.25 m s$^{-1}$. Fig. 6.8b also shows that air cooling downstream of the trees decreases with increasing wind speed. Dimoudi and Nikolopoulou (2003) also provide similar finding in their CFD study of vegetation in urban environment, where the effect of vegetation seems to decrease with increasing wind speed. This occurs as, for higher wind speeds, the trees extract a similar amount of heat per second from a larger air volume, resulting in a smaller overall temperature reduction. At low wind speeds, the heat extraction is done over a small volume or air, i.e., a lower flow rate, providing a larger temperature reduction. Similarly, during non-transpiring conditions, the air temperature substantially increases near the trees, since in this case the radiative heat is not converted into latent heat, but convected as sensible heat into the air domain. Therefore, when the goal is to provide maximum reduction in air temperature in the vicinity of the tree row, lower wind speeds are preferable. As such, at low wind speeds, a local cool region is created around the vegetation. However, at higher wind speeds, the total amount of sensible heat that is extracted from the flow by transpiration is larger. Thus, for global heat island mitigation, high wind speeds are more beneficial, while low wind speeds are favorable to improve the local thermal comfort around a tree.

Fig. 6.8c shows the UTCI in transpiring and non-transpiring conditions. For both conditions, the UTCI reduces with increasing wind speed at all locations, as expected. The upstream probe point shows that high wind speeds result in a reduced UTCI as wind speed has a direct influence on the comfort reducing the heat stress levels. This characteristic is also visible for the downstream and the shaded probe point. However, the shaded probe point is always in a lower HS levels for all wind speeds. This is due to the reduced radiation levels, indicating the importance of shading provided by the trees yielding a $4 - 6$ °C reduction in the UTCI. The impact of transpirative cooling is visible by studying the difference between transpiring and non-transpiring conditions, $UTCI_t - UTCI_{nt}$ (indicated in shaded area). The figure shows that the transpirative cooling provided by the trees, i.e. $UTCI_t - UTCI_{nt}$, only has an impact downstream of the tree row as it is negligible at both upstream and

shaded regions. At low wind speeds, the transpirative cooling is the largest whereas, at higher wind speeds, the impact of transpirative cooling on the UTCI is negligible. This indicates that a pedestrian downstream of a tree row only notices the benefit of transpirative cooling when wind speeds are low. However, vegetation extracts more heat from the environment when wind speeds are higher.

### 6.8.2 *Influence of relative humidity and air temperature*

The vapor pressure varies depending on relative humidity ($RH$) and air temperature $T$. A variation in vapor pressure of the air has a direct influence on the rate of transpiration, since mass flux from leaf surface is driven by the gradient in vapor pressure between the leaf surface and the ambient air (Eq. (5.34)). As a result, RH and ambient air temperature have a direct influence on the cooling power of the tree row. Fig. 6.9a shows the influence of RH and air temperature on the heat exchanges. We observe that, at low RH, the magnitudes of the latent and sensible heat fluxes are high. This indicates high transpiration rate and similarly large cooling, as indicated by the downstream probe point in transpiring conditions, as seen in Fig. 6.9b. However, at high RH, the transpiration is much lower and results in a higher leaf temperature leading to heating of the air. This is due to air vapor pressure approaching saturation resulting in a reduced capacity for air to take up additional humidity from the leaves. At lower air temperature, $T = 20$ °C, the saturation vapor pressure of the air is lower and, therefore, the air has less capacity to take in the humidity from the leaves. With a reduced transpiration rate, the latent heat flux is reduced, leading to higher air temperature (Fig. 6.9b). Thus, we see that the trees provide the maximum cooling during hot dry conditions providing approximately 4.5 times larger air temperature drop (at $T = 30$ °C and $RH = 20$ %) than the colder humid condition (at $T = 20$ °C and $RH = 80$ %).

Fig. 6.9c shows the influence of RH on thermal comfort at $T = 30$ °C. With increasing RH from dry to humid conditions, the UTCI increases. This effect is independent of the trees as RH and temperature play themselves also a direct role on the thermal comfort as high humidity results in lower comfort for a pedestrian. Studying the influence of transpirative cooling, we see that the shaded and upstream locations are unaffected, showing a negligible $UTCI_t -$

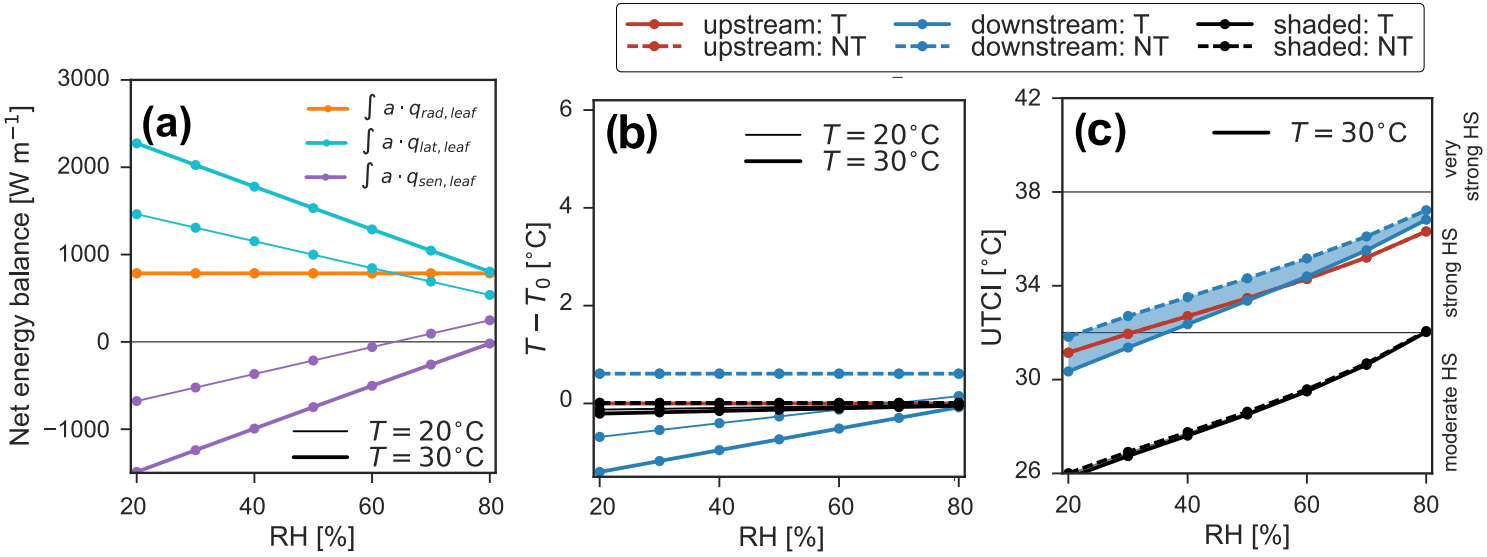


Figure 6.9: Influence of relative humidity $RH$ (%) at air temperature $T = 20$ °C (thin) and $T = 30$ °C (thick) on **(a)** on the net energy balance of radiation, sensible and latent heat fluxes at the trees, $\int a \cdot (q_{rad,leaf} - q_{sen,leaf} - q_{lat,leaf})\, dA = 0$ (W m$^{-1}$), **(b)** on air temperature $T - T_0$ (°C), and **(c)** on $UTCI$ (°C). Point measurement of air temperature and $UTCI$ at three locations as shown in Fig. 6.1: *upstream* (**red**), *downstream* (**blue**) and *shaded* (**black**) for transpiring (T) (solid, —) and non-transpiring (NT) conditions (dashed, - - -).

$UTCI_{nt}$. However, we note that transpirative cooling consistently improves thermal comfort in the downstream region, with a greater influence in the dry condition. At higher RH, even though transpiration reduces the UTCI, the UTCI downstream of the tree row is higher than the upstream region. However, this does not indicate that the presence of trees is detrimental, as the thermal influence of the ground is not modeled in the present study. The trees provide shading to the ground and we recall that the resulting additional cooling due to lower ground temperature is not taken into account in the present study.

### 6.8.3 *Influence of solar radiation intensity*

The net absorbed solar radiation, $\int aq_{rad,leaf}\, dV$, has a direct influence on the transpiration rate from the leaves. Fig. 6.10a shows the influence of solar radiation on the energy balance. The magnitude of the latent heat flux increases with increasing solar radiation. However, we notice that, even though there is a higher transpiration rate from the trees (as CMTC is constant), the sensible heat flux becomes more positive resulting in less cooling, as depicted in Fig. 6.10b. This indicates that, at high solar radiation, the transpiration rate is not sufficiently high to ensure cooler leaves as seen in the low radiation intensity case. Studying the temperature variations in the upstream and the shaded regions, no influence of radiation on transpirative cooling is seen.

Fig. 6.10c shows the influence of solar radiation on thermal comfort. The UTCI in both the downstream region and the upstream regions is almost similar. At both locations, the UTCI increases from moderate HS to strong HS simply due to the higher value of solar radiation. The transpirative cooling effect, indicated by $UTCI_t - UTCI_{nt}$, is nearly constant at all solar radiation levels. Therefore, we see that the transpirative cooling provided by the trees is weakly dependent on the solar radiation. In the shaded region indicated by the black line, the UTCI is much lower and is independent of the solar radiation due to the shadowing effect.

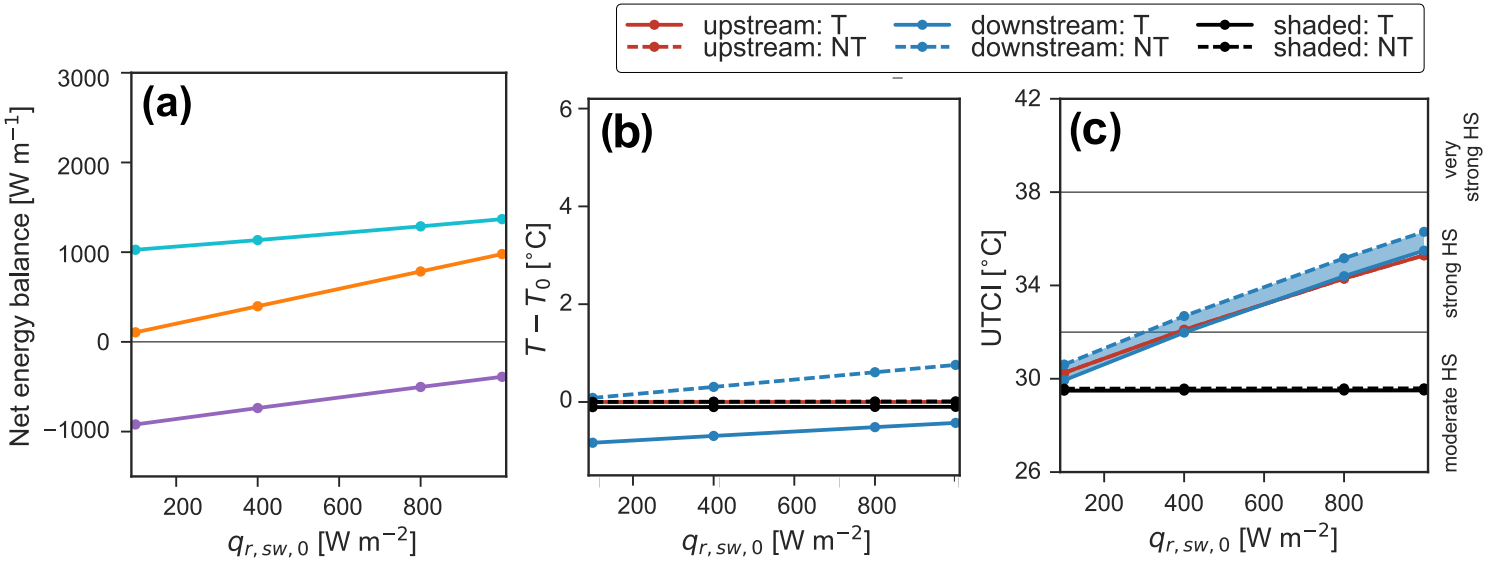


Figure 6.10: Influence of solar radiation $q_{r,sw,o}$ (W m$^{-2}$) on **(a)** on the net energy balance of radiation, sensible and latent heat fluxes at the trees, $\int a \cdot (q_{rad,leaf} - q_{sen,leaf} - q_{lat,leaf})\, dA = 0$ (W m$^{-1}$), **(b)** on air temperature $T - T_0$ (°C), and **(c)** on $UTCI$ (°C). The shaded region shows the difference $UTCI_t - UTCI_{nt}$ (°C). Point measurement of air temperature and $UTCI$ at three locations as shown in Fig. 6.1: *upstream* (**red**), *downstream* (**blue**) and *shaded* (**black**) for transpiring (T) (solid, —) and non-transpiring (NT) conditions (dashed, - - -).

### 6.8.4 *Summary on the impact of environmental factors*

For this case study, the transpirative cooling effect of a single row of trees is highest at lower wind speed when $U < 1\ \mathrm{m\,s^{-1}}$. At higher wind speed, the impact of wind speed on latent and sensible heat fluxes becomes weak and a non-linear dependency is observed for wind speed (Fig. 6.8a). This also results in very small changing air temperature at higher wind speeds (Fig. 6.8b). Changes in relative humidity and solar radiation result in a rather linear change in air temperature. We observe that a pedestrian locally notices the benefit of transpirative cooling when wind speeds are low as indicated by UTCI. However, the trees extract the maximum heat from the environment at high wind speeds. Thus, policies focused on mitigation of the citywide heat island effect should ensure that trees with low blockage effect are planted and in well-ventilated areas. Whereas, policies aimed at creating oasis of cool areas should focus on making dense vegetation areas such as parks that can substantially reduce the wind speed. Furthermore, we also observe that the trees provide the largest cooling effects during hot conditions with low RH. However, to ensure transpirative cooling, the plants need to be well irrigated, which can be difficult in hot and dry cities. Therefore, in such climatic conditions, cities can focus on developing parks and similar dense localized vegetated areas that not only create oases of cool and humid areas but also the irrigation of such areas can be more efficient. Whereas, in humid conditions, the transpirative cooling effect is negligible and the comfort is only improved by the shadowing effect. Therefore, cities with hot and humid conditions should focus on integrating tall-wide canopy trees that can maximize the shadowing effect.

## 6.9 INFLUENCE OF TREE PROPERTIES

The influence of tree properties on the transpirative cooling effect of a tree row is investigated by varying the leaf size $l$, minimum stomatal resistance $r_{s,min}$ and the leaf area density $a$.

### 6.9.1 *Influence of leaf size*

Fig. 6.11a shows the impact of leaf size on the energy balance. The figure shows that the sensible and latent fluxes reduce in strength with increasing leaf size. The behavior is due to inverse relation of CHTC (Eq. (5.31)) and CMTC (Eq. (5.33)) with leaf size. A large leaf size results in reduced heat and mass fluxes from the trees, yielding the reduced cooling seen in Fig. 6.11b. The highest cooling effect is observed when leaf size is small since CHTC and CMTC are then higher, when convective transfer is more efficient. This is also evident from field measurements of forest trees where smaller-leaves species is observed to be cooler(Leuzinger and Körner 2007; Leuzinger et al. 2010). The influence of transpirative cooling is negligible in the upstream and shaded region and the thermal comfort, indicated by UTCI is nearly unaffected by the leaf size, Fig. 6.11c. Even though there is a variation in the air temperature (Fig. 6.11b), the UTCI is relatively unaffected as there is also an increase in humidity downstream of the trees, countering the benefit provided by the reduced air temperature. The use of leaf size in determining CHTC and CMTC shows that a higher developing length, resulting in a larger aerodynamic resistance over the leaf surface, reduces convective exchanges.

### 6.9.2 *Influence of stomatal resistance*

The stomatal resistance has a larger influence on the heat and mass fluxes than the leaf sizes as shown in Fig. 6.12a. As CMTC is inversely dependent on the stomatal resistance, increasing the stomatal resistance causes the transpiration from the leaf to decrease. Less transpiration leads to less heat removal causing an increase of leaf temperature and a reduced cooling effect, as shown in Fig. 6.12b. Therefore, plants with low stomatal resistance such as the impatiens plant or grass can provide more cooling than deciduous plant, for similar leaf sizes and leaf area densities. Fig. 6.12c shows that stomatal resistance has a weak influence on the UTCI. As seen with leaf size, a stomatal resistance variation results in a negligible change in UTCI downstream of the trees as the lower air temperature is counter-balanced with higher air humidity. However comparing the transpiring and non-transpiring cases, we see that transpiration still

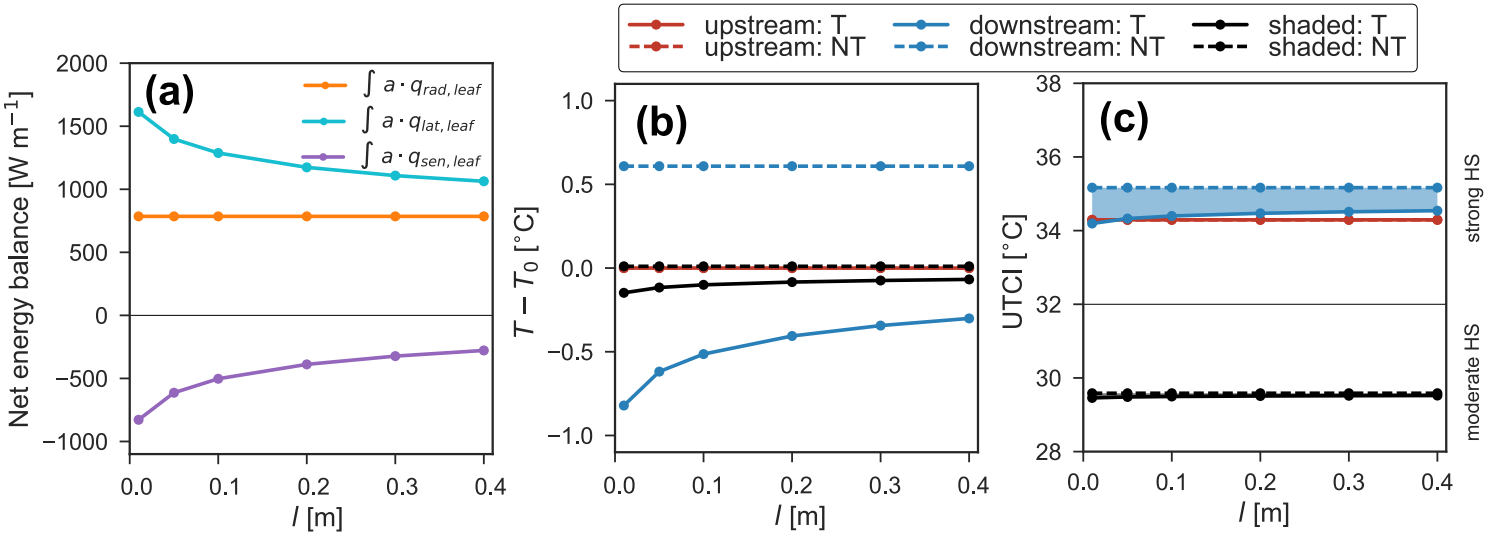


Figure 6.11: Influence of leaf size $l$ (m) **(a)** on the net energy balance of radiation, sensible and latent heat fluxes at the trees, $\int a \cdot (q_{rad,leaf} - q_{sen,leaf} - q_{lat,leaf})\, dA = 0$ W m$^{-1}$, **(b)** on air temperature $T - T_0$ (°C), and **(c)** *UTCI* (°C). Point measurement of air temperature and *UTCI* at three locations as shown in Fig. 6.1: *upstream* (**red**), *downstream* (**blue**) and *shaded* (**black**) for transpiring (T) (solid, —) and non-transpiring (NT) conditions (dashed, - - -).

provides an improvement in thermal comfort showing a positive difference $UTCI_t - UTCI_{nt}$, Fig. 6.12c.

### 6.9.3 *Influence of leaf area density*

Fig. 6.13a shows that, when leaf area density is low, the net radiation absorbed by vegetation is lower due to the lack of leaf surfaces to absorb the radiation, which means more solar radiation can passes through the vegetation. Fig. 6.13c shows that there is a decrease in the UTCI in the shaded region with higher leaf density, which increases shading of solar radiation. In the case of low leaf area density, more leaf surfaces are exposed to a higher solar radiation over the whole volume of vegetation, resulting in higher air temperature while the transpiration rate is not sufficient to cool the leaves, Fig. 6.13b. Hiraoka (2005) also observes that, for a single tree with leaf area density $a = 1$, at environmental condition of $T = 30$ °C and $RH = 80$ %, sensible heat is added to the air domain. However, with a higher leaf area density, more solar radiation is absorbed at the top of the vegetation, shading the lower regions from the solar radiation. This is beneficial as leaf surfaces at lower regions are then able to dissipate the absorbed solar radiation through transpiration and to cool the air. Therefore, the leaf area density should be sufficiently high such that solar radiation is mostly absorbed at the top of the vegetation volume.

### 6.9.4 *Summary on the influence of tree properties*

The study on the influence of tree properties on the net energy balance shows that both leaf size and stomatal resistance have a nonlinear effect. Both leaf size and stomatal resistance influence the convective heat and mass transfer coefficients at the surface of leaves. Plants with larger leaves provide less cooling effect than plant with small leaves, Fig. 6.12a. We also observe that, to provide the highest cooling, the stomatal resistance should be low such that transpiration rate is high. However, higher rate of transpiration results also in increased humidity in the air and counters the thermal comfort provided by reduced air temperature. The study on the impact of leaf area density shows that leaf area density should be sufficiently high

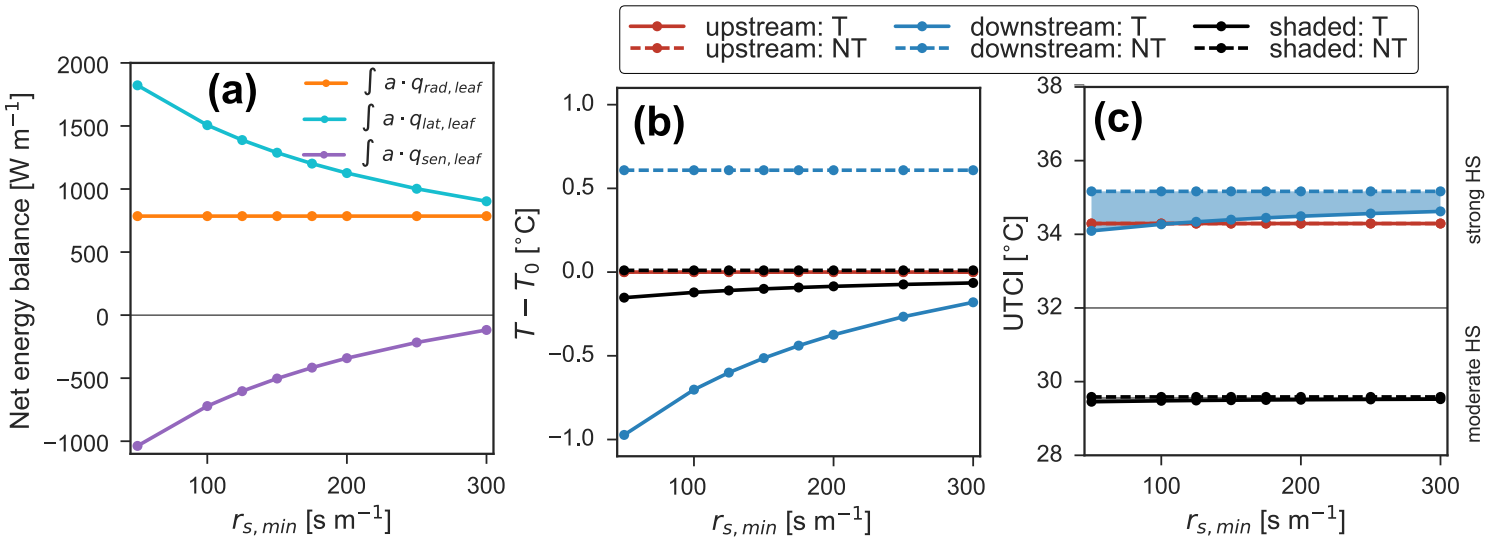


Figure 6.12: Influence of stomatal resistance $r_{s,min}$ (s m$^{-1}$) on **(a)** the net energy balance of radiation, sensible and latent heat fluxes at the trees, $\int a \cdot (q_{rad,leaf} - q_{sen,leaf} - q_{lat,leaf})\ dA = 0$ W m$^{-1}$, **(b)** on air temperature $T - T_0$ (°C), and **(c)** *UTCI* (°C). Point measurement of air temperature and *UTCI* at three locations as shown in Fig. 6.1: *upstream* (**red**), *downstream* (**blue**) and *shaded* (**black**) for transpiring (T) (solid, —) and non-transpiring (NT) conditions (dashed, - - -).

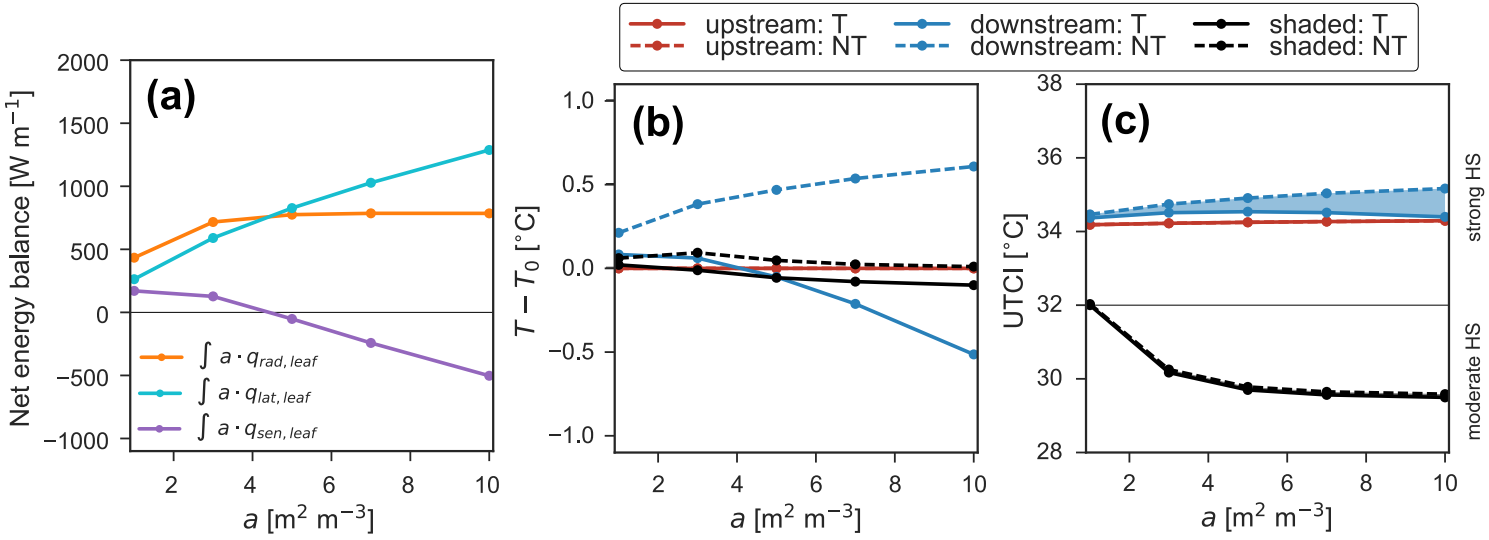


Figure 6.13: Influence of leaf area density $a$ (m$^2$ m$^{-3}$) on **(a)** the net energy balance of radiation, sensible and latent heat fluxes at the trees, $\int a \cdot (q_{rad,leaf} - q_{sen,leaf} - q_{lat,leaf})\, dA = 0$ W m$^{-1}$, **(b)** on air temperature $T - T_0$ (°C), and **(c)** *UTCI* (°C). Point measurement of air temperature and *UTCI* at three locations as shown in Fig. 6.1: *upstream* (**red**), *downstream* (**blue**) and *shaded* (**black**) for transpiring (T) (solid, —) and non-transpiring (NT) conditions (dashed, - - -).

such that solar radiation is mostly absorbed at the top of the vegetation volume. Therefore, the lower part of the volume is shaded and can provide cooling to the air. A similar observation is found in the field measurements of rooftop gardens in Singapore where thicker foliated plants are shown to provide more cooling (Wong et al. 2003). The cooling provided by the single row of trees is seen to grow almost linearly with leaf area density providing a much higher temperature drop at $a = 10$ m$^2$ m$^{-3}$ compared to a weakly foliated tree row of $a = 1$ m$^2$ m$^{-3}$. Therefore, cities focused on mitigating UHI through shading of vegetation should ensure that the trees are sufficiently foliated to reduce the transmission of short-wave radiation through vegetation.

## 6.10 INFLUENCE OF VEGETATION SIZE

Finally we investigate how vegetation size influences the transpirative cooling effect. The size of vegetation in the domain can be described in terms of its length, i.e. number of tree rows $n$, or the height of the trees $n\,H$ as shown in Fig. 6.14. The impact of the tree height on the air temperature is determined by probing the *upstream* region $(x = -H, y = H)$, the *shaded* region $(x = 0, y = H/4)$ and the *downstream* region $(x = H, y = H)$ at fixed heights. The probe locations have fixed heights as they represent a reference pedestrian standing next to trees with varying heights. The impact of number of tree rows on the air temperature is determined for three positions: *upstream* $(x = -H, y = H)$, *shaded* $(x = 0, y = H/4)$ and downstream region $(x = nH + H, y = H)$. The downstream probe point is located at distance $H$ away from the last downwind tree row.

### 6.10.1 *Influence of number of tree rows*

A study on the influence of the number of tree rows provides an understanding on how increasing vegetation along the downstream direction has an effect on the overall cooling of the environment. Fig. 6.15a shows the influence of number of tree rows on the net energy balance. The net absorbed radiation is linearly increasing with number of tree rows. The latent heat flux increases as well

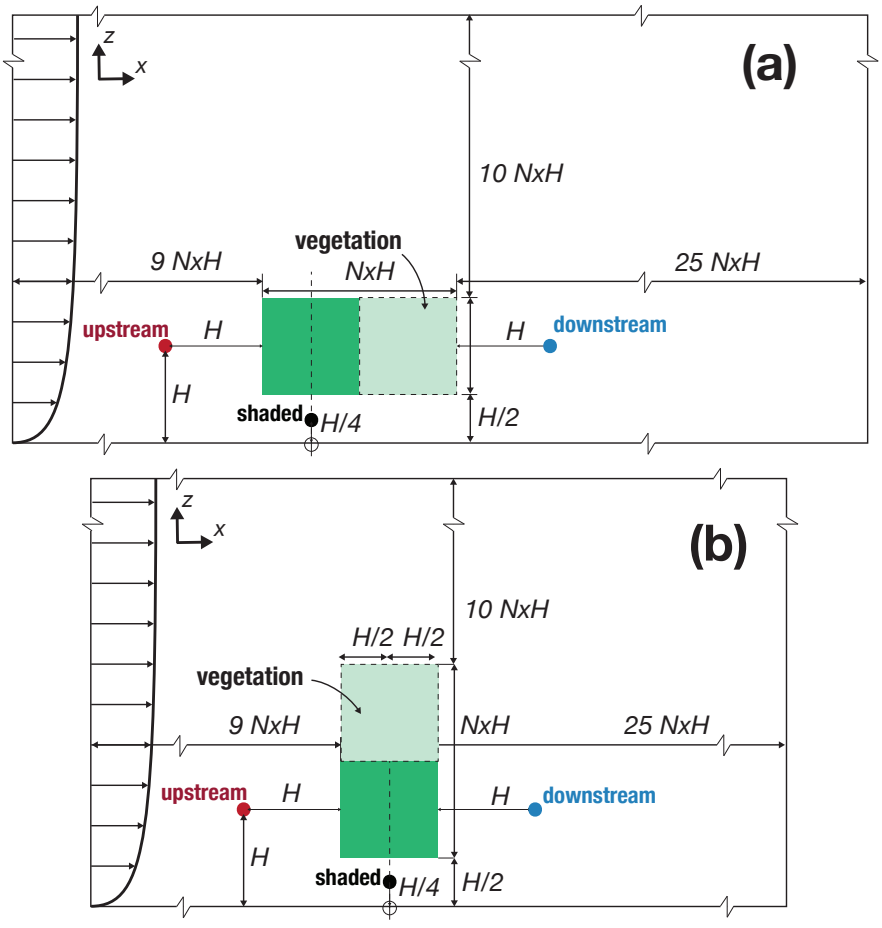


Figure 6.14: Simulation domain for the study on the size of vegetation, where vegetation region is indicated in green (■), **(a)** study on the number of tree rows $n = [1, 2, 5, 10]$, and **(b)** study on the tree height $n\,H$ with $n = [1, 2, 3, 5, 10]$. The sample points at three locations: *upstream* (**red**), *downstream* (**blue**) and *shaded* (**black**).

whereas the sensible heat flux approaches zero. Despite an increase in net transpiration, the cooling reduces. Since each additional tree row results in a lower wind speed due to the increased momentum drag, the lower CHTC and CMTC result in a reduction of transpiration and a reduced cooling of the air downstream of the tree row Fig. 6.15b. When the trees does not transpire, an increase in the number of tree rows causes more heating of the flow. Reversely, transpiration ensures that the air domain is cooled regardless of the number of tree rows. The study of the impact of number of tree rows on the thermal comfort Fig. 6.15c shows that there is large change in the thermal comfort comparing transpiring and non-transpiring conditions. The transpirative cooling provided by the trees regulates the thermal comfort downstream of the tree row. The absence of transpiration yields growing deterioration of the thermal comfort with an increasing number of tree rows. Thus, the transpirative cooling effect plays a critical role when increasing the number of tree rows in the domain.

### 6.10.2 *Influence of tree height*

Fig. 6.16a shows the influence of tree height on the net energy balance. The solar radiation absorbed by the trees does not change with increasing height as the top of the trees has absorbed all the incident solar radiation independently from tree height. However, the magnitudes of latent and sensible heat fluxes increase linearly with tree height as there is a linear increase of leaf surfaces, thus in transpirative cooling effect. Fig. 6.16b shows that the cooling of the air at the downstream location converges to $-1$ °C in the transpiring condition and, for the non-transpiring condition, the temperature change approaches zero. This occurs because the top of the trees, which is hotter, is further away from the pedestrian level. Therefore, at the lower regions of the trees, the magnitude of the sensible heat flux remains uniform in height, providing equal change in air temperature. This is also evident from observing the thermal comfort, Fig. 6.16c. The UTCI does not vary after the trees are higher than 3 m. The shaded region can be assumed to be unaffected by the change in tree height as indicated by a negligible temperature change, Fig. 6.16b, and a negligible UTCI change, Fig. 6.16c.

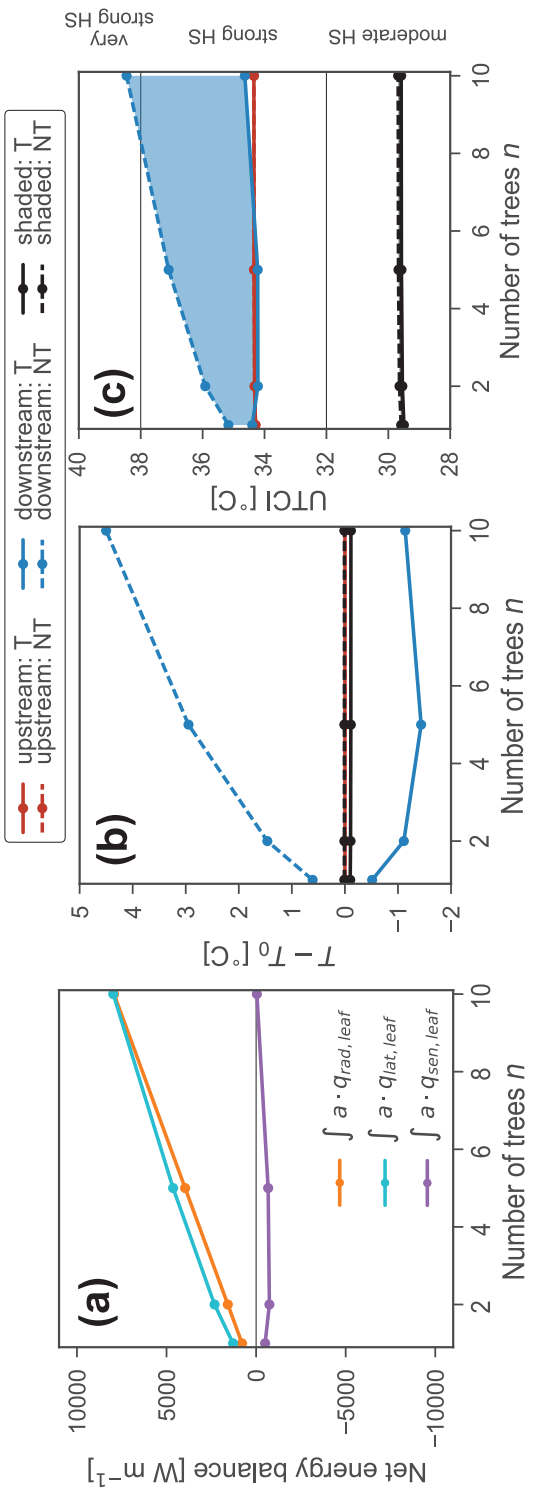


Figure 6.15: Influence of number of tree rows $n$ on **(a)** the net energy balance of radiation, sensible and latent heat fluxes at the trees, $\int a \cdot (q_{rad,leaf} - q_{sen,leaf} - q_{lat,leaf})\ dA = 0$ W m$^{-1}$, **(b)** on air temperature $T - T_0$ (°C), and **(c)** *UTCI* (°C). Point measurement of air temperature and *UTCI* at three locations as shown in Fig. 6.14: *upstream* (**red**), *downstream* (**blue**) and *shaded* (**black**) for transpiring (T) (solid, —) and non-transpiring (NT) conditions (dashed, - - -).

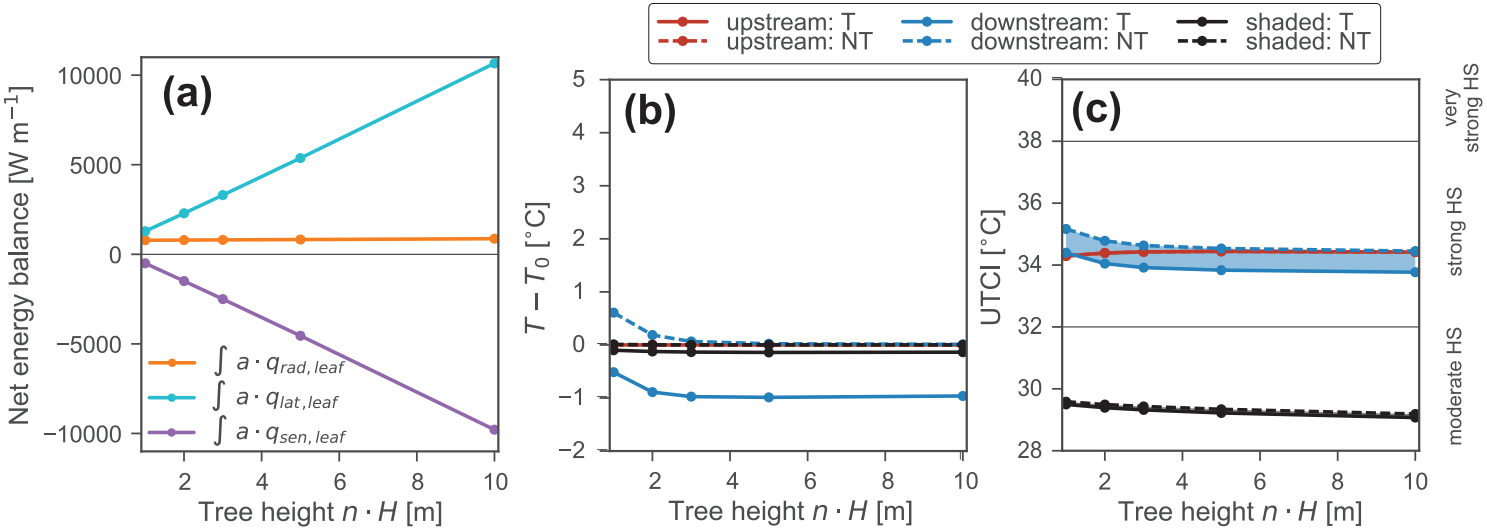


Figure 6.16: Influence of tree height $n\,H$ (m) on **(a)** the net energy balance of radiation, sensible and latent heat fluxes at the trees, $\int a \cdot (q_{rad,leaf} - q_{sen,leaf} - q_{lat,leaf})\ dA = 0$ W m$^{-1}$, **(b)** on air temperature $T - T_0$ (°C), and **(c)** *UTCI* (°C). Point measurement of air temperature and *UTCI* at three locations as shown in Fig. 6.14: *upstream* (**red**), *downstream* (**blue**) and *shaded* (**black**) for transpiring (T) (solid, —) and non-transpiring (NT) conditions (dashed, - - -).

### 6.10.3 *Summary on the influence of vegetation size*

The study on the influence of vegetation size is performed by varying the tree height and the number of tree rows. An increase in the number of tree rows has an influence on the CHTC and the CMTC due to the reduction in wind speed. A reduced wind speed results in a lower transpiration leading to a reduced transpirative cooling effect of the air at the downstream location. However, overall more sensible heat is extracted with increasing vegetation volume. A study on the influence of tree height shows that the top of the trees, which is hotter and is far high enough from the ground, the thermal comfort at pedestrian level is higher. This indicates that ideally, cities should focus on implementing a combination of tall wide-canopy trees and dense foliated pedestrian-level trees to maximize the cooling from shading. The tall wide-canopy trees can provide shading to the building surfaces, and the warmer leaves are also further away from the pedestrian level to not have a negative influence on the thermal comfort. Furthermore, the densely foliated pedestrian-level trees can provide transpirative cooling and generate cool oasis at the ground level. However, one must note that, high vegetation density can negatively impact the ventilation potential due to wind. Therefore, ideal vegetation density must be compromise between thermal comfort and ventilation needs at pedestrian level.

## 6.11 CONCLUSION

In this study, we investigated the influence of environmental factors, tree properties and size on the transpirative cooling effect of a single row of trees. A 2D computational fluid dynamics (CFD) model is used for modelling the flow in the air domain and through the vegetation. Vegetation is modeled as a porous medium where the heat exchange is solved using a leaf energy balance model. The long-wave radiative transfer between vegetation and the environment is empirically modeled. The vegetation model is compared with the numerical study and validated against the experiment study of Kichah et al. (2012). Thereafter, a parametric study is performed to determine the transpirative cooling effect of vegetation at noon with a solar al-

titude of 90°. The following conclusions were determined from the parametric study:

1. The transpirative cooling effect of a single row of trees is highest at lower wind speed when $U < 1\ \mathrm{m\,s^{-1}}$.

2. A pedestrian perceives transpirative cooling mainly when wind speeds are low, as indicated by the UTCI showing a cool zone locally around the trees. However, trees extract more sensible heat from the flow by transpiration when wind speeds are higher.

3. The transpirative cooling effect of a row of trees is diminished in humid and low temperature conditions, where the vapor pressure of air is closer to saturation and the transpiration from vegetation diminishes. Cities in such climatic condition should develop mitigation strategies focusing on cooling by shading and less on maximizing transpirative cooling.

4. Solar radiation has a large influence on the thermal comfort and, in all cases, the comfort level below the trees is substantially higher than downstream of the tree row due to shadowing effects. The additional benefit of transpirative cooling is smaller, since solar radiation is found to be the dominant factor in the thermal comfort.

5. The tree properties, leaf size $l$ and minimum stomatal resistance $r_{s,min}$, have a small influence on the transpirative cooling effect of vegetation, compared to the environmental factors such as wind speed, temperature and relative humidity.

6. The transpirative cooling effect of vegetation depends on its leaf area density due to the coupled effect on both wind speed and air temperature.

7. An increase in vegetation height is beneficial as the top of the trees with higher leaf temperatures is further away from the pedestrian level. This ensures that the transpirative cooling effect is high at the pedestrian level.

8. If vegetation does not transpire, increasing the number of tree rows result in an increase in air temperature and UTCI downstream of the vegetation.

9. In general, cities should use a combination of tall wide-canopy trees, that can provide shading to urban surfaces, and pedestrian-level trees, that can provide transpirative cooling near the ground. Such combination can maximize the cooling through shading and transpiration.

10. To improve the UHI, it is best achieved by maximizing the sensible heat extraction. We observed that increasing the vegetation density and tree height strongly correlated with an increase in sensible heat extraction and a reduction in the air temperature. Thus, increasing vegetation in cities is seen to be best strategy to improve the global UHI.

Future studies will consider the long-radiative exchanges between terrestrial objects and varying solar altitude. Chapter 8 focuses on the influence of vegetation in built environment and the influence of diurnaly varying solar altitude and intensity. This enables to study the influence of vegetation in urban areas and understand the thermal role of the ground and buildings on the transpirative cooling effect of vegetation. Furthermore, the influence of water availability at the roots on the transpiration rate and the impact on transpirative cooling effect will be studied.

# 7

# COMPARISON STUDY OF CFD MODEL AND WIND TUNNEL MEASUREMENT

## 7.1 INTRODUCTION

In this chapter, we compare the numerical method described in Chapter 6 with the measurements of Chapter 4. The measurements were performed for a small *Buxus sempervirens* plant. The measurements consisted of: i) X-ray tomography measuring plant microstructure metrics such as net leaf area and leaf area density, ii) stereoscopic particle image velocimetry (SPIV) measuring the wake flow characteristics such as mean velocity and turbulence kinetic energy (TKE), iii) infrared thermography measuring the spatiotemporal leaf temperature profile, and iv) hygrothermal in-foliage measurement probes measuring the vertical distribution of relative humidity (RH) and air temperature. Therefore, the goal of the present study is to compare the numerical simulation of the Buxus plant setup using the porous medium approach detailed in this thesis and compare with the high-resolution dataset to quantify the discrepancies. The present study aims at providing insight into the feasibility of employing such numerical techniques and possible limitations.

The fully-coupled numerical model described in Chapter 5 is not used in this chapter for the comparison with the wind tunnel measurement. This is mainly because the measurement campaign detailed in Chapter 4, although providing a high-quality measurement dataset of the air domain, still lacks necessary input parameters of the plant physiology such as $CO_2$ flux, stomatal conductance, xylem conductance, rhizosphere conductance, and the soil composition. It is recommended that to validate the full model, a more exhaustive measurement campaign should be designed measurements of air domain, soil domain, and plant physiology. Even with this limita-

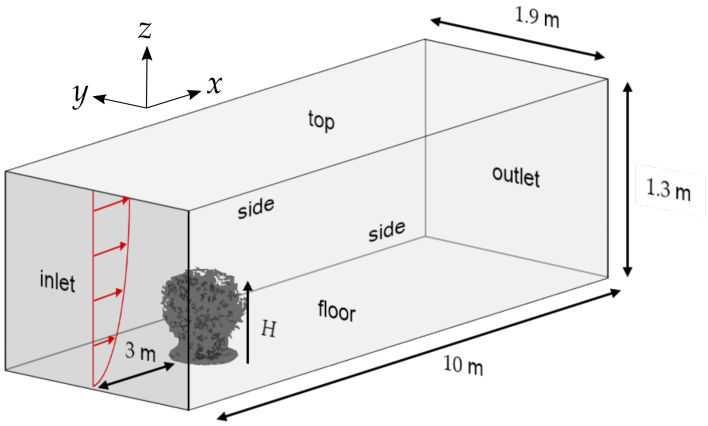


Figure 7.1: Numerical domain used for the wind-tunnel-CFD comparison study with plant-canopy height $H = 0.21$ m (not to scale).

tion, the partial vegetation model,i.e., the air domain can be cross-examined with a real setup. Finally, we must note that as we use the simplified stomatal model described in Chapter 6 in this chapter, hysteresis as observed in Chapter 4 cannot be modeled. This is because the stomatal resistance is only dependent on the atmospheric condition and not on the soil moisture content.

## 7.2 SIMULATION DOMAIN AND BOUNDARY CONDITION

The simulation setup consisting of the numerical domain and its boundary conditions are that of the wind tunnel experiment with wind tunnel set wind speed $U_{ref} = 1\ \mathrm{m\,s^{-1}}$. The reference velocity used for the study is the plant-canopy height velocity $U_h = 0.77\ \mathrm{m\,s^{-1}}$ at $H = 0.21$ m.

### 7.2.1 *Numerical domain*

The numerical domain is based on the geometry of the wind tunnel test-section with a wind tunnel height $H = 1.3$ m and a lateral dimension $W = 1.9$ m, as depicted in Fig. 7.1. The upstream and downstream dimensions are chosen based on CFD best practices (Blocken 2015; Franke et al. 2007; Tominaga et al. 2008). The inlet

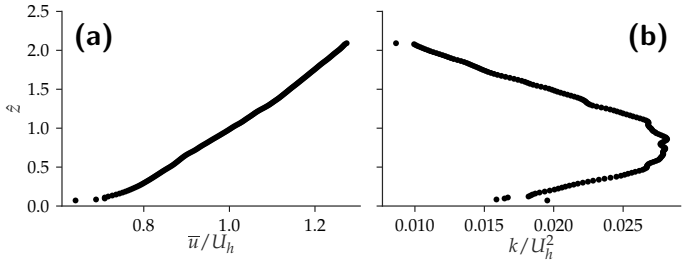


Figure 7.2: Vertical profiles of incoming normalized **(a)** mean stream-wise velocity $\overline{u}/U_h$ and **(b)** turbulent kinetic energy $k/U_h^2$ , obtained from PIV measurements.

is located $15H$ upstream from the plant, and the outlet is located at $32H$ downstream from the plant, well above the recommended values of best practice guidelines. Thus, the downstream fetch of the numerical domain after the plant ensures a developed flow at the outlet of the numerical domain. Furthermore, the numerical scheme is also chosen to satisfy the best practice guidelines (see Section 7.2.4). The numerical domain is discretized into 413 820 hexahedral cells with minimum cell size of $7.81 \times 10^{-6}$ m$^{-3}$ (near the plant is present with a regular hexahedron) and a maximum cell size of $2.2 \times 10^{-3}$ m$^{-3}$ at the top-outlet region. A grid refinement study was used to determine sufficient mesh resolution. The ground and lateral boundary $y^+$ are determined to be 37.9 and 83.8, respectively, satisfying the requirement for a valid wall function (Franke et al. 2007).

### 7.2.2 *Boundary conditions*

Fig. 7.2 shows the inlet boundary condition of mean velocity $\overline{u}$ (m s$^{-1}$) and the turbulent kinetic energy $k$ obtained from the wind tunnel experiment, normalized with $U_h = 0.77$ m s$^{-1}$. The turbulent dis-

sipation rate $\varepsilon$ is obtained through the atmospheric boundary layer (ABL) profile equations (Richards and Hoxey 1993):

$$\overline{u}(z) = \frac{u_*}{\kappa} \ln\left(\frac{z + z_0}{z_0}\right) \tag{7.1}$$

$$k = \frac{{u_*}^2}{\sqrt{C_\mu}} \tag{7.2}$$

$$\varepsilon = \frac{u_*^3}{\kappa\,(z + z_0)} \tag{7.3}$$

where $\overline{u}(z)$ (m s$^{-1}$) is the mean horizontal velocity, $u_* = 5.053 \times 10^{-2}$ m s$^{-1}$ is the friction velocity, $\kappa = 0.41$ is von Kármán constant, $z_0 = 1.335 \times 10^{-3}$ m is the aerodynamic roughness length and $C_\mu = 0.09$. The inlet turbulent intensity is $I = \sqrt{2/3\,k}/U_{ref} = 12.1\%$. The roughness length $z_0$ and the friction velocity $u_*$ is obtained using curve-fit of the measured PIV profile. The outlet boundary condition is defined as pressure outlet with a static pressure $p = 0$. A zero-gradient boundary condition is enforced for $\boldsymbol{u}$, $k$, and $\varepsilon$. The remaining boundaries (i.e., top-wall and side-walls) are modeled as no-slip wall-boundary and with standard wall functions.

### 7.2.3 *Vegetation: Leaf area density*

The vegetation is modeled as a porous medium parameterized using a leaf area density $a$ (m$^2$ m$^{-3}$) distribution and a constant leaf drag coefficient $c_d$. For a detailed description, see Section 5.2. The source terms for momentum $\boldsymbol{s}_u$ (N m$^{-3}$) , turbulence kinetic energy $s_k$ (W m$^{-3}$), and the turbulence dissipation rate $s_\varepsilon$ (W m$^{-3}$ s$^{-1}$) are given as (Katul et al. 2004; Kenjereš and ter Kuile 2013; Sanz 2003):

$$\boldsymbol{s}_u = -\rho c_d a\,|\overline{\boldsymbol{u}}|\,\overline{\boldsymbol{u}} \tag{7.4}$$

$$s_k = \rho c_d a\left(\beta_p\,|\overline{\boldsymbol{u}}|^3 - \beta_d\,|\overline{\boldsymbol{u}}|\,k\right) \tag{7.5}$$

$$s_\varepsilon = \rho c_d a\left(\beta_p C_{4\varepsilon}|\overline{\boldsymbol{u}}|^3\frac{\varepsilon}{k} - \beta_d C_{5\varepsilon}\,|\overline{\boldsymbol{u}}|\,\varepsilon\right) \tag{7.6}$$

where $c_d$ is the leaf drag coefficient (Wilson and Shaw 1977) and experimental measurements suggesting that $c_d \in [0.2, 0.5]$ (Vogel 1989). The closure coefficients $C_{4\varepsilon} = 0.9$ and $C_{5\varepsilon} = 0.9$ are obtained from literature (Katul et al. 2004; Kenjereš and ter Kuile 2013; Sanz 2003).

The coefficients $\beta_p = 1.0$ and $\beta_d = 5.1$ are energy conversion ratio from MKE to TKE and TKE to heat, respectively. These parameters are dependent on the specific plant type and plant sample and would ideally require calibration. An insight to this is given in Section 7.3.3.

In this study, the X-ray tomography measured is used to determine the leaf area density $a$ distribution. Thereafter, the values are interpolated onto the numerical domain. A simple tri-linear interpolation scheme is employed to interpolate onto the finite volume cells. The leaf area density $a$ ($m^2\,m^{-3}$) is defined as the one-sided leaf surface area in a given volume and quantifies the spatial distribution of the vegetation in the environment. In our study, we determine the leaf area density $a$ using the porosity distribution measured in Chapter 4:

$$a = \frac{1}{2} A_l \frac{1-\phi}{\int 1-\phi \, \mathrm{d}V} \tag{7.7}$$

where $A_l$ ($m^2$) is the net plant leaf area (both sides of the leaves) and $\phi$ is the plant porosity. The leaf drag coefficient of $c_d = 0.5$ is chosen after the sensitivity study in Section 7.3.1. It is seen to provide the closest prediction with the experimental measurements.

### 7.2.4 *Numerical solution*

The problem is solved using the SIMPLE pressure-velocity coupling algorithm, obtaining a steady-state solution. The gradient terms are discretized using Gauss integration and interpolated using second-order central differencing scheme (`linear`). Similarly, the divergence terms are interpolated using a second-order linear upwind differencing scheme (`linearUpwind`). The pressure is solved using geometric-algebraic multi-grid (GAMG) solver and preconditioned with diagonal incomplete-Cholesky (DIG) smoother, whereas velocity is solved using Preconditioned bi-conjugate gradient (PBiCG) solver with diagonal incomplete-LU (DILU) preconditioner. The matrix solvers are iteratively solved until the scaled residuals of pressure are below $1 \times 10^{-5}$ and below $1 \times 10^{-6}$ for all the other variables. Furthermore, under-relaxation factors are used with $\alpha_p = 0.3$ for pressure, $\alpha_u = 0.7$ for velocity (ensuring $\alpha_p + \alpha_u = 1$) and $\alpha_k = \alpha_\varepsilon = 0.5$. The

Table 7.1: An overview of parameters varied in the sensitivity study along with the reference condition.

| Parameter | reference | sensitivity study |
|---|---|---|
| drag coefficient $c_d$ | 0.5 | $[0.2, 0.3, 0.4, 0.5, 0.6]$ |
| leaf area density $a$ | varying | constant vs. varying |
| turbulence model | por. real. $k-\varepsilon$ | [$k-\varepsilon$, real. $k-\varepsilon$, por. $k-\varepsilon$, por. real. $k-\varepsilon$] |

under-relaxation factors are modified to $\alpha_p = 0.7$ and $\alpha_u = 0.3$ when solving for non-isothermal case to ensure stable convergence.

## 7.3 FLOW FIELD

In this section, the influence of the leaf area density distribution, plant drag coefficient, and the turbulence model is investigated. A preliminary assessment of the discrepancy between CFD and wind tunnel results is performed by comparing the mean velocity and TKE of the plant wake. Thereafter, the microclimate inside the plant is investigated by comparing the vertical profile of the air temperature and relative humidity for both the daytime and nighttime conditions (see Section 7.4). A summary of parameters varied for the sensitivity study is given in Table 7.1. The reference case values for drag coefficient, leaf area density distribution, and the turbulence model also indicated in Table 7.1.

Fig. 7.3 shows the stream-wise velocity $\overline{u}/U_H$ and TKE $k/U_H^2$ around (and within) the plant. The leaf area density is depicted using the iso-contour lines of $a = [20, 40, 60, 80, 100, 120, 140]$ $\mathrm{m^2\,m^{-3}}$ determined using Eq. (7.7). It is seen to vary in space with peak density located approximately in the middle of the plant ($\hat{x} = -0.5$, $\hat{z} = 0.5$). The velocity field is plotted together with the streamlines (Fig. 7.3a). The near-wake of the plant is consists of recirculation zone below $\hat{z} = 0.5$, indicated by negative stream-wise velocity. The highest TKE is observed at the plant-canopy height $\hat{z} = 1$, with peak TKE at approximately $\hat{x} = 1$. Therefore, the wake turbulence

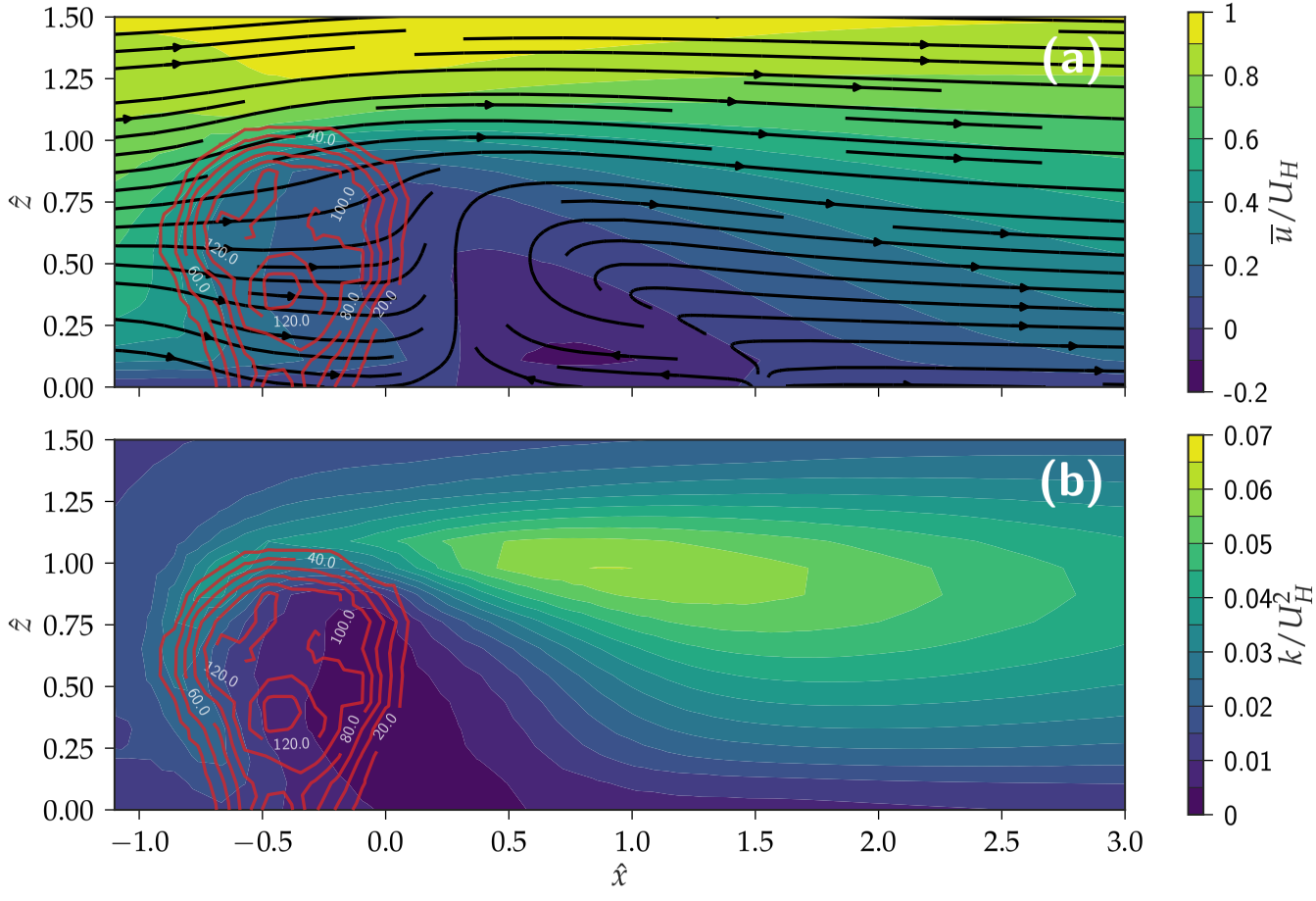


Figure 7.3: Vertical plane at the center-line (i.e., at $\hat{y} = 0$) from numerical simulation: **(a)** normalized streamwise velocity $\overline{u}/U_H$ and **(b)** normalized turbulent kinetic energy $k/U_H^2$ around the plant. The heterogeneous leaf area density $a$ is indicated with red iso-contour lines of $a = [20, 40, 60, 80, 100, 120, 140]$ $\mathrm{m^2\,m^{-3}}$ and the drag coefficient is $c_d = 0.5$.

is seen to dominantly affected by the shear-zone generated by the plant canopy.

Fig. 7.4 show the normalized mean velocity magnitude at 8 horizontal planes where the PIV measurement were obtained in Chapter 4 as shown in Fig. 4.10. Additionally, the velocity field is plotted together with the streamlines. Comparing with experimental data, we see that both the numerical model and experiment measurement shows a recirculation zone behind the tree at $\hat{z} = [0.29, 0.43]$. However, at $\hat{z} = 0.57$ and $\hat{z} = 0.71$, the numerical prediction deviates from the experimental observations. The complex streamlines as observed from experimental data are not present in the numerical simulation but instead show more of a bleed type of flow. Furthermore, the velocity deficit predicted by the simulation at $\hat{z} \leq 1$ is slightly lower than in the experimental observation. This minor discrepancy can be attributed to the plant foliage is represented in the simulation. We have employed a porous media approach, where instead of directly representing the topology of the plant, we have parameterized it using leaf area density. Essentially, a spatial low pass filter has been applied to the plant topology and is represented by a density function. Such representation is known to comprise the prediction of spatial variability of the wake velocity statistics (Endalew et al. 2009).

A preliminary comparison of the numerical prediction and the experimental measurement is performed by comparing the stream-wise velocity and the TKE at $\hat{x} = [0.4, 0.6, 0.8, 1.0, 1.2, 1.4, 1.6]$. Fig. 7.5 shows the vertical profiles at these seven locations, where the lateral position is at the plant center-line (i.e., $\hat{y} = 0$). The comparison shows a reasonable prediction of the near-wake statistics of the plant. The prediction especially demonstrates a good prediction of the magnitude and the gradient of the stream-wise velocity. However, the largest discrepancy is for the vertical velocity $\overline{w}$, very close to the tree $\hat{x} < 0.6$. The numerical model predicts a large updraft near the ground and under-predicts the downdraft downstream of the plant. Similarly, very close to the tree, $\hat{x} < 0.6$, the deficit in the velocity is seen to be under-predicted. The TKE shows a good comparison as well with an accurate prediction of the peak TKE at the plant-canopy shear-layer. However, as with the stream-wise velocity, very close to the tree, there is a slight overestimation. Furthermore, the variation over height is seen to less apparent than the

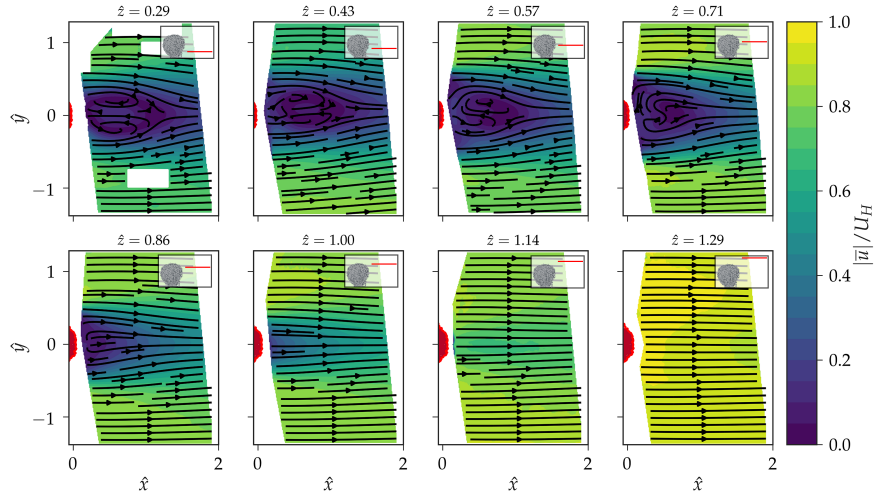


(a) PIV measurement

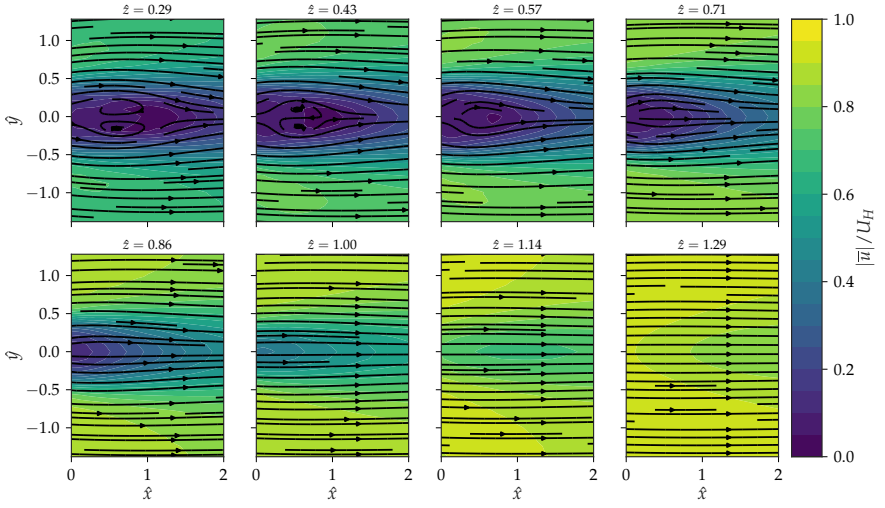


(b) CFD simulation

Figure 7.4: Normalized mean velocity magnitude $|\overline{\boldsymbol{u}}|/U_H$ at 8 horizontal planes, $\hat{z} = [0.29, 0.43, 0.57, 0.71, 0.86, 1.0, 1.14, 1.29]$.

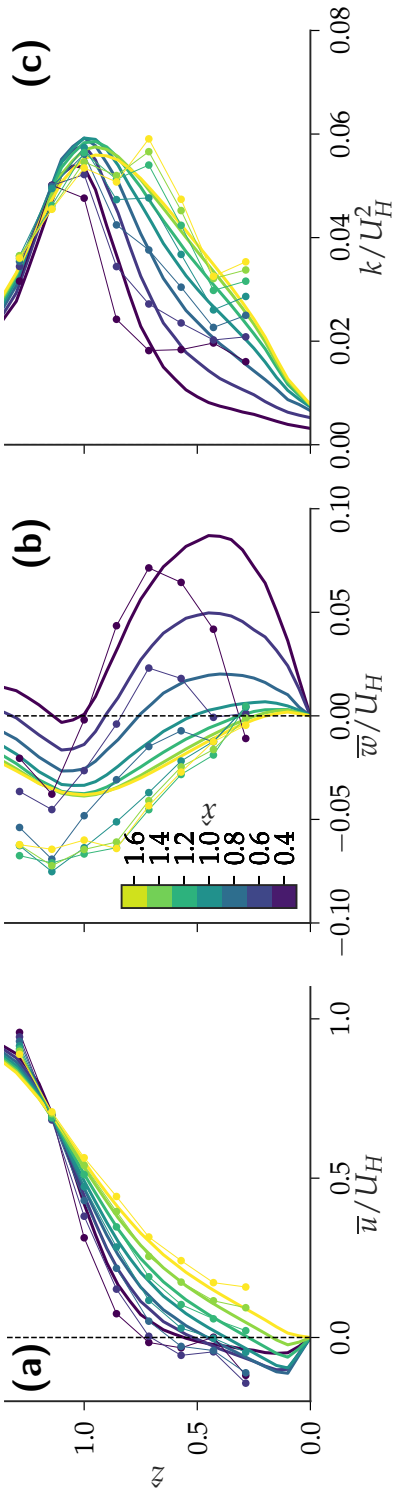


Figure 7.5: Mean vertical profiles at 7 streamwise positions $\hat{x}$, at center-line of the plant $\hat{y} = 0$: **(a)** streamwise velocity $\overline{u}/U_H$, **(b)** vertical velocity $\overline{w}/U_H$**(b)** turbulent kinetic energy $k/U_H^2$. The numerical and experimental results (obtained from Fig. 4.12) are plotted using solid smooth (—) and marked line (– • –), respectively.

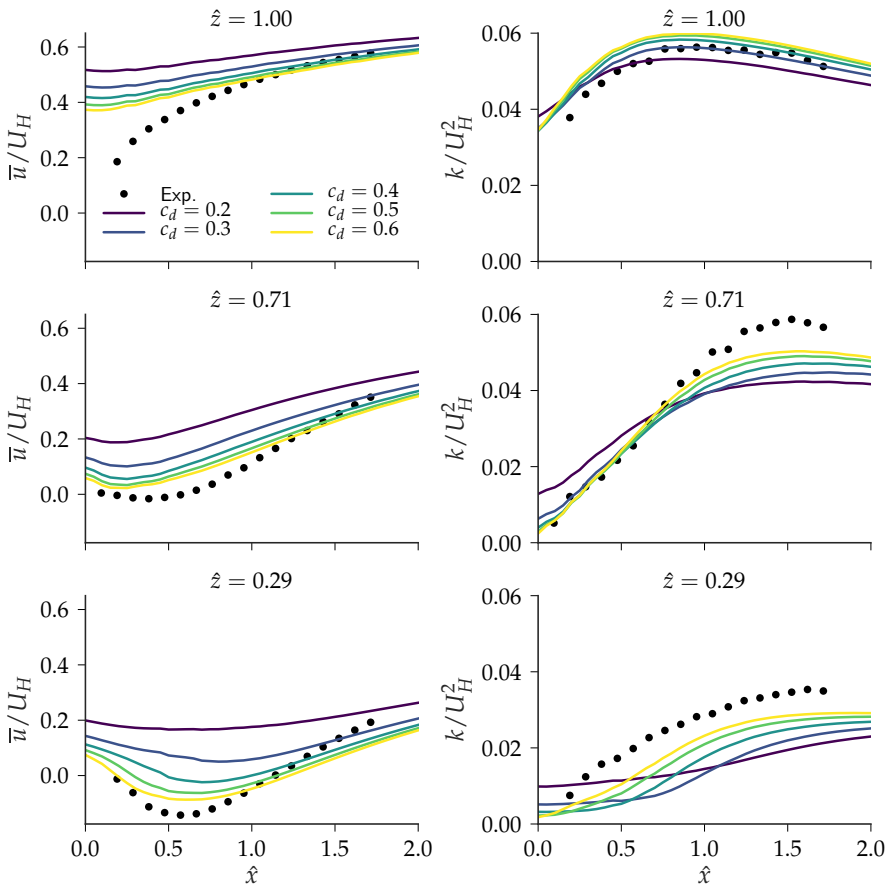


Figure 7.6: Influence of drag coefficient $c_d = [0.2, 0.3, 0.4, 0.5, 0.6]$: Horizontal profile of normalized stream-wise velocity $\overline{u}/U_H$ and turbulent kinetic energy $k/U_H^2$ at heights $\hat{z} = [0.29, 0.71, 1]$ and $\hat{y} = 0$.

experimental observation. This is most likely due to the numerical approach being a porous media approach where instead of explicitly resolving the plant elements (i.e., branches and leaves), they are aggregated into a distribution function.

### 7.3.1 *Influence of drag coefficient*

A second plant property that determines the net influence of the vegetation on the flow is the drag coefficient $c_d$ in Eqs. (7.4) to (7.6). Generally, the drag coefficient is associated with the leaf drag coefficient and determined to be $c_d \in [0.2, 0.5]$ (Vogel 1989; Wilson and Shaw 1977). However, as there is a high quantity of branch elements in the small Buxus plant, the validity of the assumption is investigated by a parametric study on the drag coefficient.

Fig. 7.6 shows the horizontal profile of stream-wise velocity and turbulent kinetic energy at three heights $\hat{z} = [0.29, 0.71, 1]$ and $\hat{y} = 0$, and the influence of drag coefficient on them. We observe clearly that the numerical prediction approaches to the experimental results as $c_d$ increases. Therefore, there is a clear indication that the drag coefficient of the plant is not just that of the leaf but should also take into account the contribution of the remaining plant elements such as branches. Thus, a drag coefficient of $c_d = 0.5$ is chosen as it not only provides a very good prediction accuracy, but is also within the constraint of $c_d \in [0.2, 0.5]$ (Vogel 1989; Wilson and Shaw 1977) even though we observe that $c_d = 0.6$ provides a slightly better prediction. However, the wake velocity deficit still shows a slight under-prediction. Similarly, in the wake zone (i.e., $\hat{z} < 1$), the peak TKE is under-predicted.

### 7.3.2 *Influence of heterogeneity in leaf area density distribution*

The influence of heterogeneity in the leaf area density distribution is investigated by comparing a spatially *varying* leaf area density and a spatially *constant* (average) leaf area density. Applying a spatial averaging operator to Eq. (7.7), we obtain the average leaf area density $\langle a \rangle$ ($\mathrm{m}^2\,\mathrm{m}^{-3}$) as:

$$\langle a \rangle = \frac{1}{2} A_l \frac{1 - \langle \phi \rangle}{\int 1 - \phi \, \mathrm{d}V} \tag{7.8}$$

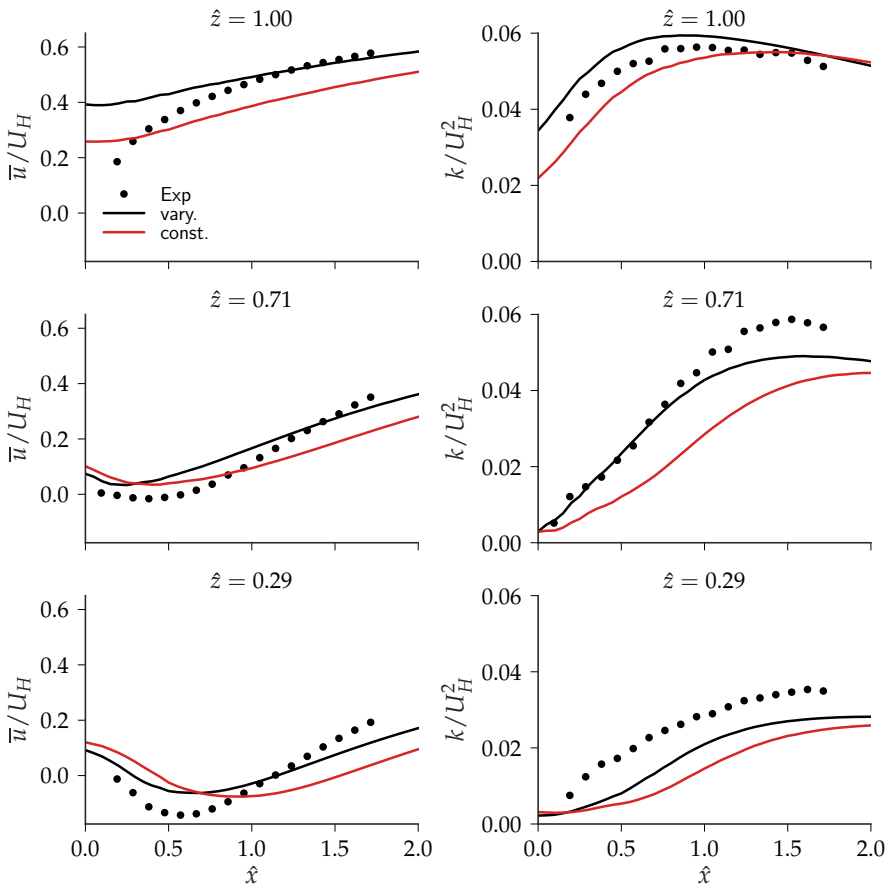


Figure 7.7: Influence of constant and varying leaf area density $a$ ($m^2\,m^{-3}$): Horizontal profile of stream-wise velocity $\overline{u}/U_H$ and turbulent kinetic energy $k/U_H^2$ at heights $\hat{z} = [0.29, 0.71, 1]$ and $\hat{y} = 0$.

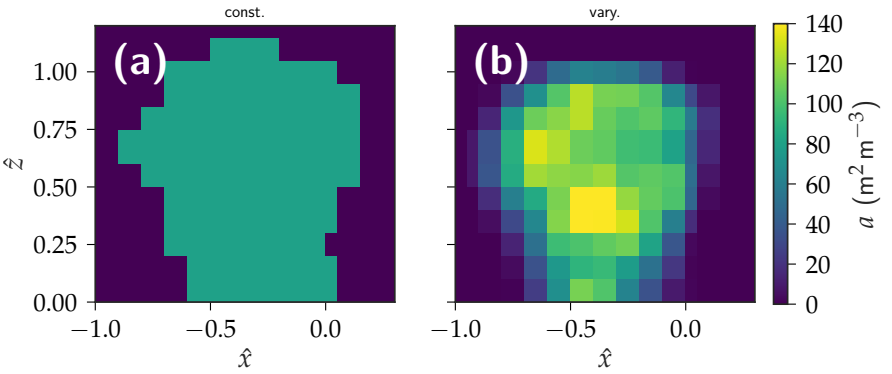


Figure 7.8: Two types of leaf area density $a$ distribution: **(a)** constant distribution and **(b)** varying distribution.

where it is simply related to net leaf area $A_l$ and the average plant porosity $\langle\phi\rangle$. Therefore, the *constant* leaf area density distribution in the air domain $\Omega_a$ is defined:

$$a(\boldsymbol{x}) = \begin{cases} \langle a \rangle & \text{if } 0 \leq \phi < 1 \\ 0 & \text{if } \phi = 1 \end{cases} \tag{7.9}$$

Fig. 7.8 shows the two types of leaf area density distribution at $\hat{y} = 0$. A spatially-averaged leaf area density is seen to be around $\langle a \rangle \approx 80$ m$^2$ m$^{-3}$, with maximum leaf area density $\max(a) = 140$ m$^2$ m$^{-3}$.

To study the impact of heterogeneous leaf area density distribution, both cases are compared with the wind tunnel measurements. Fig. 7.7 shows the horizontal profile of stream-wise velocity and turbulent kinetic energy at three heights $\hat{z} = [0.29, 0.71\ 1]$. The figure reveals that both constant and varying leaf area density distribution shows similar behavior where the more realistic description of the varying leaf area density distribution is seen to provide better predictions. The stream-wise velocity profile shows that the numerical model under-predicts the peak wake velocity deficit at all heights. Furthermore, the wake recovery from the numerical model is seen to be slower than the measurements. Therefore, the recirculation length of the numerical model is seen to be larger than in reality. One of the possible contributing factors to the recirculation length

is the accuracy of the turbulence closure. Therefore, the influence of the turbulence model is investigated in more detail.

### 7.3.3 *Influence of turbulence model*

For the study of the turbulence model, four similar closure approaches were investigated: i) $k-\varepsilon$, ii) realizable $k-\varepsilon$, iii) porous $k-\varepsilon$, and iv) porous realizable $k-\varepsilon$. The porous turbulence models (i.e., por. $k-\varepsilon$ and por. real. $k-\varepsilon$) have been modified with additional source terms, i.e., Eqs. (7.4) to (7.6), which models the influence of vegetation on the flow turbulence.

Fig. 7.9 shows the influence of the four turbulence closure approaches on the stream-wise horizontal profile of stream-wise velocity $u$ and turbulent kinetic energy $k$ at three heights $\hat{z} = [0.29, 0.71\ 1]$. The study shows the clear importance of an accurate turbulence closure to obtain the real observed plant wake. Let us first look at the influence of the turbulence model by comparing $k-\varepsilon$ and realizable $k-\varepsilon$. We see that this change already has a good improvement of the numerical prediction. The realizable turbulence model is seen to outperform the $k-\varepsilon$ model providing more realistic velocity deficit and reduces the overestimation of the TKE. However, we see that the turbulence closure terms of the vegetation have a significantly stronger impact on the accuracy of the prediction. With the addition of vegetation source terms (i.e., por. $k-\varepsilon$ and por. real. $k-\varepsilon$), the models are seen to perform drastically better than the standard models. We see that, not only is the wake velocity deficit more pronounced as with observation, but the TKE at the vicinity of the plant is seen to be less over-predicted. Therefore, the impact of foliage, such as the TKE suppression from the fluid-structure interaction of the foliage and airflow, is seen to be an important aspect of vegetation. As the standard turbulence models do not model such shortcuts in turbulence cascade (i.e., from TKE to heat), an over-prediction of turbulence is observed. The best performance in prediction accuracy is seen to be obtained from the porous realizable $k-\varepsilon$ model, where the stream-wise velocity deficit and the magnitude of the TKE are predicted with good accuracy. However, at the plant-canopy height (i.e., $\hat{z} = 1$), very close to the foliage (i.e., $\hat{x} \to 0$), the strong plant wake velocity deficit is not captured. This could be fundamentally due to the shortcomings of a porous

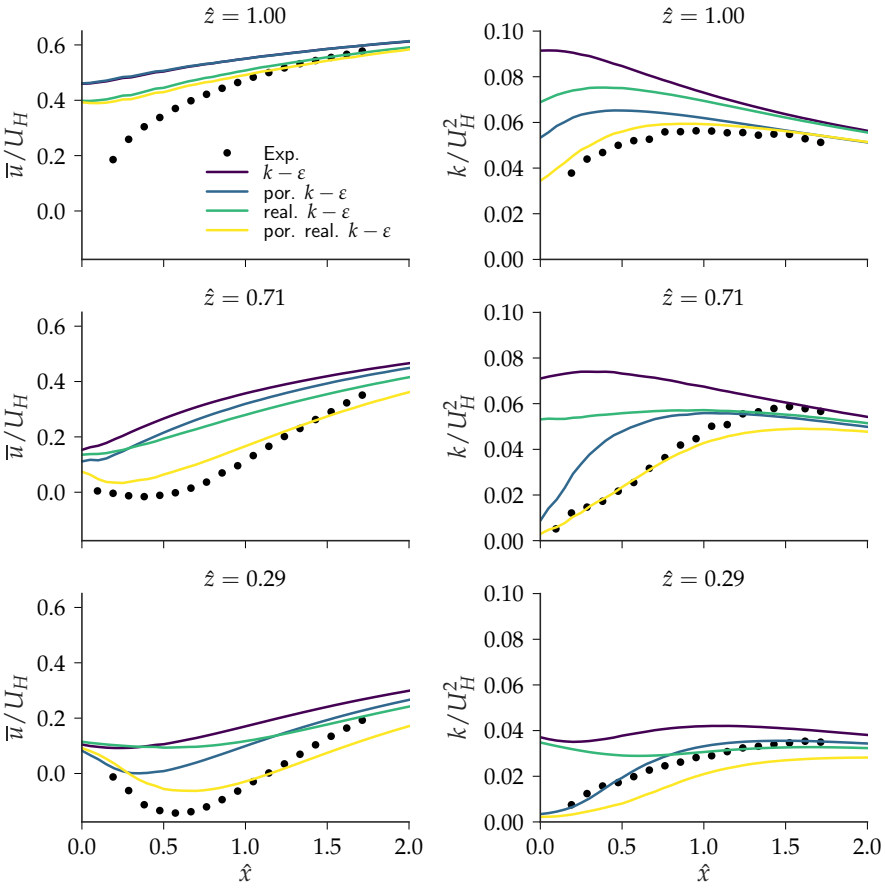


Figure 7.9: Influence of turbulence model std. $k-\varepsilon$, std. real. $k-\varepsilon$, por. $k-\varepsilon$ and por. real. $k-\varepsilon$: Horizontal profile of normalized stream-wise velocity $\overline{u}/U_H$ and turbulent kinetic energy $k/U_H^2$ at heights $\hat{z} = [0.29, 0.71, 1]$ and $\hat{y} = 0$.

media and similar immersed boundary approach where boundary layer flow phenomena are weakly captured. The flow characteristics prevalent the interfaces such as shear-flow are no longer captured with such spatial definition and intensity. In future, the present study on the influence of the turbulence model can be expanded to investigate additional eddy-viscosity models such as $k-\omega$ or $k-\omega$ SST, Reynolds stress models (RSM), or even Large-eddy simulation (LES) . A more complex, computationally expensive turbulence modeling approach has been shown to improve the prediction accuracy (Hiraoka 2011; Lopes et al. 2013; Yue et al. 2008). However, it is currently out of scope for the the present thesis but can potential be a topic for for future research.

An additional aspect of the turbulence closure is the model coefficients such as $c_\mu$, $C_{1\varepsilon}$, $C_{2\varepsilon}$, $C_{4\varepsilon}$, $C_{5\varepsilon}$, $\beta_p$ and $\beta_d$. These are also typically referred to as *free* coefficients and typically requires rigorous calibration (i.e., tuning) to capture and recover the experimental observations. The calibration of these coefficient to the experiment results can be described as an optimization problem (Couplet et al. 2005; Duraisamy et al. 2018; Gorlé et al. 2015; LUCOR et al. 2007; Margheri et al. 2014; Najm 2009), where data assimilation techniques are well regarded as an effective methodology to ensure the accurate, efficient convergence to global optima:

$$\arg\min_{\boldsymbol{c}} \; \epsilon(\boldsymbol{x},\boldsymbol{c}) = \|\mathcal{N}(\boldsymbol{x}) - \mathcal{M}(\boldsymbol{x},\boldsymbol{c})\|_2 \tag{7.10}$$

where $\boldsymbol{c} = (c_\mu, c_{1\varepsilon}, c_{2\varepsilon}, c_{4\varepsilon}, c_{5\varepsilon}, \beta_p, \beta_d)^T$ is a vector of the free coefficients and $\boldsymbol{c}$ spans $\mathbb{R}^7$, $\mathcal{N}$ is the true Navier-Stokes solution (neglecting the experimental uncertainties) and $\mathcal{M}$ is the numerical model. Therefore, the numerical model can be regarded as a "black-box" simply dependent on the free coefficient vector $\boldsymbol{c}$. We see that a brute-force search for coefficient vector $c$ that minimizes the error $\epsilon$ is intangible as the search needs to be formed in a 7-dimensional space, requiring a rigorous search algorithm. Therefore, the calibration of the turbulence model is beyond the scope of the study, but an important aspect for future studies.

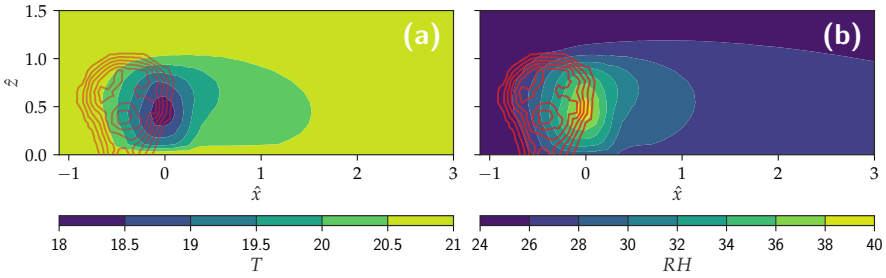


Figure 7.10: Center-plane (i.e., $y = 0$) hygrothermal condition of the flow at day-time with $T = 21$ °C, $RH = 25\%$ and $q_{r,sw,o} = 100\ \mathrm{W\,m^{-2}}$: **(a)** air temperature $T$ (°C) and **(b)** relative humidity $RH$ (%).

## 7.4 MICROCLIMATE

Finally, the numerical prediction of the thermal impact of the plant is compared with the hygrothermal wind tunnel measurements with ambient conditions $T = 21$ °C, 25% relative humidity and plant-canopy incident solar radiation levels $q_{r,sw} = [0,\ 100]\ \mathrm{W\,m^{-2}}$. To study the hygrothermal conditions, the temperature and humidity equations are solved where the additional plant source is determined using the leaf energy balance approach described in Chapter 6. Additionally, the resistance-based aerodynamic and stomatal models described in the chapter are used to parameterize the heat and mass flux between the foliage and air. The minimum stomatal resistance of the plant is set to $r_{s,min} = 400\ \mathrm{s\,m^{-1}}$ (in Eq. (6.7)), a typical value for deciduous plants (Baille et al. 1994; Bruse and Fleer 1998). Furthermore, it is equivalent to a stomatal conductance of $k_{st} = 40\ \mathrm{mmol\,m^{-2}\,s^{-1}}$ (see Eq. (5.98) ), typical of a *Buxus sempervirens* (Letts et al. 2012; Rodríguez-Calcerrada et al. 2013). In our study, the characteristic plant leaf size is set to $l = 3$ cm, obtained from measurements.

Fig. 7.10 shows the temperature and relative humidity at the center-plane of the plant ($y = 0$) during day time. A peak temperature drop of approximately $\Delta T = -2.5$ °C and humidity rise of $\Delta RH = +12\%$ is observed near the mid-aft region of the plant ($\hat{x} = 0$, $\hat{z} = 0.5$). We also note that there is no observed heating of the flow, typically present at the plant canopy height, possibly due to the lower level

of incident solar radiation $q_{r,sw,o} = 100\ \mathrm{W\,m^{-2}}$ and high convective heat transfer arising from the presence of wind.

To accurately assess the discrepancy between the hygrothermal prediction and the experiment observation, the in-foliage air temperature, and relative humidity are compared at various vertical locations. Fig. 7.11 shows the vertical profile of the air temperature and relativity humidity during day and night where the results of the numerical simulation are plotted with dashed lines. At night, the hygrothermal parameters are well predicted with a minimal discrepancy. During the day, we see that there is an overestimation of the transpirative cooling. It is indicated by lower air temperature and higher relative humidity as respect to the experimental observations. This discrepancy is observable at the mid-foliage region (i.e., $\hat{z} = 0.5$) where the largest transpirative cooling is predicted. In contrast, the experimental results do not indicate a large cooling, maintaining a relatively similar air temperature during both day and night. Therefore, the discrepancy is associated with the overestimation of the transpiration by the plant foliage in the simulation. Inside the foliage, the maximum discrepancy between the numerical model and the experimental measurements is seen be small with approximately 0.5 °C and 2% difference in air temperature and relative humidity, respectively.

However, the high air temperature at the plant-canopy at seen in experimental measurements is not observed in the numerical prediction. The experimental observations, Chapter 4, showed that air temperature is due to solar radiation interception at the top region of the foliage resulting in an increase in air temperature. At this location, the air temperature discrepancy between the numerical model and the experimental measurements is seen to be high, approximately 1.5 °C. In the simulation, the excess radiation absorption and the resulting rise in air temperature is not observed. The discrepancy could be possible due to the porous medium approach of resolving the plant foliage. As the plant canopy region is not explicitly resolved and instead described by plant density distribution, the strong radiative absorption that is present is not captured accurately.

A more general assessment on the prediction of the plant transpiration can be assessed by examining the net plant transpiration rate during day and night. Table 7.2 shows the experimental and numer-

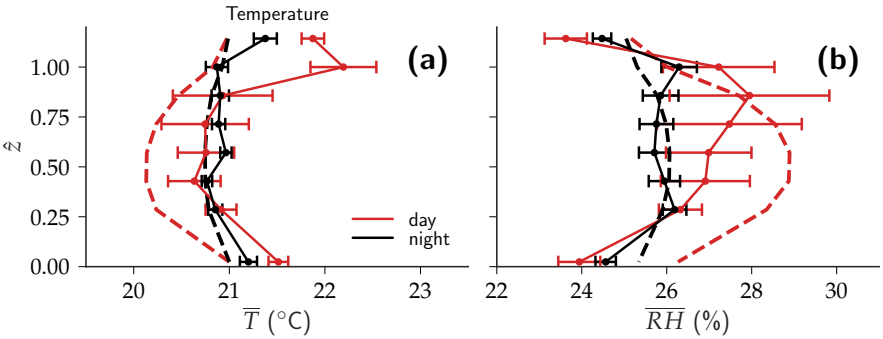


Figure 7.11: Comparison of wind tunnel (solid, —) and numerical simulation (dashed, – –): **(a)** median air temperature $T$ (°C) and **(b)** median relative humidity $RH$ (%). Vertical distribution are divided into day (08:00 - 16:00) (red) and night (20:00 – 04:00) (black).

ical value of the net transpiration rate $TR$ ($g\,h^{-1}$) during day and night. The comparison validates the finding that numerical model predicts a high transpiration rate. Especially during the daytime, a very high transpiration rate of 17.1 $g\,h^{-1}$ is predicted in contrast to the mean transpiration rate of 5.8 $g\,h^{-1}$ and a peak transpiration rate of 14.8 $g\,h^{-1}$. During the night, the net transpiration rate is predicted to be 4.9 $g\,h^{-1}$, and the experimental observation suggests a mean and peak value of 3 and 8.6 $g\,h^{-1}$, respectively. The numerical prediction of the plant transpiration is quite similar to the maximum plant transpiration rate. This indicates that time-dependent stomatal regulatory phenomena, as observed in chapter 4 is not captured as we have employed a simplified stomatal model described in Chapter 6 due to the lack of experimental data available for calibration of the advanced model described in Chapter 6 Chapter 5. In future, a measurement campaign consisting of measurement of both atmospheric conditions, soil conditions (such as soil moisture, soil moisture capacity) and plant physiology (such as leaf $CO_2$ flux, xylem conductance, root conductance can enable to model the dynamic responses of the plant.

Table 7.2: Experimental and numerical values of net plant transpiration rate $TR = \mathrm{d}m/\mathrm{d}t$ ($\mathrm{g\,h^{-1}}$) during day and night.

| period | experimental | | numerical ($\mathrm{g\,h^{-1}}$) |
|---|---|---|---|
| | mean ($\mathrm{g\,h^{-1}}$) | max. ($\mathrm{g\,h^{-1}}$) | |
| day | 5.8 | 14.8 | 17.1 |
| night | 3.0 | 8.6 | 4.9 |

## 7.5 CONCLUSION

The numerical model is compared with the experimental measurements of a *Buxus sempervirens* plant. The non-isothermal comparison study focused on the prediction accuracy of the mean airflow and the turbulence modification due to vegetation. The isothermal study concluded that spatially resolved formulation of the leaf area density provides a more accurate description of the velocity deficit and the turbulence kinetic energy of the wake. The drag coefficient of the plant was seen to play a major role in the wake velocity statistics. With increasing drag coefficient, the numerical prediction was seen to approach to the experimental measurements. Although, at the vicinity of the plant and plant canopy height of $z = H$, the wake velocity deficit is seen to be always underestimated. This is due to the shortcomings of a porous media approximation of the plant where typically, boundary layer flow phenomenon such as sharp velocity gradient is not able to be accurately captured as the geometry is not explicitly resolved. The isothermal comparison study was concluded with the assessment of the turbulence model. It was seen that the realizable $k - \varepsilon$ model with the vegetation source terms outperforms other models. The vegetation source terms were seen to be crucial at accurately predicting the wake velocity deficit. Moreover, the additional terms needed to model the suppression of the turbulence kinetic energy of the wake due to the interaction of foliage and the airflow. In contrast, the standard models were seen to always overpredict the TKE in the wake. In future, a more rigorous study can be performed by using additional eddy-viscosity models or Reynold stress models or even employing a Large-eddy simulation (LES) turbulence modeling approach for resolving the turbu-

lent flow past vegetation instead of the RANS approach employed in this thesis. The detailed study can provide insight to efficacy of the turbulence modeling approach employed in this thesis and it's limitation.

Finally, the non-isothermal comparison study assessed the prediction accuracy of the hygrothermal flow parameters such as air temperature and the relative humidity, and the transpiration rate of the plant. It was observed that the numerical model over-estimated the transpiration rate of the plant and is more in line with the peak plant transpiration rate, both during day and night. The high transpiration rate resulted in a higher transpirative cooling as observed by lower air temperature and higher relative humidity inside the foliage. The maximum discrepancy between the numerical model and the experimental measurements inside the foliage was seen be small with approximately 0.5 °C and 2% difference in air temperature and relative humidity, respectively. However, at the plant-canopy a high discrepancy of air temperature is observed, approximately of 1.5 °C. The comparative study of the numerical model and the wind tunnel experiment measurements showed that the numerical model shows a similar prediction for the airflow. Although more analysis is needed to conclude whether the agreement of the hygrothermal parameters is satisfactory.

# 8

# NUMERICAL STUDY OF IMPACT OF VEGETATION ON URBAN MICROCLIMATE

## 8.1 INTRODUCTION

In this chapter, the fully coupled (integrated) numerical model, described in Chapter 5, is used to assess the impact of vegetation on urban microclimate. To accurately assess the impact of vegetation on urban microclimate, we must determine: i) the influence of vegetation on the turbulent airflow, ii) the influence of plant transpiration on hygrothermal conditions, iii) the influence of plant shading on the urban environment, and iv), the net influence of all the parameters on the pedestrian thermal comfort. In this chapter, the influence of vegetation is assessed using two different numerical setups: a) the study on the influence of vegetation on microclimate of an urban street canyon, and b) a case study on the influence of vegetation in a realistic city topology in Zürich, Switzerland at a location known as Muensterhof (in german: Münsterhof). The Muensterhof is a town square within the city of Zurich that currently lacks vegetation. The objective of the study in the urban street canyon is to perform a parametric study and determine the parameters that play a main role in improving thermal comfort. Furthermore, the influence of soil moisture change on the plant transpiration and the leaf energy balance is investigated. The objective of the case study in Muensterhof is to determine the microclimate modification of vegetation in a realistic setting.

## 8.2 URBAN STREET CANYON

A numerical assessment of the impact of vegetation is first performed in a urban street-canyon. The study investigates the influence of

transpirative and shaded cooling due to vegetation on the pedestrian comfort inside a street canyon. In this study, we investigate the cooling potential of vegetation, such as a row of trees, on the microclimate of a street canyon using the developed CFD model in OpenFOAM. The cooling effect of isolated vegetation was studied in Chapter 6. In this chapter, we investigate the influence of vegetation in a setup described in Kubilay et al. (2018), who investigated the influence of only the building and street materials on the microclimate. In this study, we investigate how the vegetation modifies the microclimate. The vegetation integrated numerical model is described in Chapter 5 where the plant transpiration is dependent on the available soil moisture. Furthermore, vegetation modifies the street-canyon radiation balance as described in Section 5.6, where the vegetation intercepts the direct solar radiation and provides shading to the urban surfaces. The reflected (assumed to be diffused) short-wave radiation and long-wave radiation is modeled using surface-to-surface radiation model (i.e., *radiosity* approach or also known as "view factor" model) as described in Section 5.6. The goal of the advanced radiation model, in contrast, to approach described in Chapter 6, is to provide a more accurate estimation of the mean radiant temperature $T_{mrt}$, a key variable for an accurate prediction of thermal comfort index. In this study, the thermal comfort for pedestrians is evaluated using the Universal Thermal Climate Index (UTCI). The study aims to understand better the governing phenomena related to vegetation that plays a key role in improving pedestrian thermal comfort. Therefore, the study simulates multiple cases to isolate the influence of transpirative cooling and cooling due to shading by trees. Thus, we aim to understand the main contribution of natural cooling of vegetation on urban microclimate.

### 8.2.1 *Simulation setup*

The simulations are performed for a street canyon with a vegetation zone of $2 \times 10 \times 4$ m$^3$, representing a row of trees which are surrounded by two buildings of $10 \times 50 \times 10$ m$^3$ ($x \times y \times z$), as shown in Fig. 8.1. The numerical domain size is $230 \times 250 \times 60$ m$^3$ ($x \times y \times z$), where the inlet, outlet, top, and side walls are positioned $5H$, $5H$, $15H$, and $10H$ away, respectively, based on CFD best practices (Blocken 2015; Franke et al. 2007; Tominaga et al. 2008).

The numerical domain is discretized into 1 178 080 hexahedral cells with minimum cell size of $1 \times 10^{-3}$ m$^3$ near the building walls (see Fig. 8.2) and are determined following a grid-refinement study. The vegetation zone has a foliage height of 4 m (with $z_{min} = 4$ m), leaf area density $a = 1$ m$^2$ m$^{-3}$, leaf drag coefficient $c_d = 0.2$ and leaf size $l = 0.1$ m. The buildings are oriented perpendicular to the wind direction. The meteorological data are based on a typical meteorological year and the total solar radiation intensity is for a clear sky on the 21$^{st}$ of June in the city of Zurich, Switzerland used in the study of Kubilay et al. (2018). However, in the future, extreme weather events such as heat wave should also be investigated to determine how vegetation can ensure cities to be resilient to the climate of the future. It has been predicted that global warming and climate change will increase the frequency of such extreme events (Mitchell et al. 2016). The wind speed at the building height is $U_{ref} = 5$ m s$^{-1}$ (assumed constant during the day for simplicity) where turbulence kinetic energy $k$ and turbulence dissipation rate $\varepsilon$ are determined using Eq. (7.3) (Richards and Hoxey 1993) with $u_*/U = 0.072$ and $z_0 = 0.03$ m. Standard wall functions are employed for the wall boundary and a constant static pressure of $p = 0$ Pa at the outlet boundary. The inlet, top and side wall are prescribed with the ambient temperature varies between 11 °$C$ and 19 °$C$ with solar noon at 13:28 and the relative humidity varies between 62% and 86% $RH$ as shown in Fig. 8.3. The ambient $CO_2$ concentration is taken to be $c = 380$ $\mu$mol mol$^{-1}$ (assumed constant during the day for simplicity).

The coupling of air domain, the solid domains (including soil region), with the vegetation is discussed in Section 5.7. Fig. 8.4 shows the setup of the solid domain used in the study. The figure depicts the configuration of two buildings forming a street-canyon with a vegetation zone in the middle. The cross-section is a $x - z$ plane at $y = 125$ m (i.e., $y$-center of the street-canyon). The two buildings have size $10 \times 50 \times 10$ m$^3$ ($x \times y \times z$) each with a brick layer of 0.09 m inside the street-canyon and a soil region at the street where the vegetation roots is present. The soil is composed of equal composition of sand, silt, and clay with a uniform root area density $r = 5$ m$^2$ m$^{-3}$ of the size of $4 \times 14 \times 1$ m$^3$ directly below the foliage region, spanning $\boldsymbol{x}_{min} = (62, -1, 118)$ and $\boldsymbol{x}_{max} = (68, 0, 132)$. The temperature inside the building $T_{in}$, thermal resistance $R$ of wall

Table 8.1: Soil-plant-atmosphere continuum (SPAC) vegetation parameters of Loblolly pine (*Pinus taeda*) are used in the study (Launiainen et al. 2015; Manoli et al. 2014b; Manzoni et al. 2011; Vogel et al. 2016; Volpe et al. 2013)

| Parameter | Description | Value | Unit |
|---|---|---|---|
| $c$ | Ambient $CO_2$ concentration | 380 | $\mu$mol mol$^{-1}$ |
| $c_*$ | $CO_2$ concentration at max. WUE | 400 | $\mu$mol mol$^{-1}$ |
| $c_o$ | Ambient $O_2$ concentration | 210 | mmol mol$^{-1}$ |
| $a$ | leaf area density | 1 | m$^2$ m$^{-3}$ |
| $l$ | leaf size | 0.1 | m |
| $\lambda_{max}$ | Maximum WUE | 2912 | $\mu$mol mol$^{-1}$ |
| $\beta_L$ | WUE coefficient | $0.78 \times 10^{-12}$ | |
| $\psi_L^{max}$ | leaf water potential at max. WUE | $-1.85 \times 10^{-6}$ | Pa |
| $k_x$ | xylem conductance | $5 \times 10^{-6}$ | s$^{-1}$ |
| $A_x$ | xylem cross-section area | 0.06 | m$^2$ |
| $k_{st,n}$ | nocturnal stomatal conductance | 0.018 | mol m$^{-2}$ s$^{-1}$ |
| $r$ | root area density | 5 | m$^2$ m$^{-3}$ |
| $r_{radius}$ | root radius | 0.02 | m |
| $\beta$ | soil conductance coefficient | $3 \times 10^8$ | |
| $k_r$ | root conductance | $3 \times 10^{-11}$ | s$^{-1}$ |

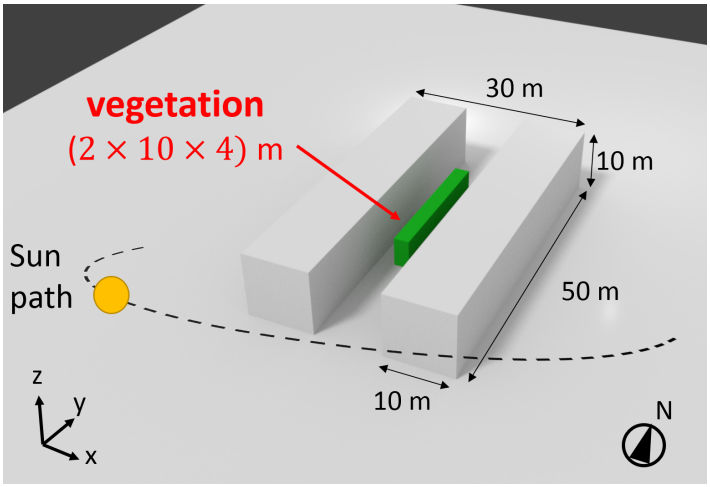


Figure 8.1: The simulation setup of a street canyon composed of two buildings measuring $10 \times 50 \times 10$ m$^3$ ($x \times y \times z$) with vegetation band of size $2 \times 10 \times 4$ m$^3$ in the center. The setup is based on the study of Kubilay et al. (2018) awa with wind.

and roof, the density $\rho_0$, thermal conductivity $\lambda$, emissivity $\epsilon$ and albedo $\alpha$ of the various solid regions are also indicated in Fig. 8.4. The vegetation parameters used in the soil-plant-atmosphere continuum (SPAC) vegetation model are given in Table 8.1. The vegetation properties are for Loblolly pine (*Pinus taeda*) (Launiainen et al. 2015; Manoli et al. 2014b; Manzoni et al. 2011; Vogel et al. 2016; Volpe et al. 2013). Although not common in cities, this species was used due to the availability of vegetation properties. In future, this numerical modeling approach should enables to study various other species that are more common in cities.

### 8.2.2 *Results and Discussion*

The influence of water availability is studied by investigating the evolution of root, leaf, and soil water potentials. We study how the root water uptake changes spatially and diurnally for around 24 days. Such a long time evolution is required to analyze the gradual change in soil moisture. By day 21, the plant is under water stress, and we investigate the impact on the energy balances and the

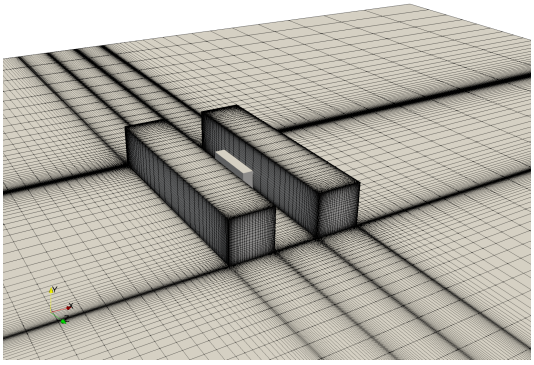

Figure 8.2: Simulation domain showing the surface layer mesh refined closed to the building walls. The numerical domain is discretized into 1 178 080 hexahedral cells with minimum cell size of $1 \times 10^{-3}$ m$^3$ at the building corner. The mesh is based on the grid refinement study of Kubilay et al. (2018).

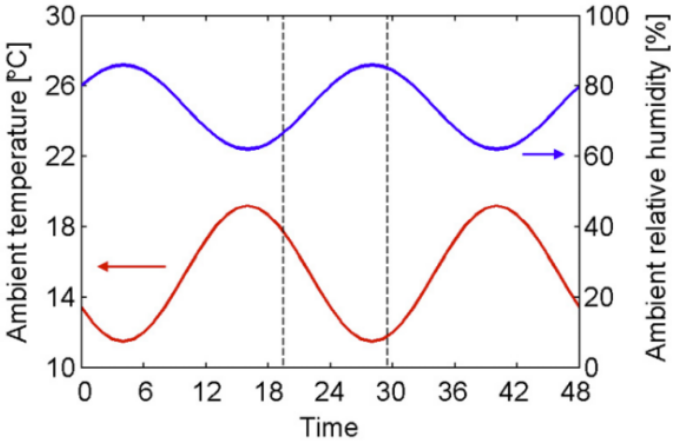


Figure 8.3: Diurnal ambient temperature $T$ ($^\circ C$) and relative humidity $RH$ (%) profile obtained from Kubilay et al. (2018). The meteorological data are based on a typical meteorological year and the total solar radiation intensity is for a clear sky on the 21$^{st}$ of June in the city of Zürich, Switzerland.

urban microclimate conditions. The influence of vegetation in an urban street-canyon is determined by separately studying the influence of shading and the plant transpiration. The influence of these two parameters on the microclimate inside the street-canyon is studied by determining the influence on air temperature, mean radiation temperature, short-wave radiation intensity, and finally UTCI distribution.

*Influence of water availability*

As the plant transpires throughout the day, the soil moisture will reduce due to the root water uptake (in addition to soil surface evaporation). Therefore, after a longer period (i.e., days), the soil moisture will be reduced and could have an impact on the plant transpiration rate, directly influencing the leaf energy balance. Fig. 8.5 shows the long-term evolution of the plant properties such as bulk leaf water potential $\psi_L$ (MPa), bulk root water potential $\psi_R$ (MPa), rhizosphere-averaged soil water potential $\langle \psi_s \rangle$ (MPa), and average plant transpiration rate $\langle g_{v,leaf} \rangle$ ($\mathrm{g\,m^{-2}\,s^{-1}}$). The rhizosphere-averaged soil water potential is defined as:

$$\langle \psi_s \rangle = \frac{\int_{\Omega_{soil}} r \psi_s \, \mathrm{d}V}{\int_{\Omega_{soil}} r \mathrm{d}V} \tag{8.1}$$

and average plant transpiration rate is defined as:

$$\langle g_{v,leaf} \rangle = \frac{\int_{\Omega_{air}} a \, g_{v,leaf} \, \mathrm{d}V}{\int_{\Omega_{air}} a \, \mathrm{d}V} \tag{8.2}$$

We see that leaf and root water potential varies at two timescales: i) hourly and ii) daily. The hourly cycling behavior is directly correlated with atmospheric conditions such as solar radiation as depicted in Fig. 8.11. Around early afternoon (i.e., 15:00), when the solar radiation is highest, the atmospheric evaporative demand (AED) is highest, as experimentally observed in Chapter 4. A large transpiration demand is reflected by the large drop in leaf water potential (Fig. 8.5a). Similarly, the root water potential becomes more negative, albeit at a higher than the leaf water potential. The soil water potential follows a similar trend with an even smaller fluctuation between day and night values. However, what is interesting is that

the average nocturnal rhizosphere soil water potential is lower than the root water potential. As the night progresses to dawn, we see that soil water potential becomes less negative. It is, therefore, evident that hydraulic redistribution occurs (Huang et al. 2017; Volpe et al. 2013). Figure Fig. 8.6 shows the time evolution of root water uptake from the soil for up to 24 days. We see that during day time, there is a strong water uptake from the soil due to leaf transpiration. However, during the night, as the days progress, we observe hydraulic redistribution from the bottom region of the rhizosphere to the surface layer. The rhizosphere region soil moisture is highest just before dawn and is a common metric used in plant science (i.e., pre-dawn soil water potential). The night-time hydraulic redistribution occurs when the soil water potential near the surface is lower than the bulk root water potential. Therefore, the roots act as a mechanism to redistribute the lower-ground water where the water potential is higher (i.e., more saturated), to upper layers of the rhizosphere through the roots. The advantage is that the near-surface soil can be re-moisturized, improving surface evaporative cooling or providing ecological support to ground level vegetation such as grass. The study shows the importance of deep-rooted vegetation which can access the water near the water table and redistribute to regions of driest soil where the soil water potential is lowest.

Fig. 8.5b shows the variation in the average plant transpiration rate. The plant transpiration is correlated with the leaf water potential as they are directly dependent, with peak plant transpiration around early afternoon (15:00). The long-term dynamics of water availability is also visible in the Fig. 8.5. As the number of days passes, a larger gradient in the leaf and root water potential is required to provide the adequate transpiration needed by the atmospheric demand. Furthermore, after day 20, we observe an exponential behavior in the daily variability indicating that plants are more susceptible after an extended period of low soil moisture. Furthermore, if we quantify water stress as a difference between the leaf and soil water potential, we see that plant water stress increases exponentially as the day passes. Fig. 8.7 shows the plant transpiration rate $\langle g_{v,leaf} \rangle$ ($\mathrm{g\,m^{-2}\,s^{-1}}$), where all the 24 days are collapsed to an hourly plot. We see that with an increasing number of days without irrigation, the plant transpiration decays throughout the day and is

proportional to the level of the plant transpiration. The largest drop in plant transpiration is observed at peak solar hour.

To understand how the decaying transpiration rate affects the plant energy balance, the hourly variation of the average sensible heat flux $\langle q_{sen,leaf} \rangle$ (W m$^{-2}$) and average latent heat flux $\langle q_{lat,leaf} \rangle$ (W m$^{-2}$) is investigated, Fig. 8.8. The figure shows that with reducing water availability, the sensible heat flux increases throughout the day with an equal reduction in the latent heat flux. This results in the diminished cooling provided by the vegetation, as observed in Fig. 8.13. The study shows the importance of the regular irrigation of the vegetation. Without adequate irrigation, a lack of water for plant transpiration can remove the transpirative cooling effect observed in Fig. 8.13. If the amount of water in the soil reaches $\psi = -1.5 \times 10^6$ (Pa), it is known as the permanent wilting point (PWP) where plants can no longer transpire due to loss of cell turgidity (Idso 1977). So, to ensure the health of the plant, it is important that plants are regularly irrigated. The study shows that, with an increasing number of days (for the previous irrigation), the need for irrigation grows exponentially, reflected by the increasing water stress.

*Influence of plant transpiration and shading*

Fig. 8.9 shows the direct short-wave radiation intensity $q_{s,dir}$ (W m$^{-2}$) inside the street-canyon (i.e., $x - z$ plane at $y = 125$ m) where the vegetation zone is indicated by a green box. Nine subplots are shown of different times of the days from 03:00 to 23:00 (HH:MM) at 150 minutes interval. The figure shows the contribution of the vegetation to the solar radiation intensity inside the street-canyon. We see that vegetation intercepts the solar radiation during the day providing shading to the nearby urban surfaces. The vegetation acts as a radiation sink especially when the solar radiation is high during noon. It is important as the urban materials with high thermal capacity contribute to the urban heat island by absorbing the solar radiation. By providing shading to the urban environment, vegetation can, therefore, reduce the urban heat island effect.

Fig. 8.10 shows the mean radiant temperature $T_{mrt}$ (°C) inside the street-canyon throughout the day that a person would experience. Although $T_{mrt}$ is a surface related value, in this study we calculate $T_{mrt}$ everywhere in the street-canyon to determine how UTCI felt by

a person is varying inside the street-canyon. The goal is to have a better understanding of the driving factors behind the thermal comfort and how they are interrelated. The mean radiant temperature is determined as follows:

$$T_{mrt} = \left( T_{umrt}^4 + \frac{f_p a_b}{\epsilon_p \sigma} q_{s,dir} \right)^{\frac{1}{4}} \tag{8.3}$$

where $T_{umrt}$ is the mean radiant temperature component belonging to the diffused or reflected part (i.e., from terrestrial source), $f_p$ is projected surface area of the person exposed to the sun, $\alpha_p$ is the albedo, $\epsilon_p$ is the emission coefficient and $q_{s,dir}$ ($\mathrm{W\,m^{-2}}$) is the direct solar radiation. The diffused/reflected component of the MRT is defined as:

$$T_{umrt} = \left[ \frac{1}{\sigma} \sum_{i}^{N} \left( q_{r,i} + \frac{a_b}{\epsilon_p} q_{s,i} \right) F_i \right]^{\frac{1}{4}} \tag{8.4}$$

where $q_{r,i}$ ($\mathrm{W\,m^{-2}}$) is the long-wave radiation emitted from surface $i$, $q_{s,i}$ ($\mathrm{W\,m^{-2}}$) is the reflected (assumed to be diffused) short-wave radiation from surface $i$, and $F_i$ is the view-factor between surface $i$ and the person. Thus, the mean radiant temperature $T_{mrt}$ is directly dependent on the long-wave and the short-wave radiation fluxes in the street-canyon, including the contribution from the direct solar radiation $q_{r,dir}$. Fig. 8.10 is seen to be directly correlated with the short-wave radiation plots depicted in Fig. 8.9. At regions of high direct solar radiation, the mean radiant temperature approaches $T_{mrt} \rightarrow 60$ (°C). In the shaded regions, there is an 18 (°C) difference in the mean radiant temperature. This indicates that solar radiation plays a crucial role in the mean radiant temperature and thereby the thermal comfort (investigated in detail in the next section). Furthermore, we see that between the vegetation and the buildings, the mean radiant temperature is at the highest. This is related to the emitted (or reflected) radiation from urban surfaces. At these locations, the region is exposed to (or "views") more surfaces emitting and reflecting the radiation. Therefore, the diffused radiation from the building surfaces is also contributing to the mean radiant temperature. During night-time, we see that the mean radiant temperature gradually reduces. This is due to the nocturnal radiation cooling, where the long-wave radiation from the building surfaces is emitted to the at-

mosphere during the night, thereby cooling the building surfaces. Trapping of this radiation such as due to cloud cover or even the presence of vegetation can negatively affect the nocturnal radiation cooling.

To better investigate the impact of plant shading and the changes in mean radiant temperature in the street-canyon due to vegetation, a single point below the vegetation at $(x, y, z) = (65, 125, 2)$ is investigated for three different cases: the configuration without vegetation (*None*), a configuration with vegetation but providing only shading (*Shad.*), and a configuration with vegetation providing both shading and plant transpiration (*TR + Shad.*), Fig. 8.11. Fig. 8.11a shows the diurnal variation of the direct short-wave radiation intensity $q_{s,dir}$ ($\mathrm{W\,m^{-2}}$) below the vegetation. At the presence of vegetation, we see a strong drop in the solar radiation, especially during middays from $q_{dir} \approx 800\ \mathrm{W\,m^{-2}}$ to around $100\ \mathrm{W\,m^{-2}}$ at midday. The diurnal profile of the mean radiant temperature $T_{mrt}$ (°C), Fig. 8.11b, shows that shading provides up to $\approx 20$ °C drop when shaded and transpiring. This is especially beneficial as the largest temperature drop is found at the time of the highest solar radiation. Thus, shading can be a vital component in improving pedestrian thermal comfort. A detailed investigation of the impact of shading on UTCI is performed in the next section. At night we see that the vegetation instead increases the mean radiant temperature inside the street-canyon. This occurs because vegetation results in a radiation trapping intercepting the long-wave radiation emitted from the urban surfaces to the sky. This phenomenon can, therefore, harm thermal comfort during night time. There is a slight difference between the shaded only case and transpiring case, due the cooler air temperature from transpirative cooling (see Fig. 8.11c). The reduced air temperature results in a reduced surface temperatures, providing a lower long-wave radiation emissions.

Fig. 8.12 shows the air temperature $T$ (°C) inside the street-canyon (i.e., $x - z$ plane at $y = 125$ m) allowing to see the influence of vegetation on the air temperature through the diurnal cycle. The air temperature $T$ depicted in the figures results from the net effect of solar radiation, plant shading, thermal storage in buildings and air temperature change due to plant transpiration. It is apparent that the highest air temperature is at building surfaces mainly due to the solar radiation observed in Fig. 8.9. Below the vegetation, we see that

the air temperature is lower whereas a slight rise in air temperature is observed at the top of the foliage, where most of the solar radiation is intercepted. To better assess the influence of the transpiration and the influence of shading, the air temperature $T$ (°C) and $UTCI$ (°C) below the vegetation at $(x, y) = (65, 125)$ and at three different heights $z = [1, 2, 3]$ are investigated. We compare various cases: i) no vegetation, ii) only shading at day 1, iii) shading and plant transpiration at day 1, and iv) shading and plant transpiration at day 21 (i.e., 20 days after initial irrigation). The last case focuses on the impact of water stress on the cooling provided by vegetation. Fig. 8.13(a-b) show the diurnal variation of the air temperature and the comfort index at $z = 2$ m, respectively. Fig. 8.13(c-d) show the difference between *with* and *without* vegetation case (i.e., $\phi_{case,i} - \phi_{none}$) at the three different heights. It is found that on the first day, for both cases of with both transpiration and shading, and with only shading, there is a significant reduction in the air temperature, especially during the afternoon. On day 1 with the addition of transpiration (i.e., *TR + Shad. - day 1*), we notice an additional cooling that persists till night. We see that after a long period without irrigation (i.e., 20 days), the plant cooling diminishes to the case similar to *without* vegetation. It is possibly due to additional heating up by convective air flow arising from the now present heated up tree with reduced water availability. Fig. 8.13c shows the difference in air temperature *with* and *without* vegetation at three different heights $z = [1, 2, 3]$. We observe that most cooling is obtained on day 1 with transpiration and shading (i.e., *TR + Shad. - day 1*) at the height $z = 1$ m. Away from the ground, the cooling is seen to reduce. So, the strongest cooling is present closer to the ground surface at midday due to cooling from shading and surface evaporation of plant soil. After 20 days, we see that cooling is substantially lower, and the air temperature is even higher during the night. This shows that with water stress in combination with radiation trapping could have negative consequences on the urban microclimate. Due to the lack of transpirative cooling and reduced night-time long-wave radiation escape, the street-canyon air temperature becomes higher over time. The implication of this on thermal comfort on various cases is studied in the next section.

*Impact on thermal comfort*

The influence of vegetation on pedestrian comfort is determined by evaluating the Universal Thermal Climate Index (*UTCI*) (°C) (Fiala et al. 2001; Manickathan et al. 2018b). We employ the formulation used in Chapter 6, however, with a more accurate estimation of the mean radiant temperature, as shown in Eq. (8.3), taking in account of the solar altitude change during the day, long-wave and short-wave radiation emitted and reflected from the urban surfaces. Fig. 8.14 shows the *UTCI* (°C) inside the street-canyon (i.e., $x - z$ plane at $y = 125$ m) at 9 separate times of the day. It is apparent that pedestrian comfort is significantly reduced due to the exposure to solar radiation at noon. However, inside the shaded zone of the vegetation, the thermal comfort is substantially improved, as indicated by the reduced UTCI values. In contrast, the impact of humidity generated from vegetation is not discernible in the UTCI distribution. For more clarity, we investigate the diurnal variation of UTCI at a single point and compare with different cases, as seen in Fig. 8.13b. Fig. 8.13b shows that at day, the UTCI is lowest during day 1. When the plant is shading, the thermal comfort improves substantially due to reduced mean radiant temperature. Closer to vegetation, we see that UTCI becomes higher, as shown in Fig. 8.13d, due to the increase in air temperature. By the late afternoon, the UTCI due to additional transpiration is lower than for the case with only shading. However, after 20 days (i.e., day 21), we see a rise in UTCI throughout the day (and night) This is possibly due to transpiration increasing the relative humidity, counterbalancing the cooling provided by the effect of air temperature decrease due to transpiration. The thermal comfort inside the street-canyon is seen to reduce due to the diminished transpiration, higher surface and air temperatures due to radiation trapping. The impact of radiation trapping is especially apparent when comparing the UTCI at night. We see that the lowest UTCI is shown for the case without vegetation. When vegetation is not present, the long-wave radiation is emitted from the surfaces to the sky, thereby cooling the surfaces. However, with extended periods of low water availability, the transpiration benefit provided by vegetation diminishes, and the sustained radiation trapping gradually increases the street-canyon temperature.

### 8.2.3 *Conclusion*

The present study investigates the influence of transpirative and tree shading on the microclimate of a street canyon. The shading provided by vegetation has a large influence on the street-canyon mean radiant temperature with a drop of around 18 °C in the shadow. A significant drop in the mean radiant temperature means a substantial improvement in the measured thermal comfort. At midday, when the solar radiation is at highest, vegetation provides a significant reduction in mean radiation temperature and equally on the thermal comfort. We also observed that, when the plant has sufficient water available, the air temperature below vegetation is also improved due to transpiration. However, with an increasing number of days with reduced water available, the benefits provided by vegetation diminishes over time. This is attributed to reduced plant transpiration due to water stress, lower soil moisture reducing surface evaporation, and the sustained radiation-trapping resulting in larger surface temperatures. Thus, water availability and the nocturnal radiation trapping are important aspects of vegetation when considering them as a mitigation strategy. With an increasing number of days without irrigation, the soil loses the available water for the plant transpiration and for surface evaporative cooling. Furthermore, a prolonged period without irrigation is shown to increase the water stress of the plant (i.e., the difference between leaf and soil water potential), which increases at an exponential rate. Therefore, the demand for irrigation also grows exponentially with time. Urban vegetation irrigation measure should, therefore, take into account the growth in water stress when exposed to a prolonged period of drought. Such conditions can be more frequent in today's changing climate. Furthermore, the nocturnal radiation trapping shows that, vegetation, counter-intuitively stagnates the cooling of cities during the night. So, cities should not ignore this contribution of vegetation when employing UHI mitigation measures using vegetation. Finally, we observed that the complex modeling approach implemented in this study can capture import plant dynamics such as hydraulic redistribution. It can have an important contribution to the water availability of the shallow-rooted plant species such as grass or small shrubs.

## 8.3 CASE STUDY: MUENSTERHOF

The Muensterhof case study demonstrates the application of the developed model to a realistic urban setting. The Muensterhof is a town square within the city of Zurich that currently lacks vegetation. In this study, we investigate the influence of vegetation and the impact on the atmospheric conditions such as air temperature, relative humidity and furthermore, the contribution of foliage to intercepting the short-wave radiation.

### 8.3.1 *Simulation setup*

The simulation is performed focusing on the Muensterhof square (see Fig. 8.15). Therefore, highest level of building details is found near the square and to increase the computation performance, the level of detail is reduced further away from the square. Similarly, the mesh is refined with highest level of refinement inside the Muensterhof square. Fig. 8.16 shows the surface layer close to the building walls with i) a single isolated tree inside the square, and ii) multiple tree configuration with 4 identical trees. In the first case, the numerical domain is discretized into 4 432 297 cells with minimum cell size of $2.38 \times 10^{-3}$ m$^3$ near the building and similarly, 4 453 514 cells in the second case with multiple trees.

The location of the trees are chosen based on the requirements of the city of Zurich. The eastern exit towards the river Limmat is required to be unrestricted to enable transport to and from Muensterhof square. Furthermore, the center of the Muensterhof is required to be unrestricted to provide space of public events. A possible region that can be utilized for trees is near the north-east corner of the square, as indicated in Fig. 8.16. Therefore, trees was placed at this location to study the influence of vegetation. The tree has a radius of 4 m and a high of 10 m with foliage base at 2 m. The simulation is driven with boundary conditions obtained from mesoscale simulation of Zurich, see Fig. 8.17. The solar radiation intensity and the wall function are applied as described in the previous sections. Similarly, the plant properties are set to similar that of the previous study of vegetation in the urban street canyon.

### 8.3.2 *Results and Discussion*

#### 8.3.2.1 *Single tree case*

The single tree case simulation is ran for two different configuration: *with* and *without* tree. Fig. 8.18 shows the air temperature $T$ (°C) at $z = 4$ m (i.e., $x - y$ plane) at 3 different time of the day (09:00, 12:00, and 15:00 (HH:MM)). The tree is outlined using a red outline to indicate its location. We observe that there is only a slight change in the air temperature contours. However, as it is hard to discern, Fig. 8.19 shows the air temperature difference between the *with* and *without* tree case. We also investigate additional times of the day (03:00, 06:00, 09:00, 12:00, 15:00, and 18:00). We see that the strongest change in air temperature occurs during day time, mainly when shading and plant transpiration occurs. Furthermore, the influence of a single tree is observed to affect the entire square and the strongest change in air temperature occurring at walls near the tree. However, we also observe that near the north-west region of the square, a hot spot is present near the wall. The cause of this is not obvious and could be due to changes in the flow field shifting the hot-spot as we also observe a cold-spot directly nearby. To take into account of possible time-shift effects, the air temperature difference is performed for the hourly-averaged values. Figure 8.20 shows the hourly-averaged air temperature difference between the cases *with* and *without* tree between 6 different times of the day (03:00 - 04:00, 06:00 - 07:00, 09:00 - 10:00, 12:00 - 13:00, 15:00 - 16:00, and 18:00 - 19:00 (HH:MM)). Comparing the hourly-averaged with the 10-minute averaged plot (i.e., Figure 8.19), we notice the strong difference in the air temperatures has diminished. This indicates that the high temperature difference was predominately due to a time-shift in the temperature profile. Studying the hourly-averaged temperature field, we see that a single tree generally provides cooling to the flow. Between 15:00 and 16:00, we observe that the building walls close to the tree are cooler with up to 1 °C drop in air temperature. During night-time, we see that the changes in the air temperature due to vegetation reduces. Fig. 8.21 shows the humidity ratio difference between the cases *with* (T) and *without* (NT) tree $\overline{w}_T - \overline{w}_{NT}$ (g kg$^{-1}$). We see that vegetation is an important source of humidity in the Muensterhof as high values of humidity ratio

is convected from the foliage especially during afternoon when solar radiation is present. Due to the wind direction, the humidity is most convected towards the building on the north-east side. It could potential have an influence on the moisture content of the building walls and thereby influencing cooling from evaporative drying of the surfaces.

Fig. 8.22 shows direct short-wave radiation intensity $q_{s,dir}$ ($\mathrm{W\,m^{-2}}$) and the interception of solar radition by the foliage. It is apparent that tree provides shading throughout the day. As we determined in the previous section, solar radiation is an important contributor to mean radiant temperature and the thermal comfort. Fig. 8.23 shows the mean radiant temperature difference between the cases *with* (T) and *without* (NT) tree $\overline{T}_{mrt,T} - \overline{T}_{mrt,NT}$ (°C) of the ground of the Muensterhof square. We see that shading provided by the tree substantially reduces the mean radiation temperature. We see that depending on the solar angle, the location of shading provided by the tree varies in time. However, during night below the foliage, we observe a rise in mean radiant temperature instead. This indicates the radiation trapping at the vicinity of the foliage. Thus, the location of the tree should be optimized to provide the maximum transpirative and cooling due to shading and minimize the negative effect of radiation trapping.

#### 8.3.2.2 *Multiple tree case*

To investigate further the influence of vegetation, we study the multiple tree configuration case and compare with the single tree setup. The setup and domain are described in Section 8.3.1. Fig. 8.24 shows the air temperature difference between *with* and *without* trees. Comparing with the single-tree case configuration (Fig. 8.20), we see a stronger change in air temperature, especially at the walls near the trees. Still, we also see that sometimes (i.e., between 09:00 and 10:00), the average Muensterhof temperature seems to be higher. However, we observe that the cooler regions are more extended than warmer regions. Fig. 8.25 shows the humidity ratio difference between the cases *with* and *without* trees. The figure shows that humidity inside the square is substantially higher (than compared to Fig. 8.21) due to the higher density of vegetation, especially near the trees. Due to this, we see that the wall regions near the trees are cooler than in the single tree case.

Furthermore, the study of mean radiant temperature change, Fig. 8.26, shows two important aspects of increasing the number of trees. Firstly, we see that below the trees during night, the mean radiant temperature is more positive than with a single tree (see Fig. 8.23). This indicates an increased radiation trapping due to higher vegetation density in the area. Secondly, we see that as there are more trees, more areas of the square are cast by shadow, resulting in a larger area with low mean radiation temperature. So, it indicates that more space in the square can provide comfort for the pedestrians. However, due to the location of tree, building and the sun's position, the tree shadow is predominant cast on the nearby buildings instead of the middle of the square where most pedestrians might travel. A better location for trees to cast a shadow would be at the middle of the square. However, due to regulatory constraints (as mentioned in Section 8.3.1), the present location is the only available area of planting trees. We see that, albeit a better site for trees to improve comfort, such regulations finally decide on the feasibility of natural cooling.

### 8.3.3 *Comparison of the cases*

In this study, we observe that the multiple tree case provides more cooling of the flow. Comparing Fig. 8.20 with Fig. 8.24, we see that air temperature is typically lower, especially near the trees. This observation correlates with the humidity ratio of the flow, i.e., Fig. 8.21 and Fig. 8.25. This indicates that the increased cooling is most likely due to the increasing transpirative cooling of the flow from the additional trees. To better understand the effect of adding trees in the square, the diurnal variation of the average thermal condition of the Muensterhof ground are compared. The spatial averaging is performed on the surface shown in Fig. 8.26. Fig. 8.27 shows the diurnal variation of the average ground surface temperature $\langle T \rangle_g$ (°C) and the average mean radiation temperature $\langle T_{mrt} \rangle_g$ (°C). It is apparent that adding trees improve (i.e., reduce) the ground surface temperature, as clarified by the difference plot (Fig. 8.27c). However, occasionally, the single tree is seen to outperform the multiple tree configuration. It is seen to occur during the morning (between 08:00 and 10:00) and the evening (between 15:00 and 18:00). A direct cause of this observation is not evident. It might be possibly due to the interplay between various environmental conditions such as air temperature, air relative humidity, total shading, soil moisture condition, wind speed, and wind direction. A variation in the flow configuration due to the additional sheltering from the plant or the increased humidity in the air may contribute to the changes in the surface cooling rate and thus the surface temperature. When comparing the mean radiation temperature of the surface (Fig. 8.27b and Fig. 8.27d), we observe that both cases are very similar to each other, indicating that the shadowing effect of both configurations is similar on the whole Muensterhof ground. Interestingly, it is apparent that during the night, more trees result in a larger rise in the mean radiant temperature. This is indicative of the negative impact of radiation trapping as observed in the previous street-canyon study. However, at daytime, we see the classical benefit of shading as observed in the previous street-canyon study, where maximum reduction in mean radiant temperature was seen to occur during peak solar hours. This implies that, in general, there will be an improvement in the comfort for pedestrians in the Muensterhof square with more trees. In the future, we aim to assess the thermal comfort

index (i.e., UTCI) directly inside such complex geometry. Due to computational constraints, it could not be calculated in this study.

### 8.3.4 *Conclusion*

The goal of the present study was to demonstrate the application of the developed numerical model in a realistic setup. Muensterhof in Zurich was chosen due to its high interest in urban reforestation by the Zurich city council (DE: Stadrat). The study showed how vegetation modifies the air temperature, humidity ratio and the shortwave radiation inside Muensterhof. We observed several parallels between the academic case of street-canyon and the present case study of real complex configuration. Phenomena observed in complex case such as transpirative cooling effect and the cooling due to shading were also observed in the previous study. In both studies, peak cooling was observed around solar noon when plant transpiration is highest and when the foliage absorbs most solar radiation. The benefit of the academic study was that one could perform a rigorous study on the interplay between various parameters such as soil moisture and the transpirative cooling and assess the influence of water stress on the cooling performance of a plant. However, to understand the true impact of vegetation in reality, cases studies such as in the Muensterhof square was needed. It was seen that the performance of the plant also depends on the flow and building configuration. Even though the trees provide shading throughout the day, the shadowing was seen to depend on the location, its proximity to the buildings, and the path of the sun. Due to the position of the trees, the shading was localized to a sub-region of the Muensterhof square. Though, it must be noted that the location was chosen based on city regulation. The exits of the square and the center of the square are required to be unhindered to enable transit and public event use, respectively. Thus, the city regulation constraints are also vital to accurately assess the impact of vegetation on the climate which cannot be taken into account in academic studies such as the street-canyon case.

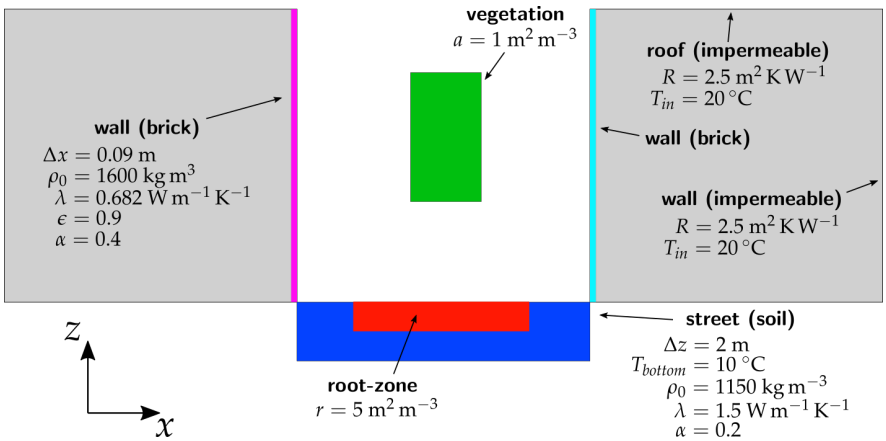


Figure 8.4: Description of the solid domain consisting of two impervious buildings of size $10 \times 50 \times 10$ m$^3$ ($x \times y \times z$) each with a brick layer of 0.09 m inside the street-canyon and a soil region at the street with vegetation roots. The temperature $T_{in}$, thermal resistance $R$, the density $\rho_0$, thermal conductivity $\lambda$, emissivity $\epsilon$, albedo $\alpha$, leaf area density $a$ and root area density $r$ and also provided.

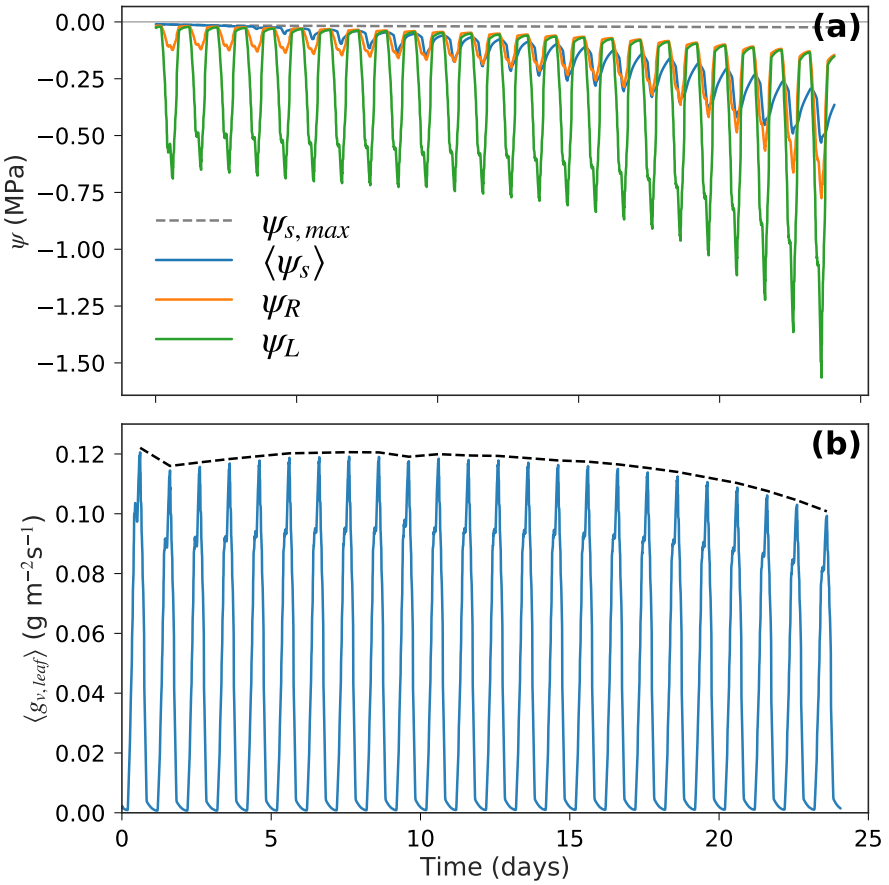


Figure 8.5: Long-term evolution of the plant properties changing due reducing water availability, simulated for 24 days: **(a)** bulk leaf water potential $\psi_L$ (MPa), bulk root water potential $\psi_R$ (MPa), rhizosphere-averaged soil water potential $\langle\psi_s\rangle$ (MPa) and maximum rhizosphere soil water potential $\psi_{s,max}$ (MPa) **(b)** average plant transpiration rate $\langle g_{v,leaf}\rangle$ (g m$^{-2}$ s$^{-1}$).

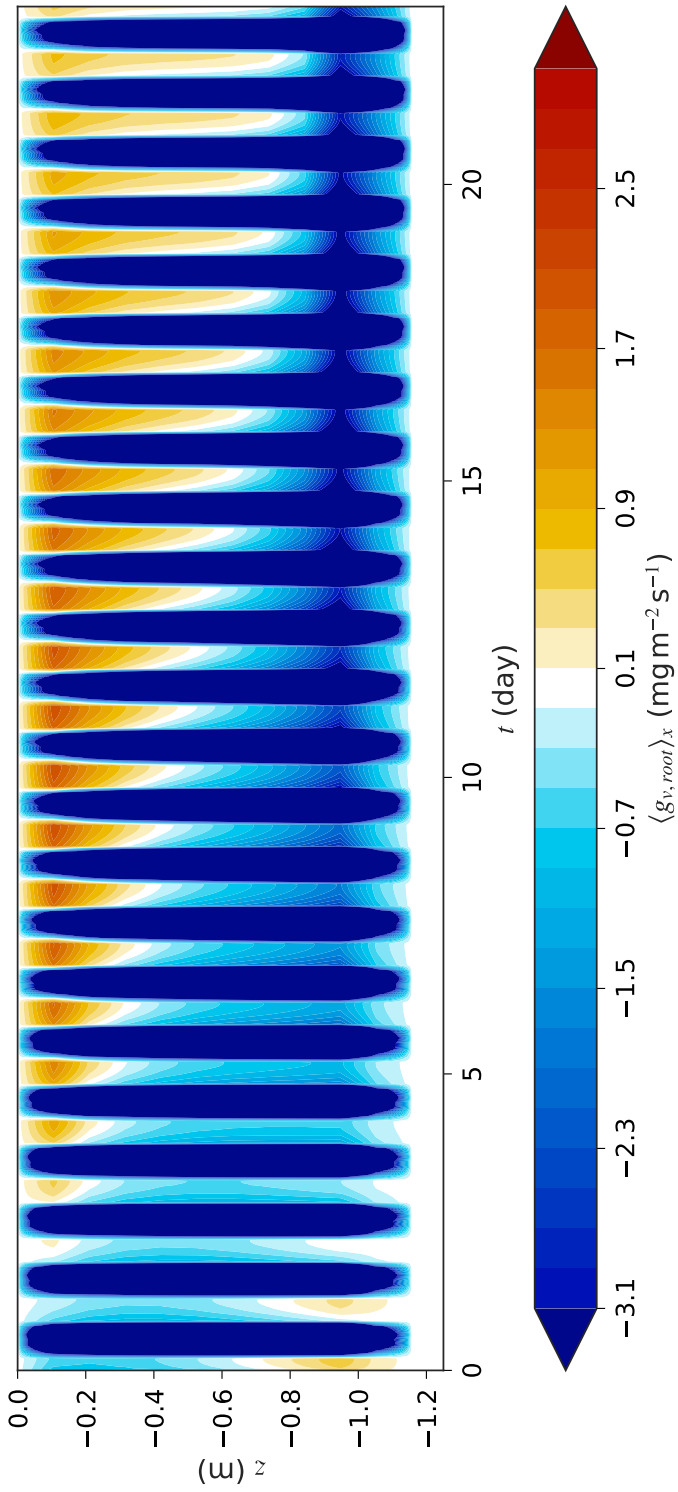


Figure 8.6: Time evolution of root water uptake vertical distribution $\langle g_{v,root} \rangle$ ($\mathrm{mg\,m^{-2}\,s^{-1}}$) (laterally-averaged). Negative value indicated root uptake from soil to roots and positive value indicates into soil.

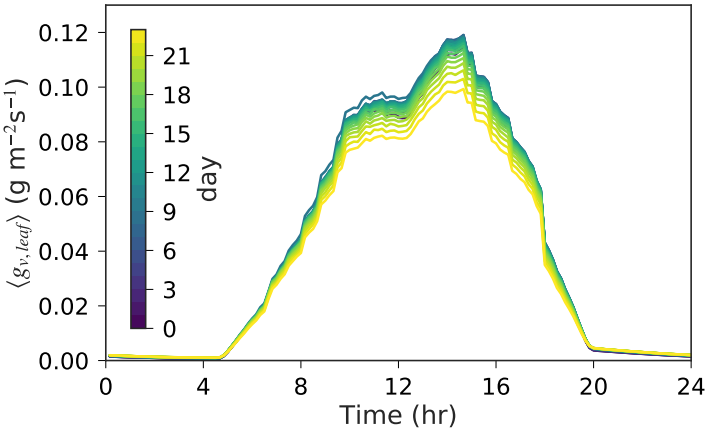


Figure 8.7: Hourly variation of plant transpiration rate $\langle g_{v,leaf} \rangle$ (g m$^{-2}$ s$^{-1}$ for all 24 days.

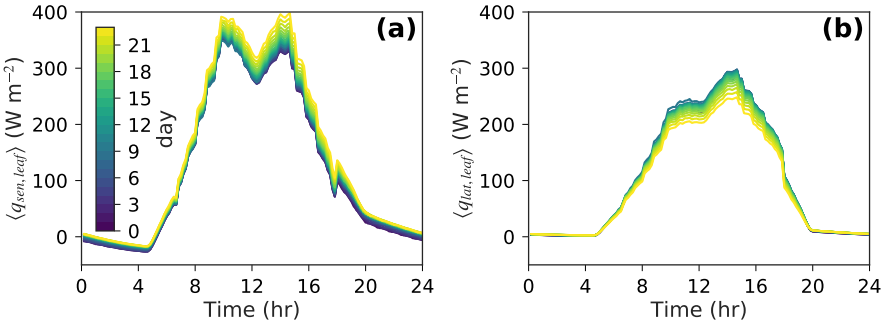


Figure 8.8: Hourly variation of plant energy fluxes changing due to reducing water availability: **(a)** average sensible heat flux $\langle q_{sen,leaf} \rangle$ (W m$^{-2}$) and **(b)** average latent heat flux $\langle q_{lat,leaf} \rangle$ (W m$^{-2}$).

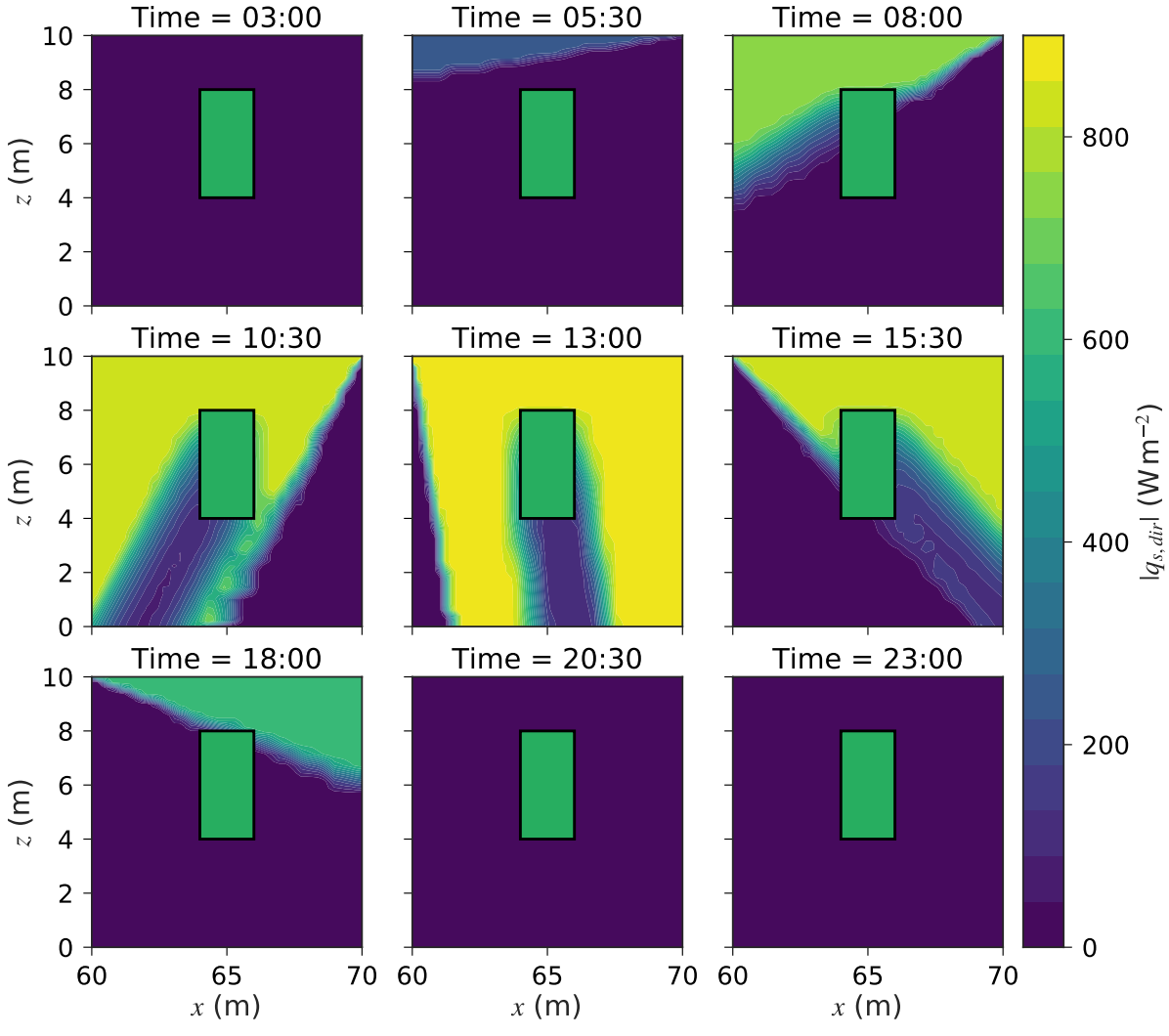


Figure 8.9: Direct short-wave radiation intensity $|q_{s,dir}|$ (W m$^{-2}$) inside the street-canyon where the vegetation zone is indicated by a green box. The plot shows the fields with a 150 minutes interval from 03:00 to 23:00 (HH:MM).

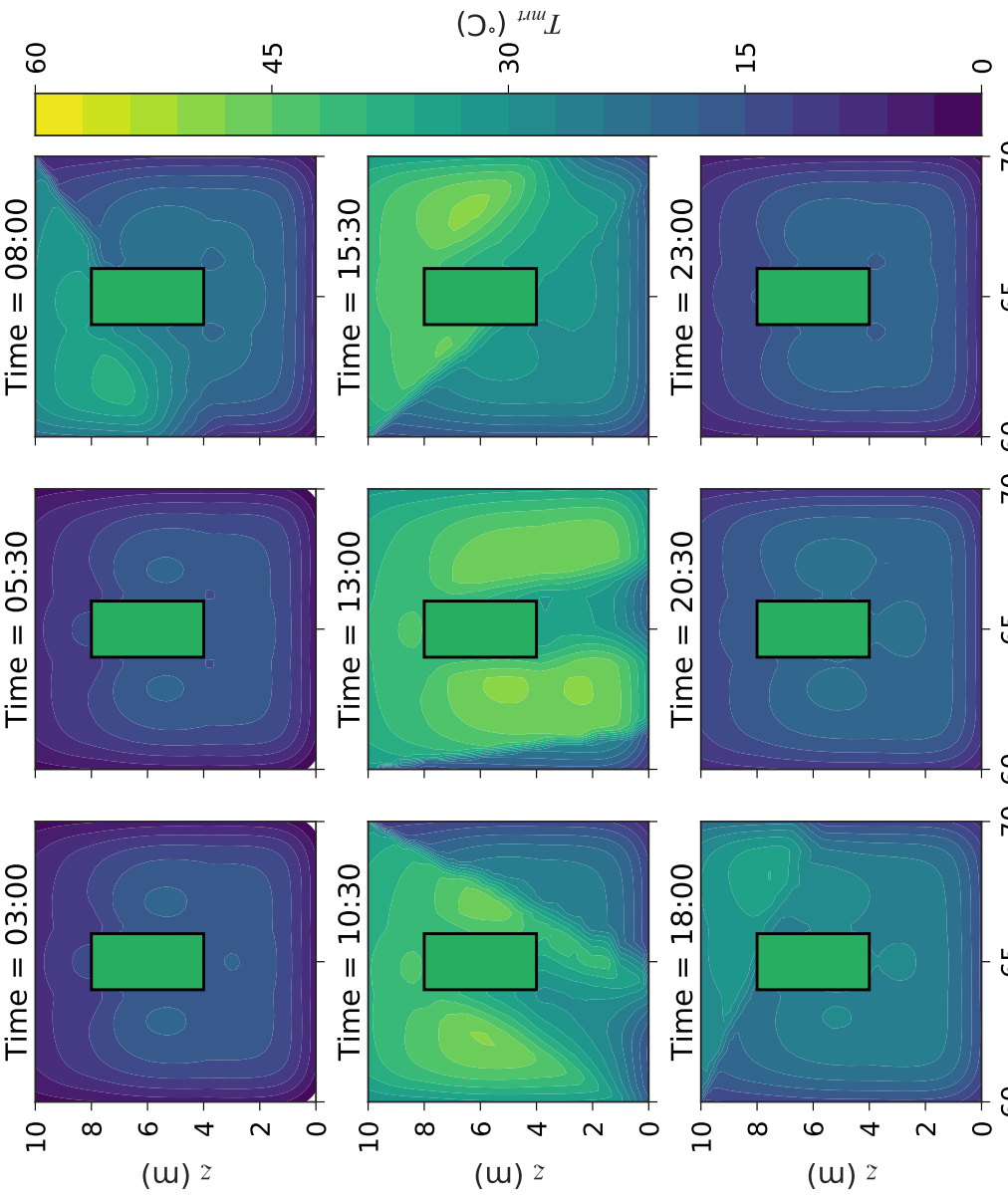


Figure 8.10: Mean radiant temperature $T_{mrt}$ (°C) inside the street-canyon where the vegetation zone is indicated by a green box. The plot shows the fields with a 150 minutes interval from 03:00 to 23:00 (HH:MM).

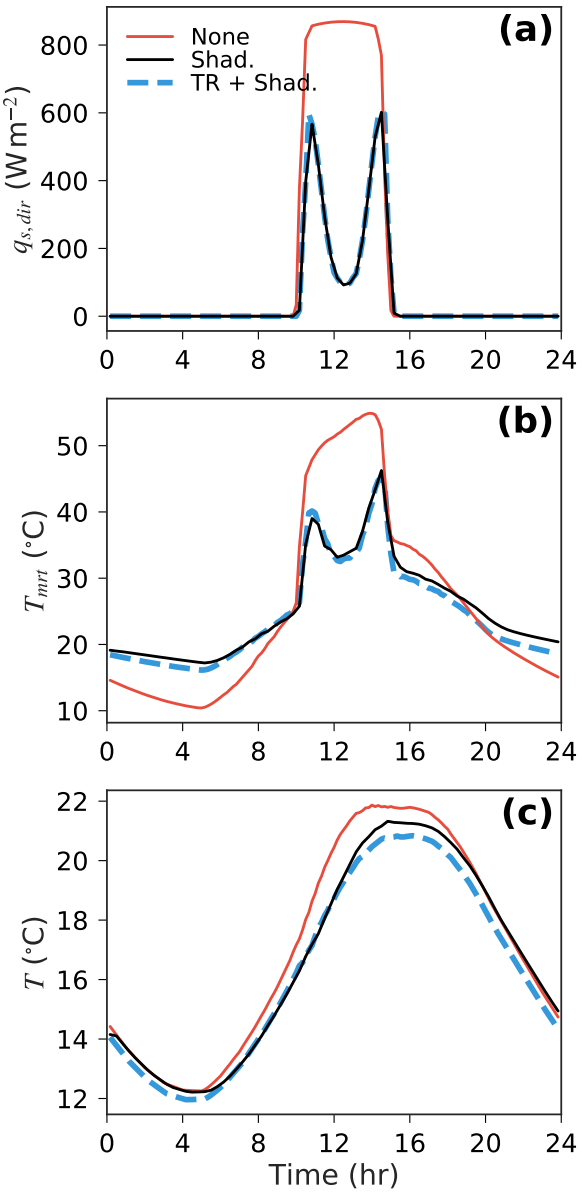


Figure 8.11: Diurnal profile below the vegetation at $(x, y, z) = (65, 125, 2)$ comparing three cases: no vegetation (*None*), vegetation with only shading (*Shad.*), and vegetation providing shading and transpirative cooling (*TR + Shad.*): **(a)** direct short-wave radiation intensity $q_{s,dir}$ (W m$^{-2}$), **(b)** mean radiant temperature $T_{mrt}$ (°C), and **(c)** air temperature $T$ (°C).

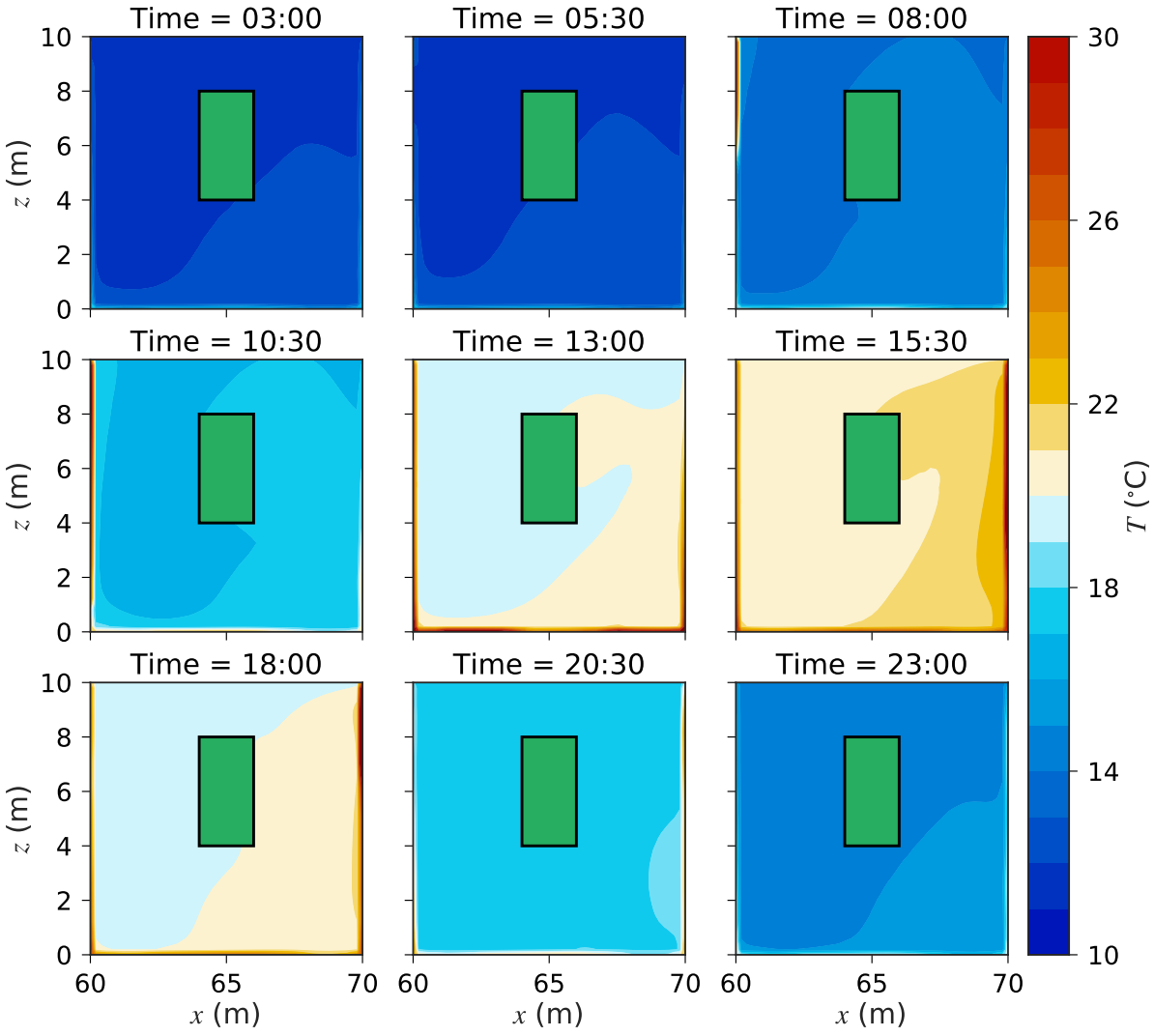


Figure 8.12: Air temperature $T$ (°C) inside the street-canyon where the vegetation zone is indicated by a green box. The plot shows the fields with a 150 minutes interval from 03:00 to 23:00 (HH:MM).

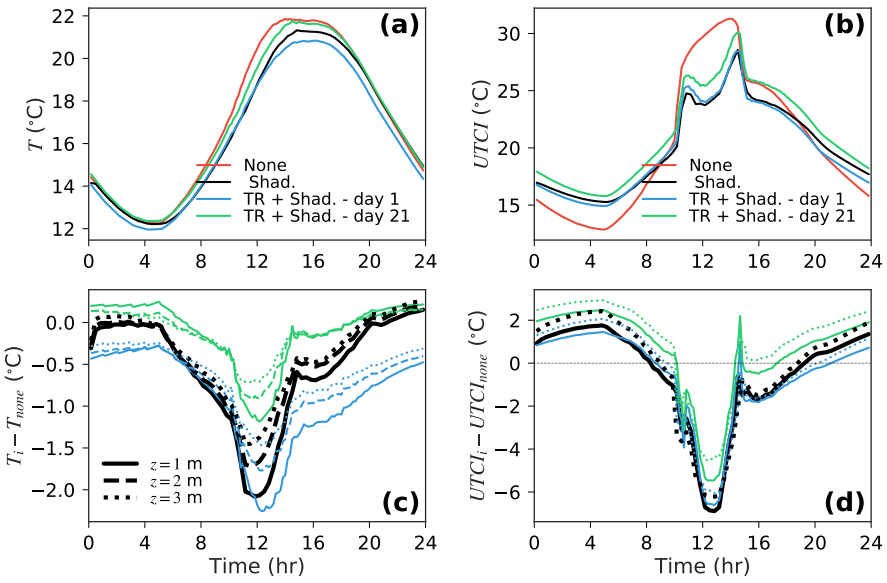


Figure 8.13: Diurnal profile below the vegetation for various cases: no vegetation (*None*), vegetation with only shading at day 1 (*Shad.*), vegetation providing shading and transpirative cooling at day 1 (*TR + Shad. - day 1*), and vegetation providing shading and transpirative cooling at day 1 (*TR + Shad. - day 21*): **(a)** air temperature $T$ (°C) at $(x, y) = (65, 125)$, height $z = 2$ m, **(b)** universal thermal climate index *UTCI* (°C) at $(x, y) = (65, 125)$, height $z = 2$ m, **(c)** Air temperature difference with no vegetation case at $z = [1, 2, 3]$ m, and **(d)** UTCI difference with no vegetation case at $z = [1, 3]$ m ($z = 2$ removed for brevity).

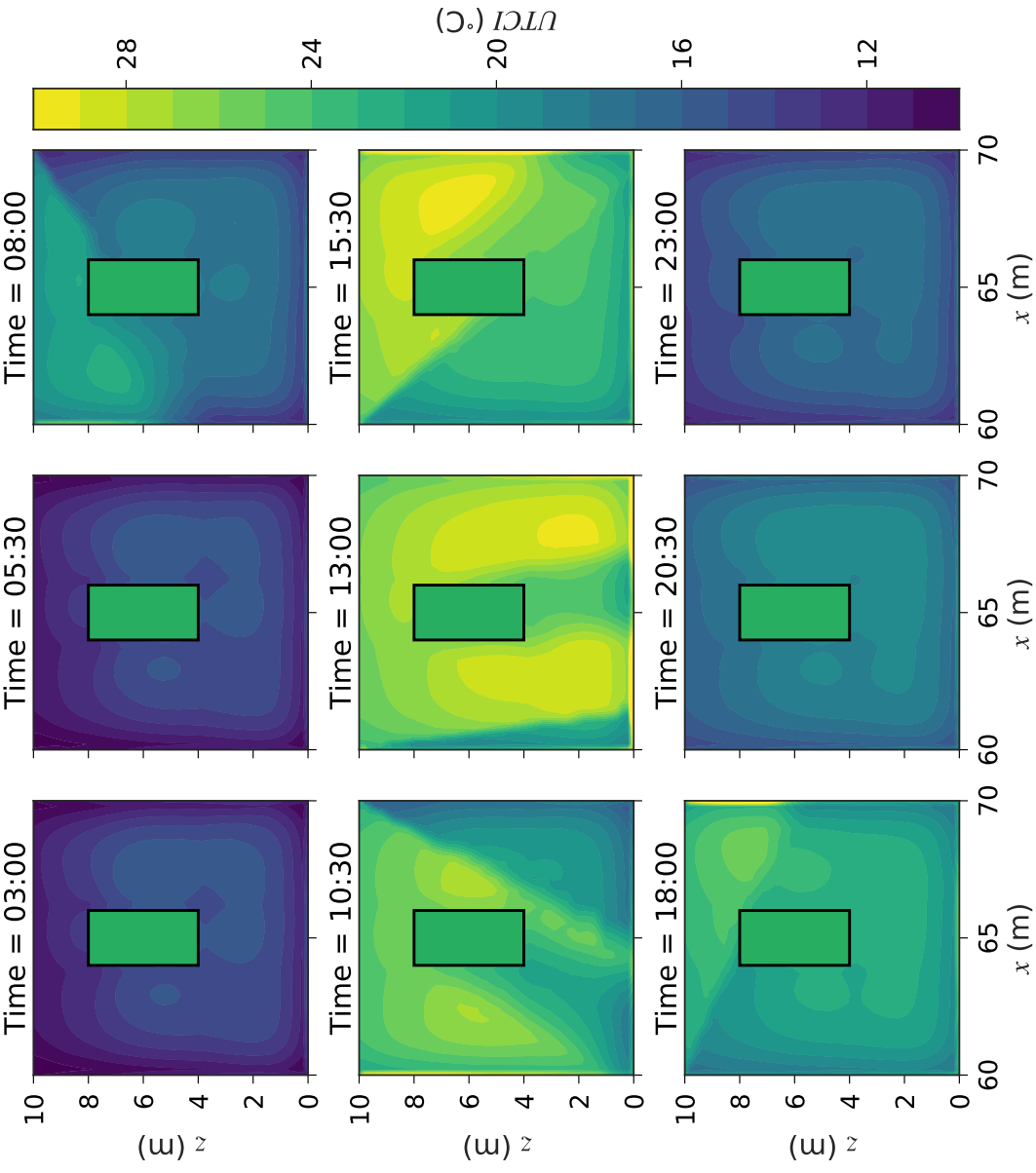


Figure 8.14: Universal thermal climate index *UTCI* (°C) inside the street-canyon where the vegetation zone is indicated by a green box. The plot shows the fields with a 150 minutes interval from 03:00 (HH:MM) to 23:00 (HH:MM).

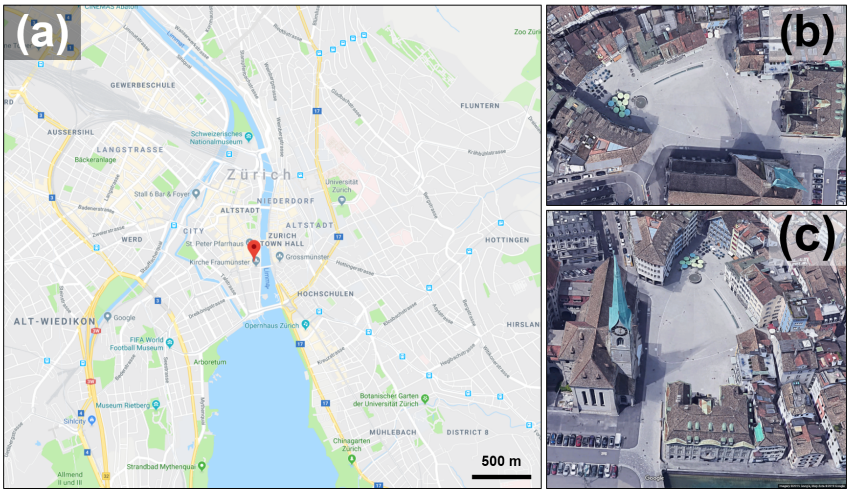


Figure 8.15: Satellite view of the Muensterhof obtained from Google Map Data showing: **(a)** map view, **(b)** top view (i.e., eagle eyes view), and **(c)** west-looking view of the Muensterhof square.

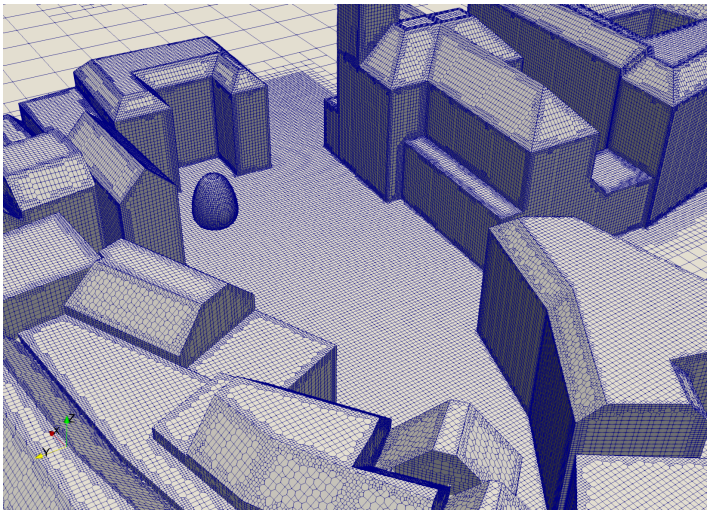

(a) A single isolated tree: $N_{cells} = 4\,432\,297$

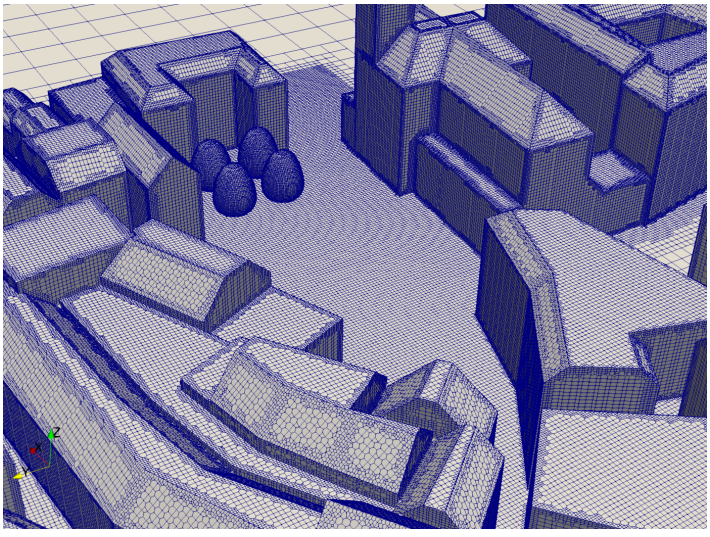

(b) A group of four trees: $N_{cells} = 4\,453\,514$

Figure 8.16: Simulation sub-domain showing the surface layer mesh refined closed to the building walls in Muensterhof.

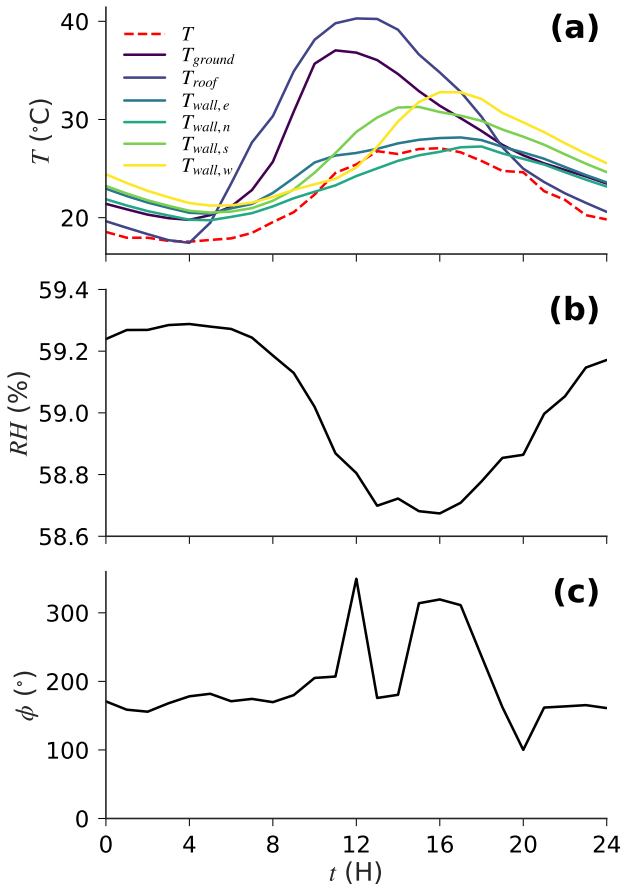


Figure 8.17: Boundary conditions obtained from mesoscale model: **(a)** air temperature $T$ (°C), ground temperature $T_{ground}$ (°C) (note: only for the ground outside the Muensterhof square), roof temperature $T_{roof}$ (°C), wall temperatures $T_{wall}$ (°C) for north (N), south (S), east (E), and west side (W); **(b)** relative humidity $RH$ (%); **(c)** wind direction $\phi$ (°).

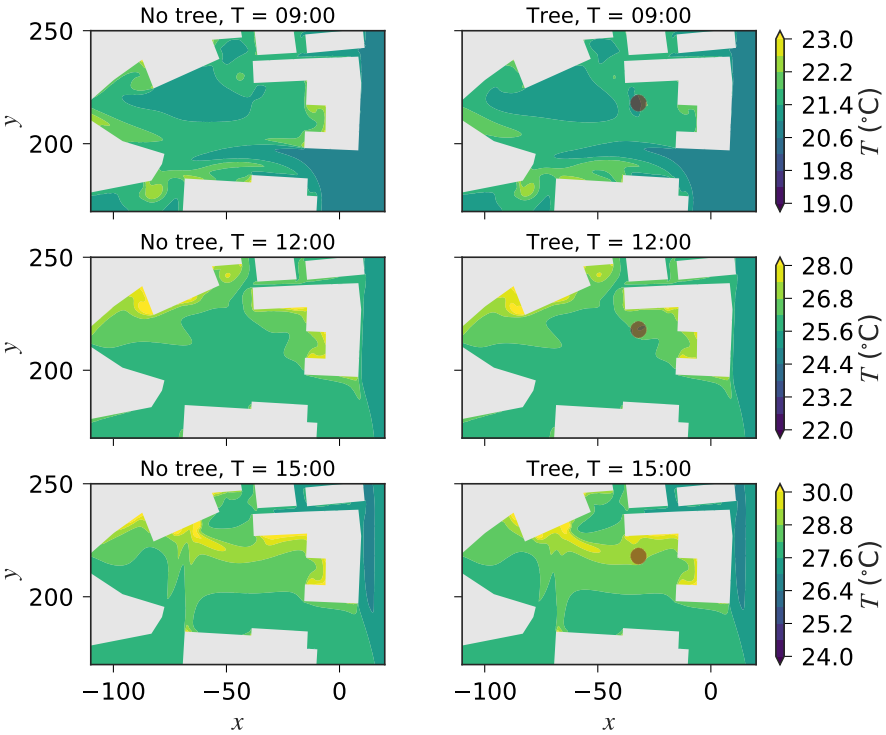


Figure 8.18: Air temperature $T$ (°C) at $z = 4$ m at 3 different times of the day (09:00, 12:00, and 15:00 (HH:MM)). The region of tree is indicated by a red outline.

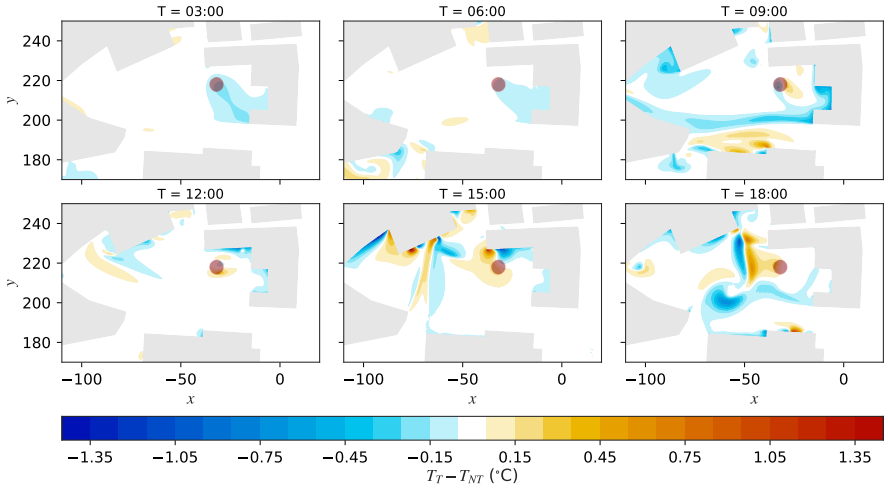


Figure 8.19: Air temperature difference $T_T - T_{NT}$ (°C) between the cases *with* (T) and *without* (NT) tree at $z = 4$ m at 6 different times of the day (03:00, 06:00, 09:00, 12:00, 15:00, and 18:00 (HH:MM)).

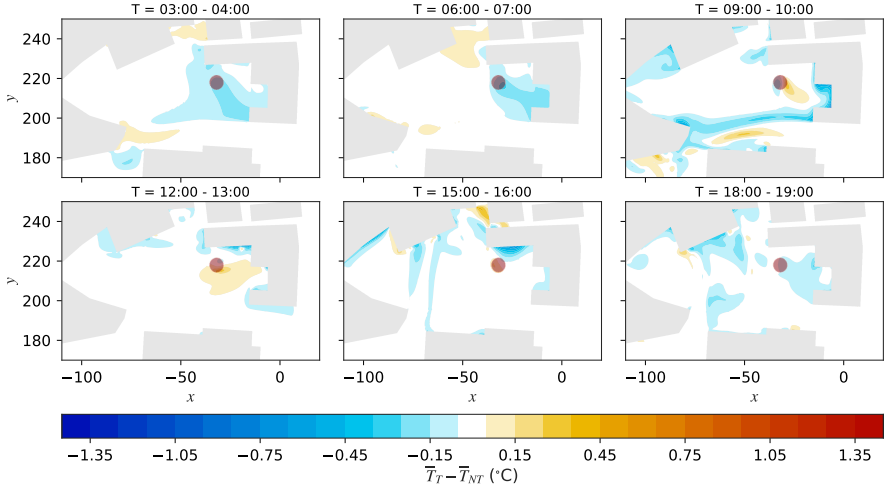


Figure 8.20: Hourly-averaged $\overline{T}_T - \overline{T}_{NT}$ (°C) at $z = 4$ m between 6 different times of the day (03:00 - 04:00, 06:00 - 07:00, 09:00 - 10:00, 12:00 - 13:00, 15:00 - 16:00, and 18:00 - 19:00).

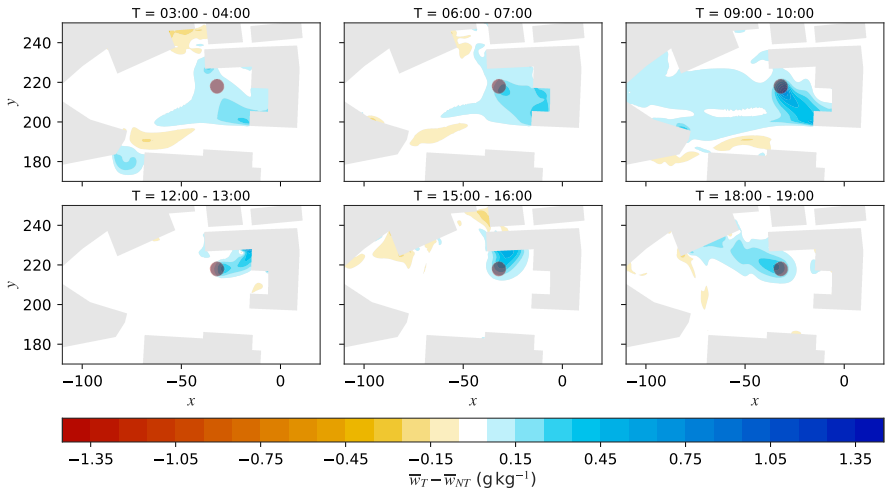


Figure 8.21: Hourly-averaged $\overline{w}_T - \overline{w}_{NT}$ (g kg$^{-1}$) at $z = 4$ m between 6 different times of the day (03:00 - 04:00, 06:00 - 07:00, 09:00 - 10:00, 12:00 - 13:00, 15:00 - 16:00, and 18:00 - 19:00).

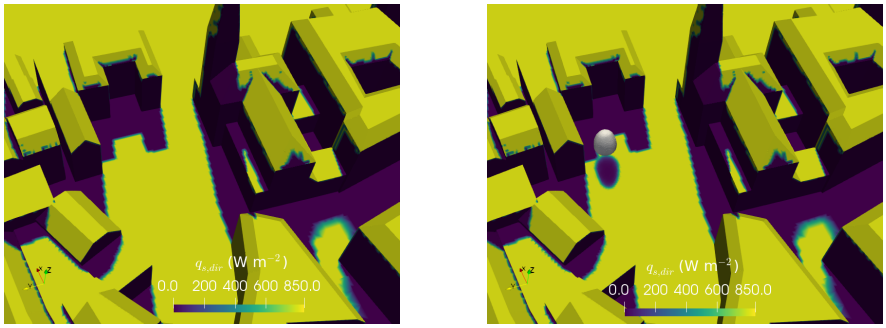


(a) 09:00 (b) 09:00

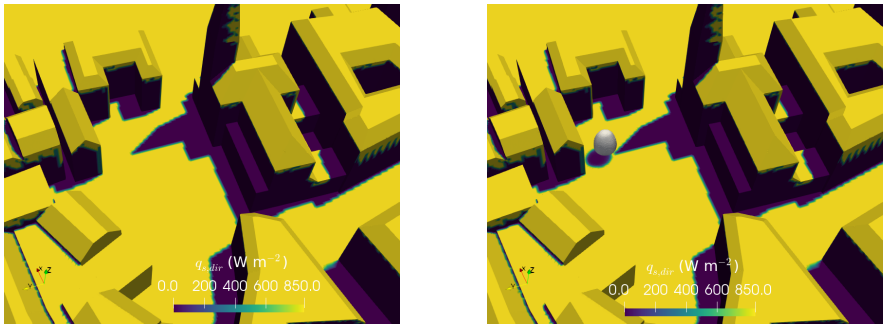


(c) 12:00 (d) 12:00

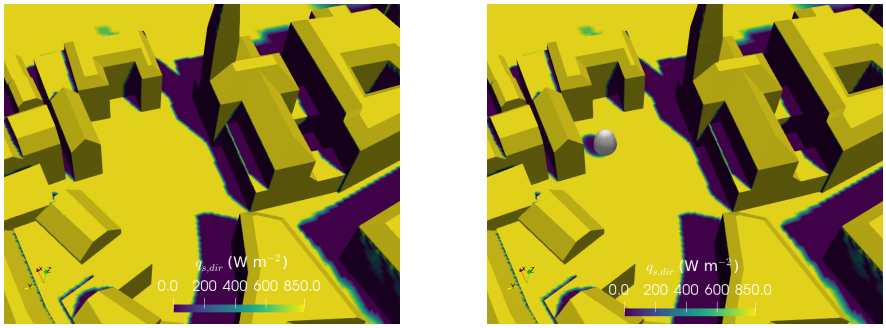


(e) 15:00 (f) 15:00

Figure 8.22: Direct short-wave radiation intensity $q_{s,dir}$ (W m$^{-2}$) arriving at the surface at 3 different time of the day (09:00, 12:00, and 15:00 pm). **(a,c,d)** *without* tree and **(b,d,f)** *with* tree. The region of tree is indicated by a white surface.

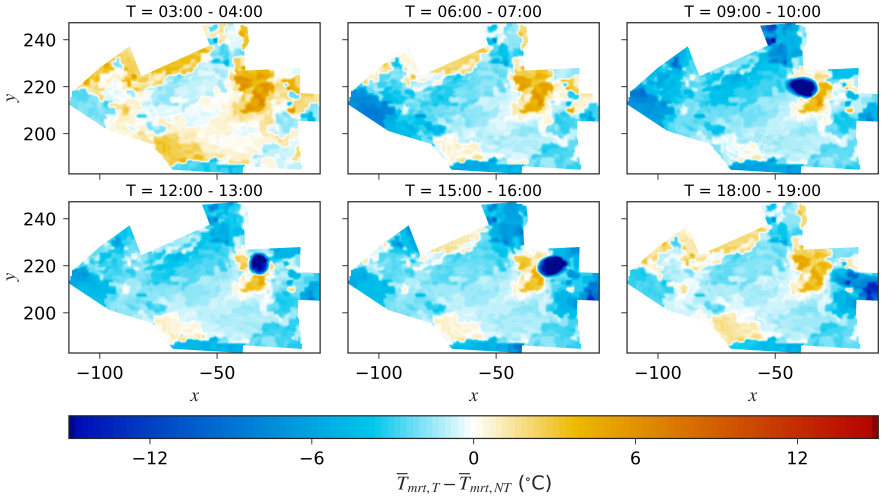


Figure 8.23: Hourly-averaged $\overline{T}_{mrt,T} - \overline{T}_{mrt,NT}$ (°C) at Muensterhof square ground between 6 different times of the day (03:00 - 04:00, 06:00 - 07:00, 09:00 - 10:00, 12:00 - 13:00, 15:00 - 16:00, and 18:00 - 19:00).

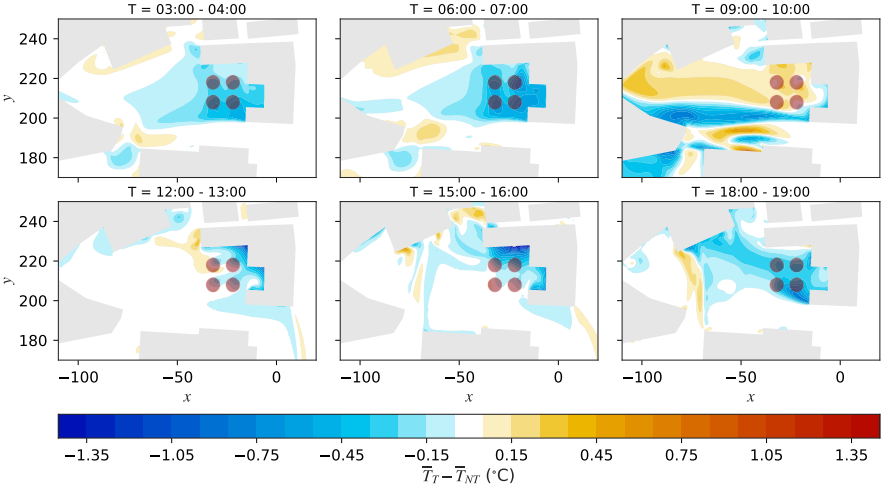


Figure 8.24: Hourly-averaged $\overline{T}_T - \overline{T}_{NT}$ (°C) at $z = 4$ m between 6 different times of the day (03:00 - 04:00, 06:00 - 07:00, 09:00 - 10:00, 12:00 - 13:00, 15:00 - 16:00, and 18:00 - 19:00).

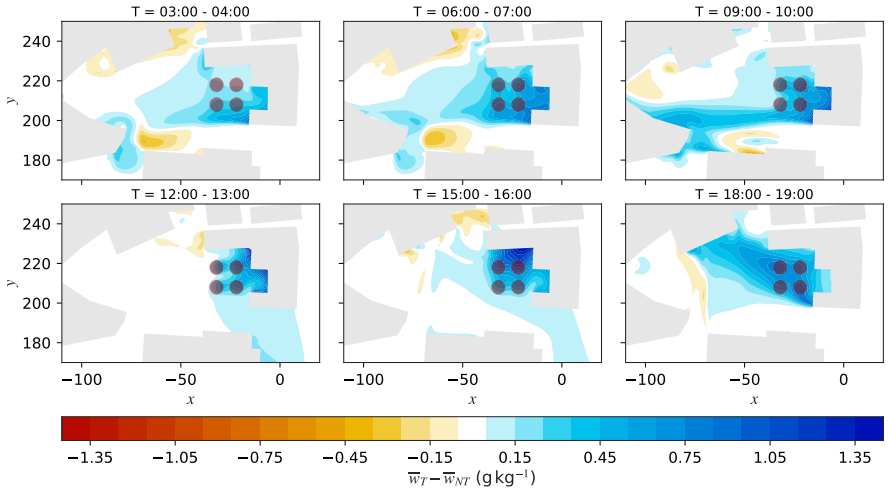


Figure 8.25: Hourly-averaged $\overline{w}_T - \overline{w}_{NT}$ (g kg$^{-1}$) at $z = 4$ m between 6 different times of the day (03:00 - 04:00, 06:00 - 07:00, 09:00 - 10:00, 12:00 - 13:00, 15:00 - 16:00, and 18:00 - 19:00).

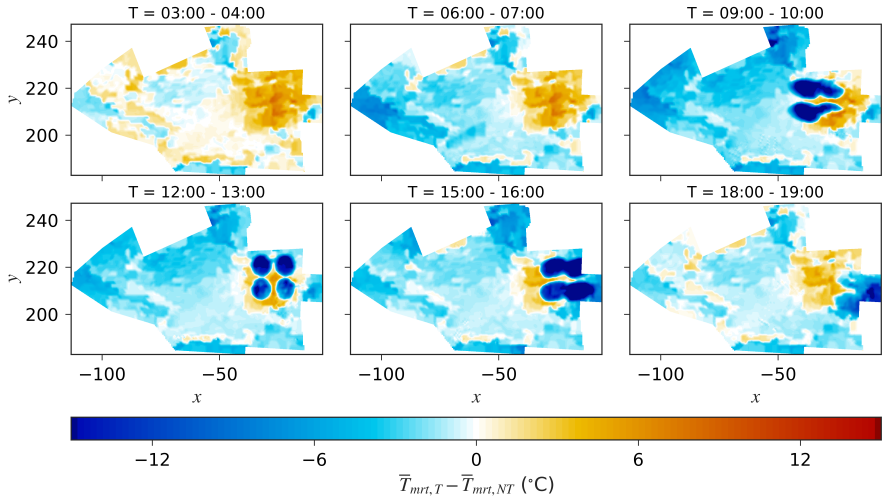


Figure 8.26: Hourly-averaged $\overline{T}_{mrt,T} - \overline{T}_{mrt,NT}$ (°C) at Muensterhof square ground between 6 different times of the day (03:00 - 04:00, 06:00 - 07:00, 09:00 - 10:00, 12:00 - 13:00, 15:00 - 16:00, and 18:00 - 19:00).

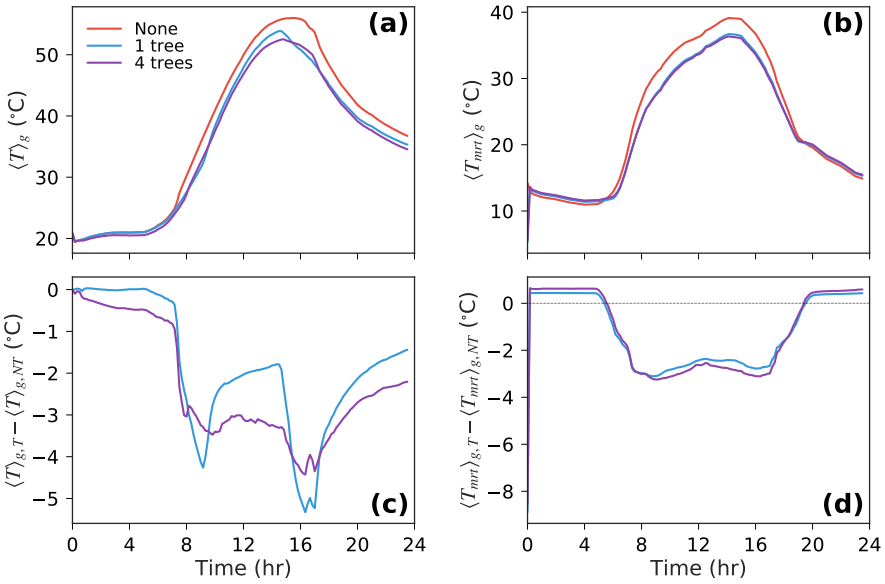


Figure 8.27: Diurnal profile comparing three cases: no trees (*None*), single tree (*1 tree*), four trees (*4 trees*): **(a)** average air temperature $\langle T \rangle_g$ (°C), **(b)** average mean radiant temperature $\langle T_{mrt} \rangle_g$ (°C), **(c)** air temperature difference with no tree case, and **(d)** mean radiant temperature with no tree case. The values are averaged over the entire Muensterhof square ground.

# 9

# CONCLUSION AND OUTLOOK

This chapter provides the conclusions obtained from the chapters in this thesis. The goal of the present thesis was to accurately assess the impact of vegetation at a microclimate scale, enabling a more accurate assessment of urban heat island (UHI) mitigation strategies for improving human health and thermal comfort in cities.

## 9.1 MAIN RESULTS AND CONCLUSIONS

The thesis employed both experimental and numerical approaches to provide an assessment of the impact of vegetation on the urban microclimate. The experimental campaigns consisted of wind tunnels measurements in an atmospheric boundary layer (ABL) wind tunnel where the impact of vegetation is determined by first studying the influence of vegetation on the airflow and secondly the influence of vegetation on the overall climate. The first measurement campaign focused on isothermal flow conditions where model and small natural trees were used. Smaller plants had to be used to ensure minimal blockage effect inside the tunnel. The impact on the airflow was determined using a load cell to measure the drag force and a particle image velocimetry (PIV) to measure the wake flow. The second measurement campaign focused on the hygrothermal flow parameters such as air temperature, relative humidity, solar radiation, leaf temperature along with the wake velocity statistics. Towards this, stereoscopic particle image velocimetry (SPIV), infrared thermography and hygrothermal sensor analysis were employed. To link the plant porosity to the wake flow configuration, X-ray tomography was employed to reconstruct the topology of the foliage. Furthermore, a need for an integrated approach that couples the conditions of the atmosphere with soil properties was seen

to determine the impact of water availability on the transpirative cooling potential. Therefore, in this thesis, a coupled model was developed to assess the hygrothermal impact of vegetation on the urban microclimate. The soil-plant-atmosphere continuum (SPAC) model was used to link the plant transpiration with the soil moisture. The developed numerical approach simultaneously resolved turbulence modification, radiation balance, heat and mass fluxes, and the sensitivity to soil moisture. Finally, the net effect of all these factors on the pedestrian thermal comfort was investigated using the mean radiant temperature and the universal thermal climate index (UTCI).

In this thesis, it was demonstrated that the behavior of natural trees can be approximated by model trees only if they have a similar aerodynamic porosity and if they are capable of reconfiguring at high wind speeds. The PIV measurements showed that low porosity model trees have a similar wake structure as of a natural cypress tree. In the study, it was evident that the foliage where branches and leaves deform due to airflow in both drag measurements and wake velocity statistics. It was seen that due to reconfiguration, the drag coefficient decays at high wind speeds. Young natural trees and model trees with artificial leaves showed reconfiguration resulting in a linear drag-force-wind speed relationship. The Vogel exponent was used to identify the strength of the reconfiguration. The study showed that the aerodynamic porosity and the drag coefficient are vital parameters that should be matched to those of the natural trees of interest. When studying the influence of reconfiguration of the plant on the flow field, the Vogel exponent of the model tree is a recommended parameter to compare model and natural trees.

It was observed that there is no apparent link between the spatial distribution of the plant porosity and the spatial variation in turbulent kinetic energy (TKE). The TKE intensity was seen to be governed by the net plant porosity and the outer geometry of the plant foliage that generates the shear-layer and they determine how the flow interacts with the upstream boundary layer profile. However, a parametric study of the plant drag forces showed that the wake TKE intensity is negatively correlated with the total plant porosity. At high plant porosity (i.e., very low plant drag), vegetation has less impact on the TKE. It was also shown that the aerodynamic and

optical porosities typically used in the wind tunnel studies do not reflect the true porosity distribution of the plant.

The diurnal variation in the leaf temperature and the net plant transpiration rate enabled us to quantify the diurnal hysteresis resulting from the stomatal response lag. Experimentally, the plant was seen to comprise of four stages *no-cooling* (i.e., the stage when stomata have not responded to the increase in solar radiation), *high-cooling* (i.e., when stomatal response tries to compensate for increased leaf temperature), *equilibrium* (i.e., when stomatal response and leaf temperature equilibrates) and *decaying-cooling* stage (i.e., when the transpiration rate starts to weaken).

The transpirative cooling effect of a single row of trees is highest at lower wind speed when $U < 1\ \mathrm{m\,s^{-1}}$. An increase in vegetation height was also seen to be beneficial as the top of the trees with higher leaf temperatures is further away from the pedestrian level. This ensures that the transpirative cooling effect is higher at the pedestrian level. To improve the UHI, it is best achieved by maximizing the sensible heat extraction. It was observed that increasing the vegetation density and tree height strongly correlated with an increase in sensible heat extraction and a reduction in air temperature. Thus, increasing vegetation in cities is seen to be the best strategy to improve global UHI. Moreover, cities should use a combination of tall wide-canopy trees, that can provide shading to urban surfaces, and pedestrian-level trees, that can provide transpirative cooling near the ground. Such a combination can maximize the cooling through shading and transpiration. It was seen that plant shading contributes more to the improvement of the pedestrian thermal comfort than the plant transpiration. The transpiration only has a direct influence on the plant vicinity air temperature and negligible effects on the thermal comfort measured through the Universal Thermal Climate Index (UTCI). In contrast, the shading provided by vegetation has a large influence as indicated by the drop in mean radiant temperature in the shadow. A large drop in the mean radiant temperature substantially improves the measured thermal comfort.

It was determined that the nocturnal radiation trapping due to the presence of vegetation is an important aspect that should be considered. At night, due to obstruction of long-wave radiation emission from urban surfaces to the sky by vegetation, the mean radiant temperature and equally UTCI is higher during night time. So, at night,

vegetation can dampen the cooling of cities and thereby negatively affect the UHI.

The plant is seen to redistribute the water from deep ground to the upper layer of the soil through hydraulic redistribution. This can have an important contribution to the water availability of the shallow-rooted plant species such as grass or small shrubs, showing the importance of a mixed vegetation setup in urban areas.

Finally, an important aspect that also plays an important role is water availability. With an increasing number of days without irrigation, the soil was seen to lose the available water for the plant. We observed that due to this, the transpiration rate decays over time, resulting in a reduced transpirative cooling as determined through an increase in sensible heat flux. Moreover, a prolonged period without irrigation showed that water stress increases exponentially every day.

### 9.1.1 *Contributions to the research field*

This thesis presents various novel applications of experimental and numerical techniques towards understanding the impact of vegetation on the urban microclimate. The contribution of this thesis consists of experimental understanding of the impact of vegetation on the airflow and the microclimate. Furthermore, a novel vegetation integrated urban microclimate model is presented to understand the influence of vegetation on the atmosphere, coupled with the soil properties. The scientific contributions can be summarized as as follows:

- Development of an integrated, multi-domain coupled vegetation model in OpenFOAM. The *air* domain solver and the *solid* domain solver is linked together with the soil-plant-atmosphere continuum (SPAC) modeling approach to model the water transport due to vegetation. An advanced stomatal model is implemented that responds to water availability in addition to the atmospheric evaporative demand (AED).

- Development a novel radiation modeling approach for describing short-wave and long-wave interaction of vegetation in an urban environment.

- Development of a thermal comfort index analysis technique that quantifies the impact of vegetation in an urban setting.

- A quantitative understanding of the sheltering provided by model and small natural trees and how it differs from a mature tree. The influence of vegetation on the airflow is studied in an atmospheric boundary layer (ABL) wind tunnel using small model and natural trees. In the study, the turbulent airflow behind the trees is studied using particle image velocimetry (PIV) measurement technique and is linked to the drag force measurements using a load cell.

- A high-resolution dataset of *Buxus sempervirens* obtained through multiple non-intrusive imaging techniques. The dataset consists of wake velocity statistics obtained through particle image velocimetry (PIV), plant foliage temperature using infrared thermography, diurnal variation of net plant transpiration rate using a mass balance, and a high-resolution the plant microstructure metrics using X-ray tomography. The high-resolution dataset can be employed for comparing with numerical models as demonstrated in Chapter 7

- A novel application of X-ray tomography to quantify the plant microstructure metrics plant porosity and the leaf area density distribution.

- A rigorous parametric study on the impact of vegetation on the transpirative cooling potential. An understanding is provided on how much environmental factors (i.e., wind speed, air temperature, relative humidity, and solar radiation intensity) and tree properties (i.e., leaf size, stomatal resistance, and leaf area density) can affect to the plant cooling performance and the pedestrian comfort.

- A study on the impact of vegetation on urban microclimate of street-canyon and the influence of water availability.

- Application of integrated vegetation model in a realistic setup of Muensterhof (Zurich, Switzerland) with a more realistic tree geometry.

## 9.2 OUTLOOK AND FURTHER RESEARCH

- *Improved radiation model*: Approaches such as discrete ordinate method (DOM) should be employed to explicitly model the absorption, scattering, and transmission of short-wave radiation through vegetation (Bailey et al. 2014; Gastellu-Etchegorry et al. 1996; Sinoquet et al. 2001).

- *Turbulence modeling*: The vegetation turbulence model can be expanded to investigate additional eddy-viscosity models such as $k-\omega$ or $k-\omega$ SST, Reynolds stress models (RSM), and even Large-eddy simulation (LES). A more complex, computationally expensive turbulence modeling approach has been shown to improve the prediction accuracy (Hiraoka 2011; Lopes et al. 2013; Yue et al. 2008).

- *Turbulence inside plant*: Refractive-index-matching (RIM) tunnel experiments can be employed to study the flow inside transparent models. The turbulence inside the foliage could be experimentally measured using transparent vegetation models in such tunnels (Bai and Katz 2014; Bai et al. 2012; Harshani et al. 2017; Weitzman et al. 2014). So, RIM experiments of model trees can be employed to validate and improve turbulence modeling of vegetation.

- *Validation of the full-model with field measurements*: One of the missing element in the present study is the validation of the full numerical model. Field measurements (such as the BUBBLE measurement campaign (Rotach et al. 2005)), can provide a means of validating the full numerical model. The validation requires the conditions in the soil region, and the measurements of the plant responses such as stomatal conductance, root conductance and xylem conductance.

- *Varying drag coefficient*: In this thesis, we demonstrated that the drag coefficient is a function of wind speed. In the future, this could be incorporated to improve the prediction of sheltering provided by vegetation.

- *Groundwater modeling*: The groundwater level was not modeled in the thesis. In the future, the water table can be a driving

boundary condition for assessing water availability providing a more accurate estimation of the soil moisture.

- *Precipitation and irrigation*: Soil moisture also depends on environmental conditions such as rainfall or irrigation. Therefore, modeling the change in soil moisture due to them can provide a more accurate estimation of the spatiotemporal variability in water availability for plants. Furthermore, rainfall dynamics such as rainwater drainage and rainwater runoff can additionally improve the prediction of the distribution of soil moisture.

- *Rain interception*: The interception of rain due to foliage is an important aspect of wind-driven rain. The present model can be extended to model the influence of vegetation on wind-driven rain.

- *Pollutant dispersion*: One of the fundamental aspects of vegetation is the wind sheltering provided by vegetation. The implication of this on the pollutant dispersion characteristics is an important aspect of future research.

- *Seasonal variation*: It is known that the leaf area density varies monthly for certain species. So, the shading and the sheltering provided by vegetation is dependent on the month. As deciduous species do not provide transpiration after autumn, the impact on transpirative cooling potential should be studied.

- *Nested simulation*: A nested simulation approach can be employed to drive the urban microclimate model with a large mescoscale climate model (e.g., COSMO). The advantage is to provide more realistic boundary conditions for assessing the impact of vegetation.

- *Biotic influences*: The hydraulic redistribution from deep-rooted plants was observed in this study. The influence of this on other species can be investigated in the future such as the physiology of surface-bounded grass layer.

- *Soil salinity*: The soil salinity (i.e., osmotic potential) plays an important role in plant physiology. Especially in cities, salt deposition during winter seasons can have adverse effects on the soil salinity, potentially impacting the plant health.

- *Sap flow*: The Cohesion-tension theory can be used to model water and sap transport in xylem and phloem, respectively, and the resulting water potential inside the plant. This approach can be an alternative to the presently used simplified bulk xylem transport model with a bulk value for the leaf, root, and xylem water potentials. The benefits include resolving the hydraulic architecture of the plant, the various xylem layers, and its influence on water transport. Plant water storage and release, known to affect the water transport dynamics, can be also be modeled.

- *Climate change*: The influence of climate change results in increased average air temperature, $CO_2$ concentration and a change in rainfall events. These environmental changes could have implications on the predicted transpirative cooling potential of vegetation.

- *Inverse uncertainty quantification*: Such approaches can be used to estimate bias of a mathematical model based on experimental data. The method can enable parameter calibration for the unknown parameters of the model.

- $C_4$ *plant species*: Investigating plant physiology and climatic impact of plants employing $C_4$ carbon fixation instead of the typical $C_3$ carbon fixation. The $C_4$ plants are known to employ a more efficient photosynthetic process with higher water use efficiency, outperforming at conditions with high water stress and higher temperature. Therefore, such a plant is ideal for surviving in urban climate. However, studies on urban thermal comfort impact of such plants are lacking.

- *Different climates*: The present thesis focused on the oceanic climate of Zurich (i.e., *Cfb*). The transpiration cooling potential of vegetation was seen to be directly dependent on the atmospheric evaporative demand (AED) and, so, studies on different climates such tropical climates (i.e., *Af, Am, Aw/As*; cities such as Singapore) or Mediterranean climates (i.e., *Csa, Csb, Csc*; cities such as Rome), can provide a more universal assessment of vegetation as UHI mitigation strategy.

- *City-scale assessment*: In the present thesis, the microclimate assessment has been confined to a city-square or smaller. In the future, the evaluation of the influence of vegetation can be expanded to the scale of a full city to determine the overall effect of vegetation in a city. Although, some aspects of the present modeling approach might need to be simplified to ensure computational tractability of the model.

- *Further case studies*: The influence of vegetation can be better understood through additional cases studies, investigating different tree-building configurations, various plant size, shape, species, density, and impact of building materials properties.

- *Application of machine learning*: Machine learning (ML) is a popular field of research now. Towards this growing demand and applicability, ML can be introduced at various facets of the present research. For example, the plant water transport model can be encoded into an ML model potentially providing a substantial improvement in the run-time computational performance.

# A

# THERMODYNAMICS OF MOIST AIR

## IDEAL GAS LAW

The ideal gas law is defined as:

$$p = \rho \frac{\mathcal{R}}{M} T \tag{A.1}$$

where $p$ is the pressure (Pa), $\rho$ is density ($\mathrm{kg\,m^{-3}}$), $\mathcal{R} = 8.314\,559\,8$ $\mathrm{J\,mol^{-1}K^{-1}}$ is universal gas constant, $M$ is molar mass ($\mathrm{kg\,mol^{-1}}$), and $T$ is temperature (K). The specific gas constant $R$ ($\mathrm{J\,kg^{-1}K^{-1}}$) is defined as:

$$R = \frac{\mathcal{R}}{M} \tag{A.2}$$

and substituting Eq. (A.2) into Eq. (A.1), we get:

$$p = \rho R T \tag{A.3}$$

or similarly:

$$p_i = \rho_i R_i T_i \tag{A.4}$$

## PARTIAL PRESSURES

Using Dalton's law of partial pressures, the pressure of moist air is assumed to be sum of partial pressure of dry air $p_a$ (Pa) and partial pressure of water vapor $p_v$ (Pa):

$$p = \sum_i p_i = p_v + p_a \tag{A.5}$$

We assuming that all the species are in thermal equilibrium ($T = T_v = T_a$) (K) and so:

$$p = (\rho_a R_a + \rho_v R_v)\, T \tag{A.6}$$

The molar mass of dry air and water vapor are $M_a = 18.0149$ g mol$^{-1}$ and $M_v = 28.964$ g mol$^{-1}$, respectively. The specific gas constant of dry air and water vapor are $R_a = 287.055$ J kg$^{-1}$K$^{-1}$ and $R_v = 461.5$ J kg$^{-1}$K$^{-1}$ , respectively (ASHRAE 2013).

The vapor pressure $p_v$ is related to relative humidity $\phi$ as follows:

$$\frac{p_v}{p_{vsat}} = \phi \tag{A.7}$$

where $p_{vsat}$ is the saturation vapor pressure. The relative humidity (RH) is also defined as RH $= \phi \times 100$. The saturation vapor pressure, $p_{vsat}$ (Pa), is determined directly from temperature as follows (Singh et al. 2002):

$$p_{vsat} = 610.78 \exp\left\{\frac{17.269\ (T - 273.15)}{T - 35.85}\right\} \qquad (0°\text{C} < t < 63°\text{C}) \tag{A.8}$$

where $t = T - 273.15$ (°C) or similarly (ASHRAE 2013):

$$p_{vsat} = \exp\left\{\frac{C_1}{T} + C_2 + C_3 T + C_4 T^2 + C_5 T^3 + C_6 \log(T)\right\} \tag{A.9}$$

$$(0°\text{C} < t < 200°\text{C}) \tag{A.10}$$

where $C_1 = -5.800\,220\,6 \times 10^3$, $C_2 = 1.391\,499\,3$, $C_3 = -4.864\,023\,9 \times 10^{-2}$, $C_4 = 4.176\,476\,8 \times 10^{-5}$, $C_5 = -1.445\,209\,3 \times 10^{-8}$, and $C_6 = 6.545\,967\,3$.

### MASS FRACTIONS

The mass of moist gas mixture is :

$$m = m_v + m_a \tag{A.11}$$

where it is composed of water vapor $m_v$ (kg) and dry air $m_a$ (kg).

### MASS CONCENTRATION

The mass concentration of species $i$, $x_i$ ($\mathrm{kg}_i\,\mathrm{kg}^{-1}$), is defined as:

$$x_i \equiv \frac{m_i}{m} = \frac{\rho_i}{\rho} \tag{A.12}$$

where $m_i$ ($\mathrm{kg}_i$) is the mass of species $i$, and $m$ (kg) is the total mass of the gas mixture. The mass fractions are related as follows:

$$\sum_i x_i = x_v + x_a = 1 \tag{A.13}$$

### SPECIFIC HUMIDITY

The specific humidity or mixing ratio $q$ ($\mathrm{kg}\,\mathrm{kg}^{-1}$) is defined as:

$$q \equiv \frac{m_v}{m} = \frac{\rho_v}{\rho} \tag{A.14}$$

where it the mass ratio of water vapor to the total mass. It also satisfies:

$$q = \frac{\rho - \rho_a}{\rho} \tag{A.15}$$

and so solving for total density $\rho$, we obtain:

$$\rho = \frac{\rho_a}{1 - q} \tag{A.16}$$

It is related to the humidity ratio $w$ ($\mathrm{kg}\,\mathrm{kg}^{-1}$) as follows:

$$q = \frac{w}{1 + w} \tag{A.17}$$

### HUMIDITY RATIO

The humidity ratio $w$ ($\mathrm{kg}\,\mathrm{kg}^{-1}$) (i.e., or moisture content or mixing ratio) is the ratio of mass of water vapor to dry air (ASHRAE 2013):

$$w \equiv \frac{m_v}{m_a} = \frac{x_v}{x_a} = \frac{\rho_v}{\rho_a} \tag{A.18}$$

Substituting, Eq. (A.13) into Eq. (A.18) we get

$$w = \frac{x_v}{1 - x_v} \tag{A.19}$$

We can rewrite Eq. (A.19) to determine $x_v$ from $w$:

$$x_v = \frac{w}{1 + w} \tag{A.20}$$

We can determine $w$ from $p_v$:

$$w = \frac{p_v / R_v T}{p_a / R_a T} = \frac{p_v}{p_a} \frac{R_a}{R_v} \tag{A.21}$$

and substituting Eq. (A.5) into Eq. (A.21), we get:

$$w = \frac{p_v}{p - p_v} \frac{R_a}{R_v} \tag{A.22}$$

and rewriting A.22 for $p_v$, we get:

$$p_v = \frac{pw}{R_a / R_v + w} \tag{A.23}$$

### ENTHALPY

The specific enthalpy $h$ ($\mathrm{J\,kg^{-1}}$) of a unit mass is defined as:

$$h = e + \frac{p}{\rho} \tag{A.24}$$

where $e$ ($\mathrm{J\,kg^{-1}}$) is the specific internal energy per unit mass.

**Assumption:** *We assume perfect gas.*

For perfect gas, we have:

$$\mathrm{d}e = c_v \,\mathrm{d}T \tag{A.25}$$

$$\mathrm{d}h = c_p \,\mathrm{d}T \tag{A.26}$$

where $c_v$ and $c_p$ are the specific heat capacity at constant volume and pressure, respectively.

**Assumption:** *We assume that the moist air is calorically perfect gas, i.e., $c_v$ = constant, $c_p$ = constant*

The specific enthalpy is therefore:

$$h = c_p \int_{T_{ref}}^{T} \mathrm{d}T = c_p \left(T - T_{ref}\right) \tag{A.27}$$

where we take $T_{ref}$ at the reference temperature ($t = 0$ °C).

**Assumption:** *We assume thermal equilibrium between all the mixtures, i.e., $T = T_a = T_v$ (K) (Defraeye 2011).*

**Assumption:** *We assume a binary gas mixture of dry air and water vapor. We assume $CO_2$ does not play a role in the conservation of energy and is simply a passive scalar.*

Therefore, the specific enthalpy of moist air is

$$h = \sum_i x_i h_i = x_a h_a + x_v h_v \tag{A.28}$$

where $x_a$ and $x_v$ (kg kg$^{-1}$) are dry air and vapor mass concentration, and $h_a$ and $h_v$ (J kg$^{-1}$) are:

$$h_a = c_{pa} \left(T - T_{ref}\right) \tag{A.29}$$

$$h_v = c_{pv} \left(T - T_{ref}\right) + L_v \tag{A.30}$$

where $L_v$ (J kg$^{-1}$) is the latent heat of vaporization (more accurately, it is referenced at the same reference temperature as $T_{ref}$). The reference temperature $T_{ref}$ (K) is usually taken to be $t = 0$°C, i.e., $T_{ref} = 273.15$ K and the latent heat of vaporization taken at the same temperature $L_v = 2.5 \times 10^6$ J kg$^{-1}$ at $t = 0$°C. Thus the specific heat of moist air $h$ (J kg$^{-1}$) becomes:

$$h = \left(x_a c_{pa} + x_v c_{pv}\right) \left(T - T_{ref}\right) + x_v L_v \tag{A.31}$$

where the total specific heat capacity of gas $c_p$ (J kg$^{-1}$ K$^{-1}$) is defined as:

$$c_p = x_a c_{pa} + x_v c_{pv} \tag{A.32}$$

# B

# CONSERVATION EQUATIONS OF MOIST FLUID FLOW

This appendix consists of detailed derivation of conservation of *mass*, *momentum*, and *energy* of moist fluid flow. Additional details are also provided in the thesis of Defraeye (2011). The following chapter derives the conservation equation in the conservative form.

## B.1 CONSERVATION PRINCIPLE

Let us consider a fluid flow in Euclidean vector space $(\mathbb{R}^3, ||\cdot||)$ with coordinate vector $\boldsymbol{x} = (x, y, z) \in \mathbb{R}^3$. The volume of fluid of interest (or control volume CV) is $\Omega \in \mathbb{R}^3$, bounded by a surface $\partial\Omega$. In the domain, any extensive property in $\Omega$ is defined as an integral of its intensive property:

$$\Phi(\boldsymbol{x}, t) \equiv \int_{\Omega} \phi(\boldsymbol{x}, t) \; dV \tag{B.1}$$

where $\Phi$ is the extensive property of interest, and $\phi$ is the intensive property. For example, the extensive property mass $m$ (kg), is the integral of intensity property density $\rho$ (kg m$^{-3}$) of the fluid.

The Reynolds transport theorem is defined as:

Rate of increase of $\Phi$ in domain $\Omega$
$=$
Net rate of transfer of $\phi$ due to *advection* at boundary $\partial\Omega$
$+$
Net rate of transfer of $\phi$ due to *diffusion* at boundary $\partial\Omega$
$+$
Net rate of transfer of $\phi$ within domain $\Omega$ (i.e., source/sink)

In simpler terms, the rate of increase of any extensive property $\Phi$ over time in the domain $\Omega$ is simply due to rate of transfer of the intensive property $\phi$ at the boundary of the domain $\Omega$ (i.e., $\partial\Omega$) due to *convection* and the net rate of transfer of intensive property $\phi$ within the domain $\Omega$ (i.e., introduced into the domain as source of sinks). It must be note that a *convection* is the sum of *advection* (transport due to velocity) and *diffusion* (transport due to molecular transfer). The rate of transfer of $\phi$ at the boundary is also commonly referred to as a *flux* of $\phi$ at the boundary. A mathematical formulation of the Reynolds transport theorem is given as:

$$\frac{\mathrm{d}}{\mathrm{d}t}\Phi(\boldsymbol{x},t) = \frac{\mathrm{d}}{\mathrm{d}t}\int_\Omega \phi \,\mathrm{d}V = -\int_{\partial\Omega} \phi\, \boldsymbol{u}\cdot\hat{\boldsymbol{n}}\,\mathrm{d}A + \int_\Omega s\,\mathrm{d}V \tag{B.2}$$

where $\boldsymbol{u}$ is velocity, $\hat{\boldsymbol{n}}$ is the normal vector (*pointing outward*, hence the negative sign), and $s$ is the *positive* source term in $\Omega$.

Using the divergence theorem, surface integral can be converted into volume integral, i.e.:

$$\int_{\partial\Omega} \phi\, \boldsymbol{u}\cdot\hat{\boldsymbol{n}}\,\mathrm{d}A = \int_\Omega \nabla\cdot(\phi\boldsymbol{u})\,\mathrm{d}V \tag{B.3}$$

and so B.2 becomes:

$$\frac{\mathrm{d}}{\mathrm{d}t}\int_\Omega \phi\,\mathrm{d}V = -\int_\Omega \nabla\cdot(\phi\boldsymbol{u})\,\mathrm{d}V + \int_\Omega s\,\mathrm{d}V \tag{B.4}$$

**Assumption:** *We assume $\phi$ is a continuous function both in space and time. So using Leibniz's rules, the integral and derivative can be rearranged.*

Using the Leibniz's rules, we have:

$$\frac{\mathrm{d}}{\mathrm{d}t}\int_\Omega \phi\,\mathrm{d}V = \int_\Omega \frac{\partial}{\partial t}\phi\,\mathrm{d}V \tag{B.5}$$

Therefore, Eq. (B.4) becomes:

$$\int_\Omega \frac{\partial}{\partial t}\phi\,\mathrm{d}V = -\int_\Omega \nabla\cdot(\phi\boldsymbol{u})\,\mathrm{d}V + \int_\Omega s\,\mathrm{d}V \tag{B.6}$$

and by combining the terms under the same integral simplifies to:

$$\int_{\Omega} \left( \frac{\partial}{\partial t}\phi + \nabla \cdot (\phi \boldsymbol{u}) - s \right) \, \mathrm{d}V = 0 \tag{B.7}$$

Therefore, the follow equation must also satisfy:

$$\frac{\partial \phi}{\partial t} + \nabla \cdot (\phi \boldsymbol{u}) = s \tag{B.8}$$

The resulting form in the well-known conservation form (or divergence form). Note that the second term in the LHS is a dyad or outer product, i.e.:

$$\phi \boldsymbol{u} \equiv \phi_i \boldsymbol{u}_j = \begin{pmatrix} \phi_1 \\ \phi_2 \\ \phi_3 \end{pmatrix} \begin{pmatrix} u_1 & u_2 & u_3 \end{pmatrix} = \begin{pmatrix} \phi_1 u_1 & \phi_1 u_2 & \phi_1 u_3 \\ \phi_2 u_1 & \phi_2 u_2 & \phi_2 u_3 \\ \phi_3 u_1 & \phi_3 u_2 & \phi_3 u_3 \end{pmatrix} \tag{B.9}$$

where the product of two rank-1 tensor (*vector*) results in a rank-2 tensor (*tensor*).

## B.2 CONSERVATION OF MASS

The mass of moist air $m$ (kg) is assumed to consist of dry air $m_a$ (kg), water vapor $m_v$ (kg) and carbon-dioxide (i.e., $CO_2$) $m_c$ (kg).

$$m \equiv \sum_i m_i = m_a + m_v + m_c \tag{B.10}$$

and equally

$$\rho \equiv \sum_i \rho_i = \rho_a + \rho_v + \rho_c \tag{B.11}$$

**Assumption:** *We do not model oxygen concentration change due to photosynthesis, i.e., $m_o = constant$.*

### B.2.1 *Deriving conservation of mass*

Applying the Reynolds transport theorem for mass, we can derive the conservation of mass in the fluid domain:

Rate of increase of *mass* in domain $\Omega$
=
Net rate of transfer of *density* by *advection* at boundary $\partial\Omega$
+
Net rate of transfer of *density* by *diffusion* at boundary $\partial\Omega$
+
Net rate of transfer of *density* within the domain $\Omega$ (source/sink)

The net mass of gas mixture in the domain is given as:

$$m = \int_\Omega \rho \, \mathrm{d}V \tag{B.12}$$

where $\rho$ ($\mathrm{kg\,m^{-3}}$) is density of the gas mixture. The conservation principle also applies for each individual species $i$ is given as:

$$m_i = \int_\Omega \rho_i \, \mathrm{d}V \tag{B.13}$$

The conservation of mass of individual species $i$ is given as:

$$\frac{\mathrm{d}}{\mathrm{d}t} m_i = \frac{\mathrm{d}}{\mathrm{d}t} \int_{\Omega} \rho_i \, \mathrm{d}V = -\int_{\partial\Omega} \boldsymbol{g}_i \cdot \hat{\boldsymbol{n}} \, \mathrm{d}A + \int_{\Omega} s_{\rho,i} \, \mathrm{d}V \tag{B.14}$$

where $\boldsymbol{g}_i$ ($\mathrm{kg\,m^{-2}\,s^{-1}}$) is the mass flux of species $i$ at the boundary, and $s_{\rho,i}$ ($\mathrm{kg\,m^{-3}\,s^{-1}}$) is the source of mass in domain $\Omega$. The rate of loss or gain of gas mixture at the boundary of the domain is sum of convection due bulk fluid motion and diffusion resulted by the concentration gradient. The net flux of density from the control volume $\Omega$ is a combined convection-diffusion equation:

$$\int_{\partial\Omega} \boldsymbol{g}_i \cdot \hat{\boldsymbol{n}} \, \mathrm{d}A = \int_{\partial\Omega} \left( -\rho D_i \nabla \frac{\rho_i}{\rho} + \rho_i \boldsymbol{u} \right) \cdot \hat{\boldsymbol{n}} \, \mathrm{d}A \tag{B.15}$$

where $\boldsymbol{g}_i$ ($\mathrm{kg\,m^{-2}\,s^{-1}}$) is the mass flux of species $i$, $x_i \equiv \rho_i / \rho$ ($\mathrm{kg\,kg^{-1}}$) is the mass concentration of species $i$, $D_i$ is the mass diffusivity ($\mathrm{m^2 s}$) of species $i$ and $\boldsymbol{u}$ is the bulk / mass-averaged velocity:

$$\boldsymbol{u} = \frac{\Sigma_i \rho_i \boldsymbol{u}_i}{\Sigma_i \rho_i} \tag{B.16}$$

The divergence theorem transforms B.15 into:

$$\int_{\partial\Omega} \boldsymbol{g}_i \cdot \hat{\boldsymbol{n}} \, \mathrm{d}A = \int_{\Omega} \nabla \cdot \boldsymbol{g}_i \, \mathrm{d}V = \int_{\Omega} \nabla \cdot \left( -\rho D_i \nabla \frac{\rho_i}{\rho} + \rho_i \boldsymbol{u} \right) \, \mathrm{d}V \tag{B.17}$$

The resulting conservation of mass for individual species is given as:

$$\frac{\partial \rho_i}{\partial t} + \nabla \cdot \left( \rho_i \boldsymbol{u} - \rho D_i \nabla \frac{\rho_i}{\rho} \right) = s_{\rho,i} \tag{B.18}$$

We have following system of equation for quaternary mixture of dry air, water vapor and $CO_2$:

$$\frac{\partial \rho_a}{\partial t} + \nabla \cdot \left( \rho_a \boldsymbol{u} - \rho D_a \nabla \frac{\rho_a}{\rho} \right) = s_{\rho,a} \tag{B.19}$$

$$\frac{\partial \rho_v}{\partial t} + \nabla \cdot \left( \rho_v \boldsymbol{u} - \rho D_v \nabla \frac{\rho_v}{\rho} \right) = s_{\rho,v} \tag{B.20}$$

$$\frac{\partial \rho_c}{\partial t} + \nabla \cdot \left( \rho_c \boldsymbol{u} - \rho D_c \nabla \frac{\rho_c}{\rho} \right) = s_{\rho,c} \tag{B.21}$$

where $s_{\rho,a}$, $s_{\rho,v}$ and $s_{\rho,c}$ are the mass source terms ($\mathrm{kg\,m^{-3}s^{-1}}$). The conservation of total mass is given as:

$$\frac{\partial \sum_i \rho_i}{\partial t} + \nabla \cdot \left( \left( \sum_i \rho_i \right) \boldsymbol{u} \right) = \sum_i s_{\rho,i} \tag{B.22}$$

### B.2.2 *Source of mass*

**Assumption:** *We assume there is no dry air generated in the fluid,* $s_{\rho,a} = 0$.

**Assumption:** *We assume that the source of water vapor is only due to leaf transpiration, i.e.,* $s_{\rho,v} = g_{v,leaf}$. *Water vapor condensation to water droplets or droplet evaporation and sublimation from ice is neglected.*

The leaves in control volumes $\Omega$ generate water vapour (from the transpiration process) and extract $CO_2$ during photosynthesis. Therefore, the source of water vapour and $CO_2$ in control volume is:

$$s_{\rho,v} = a\, g_{v,leaf} \tag{B.23}$$

$$s_{\rho,c} = a\, g_{c,leaf} \tag{B.24}$$

where $a$ is the leaf area density ($\mathrm{m^2m^{-3}}$), and $g_{v,leaf}$ ($\mathrm{kg\,m^{-2}s^{-1}}$) and $g_{c,leaf}$ ($\mathrm{kg\,m^{-2}s^{-1}}$) are the water vapour and $CO_2$ mass flux from the surface of the leaf.

Thus the conservation of mass of gas mixture is written as:

$$\frac{\partial \rho}{\partial t} + \nabla \cdot (\rho \boldsymbol{u}) = s_{\rho,v} + s_{\rho,c} \tag{B.25}$$

**Assumption:** *The order of magnitude of water vapor mass source* $\mathcal{O}\left(s_{\rho,v}\right) \approx 10^{-4}$ *and* $CO_2$ *mass source* $\mathcal{O}\left(s_{\rho,c}\right) \approx 10^{-6}$ *(Hiraoka 2005). Therefore the mass source of* $CO_2$ *is negligible compared to water vapour.*

**Assumption:** *The continuity equation is used to solve the momentum equation. In the momentum equation, the momentum contribution due to the mass source can be assumed to be negligible w.r.t to the drag force terms.*

Therefore, when solving the Navier-Stokes equations, the conservation of mass can be simplified to

$$\frac{\partial \rho}{\partial t} + \nabla \cdot (\rho \boldsymbol{u}) = 0 \tag{B.26}$$

## B.3 CONSERVATION OF MOMENTUM

### B.3.1 *Newton's second law of motion*

Newton's second law of motion is given as:

$$\boldsymbol{F} = \frac{\mathrm{d}}{\mathrm{d}t} m\boldsymbol{u} = \frac{\mathrm{d}}{\mathrm{d}t} \int_{\Omega} \rho \boldsymbol{u} \, \mathrm{d}V \tag{B.27}$$

where $\boldsymbol{F}$ (N) is the net force. The forces that act on the fluid are body forces (directly on volumetric mass) such as gravitational, electric, magnetic and if we have vegetation if modeled as porous media (source/sink). The vegetation is not directly modeled, but their contribution to the fluid is taken as source and sink terms in conservation equations. The surface forces are acting on the surface of the fluid, such as pressure force, normal and shear stresses on the surface. These contributions can be regarded as influences from neighboring fluid parcels.

### B.3.2 *Deriving conservation of momentum*

Conservation of momentum is given as:

Rate of increase of *momentum* in $\Omega$
$=$
Net rate of transfer of *momentum* by *advection* at the boundary $\partial\Omega$
$+$
Net rate of transfer of *momentum* by *diffusion* at the boundary $\partial\Omega$
$+$
Net rate of transfer of *momentum* by *external forces* on domain $\Omega$
$+$

Net rate of transfer of *momentum* within $\Omega$
(source/sinks)

In addition to the convective loss of momentum at the boundary, in Reynolds transport theorem, stress at the boundary of the domain results in loss of momentum. The Cauchy stress tensor $\bar{\bar{\sigma}}$ (Pa or $\mathrm{N\,m^{-2}}$ or $\mathrm{kg\,m^{-1}\,s^{-2}}$) is defined as:

$$\bar{\bar{\sigma}} = \begin{pmatrix} \sigma_{11} & \sigma_{12} & \sigma_{13} \\ \sigma_{21} & \sigma_{22} & \sigma_{23} \\ \sigma_{31} & \sigma_{32} & \sigma_{33} \end{pmatrix} = \begin{pmatrix} \sigma_x & \tau_{xy} & \tau_{xz} \\ \tau_{yx} & \sigma_y & \tau_{yz} \\ \tau_{zx} & \tau_{zy} & \sigma_z \end{pmatrix} \tag{B.28}$$

where the diagonal terms are normal stresses and the non-diagonal terms are the shear stresses.

The resulting Reynolds transport theorem for momentum equation of a gas mixture,

$$\boldsymbol{F} = \frac{\mathrm{d}}{\mathrm{d}t}\int_{\Omega} \rho \boldsymbol{u}\, \mathrm{d}V = -\int_{\partial\Omega} (\rho \boldsymbol{u}\boldsymbol{u} - \bar{\bar{\sigma}}) \cdot \hat{\boldsymbol{n}}\, \mathrm{d}A + \int_{\Omega} \boldsymbol{f}\, \mathrm{d}V + \int_{\Omega} \boldsymbol{s}_u\, \mathrm{d}V \tag{B.29}$$

Applying the divergence theorem, we get

$$\frac{\mathrm{d}}{\mathrm{d}t}\int_{\Omega} \rho \boldsymbol{u}\, \mathrm{d}V = -\int_{\Omega} \nabla \cdot (\rho \boldsymbol{u}\boldsymbol{u})\ \mathrm{d}V + \int_{\Omega} \nabla \cdot \bar{\bar{\sigma}}\, \mathrm{d}V + \int_{\Omega} \boldsymbol{f}\, \mathrm{d}V + \int_{\Omega} \boldsymbol{s}_u\, \mathrm{d}V \tag{B.30}$$

And combining under same integral, assuming momentum is continuous in space and time:

$$\int_{\Omega} \left[ \frac{\partial}{\partial t} (\rho \boldsymbol{u}) + \nabla \cdot (\rho \boldsymbol{u}\boldsymbol{u}) - \nabla \cdot \bar{\bar{\sigma}} - \boldsymbol{f} - \boldsymbol{s}_u \right] \mathrm{d}V = 0 \tag{B.31}$$

Therefore, the following relationship also satisfies ($\mathrm{N\,m^{-3}}$):

$$\frac{\partial}{\partial t} (\rho \boldsymbol{u}) + \nabla \cdot (\rho \boldsymbol{u}\boldsymbol{u}) = \nabla \cdot \bar{\bar{\sigma}} + \boldsymbol{f} + \boldsymbol{s}_u \tag{B.32}$$

The Cauchy stress tensor $\bar{\bar{\sigma}}$ ($\mathrm{N\,m^{-2}}$) can be decomposed into the deviatoric and the hydrostatic component:

$$\bar{\bar{\sigma}} = \underbrace{\frac{1}{3}\mathrm{tr}\left(\bar{\bar{\sigma}}\right)\mathbf{I}}_{\text{hydrostatic}} + \underbrace{\bar{\bar{\sigma}} - \frac{1}{3}\mathrm{tr}\left(\bar{\bar{\sigma}}\right)\mathbf{I}}_{\text{deviatoric}} \tag{B.33}$$

The hydrostatic stress component is the isotropic pressure, $\mathrm{tr}\left(\bar{\bar{\sigma}}\right)/3 = -p$ and the deviatoric component is the shear-stress tensor $\bar{\bar{\tau}}$. Thus, the Cauchy stress tensor becomes:

$$\bar{\bar{\sigma}} = -p\mathbf{I} + \bar{\bar{\tau}} \tag{B.34}$$

**Assumption:** *We assume Newtonian fluid, and therefore the viscous shear stress is symmetric and assumed to be linearly proportional to the local strain rate and equivalently the velocity gradient, i.e.,* $\tau_{ij} \propto \frac{1}{2}\left(\frac{\partial u_i}{\partial x_j} + \frac{\partial u_j}{\partial x_i}\right)$.

Applying the Newtonian fluid hypothesis:

$$\bar{\bar{\tau}} = \mu\left(\nabla\boldsymbol{u} + \left(\nabla\boldsymbol{u}\right)^T - \frac{2}{3}\left(\nabla\cdot\boldsymbol{u}\right)\mathbf{I}\right) + \lambda\left(\nabla\cdot\boldsymbol{u}\right)\mathbf{I} \tag{B.35}$$

where $\mu$ ($\mathrm{N\,s\,m^{-2}}$ or $\mathrm{kg\,m^{-1}\,s^{-1}}$) is the first coefficient of viscosity (i.e. dynamic viscosity), and $\lambda$ ($\mathrm{N\,s\,m^{-2}}$) is the second coefficient of viscosity. Thus:

$$\begin{aligned}\frac{\partial}{\partial t}\left(\rho\boldsymbol{u}\right) + \nabla\cdot\left(\rho\boldsymbol{u}\boldsymbol{u}\right) = \\ \nabla\cdot\left[-p\mathbf{I} + \mu\left(\nabla\boldsymbol{u} + \left(\nabla\boldsymbol{u}\right)^T - \frac{2}{3}\left(\nabla\cdot\boldsymbol{u}\right)\mathbf{I}\right) + \lambda\left(\nabla\cdot\boldsymbol{u}\right)\mathbf{I}\right] \\ + \boldsymbol{f} + \boldsymbol{s}_u\end{aligned} \tag{B.36}$$

and so:

$$\begin{aligned}\frac{\partial}{\partial t}\left(\rho\boldsymbol{u}\right) + \nabla\cdot\left(\rho\boldsymbol{u}\boldsymbol{u}\right) = -\nabla p + \nabla\cdot\left[\mu\left(\nabla\boldsymbol{u} + \left(\nabla\boldsymbol{u}\right)^T\right)\right] \\ + \nabla\cdot\left[\left(\lambda - \frac{2}{3}\mu\right)\left(\nabla\cdot\boldsymbol{u}\right)\mathbf{I}\right] + \boldsymbol{f} + \boldsymbol{s}_u\end{aligned} \tag{B.37}$$

**Assumption:** *We assume the only body forces are due to gravitational acceleration.*

$$\begin{aligned}\frac{\partial}{\partial t}(\rho \boldsymbol{u}) + \nabla \cdot (\rho \boldsymbol{u}\boldsymbol{u}) = -\nabla p + \nabla \cdot \left[\mu \left(\nabla \boldsymbol{u} + (\nabla \boldsymbol{u})^T\right)\right] \\ + \nabla \cdot \left[\left(\lambda - \frac{2}{3}\mu\right)(\nabla \cdot \boldsymbol{u})\,\mathbf{I}\right] + \rho \boldsymbol{g} + \boldsymbol{s}_u\end{aligned} \tag{B.38}$$

**Assumption:** *If we assume divergence-free velocity, i.e.,* $\nabla \cdot \boldsymbol{u} = 0$*, the shear-stress tensor is simply:* $\bar{\bar{\tau}} = \mu \left(\nabla \boldsymbol{u} + (\nabla \boldsymbol{u})^T\right)$.

Therefore, conservation of momentum becomes:

$$\frac{\partial}{\partial t}(\rho \boldsymbol{u}) + \nabla \cdot (\rho \boldsymbol{u}\boldsymbol{u}) = -\nabla p + \nabla \cdot \left[\mu \left(\nabla \boldsymbol{u} + (\nabla \boldsymbol{u})^T\right)\right] + \rho \boldsymbol{g} + \boldsymbol{s}_u \tag{B.39}$$

### B.3.3 *Source of momentum*

The source term due to vegetation, i.e. $\boldsymbol{s}_u$ ($\mathrm{kg\,m^{-2}\,s^{-1}}$), the volumetric force exerted by vegetation is modeled through Darcy-Forchheimer law for the flow through porous medium:

$$\boldsymbol{s}_u = -\left(\left[\frac{\mu}{K}\right]\boldsymbol{u} + \rho\left[\frac{C_F}{\sqrt{K}}\right]|\boldsymbol{u}|\,\boldsymbol{u}\right) \tag{B.40}$$

where $K$ ($\mathrm{m^2}$) is permeability, $C_F$ is the Forchheimer coefficient for non-linear momentum loss (Boulard et al. 2008; Verboven et al. 2006).

**Assumption:** *For high wind speeds, the Forcheimer term becomes the dominant influence due to the quadratic relation. Furthermore, the flow in vegetation is this regime. Therefore, we assume the linear Darcy term is negligible.*

The Forchheimer term for flow past porous screens (or windbreaks) with thickness $\delta t$ (m) is:

$$\frac{C_F}{\sqrt{k_p}} = \frac{C_D}{\delta t} \tag{B.41}$$

For vegetation the non-linear term is expressed in terms of leaf area density $a$ ($m^2_{leaf} m^{-3} \rightarrow m^{-1}$) and leaf drag coefficient $c_d$:

$$\frac{C_F}{\sqrt{k_p}} = c_d\, a \tag{B.42}$$

and the source term of vegetation as porous medium becomes (Hiraoka 2005; Kenjereš and ter Kuile 2013; Liu et al. 1996; Wilson and Shaw 1977):

$$\boldsymbol{s}_u = -\rho c_d a |\boldsymbol{u}| \boldsymbol{u} \tag{B.43}$$

Thus, the momentum transport equation becomes:

$$\frac{\partial}{\partial t}(\rho \boldsymbol{u}) + \nabla \cdot (\rho \boldsymbol{u}\boldsymbol{u}) = -\nabla p + \nabla \cdot \left[\mu \left(\nabla \boldsymbol{u} + (\nabla \boldsymbol{u})^T\right)\right] + \rho \boldsymbol{g} - \rho c_d a |\boldsymbol{u}| \boldsymbol{u} \tag{B.44}$$

### B.3.4 *Deriving drag coefficient*

When performing measurements, the drag coefficient is characterized w.r.t to the frontal surface area of vegetation $A_{frontal}$. The measured drag coefficient $C_d$ is related to the leaf drag coefficient $c_d$ from the following relationship: The total force on vegetation $F_d$ (N) is given as:

$$F_d = \frac{1}{2} \rho U_\infty^2 C_d A_{frontal} \tag{B.45}$$

and should be equal to the volumetric force, i.e.:

$$F_d = -\int_\Omega \boldsymbol{s}_u \, \mathrm{d}V = \int_\Omega \rho c_d a |\boldsymbol{u}| \boldsymbol{u} \, \mathrm{d}V \tag{B.46}$$

**Assumption:** *We assume $\rho$ = constant and $c_d$ = constant.*

So, equation Eq. (B.45) to Eq. (B.45) and substituting $U_\infty$ into $\boldsymbol{u}$, we get:

$$\frac{1}{2} \rho U_\infty^2 C_d A_{frontal} = \rho c_d U_\infty^2 \int_\Omega a \, \mathrm{d}V \tag{B.47}$$

and so, the leaf drag coefficient becomes:

$$c_d = C_d \frac{A_{frontal}}{2 A_{leaf}} \tag{B.48}$$

as the integral of leaf area density $a$ ($m^2\,m^{-2}$) is:

$$\int_{\Omega} a \, dV = A_{leaf} \tag{B.49}$$

where $A_{leaf}$ (m) is the total leaf surface area.

## B.4 CONSERVATION OF ENERGY

### B.4.1 *First law of thermodynamics*

First law of thermodynamics:

$$dE = \delta Q + \delta W \tag{B.50}$$

where $dE$ (J or $\mathrm{kg\,m^2\,s^{-2}}$) is the change in total internal energy of the system, $\delta Q$ (J) is the heat added to the system, and $\delta W$ (J) is the work done on the system. The total energy per unit mass of the mixture $\hat{E}$ is defined as:

$$E = \int_{\Omega} \rho \hat{E} \, \mathrm{d}V \tag{B.51}$$

where $\hat{E}$ ($\mathrm{J\,kg^{-1}}$) (an intensive property) is related total energy $E$ (J) (an extensive property). The total energy per unit mass of the mixture $\hat{E}$ is given as:

$$\hat{E} = e + \frac{|\boldsymbol{u}|^2}{2} + gz \tag{B.52}$$

where $e$ ($\mathrm{J\,kg^{-1}}$) is the internal energy per unit mass, $|\boldsymbol{u}|^2/2$ ($\mathrm{J\,kg^{-1}}$) is the kinetic energy per unit mass, and $gz$ ($\mathrm{J\,kg^{-1}}$) is the potential energy per unit mass. The internal energy of a gas mixture can be related to enthalpy and kinetic theory of gas:

$$e = h - RT = h - \frac{p}{\rho} \tag{B.53}$$

where $R$ ($\mathrm{J\,kg^{-1}\,K^{-1}}$) is the gas constant. The total enthalpy $h$ ($\mathrm{J\,kg^{-1}}$) of the gas mixture is defined in Appendix A, i.e., Eq. (A.31) and given as:

$$h = \sum_i x_i h_i = \left(x_a c_{pa} + x_v c_{pv}\right)\left(T - T_{ref}\right) + x_v \, L_v \tag{B.54}$$

Therefore, total energy (per unit mass) of the gas mixture $\hat{E}$ ($\mathrm{J\,kg^{-1}}$) is:

$$\hat{E} = \sum_i x_i h_i - \frac{p}{\rho} + \frac{|\boldsymbol{u}|^2}{2} + gz \tag{B.55}$$

and substituting Eq. (B.54) into Eq. (B.55):

$$\hat{E} = \left(x_a c_{pa} + x_v c_{pv}\right)\left(T - T_{ref}\right) + x_v L_v - \frac{p}{\rho} + \frac{|\boldsymbol{u}|^2}{2} + gz \tag{B.56}$$

### B.4.2 *Deriving conservation of energy*

The conservation of energy is given as:

Rate of change of total *energy* in domain $\Omega$
$=$
Rate of transfer of *energy* by *advection* at boundary $\partial\Omega$
$+$
Rate of transfer of *heat* by *heat diffusion* at boundary $\partial\Omega$
$+$
Rate of transfer of *heat* by *mass diffusion* at boundary $\partial\Omega$
$+$
Rate at which *work* done by boundary $\Omega$
$+$
Rate of transfer of *heat* by within $\Omega$ (source/sink)

Therefore, the conservation of energy ($\mathrm{J\,s^{-1}}$ or W) is given as:

$$\frac{\mathrm{d}}{\mathrm{d}t}E = \frac{\mathrm{d}}{\mathrm{d}t}\int_{\Omega} \rho\hat{E}\,\mathrm{d}V \tag{B.57}$$

and applying the Reynolds transport theorem, detailed in Appendix B.1, we attain conservation of energy ($\mathrm{W\,m^{-3}}$) as:

$$\frac{\partial}{\partial t}\left(\rho\hat{E}\right) + \nabla\cdot\left(\rho\hat{E}\boldsymbol{u}\right) = -\nabla\cdot\boldsymbol{q} - \nabla\cdot(p\boldsymbol{u}) - \nabla\cdot\left(\bar{\bar{\tau}}\cdot\boldsymbol{u}\right) + s_h \tag{B.58}$$

where $\boldsymbol{q}$ is the total heat flux due to heat diffusion and mass diffusion, $\nabla\cdot(p\boldsymbol{u})$ ($\mathrm{W\,m^{-3}}$ or $\mathrm{J\,m^{-3}\,s^{-1}}$ or $\mathrm{kg\,m^{-3}\,s^{-1}}$) is the work done due to pressure force, $\nabla\cdot\left(\bar{\bar{\tau}}\cdot\boldsymbol{u}\right)$ ($\mathrm{W\,m^{-3}}$) is the work done due to viscous force, and $s_h$ ($\mathrm{W\,m^{-3}}$) rate of energy added into the system, i.e. the energy source.

**Assumption:** *We assume pressure work is negligible due to incompressible flow approximation, and viscous heat is neglected as well (Defraeye 2011). Furthermore, the source of energy is due to radiation (at walls) and from vegetation.*

The total heat flux $\boldsymbol{q}$ ($\mathrm{W\,m^{-2}}$) is the total heat flux due to heat diffusion (i.e., conduction) and mass diffusion is given as:

$$\boldsymbol{q} = \boldsymbol{q}_c + \boldsymbol{q}_d \tag{B.59}$$

where $\boldsymbol{q}_c$ ($\mathrm{W\,m^{-2}}$) is the heat flux due to heat diffusion (i.e., conduction) and $\boldsymbol{q}_d$ ($\mathrm{W\,m^{-2}}$) is the heat flux due to mass diffusion. The conduction term is defined by the Fourier law of heat conduction:

$$\boldsymbol{q}_c = -\lambda \nabla T \tag{B.60}$$

where $\lambda = c_p \mu / \mathrm{Pr}$ ($\mathrm{W\,m^{-1}\,K^{-1}}$) is the thermal conductivity, where $c_p$ ($\mathrm{J\,kg^{-1}\,K^{-1}}$) is the specific heat capacity of gas mixture, $\mu$ ($\mathrm{kg\,m^{-1}\,s^{-1}}$) is the dynamic viscosity of gas mixture. The heat flux due to mass flux $\boldsymbol{q}_d$ ($\mathrm{W\,m^{-2}}$) is given as:

$$\boldsymbol{q}_d = \sum_i h_i \boldsymbol{g}_{d,i} \tag{B.61}$$

where $\boldsymbol{g}_{d,i}$ ($\mathrm{kg\,m^{-2}\,s^{-1}}$) diffusive flux of species $i$ contributing to the heat transport. So:

$$\boldsymbol{q} = -\lambda \nabla T + \sum_i h_i \boldsymbol{g}_{d,i} \tag{B.62}$$

Simplifying Eq. (B.58), we obtain:

$$\frac{\partial}{\partial t}\left(\rho \hat{E}\right) + \nabla \cdot \left(\rho \hat{E} \boldsymbol{u}\right) = -\nabla \cdot \boldsymbol{q} + s_h \tag{B.63}$$

We expand B.63 by substituting total energy per unit mass $\hat{E}$ ($\mathrm{J\,kg^{-1}}$), B.55, giving:

$$\begin{aligned} \frac{\partial}{\partial t}\left\{\rho\left(\sum_i x_i h_i - \frac{p}{\rho} + \frac{|\boldsymbol{u}|^2}{2} + gz\right)\right\} \\ + \nabla \cdot \left\{\rho\left(\sum_i x_i h_i - \frac{p}{\rho} + \frac{|\boldsymbol{u}|^2}{2} + gz\right)\boldsymbol{u}\right\} \\ = -\nabla \cdot \boldsymbol{q} + s_h \end{aligned} \tag{B.64}$$

and taking $\rho$ inside and substituting $\rho_i = \rho x_i$ gives:

$$\begin{aligned}\frac{\partial}{\partial t}\left(\sum_i \rho_i h_i - p + \frac{\rho\,|\boldsymbol{u}|^2}{2} + \rho g z\right) \\ + \nabla\cdot\left\{\left(\sum_i \rho_i h_i - p + \frac{\rho\,|\boldsymbol{u}|^2}{2} + \rho g z\right)\boldsymbol{u}\right\} \\ = -\nabla\cdot\boldsymbol{q} + s_h\end{aligned} \tag{B.65}$$

**Assumption:** *We assume pressure, potential energy and kinetic energy variation is small.*

Therefore, Eq. (B.65) further simplifies to:

$$\frac{\partial}{\partial t}\left(\sum_i \rho_i h_i\right) + \nabla\cdot\left(\left(\sum_i \rho_i h_i\right)\boldsymbol{u}\right) = -\nabla\cdot\boldsymbol{q} + s_h \tag{B.66}$$

Substituting enthalpies into Eq. (B.66), the conservation of moist air becomes:

$$\begin{aligned}\frac{\partial}{\partial t}\left(\rho_a\, c_{pa}\left(T - T_{ref}\right) + \rho_v\, c_{pv}\left(T - T_{ref}\right) + \rho_v\, L_v\right) \\ + \nabla\cdot\left(\left(\rho_a\, c_{pa}\left(T - T_{ref}\right) + \rho_v\, c_{pv}\left(T - T_{ref}\right) + \rho_v\, L_v\right)\boldsymbol{u}\right) \\ = -\nabla\cdot\boldsymbol{q} + s_h\end{aligned} \tag{B.67}$$

Substituting, the total heat flux $\boldsymbol{q}$ ($\mathrm{W\,m^{-2}}$) Eq. (B.59), into Eq. (B.67), we obtain conservation equation of the form:

$$\begin{aligned}\frac{\partial}{\partial t}\left(\rho_a\, c_{pa}\left(T - T_{ref}\right) + \rho_v\, c_{pv}\left(T - T_{ref}\right) + \rho_v\, L_v\right) \\ + \nabla\cdot\left(\left(\rho_a\, c_{pa}\left(T - T_{ref}\right) + \rho_v\, c_{pv}\left(T - T_{ref}\right) + \rho_v\, L_v\right)\boldsymbol{u}\right) \\ = -\nabla\cdot\left(-\lambda\nabla T + \sum_i h_i \boldsymbol{g}_{d,i}\right) + s_h\end{aligned} \tag{B.68}$$

and as $\rho_i \boldsymbol{u}_i = \rho_i \boldsymbol{u} + \boldsymbol{g}_{d,i}$ (see Appendix B.2), Eq. (B.68) can be simplified to:

$$\begin{aligned}\frac{\partial}{\partial t}\left(\rho_a\, c_{pa}\left(T - T_{ref}\right) + \rho_v\, c_{pv}\left(T - T_{ref}\right) + \rho_v\, L_v\right) \\ + \nabla \cdot \left(\rho_a\, c_{pa}\left(T - T_{ref}\right)\boldsymbol{u}_a + \rho_v\, c_{pv}\left(T - T_{ref}\right)\boldsymbol{u}_v + \rho_v\, L_v \boldsymbol{u}_v\right) \\ = \nabla \cdot (\lambda \nabla T) + s_h\end{aligned} \tag{B.69}$$

Therefore, the conservation of energy Eq. (B.69) can be rewritten for separate species as follows:

$$\begin{aligned}c_{pa}\left(\frac{\partial}{\partial t}\left(\rho_a T\right) + \nabla \cdot \left(\rho_a T \boldsymbol{u}_a\right)\right) + c_{pv}\left(\frac{\partial}{\partial t}\left(\rho_v T\right) + \nabla \cdot \left(\rho_v T \boldsymbol{u}_v\right)\right) \\ -c_{pa} T_{ref}\left(\frac{\partial}{\partial t}\left(\rho_a\right) + \nabla \cdot \left(\rho_a \boldsymbol{u}_a\right)\right) - c_{pv} T_{ref}\left(\frac{\partial}{\partial t}\left(\rho_v\right) + \nabla \cdot \left(\rho_v \boldsymbol{u}_v\right)\right) \\ +L_v\left(\frac{\partial}{\partial t}\left(\rho_v\right) + \nabla \cdot \left(\rho_v \boldsymbol{u}_v\right)\right) = \nabla \cdot (\lambda \nabla T) + s_h\end{aligned} \tag{B.70}$$

### B.4.3 *Source of energy*

The source of energy $s_h$ ($\mathrm{W\,m^{-3}}$) is given defined as:

$$s_h = a\,\left(q_{c,leaf} + q_{d,leaf}\right) \tag{B.71}$$

where $a$ ($\mathrm{m^2\,m^{-3}}$) is leaf area density, $q_{c,leaf}$ ($\mathrm{W\,m^{-2}}$) is heat flux from leaf surface due to conduction (i.e., heat diffusion), and $q_{d,leaf}$ ($\mathrm{W\,m^{-2}}$) is the heat flux due to mass diffusion from the leaf surface. Expanding, the mass diffusion term in Eq. (B.71) gives:

$$s_h = a\left(q_{c,leaf} + \sum_i h_i g_{i,leaf}\right) \tag{B.72}$$

where $g_{i,leaf}$ is the mass flux of species $i$ from the leaf surface. And so Eq. (B.72) becomes:

$$s_h = a\,\left(q_{c,leaf} + h_v g_{v,leaf} + h_c g_{c,leaf}\right) \tag{B.73}$$

where $g_{v,leaf}$ ($\mathrm{kg\,m^{-2}\,s{-}1}$) and $g_{c,leaf}$ ($\mathrm{kg\,m^{-2}\,s{-}1}$) are mass fluxes of water vapor and $CO_2$, respectively.

**Assumption:** *Note that, we assumed there is no flux of oxygen $O_2$.*

The conductive heat flux $q_{c,leaf}$ ($\mathrm{W\,m^{-2}}$) is given as:

$$q_{c,leaf} = h_{c,h}\left(T_l - T\right) \tag{B.74}$$

where $h_{c,h}$ ($\mathrm{W\,m^{-2}\,K^{-1}}$) is the convective heat transfer coefficient of the leaf and $T_l$ (K) is the leaf temperature. The source of energy due to water vapor flux $g_{v,leaf}$ is given as:

$$h_v g_{v,leaf} = c_{pv}\left(T_l - T\right) g_{v,leaf} + L_v g_{v,leaf} \tag{B.75}$$

where $g_{v,leaf}$ ($\mathrm{kg\,m^{-2}\,s^{-1}}$) is the leaf transpiration rate. Similarly, the source of energy due to $CO_2$ flux $g_{c,leaf}$ is given as:

$$h_c g_{c,leaf} = c_{pc}\left(T_l - T\right) g_{c,leaf} \tag{B.76}$$

where $g_{v,leaf}$ ($\mathrm{kg\,m^{-2}\,s^{-1}}$) is the leaf $CO_2$ assimilation rate (i.e., mass flux of $CO_2$ due to the photosynthetic process).

Thus, substituting Eqs. (B.74) and (B.76) into Eq. (B.73), and decompose to sensible (i.e., temperature dependent) and latent component, we arrive at:

$$s_h = a\left(\underbrace{\left[h_{c,h} + c_{pv}g_{v,leaf} + c_{pc}g_{c,leaf}\right]\left(T_l - T\right)}_{\text{sensible}} + \underbrace{L_v g_{v,leaf}}_{\text{latent}}\right) \tag{B.77}$$

**Assumption:** *We assume the sensible heat flux contribution of water vapor and $CO_2$ is negligible compared to the conductive heat flux (Hiraoka 2005), i.e.,*
$\left(c_{pv}g_{v,leaf} + c_{pc}g_{c,leaf}\right) \ll h_{c,h}$.

Thus, the source of energy $s_h$ ($\mathrm{W\,m^{-3}}$), Eq. (B.77), simplifies to:

$$s_h = a\left(h_{c,h}\left(T_l - T\right) + L_v g_{v,leaf}\right) \tag{B.78}$$

where:

$$q_{sen,leaf} = h_{c,h}\left(T_l - T\right) \tag{B.79}$$
$$q_{lat,leaf} = L_v g_{v,leaf} \tag{B.80}$$
$$\tag{B.81}$$

$q_{sen,leaf}$ (W m$^{-2}$) and $q_{lat,leaf}$ (W m$^{-2}$) is typically known as the sensible and latent heat flux from leaf in literature (Bruse and Fleer 1998; Hiraoka 2005; Manickathan et al. 2018b).

Substituting Eq. (B.78) into conservation of energy becomes:

$$\begin{aligned} c_{pa}\left(\frac{\partial}{\partial t}\left(\rho_a T\right) + \nabla\cdot\left(\rho_a T\boldsymbol{u}_a\right)\right) + c_{pv}\left(\frac{\partial}{\partial t}\left(\rho_v T\right) + \nabla\cdot\left(\rho_v T\boldsymbol{u}_v\right)\right) \\ -c_{pa}T_{ref}\left(\frac{\partial}{\partial t}\left(\rho_a\right) + \nabla\cdot\left(\rho_a\boldsymbol{u}_a\right)\right) - c_{pv}T_{ref}\left(\frac{\partial}{\partial t}\left(\rho_v\right) + \nabla\cdot\left(\rho_v\boldsymbol{u}_v\right)\right) \\ +L_v\left(\frac{\partial}{\partial t}\left(\rho_v\right) + \nabla\cdot\left(\rho_v\boldsymbol{u}_v\right)\right) = \nabla\cdot\left(\lambda\nabla T\right) + a\left(h_{c,h}\left(T_l - T\right) + L_v g_{v,leaf}\right) \end{aligned} \tag{B.82}$$

Substituting conservation of mass of air Eq. (B.19) and conservation of mass of water vapor, Eq. (B.82) simplifies as:

$$\begin{aligned} c_{pa}\left(\frac{\partial}{\partial t}\left(\rho_a T\right) + \nabla\cdot\left(\rho_a T\boldsymbol{u}_a\right)\right) + c_{pv}\left(\frac{\partial}{\partial t}\left(\rho_v T\right) + \nabla\cdot\left(\rho_v T\boldsymbol{u}_v\right)\right) \\ - c_{pv}T_{ref}\left(a\, g_{v,leaf}\right) + L_v\left(a\, g_{v,leaf}\right) \\ = \nabla\cdot\left(\lambda\nabla T\right) + a\left(h_{c,h}\left(T_l - T\right) + L_v g_{v,leaf}\right) \end{aligned} \tag{B.83}$$

**Assumption:** *We assume the term $c_{pv}T_{ref}$ is negligible, as $c_{pv}T_{ref} \ll L_v$.*

$$\begin{aligned} c_{pa}\left(\frac{\partial}{\partial t}\left(\rho_a T\right) + \nabla\cdot\left(\rho_a T\boldsymbol{u}_a\right)\right) + c_{pv}\left(\frac{\partial}{\partial t}\left(\rho_v T\right) + \nabla\cdot\left(\rho_v T\boldsymbol{u}_v\right)\right) \\ + L_v\left(a\, g_{v,leaf}\right) = \nabla\cdot\left(\lambda\nabla T\right) + a\left(h_{c,h}\left(T_l - T\right) + L_v g_{v,leaf}\right) \end{aligned} \tag{B.84}$$

Thus, we can cancel the latent component terms on both sides, giving:

$$c_{pa}\left(\frac{\partial}{\partial t}\left(\rho_a T\right)+\nabla\cdot\left(\rho_a T\boldsymbol{u}_a\right)\right)+c_{pv}\left(\frac{\partial}{\partial t}\left(\rho_v T\right)+\nabla\cdot\left(\rho_v T\boldsymbol{u}_v\right)\right)$$
$$=\nabla\cdot\left(\lambda\nabla T\right)+a\left(h_{c,h}\left(T_l-T\right)\right) \tag{B.85}$$

So, we see that following the assumption, the source of (sensible) energy (i.e., energy equation based on only the temperature) is simply due to sensible heat flux from the leaf surface. Thus, for such equations, the source of energy $s_h$ ($\mathrm{W\,m^{-3}}$) is:

$$s_h = a\,q_{sen,leaf} = a\,h_{c,h}\left(T_l-T\right) \tag{B.86}$$

The energy equation (i.e., now the transport equation of temperature), Eq. (B.85) can be further simplified, as density of moist air $\rho = \rho_a+\rho_v$ ($\mathrm{kg\,m^{-3}}$) and heat capacity $c_p = c_{pa}x_a + c_{pv}x_v$ ($\mathrm{J\,kg^{-1}\,K^{-1}}$):

$$c_p\left(\frac{\partial}{\partial t}\left(\rho T\right)+\nabla\cdot\left(\rho T\boldsymbol{u}\right)\right)=\nabla\cdot\left(\lambda\nabla T\right)+\underbrace{a\,q_{sen,leaf}}_{s_h} \tag{B.87}$$

# C

# STATISTICS OF TURBULENT FLOW

## PROBABILITY

We define $X$ a random (stochastic) variable of the turbulent flow with a set of outcomes $X = \{x_1, x_2, ..., x_n\}$. The mean of a random variable $X$ is defined as:

$$\langle X \rangle \equiv \mathbb{E}[X] = \frac{1}{N} \sum_{n=1}^{N} x_n \tag{C.1}$$

where $\langle X \rangle$ is the stochastic mean, or statistical average or expected value, or ensemble average (Pope 2000; Sagaut 2006) of $N$ realization assuming that each realization $x_n$ is independent and are of the same distribution, i.e. *independent and identically distributed* (i.i.d) The *central-limit theorem* states that as $N$ approaches to infinity, the distribution of $X$ become normal (Gaussian) with a probability density function (PDF) of:

$$f(x_n; \mu, \sigma^2) = \frac{1}{\sigma\sqrt{2\pi}} \exp\left\{ -\frac{1}{2} \left( \frac{x_n - \mu}{\sigma} \right)^2 \right\} \tag{C.2}$$

where $\mu$ is the mean. The $r$-th centered moment of $X$ is defined as:

$$\mu^r = \frac{1}{N} \sum_{n=1}^{N} (x_n - \langle X \rangle)^r \tag{C.3}$$

with variance of $X$ denoted as $\mathrm{Var}(X)$ and is the second order centered moment:

$$\mathrm{Var}(X) \equiv \mathbb{E}\left[ (X - \mu)^2 \right] = \frac{1}{N} \sum_{n=1}^{N} (x_n - \langle X \rangle)^2 \tag{C.4}$$

and the standard deviation is simply:

$$\sigma = \sqrt{\mathrm{Var}\,(X)} \tag{C.5}$$

The higher-order moments also provide additional informational such as *skewness* ($3^{\mathrm{rd}}$-order) which measures the asymmetry of the PDF and the *kurtosis* ($4^{\mathrm{th}}$-order) which measures the peakedness of the PDF.

The covariance of two random variables $X$ and $Y$ is defined as:

$$\mathrm{Cov}\,(X,Y) \equiv \mathbb{E}\left[(X-\mu_X)\,(Y-\mu_Y)\right] = \frac{1}{N}\sum_{n=1}^{N}\left(x_n - \langle X\rangle\right)\left(y_n - \langle Y\rangle\right) \tag{C.6}$$

### REYNOLDS DECOMPOSITION

The stochastic variable of the turbulent flow such as the velocity $u$ can be decomposed into mean $\langle u\rangle$ and turbulent component $u'$. The turbulent fluctuation $u'$ of the random variable is defined as:

$$u' = u - \langle u\rangle \tag{C.7}$$

and by definition $\langle u'\rangle \equiv 0$. So, the flow field is decomposed into:

$$u = \langle\phi\rangle + \phi' = \overline{\phi} + \phi' \tag{C.8}$$

Assuming an ergodic process, we have that:

$$\langle\phi\rangle = \overline{\phi} = \lim_{T\to\infty}\frac{1}{T}\int_0^T \phi(t)\,\mathrm{d}t \tag{C.9}$$

the time average is the same as average in the probability space.

### TIME-AVERAGED NAVIER-STOKES

The mean velocity is defined as:

$$\overline{u} = \frac{1}{N}\sum_{n}^{N} u_n \tag{C.10}$$

of $N$ realizations assuming i.i.d. The variance is defined as:

$$\overline{u'^2} = \frac{1}{N-1}\sum_{n}^{N}(u_n - \overline{u})^2 \tag{C.11}$$

with the Bessel's correction and $\sqrt{\overline{u'^2}} = \sigma_u$ is the standard deviation. The turbulent intensity $I_u$ of $u$ is defined as:

$$I_u = \frac{\sigma_u}{\overline{u}} \tag{C.12}$$

The covariance is defined as:

$$\overline{u'v'} = \frac{1}{N-1}\sum_{n}^{N}(u_n - \overline{u})\,(v_n - \overline{v}) \tag{C.13}$$

For a vector velocity field $\boldsymbol{u} = (u, v, w)$, the covariance matrix is given as:

$$\overline{\boldsymbol{u}'\boldsymbol{u}'} = \begin{bmatrix} \overline{u'u'} & \overline{u'v'} & \overline{u'w'} \\ & \overline{v'v'} & \overline{v'w'} \\ & & \overline{w'w'} \end{bmatrix} \tag{C.14}$$

and is symmetric and positive semi-definite. The covariance matrix in the context of turbulent flow is known as the *Reynolds stress tensor* $\mathbf{R}$. The turbulent kinetic energy (TKE) is defined as:

$$k \equiv \frac{1}{2}\mathrm{tr}\,(\mathbf{R}) = \frac{1}{2}\left(\overline{u'u'} + \overline{v'v'} + \overline{w'w'}\right) \tag{C.15}$$

### SAMPLE UNCERTAINTY

The standard error (SE) of the sample mean velocity $\overline{u}$ is given as:

$$\mathrm{SE}_{\overline{u}} \equiv \sqrt{\frac{\mathrm{Var}\,(u)}{N}} = \sqrt{\frac{\sigma_u^2}{N}} = \frac{\sigma_u}{\sqrt{N}} \tag{C.16}$$

and quantifies the uncertainty of the mean velocity (Wieneke 2017). The standard error of sample variance of $u$ is:

$$\mathrm{SE}_{\sigma_u} \equiv \sqrt{\frac{\mathrm{Var}\,(\sigma_u^2)}{N}} = \sqrt{\frac{2\sigma_u^4}{N-1}} = \sigma_u^2\sqrt{\frac{2}{N-1}} \tag{C.17}$$

We assume uncorrelated samples $N$, however if the population is correlated, the effective number of independent samples $N_{eff}$ is defined as:

$$N_{eff} = \frac{N}{\sum_{-\infty}^{\infty} \rho\left(n\Delta t\right)} \cong \frac{T}{2T_{int}} \tag{C.18}$$

where $\rho$ is the auto-correlation coefficient, $\Delta t$ is the sample frequency, $T_{int}$ is the integral time scale.

where $Z_{\alpha/2}$ is the coefficient of confident ( $Z_{\alpha/2} = 1.96$ for confidence level of 95%) and the relative standard error on the standard deviation (i.e $\sqrt{R_{ii}}$) is:

$$\epsilon_{\sigma_{u_i}} = \frac{Z_{\alpha/2}}{\sqrt{N}} \tag{C.19}$$

The statistics of the flow field can be determined by performing multiple measurements of size $N$ and performing statistics of measurement such as mean, standard deviation‘and further higher-moments. The primary requirements of constructing statistics is that measurement samples are *independent and identically distributed* (or iid). To obtain iid. sample, we require the samples to be uncorrelated (i.e. independent) from each other. This can be ensured by enforcing acquisition frequency of the samples are larger than the integral time scale, satisfying the Nyquist sampling theorem:

$$f_{acq} \leq \frac{1}{2\mathcal{T}} \tag{C.20}$$

where $f_{acq}$ is acquisition frequency and $T_I$ is the integral time scale. A crude estimate of the $T_I$ is from the characteristics length and speed:

$$\mathcal{T} = \frac{\mathcal{L}}{U} \tag{C.21}$$

and so:

$$f_{acq} \leq \frac{U}{2\mathcal{L}} \tag{C.22}$$

Ensuring the sampling rate below $f_{acq}$, the obtained sample population can be ensured to be a normal distribution. Thus, the probabilistic and statistical methods can be applied to the sample population, such as calculating the mean, std. deviation and so on.

## C.1 DIMENSIONAL ANALYSIS

*Reynolds number*

$$Re = \frac{UL}{\nu} \tag{C.23}$$

*Turbulent cascade*

The turbulent cascade proposed by Richardson consists of three scales: Injection scale, Inertial scale and dissipative scale. The injection scale corresponds to the scale where the driving energy of the flow resides and is where the energy cascade starts. The dissipative scale is where the energy cascade stops and is dominated by dissipation to thermal energy. The inertial scale is in between the energy scale and the dissipative scale.

*Kolmogorov scales*

Length scale:

$$\eta \sim \left(\frac{\nu^3}{\varepsilon}\right)^{1/4} \tag{C.24}$$

Time scale:

$$\tau \sim \left(\frac{\nu}{\varepsilon}\right)^{1/2} \tag{C.25}$$

### TURBULENT KINETIC ENERGY PRODUCTION

TKE or $k$ is

$$k = \frac{1}{2}\mathrm{tr}(\overline{\boldsymbol{u}'\boldsymbol{u}'}) = \frac{1}{2}\overline{u_i' u_i'} \tag{C.26}$$

Transport of TKE:

$$\frac{\partial k}{\partial t} + \overline{\boldsymbol{u}} \cdot \nabla k = \nabla \cdot \left( -\frac{\overline{\boldsymbol{u}' p'}}{\rho} - \overline{(\boldsymbol{u}' \cdot \boldsymbol{u}')\boldsymbol{u}'} + \nu \nabla k \right) \underbrace{-\overline{\boldsymbol{u}'\boldsymbol{u}'} : \nabla \overline{\boldsymbol{u}}}_{\mathcal{P}} \underbrace{- \nu \overline{\nabla \boldsymbol{u}' \nabla \boldsymbol{u}'}}_{\varepsilon} \tag{C.27}$$

where $\nabla \cdot \left(\overline{\boldsymbol{u}' p'}/\rho\right)$ is pressure diffusion, $\nabla \cdot \overline{(\boldsymbol{u}' \cdot \boldsymbol{u}')\boldsymbol{u}'}$ is turbulence transport, $\nu \nabla^2 k$ is molecular viscous transport, $-\overline{\boldsymbol{u}'\boldsymbol{u}'} : \nabla \overline{\boldsymbol{u}}$ is TKE production and $-\nu \overline{\nabla \boldsymbol{u}' \nabla \boldsymbol{u}'}$ is TKE dissipation. The closure for TKE is based on gradient diffusion hypothesis

$$\frac{\overline{\boldsymbol{u}' p'}}{\rho} + \overline{(\boldsymbol{u}' \cdot \boldsymbol{u}')\boldsymbol{u}'} = -\frac{\nu_t}{\sigma_k} \nabla k \tag{C.28}$$

and so:

$$\frac{\partial k}{\partial t} + \overline{\boldsymbol{u}} \cdot \nabla k = \nabla \cdot \left[ \left( \nu + \frac{\nu_t}{\sigma_k} \right) \nabla k \right] + \mathcal{P}_k - \varepsilon \tag{C.29}$$

or in Einstein notation:

$$\frac{\partial k}{\partial t} + \overline{u}_j \frac{\partial k}{\partial x_j} = \frac{\partial}{\partial x_j} \left[ \left( \nu + \frac{\nu_t}{\sigma_k} \right) \frac{\partial k}{\partial x_j} \right] + \mathcal{P}_k - \varepsilon \tag{C.30}$$

The TKE production $\mathcal{P}_k$ is defined as:

$$\begin{aligned} \mathcal{P}_k \equiv -\overline{\boldsymbol{u}'\boldsymbol{u}'} : \nabla \overline{\boldsymbol{u}} = & \overline{u'u'} \frac{\partial \overline{u}}{\partial x} + \overline{v'v'} \frac{\partial \overline{v}}{\partial y} + \overline{w'w'} \frac{\partial \overline{w}}{\partial z} \\ & + \overline{u'v'} \left( \frac{\partial \overline{u}}{\partial y} + \frac{\partial \overline{v}}{\partial x} \right) \\ & + \overline{u'w'} \left( \frac{\partial \overline{u}}{\partial z} + \frac{\partial \overline{w}}{\partial x} \right) \\ & + \overline{v'w'} \left( \frac{\partial \overline{v}}{\partial z} + \frac{\partial \overline{w}}{\partial y} \right) \end{aligned} \tag{C.31}$$

and in Einstein notation:

$$\mathcal{P}_k \equiv -\overline{u_i' u_j'} \frac{\partial \overline{u_i}}{\partial x_j} \tag{C.32}$$

### TURBULENT DISSIPATION RATE

The TKE dissipation rate or (TDR) $\varepsilon$ is defined as:

$$\varepsilon \equiv 2\nu \overline{\mathbf{s}' : \mathbf{s}'} \tag{C.33}$$

where

$$\mathbf{s}' = \frac{1}{2} \left( \nabla \boldsymbol{u}' + (\nabla \boldsymbol{u}')^T \right) \tag{C.34}$$

and in Einstein notation is defined as:

$$\varepsilon \equiv 2\nu\overline{s'_{ij}s'_{ij}} = \nu\overline{\left(\frac{\partial u'_i}{\partial x_j} + \frac{\partial u'_j}{\partial x_i}\right)\cdot\left(\frac{\partial u'_i}{\partial x_j} + \frac{\partial u'_j}{\partial x_i}\right)} \tag{C.35}$$

BOUSINESSQ HYPOTHESIS

$$-\overline{\boldsymbol{u}'\boldsymbol{u}'} + \frac{2}{3}k\mathbf{I} = \nu_t\left(\nabla\overline{\boldsymbol{u}} + (\nabla\overline{\boldsymbol{u}})^T\right) \tag{C.36}$$

where

$$\bar{\mathbf{s}} = \frac{1}{2}\left(\nabla\overline{\boldsymbol{u}} + (\nabla\overline{\boldsymbol{u}})^T\right) \tag{C.37}$$

and the error of Bousinessq hypothesis:

$$\epsilon_t = \|\mathbf{a} - 2\nu_t\bar{\mathbf{s}}\| \tag{C.38}$$

The eddy-viscosity is closed using $k-\varepsilon$ equations:

$$\nu_t = C_\mu\frac{k^2}{\varepsilon} \tag{C.39}$$

# BIBLIOGRAPHY


Abtew, W and A Melesse (2012). *Evaporation and Evapotranspiration: Measurements and Estimations*. SpringerLink : Bücher. Springer Netherlands.

Abtew, W. (1996). "Evapotranspiration Measurements and Modeling for Three Wetland Systems in South Florida." In: *J. Am. Water Resour. Assoc.* 32.3, pp. 465–473.

Albrecht, A., E. Badel, V. Bonnesoeur, Y. Brunet, T. Constant, P. Défossez, E. de Langre, S. Dupont, M. Fournier, B. Gardiner, S. J. Mitchell, J. R. Moore, B. Moulia, B. C. Nicoll, K. J. Niklas, M. J. Schelhaas, H. C. Spatz, and F. W. Telewski (2016). "Comment on "critical wind speed at which trees break"." In: *Phys. Rev. E* 94.6, pp. 5–6.

Alexandri, E. and P. Jones (2008). "Temperature decreases in an urban canyon due to green walls and green roofs in diverse climates." In: *Build. Environ.* 43.4, pp. 480–493.

Allegrini, J. (2018). "A wind tunnel study on three-dimensional buoyant flows in street canyons with different roof shapes and building lengths." In: *Build. Environ.* 143.May, pp. 71–88.

Amorim, J., V. Rodrigues, R. Tavares, J. Valente, and C. Borrego (2013). "CFD modelling of the aerodynamic effect of trees on urban air pollution dispersion." In: *Sci. Total Environ.* 461-462, pp. 541–551.

Arganda-Carreras, I., V. Kaynig, C. Rueden, K. W. Eliceiri, J. Schindelin, A. Cardona, and H Sebastian Seung (2017). "Trainable Weka Segmentation: a machine learning tool for microscopy pixel classification." In: *Bioinformatics* 33.15. Ed. by R. Murphy, pp. 2424–2426.

ASHRAE (2013). *2013 ASHRAE Handbook: Fundamentals*. arXiv: arXiv:1011.1669v3.

Bai, K. and J. Katz (2014). "On the refractive index of sodium iodide solutions for index matching in PIV." In: *Exp. Fluids* 55.4.

Bai, K., C. Meneveau, and J. Katz (2012). "Near-Wake Turbulent Flow Structure and Mixing Length Downstream of a Fractal Tree." In: *Boundary-Layer Meteorol.* 143.2, pp. 285–308.

Bai, K., C. Meneveau, and J. Katz (2013). "Experimental study of spectral energy fluxes in turbulence generated by a fractal, tree-like object." In: *Phys. Fluids* 25.11, p. 110810.

Bailey, B. N., M. Overby, P. Willemsen, E. R. Pardyjak, W. F. Mahaffee, and R. Stoll (2014). "A scalable plant-resolving radiative transfer model based on optimized GPU ray tracing." In: *Agric. For. Meteorol.* 198, pp. 192–208.

Baille, M., A. Baille, and J. C. Laury (1994). "Canopy surface resistances to water vapour transfer for nine greenhouse pot plant crops." In: *Sci. Hortic. (Amsterdam).* 57.1-2, pp. 143–155.

Ball, J. T., I. E. Woodrow, and J. A. Berry (1987). "A Model Predicting Stomatal Conductance and its Contribution to the Control of Photosynthesis under Different Environmental Conditions." In: *Prog. Photosynth. Res. Vol. 4 Proc. VIIth Int. Congr. Photosynth. Provid. Rhode Island, USA, August 10–15, 1986*. Ed. by J Biggins. Dordrecht: Springer Netherlands, pp. 221–224.

Bitog, J., I Lee, H Hwang, M Shin, S Hong, I Seo, E Mostafa, and Z Pang (2011). "A wind tunnel study on aerodynamic porosity and windbreak drag." In: *Forest Sci. Technol.*

Bitog, J., I. Lee, H. Hwang, M. Shin, S. Hong, I. Seo, K. Kwon, E. Mostafa, and Z. Pang (2012). "Numerical simulation study of a tree windbreak." In: *Biosyst. Eng.*

Blazejczyk, K., Y. Epstein, G. Jendritzky, H. Staiger, and B. Tinz (2012). "Comparison of UTCI to selected thermal indices." In: *Int. J. Biometeorol.* 56.3, pp. 515–535.

Błazejczyk, K., G. Jendritzky, P. Bröde, D. Fiala, G. Havenith, Y. Epstein, A. Psikuta, and B. Kampmann (2013). "An introduction to the Universal thermal climate index (UTCI)." In: *Geogr. Pol.* 86.1, pp. 5–10.

Blocken, B. (2015). "Computational Fluid Dynamics for urban physics: Importance, scales, possibilities, limitations and ten tips and tricks towards accurate and reliable simulations." In: *Build. Environ.* 91, pp. 219–245.

Boulard, T. and S. Wang (2002). "Experimental and numerical studies on the heterogeneity of crop transpiration in a plastic tunnel." In: *Comput. Electron. Agric.* 34.1-3, pp. 173–190.

Boulard, T., H. Fatnassi, H. Majdoubi, and L. Bouirden (2008). "Airflow and microclimate patterns in a one-hectare canary type green-

house: An experimental and CFD assisted study." In: *Acta Hortic.* 801 PART 2, pp. 837–845.

Bowler, D. E., L. Buyung-Ali, T. M. Knight, and A. S. Pullin (2010). "Urban greening to cool towns and cities: A systematic review of the empirical evidence." In: *Landsc. Urban Plan.* 97.3, pp. 147–155.

Bröde, P., D. Fiala, K. Blazejczyk, I. Holmér, G. Jendritzky, B. Kampmann, B. Tinz, and G. Havenith (2012). "Deriving the operational procedure for the Universal Thermal Climate Index (UTCI)." In: *Int. J. Biometeorol.* 56.3, pp. 481–494.

Bruse, M. and H. Fleer (1998). "Simulating surface-plant-air interactions inside urban environments with a three dimensional numerical model." In: *Environ. Model. Softw.* 13.3-4, pp. 373–384.

Buccolieri, R., J. L. Santiago, E. Rivas, and B. Sanchez (2018). "Review on urban tree modelling in CFD simulations: Aerodynamic, deposition and thermal effects." In: *Urban For. Urban Green.* 31.July 2017, pp. 212–220.

Cao, J., Y. Tamura, and A. Yoshida (2012). "Wind tunnel study on aerodynamic characteristics of shrubby specimens of three tree species." In: *Urban For. Urban Green.* 11.4, pp. 465–476.

Carmeliet, J. (2005). *Coupled heat and mass transfer: Theory, Moisture transport properties*. Tech. rep.

Collatz, G. J., T. Ball, C. Grivet, and J. A. Berry (1991). *Physiological and environmental regulation of stomatal conductance, photosynthesis and transpiration: a model that includes a laminar boundary layer*.

Conan, B., S. Aubrun, B. Coudour, K. Chetehouna, and J. P. Garo (2015). "Contribution of coherent structures to momentum and concentration fluxes over a flat vegetation canopy modelled in a wind tunnel." In: *Atmos. Environ.* 107, pp. 329–341.

Couplet, M., C. Basdevant, and P. Sagaut (2005). "Calibrated reduced-order POD-Galerkin system for fluid flow modelling." In: *J. Comput. Phys.* 207.1, pp. 192–220.

Cowan, I. (1978). "Stomatal Behaviour and Environment." In: *Adv. Bot. Res.* Vol. 37, pp. 117–228.

Crowell, M. L. and N. D. Mtundu (2000). *Guidelines for Quality Control and Quality Assurance of Hydrologic and Meteorologic Data*.

Dahle, G. A. and J. C. Grabosky (2010). "Variation in modulus of elasticity (E) along Acer platanoides L. (Aceraceae) branches." In: *Urban For. Urban Green.* 9.3, pp. 227–233.

Dai, Y., R. E. Dickinson, and Y.-P. Wang (2004). "A Two-Big-Leaf model for canopy temperature, photosynthesis, and stomatal conductance." In: *J. Clim.* 17.12, pp. 2281–2299.

Damour, G., T. Simonneau, H. Cochard, and L. Urban (2010). "An overview of models of stomatal conductance at the leaf level." In: *Plant, Cell Environ.* 33.9, pp. 1419–1438.

Dauzat, J., B. Rapidel, and A. Berger (2001). "Simulation of leaf transpiration and sap flow in virtual plants: model description and application to a coffee plantation in Costa Rica." In: *Agric. For. Meteorol.* 109.2, pp. 143–160.

de Langre, E. (2008). "Effects of Wind on Plants." In: *Annu. Rev. Fluid Mech.* 40.1, pp. 141–168.

de Langre, E., A. Gutierrez, and J. Cossé (2012). "On the scaling of drag reduction by reconfiguration in plants." In: *Comptes Rendus - Mec.* 340.1-2, pp. 35–40.

Deardorff, J. W. (1978). "Efficient prediction of ground surface temperature and moisture, with inclusion of a layer of vegetation." In: *J. Geophys. Res.* 83.C4, p. 1889.

Defraeye, T (2011). "Convective heat and mass transfer at exterior building surfaces." Phd Thesis. Katholieke Universiteit Leuven.

Dellwik, E., M. van der Laan, N. Angelou, J. Mann, and A. Sogachev (2019). "Observed and modeled near-wake flow behind a solitary tree." In: *Agric. For. Meteorol.* 265.August 2018, pp. 78–87.

Demuzere, M., K. Orru, O. Heidrich, E. Olazabal, D. Geneletti, H. Orru, A. Bhave, N. Mittal, E. Feliu, and M. Faehnle (2014). "Mitigating and adapting to climate change: Multi-functional and multi-scale assessment of green urban infrastructure." In: *J. Environ. Manage.* 146, pp. 107–115.

Dimoudi, A and M Nikolopoulou (2003). "Vegetation in the Urban Environment." In: *Energy Build.* 35, pp. 69–76.

Dixon, H. H. and J Jolly (1895). "XII. On the ascent of sap." In: *Philos. Trans. R. Soc. London.* 186, pp. 563–576.

Dixon, M and J Grace (1983). "Effect of wind on the transpiration of young trees." In: *Ann. Bot.* 53, pp. 45–46.

Djedjig, R., E. Bozonnet, and R. Belarbi (2015). "Experimental study of the urban microclimate mitigation potential of green roofs and green walls in street Canyons." In: *Int. J. Low-Carbon Technol.* 10.1, pp. 34–44.

Dolman, A. J. (1993). "A multiple-source land surface energy balance model for use in general circulation models." In: *Agric. For. Meteorol.* 65.1-2, pp. 21–45.

Dong, Z., W. Luo, G. Qian, and H. Wang (2007). "A wind tunnel simulation of the mean velocity fields behind upright porous fences." In: *Agric. For. Meteorol.* 146.1-2, pp. 82–93.

Dong, Z., Q. Mu, W. Luo, G. Qinan, P. Lu, and H. Wang (2008). "An analysis of drag force and moment for upright porous wind fences." In: *J. Geophys. Res. Atmos.* 113.4, pp. 1–8.

Dong, Z., W. Luo, G. Qian, P. Lu, and H. Wang (2010). "A wind tunnel simulation of the turbulence fields behind upright porous wind fences." In: *J. Arid Environ.* 74.2, pp. 193–207.

Donovan, G. H. and D. T. Butry (2010). "Trees in the city: Valuing street trees in Portland, Oregon." In: *Landsc. Urban Plan.* 94.2, pp. 77–83.

Dos Reis, R. J. and N. L. Dias (1998). "Multi-season lake evaporation: Energy-budget estimates and CRLE model assessment with limited meteorological observations." In: *J. Hydrol.* 208.3-4, pp. 135–147.

Duraisamy, K., G. Iaccarino, and H. Xiao (2018). "Turbulence Modeling in the Age of Data." In: *Annu. Rev. Fluid Mech.* Pp. 357–377. arXiv: /doi.org/10.1146/ [https:].

Endalew, a. M., M Hertog, P Verboven, B. K, M. a. Delele, H Ramon, and B. M. Nicolaï (2006). "Modelling airflow through 3d canopy structure of orchards." In: *Asp. Appl. Biol.* 77.1982, pp. 465–472.

Endalew, a. M., M. Hertog, M. G. Gebrehiwot, M. Baelmans, H. Ramon, B. Nicolaï, and P. Verboven (2009). "Modelling airflow within model plant canopies using an integrated approach." In: *Comput. Electron. Agric.* 66.1, pp. 9–24.

Farquhar, G. D., S Von Caemmerer, and J. A. Berry (1980). "A Biochemical Model of Photosynthetic CO$_2$ Assimilation in Leaves of C$_3$ Species." In: *Planta* 149, pp. 78–90.

Farquhar, G. and M. Roderick (2007). "Worldwide changes in evaporative demand." In: *Water Environ.* 2, pp. 81–103.

Fatnassi, H., T. Boulard, C. Poncet, and M. Chave (2006). "Optimisation of Greenhouse Insect Screening with Computational Fluid Dynamics." In: *Biosyst. Eng.* 93.3, pp. 301–312.

Fiala, D, K. J. Lomas, and M Stohrer (2001). "Computer prediction of human themoregulatory and temperature responses to a wide

range of environmental conditions." In: *Int J Biometeorol* 45.3, pp. 143–159.

Finnigan, J. (2000). "Turbulence in Plant Canopies." In: *Annu. Rev. Fluid Mech.* 32.1, pp. 519–571.

Finnigan, J. J. (1979). "Turbulence in Waving Wheat." In: *Boundary-Layer Meteorol.* 16.1973, pp. 213–236.

Finnigan, J. J., R. H. Shaw, and E. G. Patton (2009). "Turbulence structure above a vegetation canopy." In: *J. Fluid Mech.* 637, p. 387.

Fouillet, A., G. Rey, F. Laurent, G. Pavillon, S. Bellec, C. Guihenneuc-Jouyaux, J. Clavel, E. Jougla, and D. Hémon (2006). "Excess mortality related to the August 2003 heat wave in France." In: *Int. Arch. Occup. Environ. Health* 80.1, pp. 16–24.

Franke, J., A. Hellsten, H. Schlünzen, and B. Carissimo (2007). *Best practice guideline for the CFD simulation of flows in the urban environment: COST action 732 quality assurance and improvement of microscale meteorological models*. July 2016.

Gandemer, J. (1979). "Wind shelters." In: *J. Wind Eng. Ind. Aerodyn.* 4.3-4, pp. 371–389.

Ganguly, A. and S. Ghosh (2009). "Model development and experimental validation of a floriculture greenhouse under natural ventilation." In: *Energy Build.* 41.5, pp. 521–527.

Gastellu-Etchegorry, J. P., V. Demarez, V. Pinel, and F. Zagolski (1996). "Modeling radiative transfer in heterogeneous 3-D vegetation canopies." In: *Remote Sens. Environ.* 58.2, pp. 131–156.

German, E. R. (2000). *Regional evaluation of evapotranspiration in the Everglades*. ENGLISH. Tech. rep.

Gillner, S., J. Vogt, A. Tharang, S. Dettmann, and A. Roloff (2015). "Role of street trees in mitigating effects of heat and drought at highly sealed urban sites." In: *Landsc. Urban Plan.* 143, pp. 33–42.

Gorlé, C., C. Garcia-Sanchez, and G. Iaccarino (2015). "Quantifying inflow and RANS turbulence model form uncertainties for wind engineering flows." In: *J. Wind Eng. Ind. Aerodyn.* 144.2015, pp. 202–212.

Grace, J and G Russell (1977). "The effect of wind on grasses.pdf." In: *J. Exp. Bot.* 28.103, pp. 268–278.

Grant, P. F. and W. G. Nickling (1998). "Direct field measurement of wind drag on vegetation for application to windbreak design and modelling." In: *L. Degrad. Dev.* 9.1, pp. 57–66.

Gromke, C. (2011). "A vegetation modeling concept for Building and Environmental Aerodynamics wind tunnel tests and its application in pollutant dispersion studies." In: *Environ. Pollut.* 159.8-9, pp. 2094–2099.

Gromke, C. and B. Blocken (2015). "Influence of avenue-trees on air quality at the urban neighborhood scale. Part I: Quality assurance studies and turbulent Schmidt number analysis for RANS CFD simulations." In: *Environ. Pollut.*

Gromke, C. and B. Ruck (2007). "Influence of trees on the dispersion of pollutants in an urban street canyon-Experimental investigation of the flow and concentration field." In: *Atmos. Environ.* 41.16, pp. 3287–3302.

Gromke, C. and B. Ruck (2008). "Aerodynamic modeling of trees for small-scale wind tunnel studies." In: *Forestry* 81.3, pp. 243–258.

Gromke, C. and B. Ruck (2018). "On Wind Forces in the Forest-Edge Region During Extreme-Gust Passages and Their Implications for Damage Patterns." In: *Boundary-Layer Meteorol.* 168.2, pp. 1–20.

Gromke, C., R. Buccolieri, S. Di Sabatino, and B. Ruck (2008). "Dispersion study in a street canyon with tree planting by means of wind tunnel and numerical investigations – Evaluation of CFD data with experimental data." In: *Atmos. Environ.* 42.37, pp. 8640–8650.

Gromke, C., B. Blocken, W. Janssen, B. Merema, T. van Hooff, and H. Timmermans (2015). "CFD analysis of transpirational cooling by vegetation: Case study for specific meteorological conditions during a heat wave in Arnhem, Netherlands." In: *Build. Environ.* 83, pp. 11–26.

Gross, G. (1987). "A numerical study of the air flow within and around a single tree." In: *Boundary-Layer Meteorol.* 40.4, pp. 311–327.

Guan, D., Y. Zhang, and T. Zhu (2003). "A wind-tunnel study of windbreak drag." In: *Agric. For. Meteorol.* 118.1-2, pp. 75–84.

Hagen, L. and E. Skidmore (1971). "Windbreak drag as influenced by Porosity." In: *Trans. ASAE* 14.3, pp. 464–465.

Hagishima, A., K.-i. Narita, and J. Tanimoto (2007). "Field experiment on transpiration from isolated urban plants." In: *Hydrol. Process.* 21.9, pp. 1217–1222.

Haralick, R. M., S. R. Sternberg, and X. Zhuang (1987). "Image Analysis Using Mathematical Morphology." In: *IEEE Trans. Pattern Anal. Mach. Intell.* PAMI-9.4, pp. 532–550.

Harshani, H. M. D., S. A. Galindo-Torres, A Scheuermann, and H. B. Muhlhaus (2017). "Experimental study of porous media flow using hydro-gel beads and LED based PIV." In: *Meas. Sci. Technol.* 28.1, p. 015902.

Hiraoka, H. (2005). "An investigation of the effect of environmental factors on the budgets of heat, water vapor, and carbon dioxide within a tree." In: *Energy* 30.2-4 SPEC. ISS. Pp. 281–298.

Hiraoka, H. and M. Ohashi (2008). "A (k–$\epsilon$) turbulence closure model for plant canopy flows." In: *J. Wind Eng. Ind. Aerodyn.* 96.10-11, pp. 2139–2149.

Hiraoka, H. (2011). "Modeling of a one-equation LES for Plant Canopy Flows." In: vol. 74. 639, pp. 603–612.

Honjo, T. and T. Takakura (1990). "Simulation of Thermal Effects of Urban green Areas on Their Surrounding Areas." In: *Energy Build.* 16, pp. 443–446.

Hopmans, J. W. and K. L. Bristow (2002). "Current Capabilities and Future Needs of Root Water and Nutrient Uptake Modeling." In: 77, pp. 103–183.

Höppe, P. (1999). "The physiological equivalent temperature - A universal index for the biometeorological assessment of the thermal environment." In: *Int. J. Biometeorol.* 43.2, pp. 71–75.

Huang, C.-W., J.-C. Domec, E. J. Ward, T. Duman, G. Manoli, A. J. Parolari, and G. G. Katul (2017). "The effect of plant water storage on water fluxes within the coupled soil-plant system." In: *New Phytol.* 213.3, pp. 1093–1106.

Hwang, R. L., T. P. Lin, and A. Matzarakis (2011). "Seasonal effects of urban street shading on long-term outdoor thermal comfort." In: *Build. Environ.* 46.4, pp. 863–870.

Idso, S. B. (1977). *An Introduction to Environmental Biophysics*. Vol. 6. 4, p. 474.

James, K. R., J. R. Moore, D. Slater, and G. A. Dahle (2017). "Tree Biomechanics." In: *CAB Rev.* 12.038, pp. 1–11.

Janssen, H. (2002). *The influence of soil moisture transfer on building heat loss via the ground*. Vol. 39. 7, pp. 825–836.

Javaux, M., V. Couvreur, J. Vanderborght, and H. Vereecken (2013). "Root Water Uptake: From Three-Dimensional Biophysical Pro-

cesses to Macroscopic Modeling Approaches." In: *Vadose Zo. J.* 12.4, p. 0.

Jendritzky, G., R. de Dear, and G. Havenith (2012). "UTCI-Why another thermal index?" In: *Int. J. Biometeorol.* 56.3, pp. 421–428.

Jones, H. G. (1999). "Use of thermography for quantitative studies of spatial and temporal variation of stomatal conductance over leaf surfaces." In: *Plant, Cell Environ.* 22.9, pp. 1043–1055.

Judd, M., M. Raupach, and J. Finnigan (1996). "A wind tunnel study of turbulent flow around single and multiple windbreaks, part I: velocity fields." In: *Boundary-Layer Meteorol.* 1974, pp. 127–165.

Kane, B. and E. T. Smiley (2006). "Drag coefficients and crown area estimation of red maple." In: *Can. J. For. Res.* 36.8, pp. 1951–1958.

Katul, G., S. Manzoni, S. Palmroth, and R. Oren (2010). "A stomatal optimization theory to describe the effects of atmospheric CO2 on leaf photosynthesis and transpiration." In: *Ann. Bot.* 105.3, pp. 431–442.

Katul, G. G., L. Mahrt, D. Poggi, and C. Sanz (2004). "One- and two-equation models for canopy turbulence." In: *Boundary-Layer Meteorol.* 113.1, pp. 81–109.

Kenjereš, S. and B. ter Kuile (2013). "Modelling and simulations of turbulent flows in urban areas with vegetation." In: *J. Wind Eng. Ind. Aerodyn.* 123.PA, pp. 43–55.

Kichah, A., P.-E. Bournet, C. Migeon, and T. Boulard (2012). "Measurement and CFD simulation of microclimate characteristics and transpiration of an Impatiens pot plant crop in a greenhouse." In: *Biosyst. Eng.* 112.1, pp. 22–34.

Kinnersley, R. P., J. G. Farrington-Smith, G Shaw, and M. J. Minski (1994). "Aerodynamic characterisation of model tree canopies in a wind tunnel." In: *Sci. Total Environ.* 157.0, pp. 29–33.

Koizumi, A., M. Shimizu, Y. Sasaki, and T. Hirai (2016). "In situ drag coefficient measurements for rooftop trees." In: *J. Wood Sci.* 62.4, pp. 363–369.

Kovats, R. S. and S. Hajat (2008). "Heat Stress and Public Health: A Critical Review." In: *Annu. Rev. Public Health* 29.1, pp. 41–55.

Krayenhoff, E. S., A. Christen, A. Martilli, and T. R. Oke (2014). "A Multi-layer Radiation Model for Urban Neighbourhoods with Trees." In: *Boundary-Layer Meteorol.* 151.1, pp. 139–178.

Kubilay, A., D. Derome, and J. Carmeliet (2018). "Coupling of physical phenomena in urban microclimate: A model integrating air

flow, wind-driven rain, radiation and transport in building materials." In: *Urban Clim.* 24, pp. 398–418.

Kubilay, A. (2014). "Numerical simulations and field experiments of wetting of building facades due to wind-driven rain in urban areas." PhD thesis, p. 319.

Kuo, F. E. and W. C. Sullivan (2001). "Environment and crime in the inner city does vegetation reduce crime?" In: *Environ. Behav.*

Kurn, D. M., S. E. Bretz, B. Huang, and H Akbari (1994). "The Potential for Reducing Air Temperature and Energy Consumption Through Vegetative Cooling." In: *Energy Environ.*

Kustas, W. P. (1990). *Estimates of Evapotranspiration with a One- and Two-Layer Model of Heat Transfer over Partial Canopy Cover*.

Lai, C. T. and G. Katul (2000). "The dynamic role of root-water uptake in coupling potential to actual transpiration." In: *Adv. Water Resour.* 23.4, pp. 427–439.

Lal, S. (2016). "Multiscale investigation and numerical modeling of imbibition, drainage and drying of a macroporous medium." In: 23628.

Lal, S., L. Poulikakos, I. Jerjen, P. Vontobel, M. N. Partl, D. Derome, and J. Carmeliet (2017). "Wetting and drying in hydrophobic, macroporous asphalt structures." In: *Constr. Build. Mater.* 152, pp. 82–95.

Lambers, H, F. S. Chapin, and T. L. Pons (2008). "Ch4 - Plant Physiological Ecology." In: *Bioscience*. Vol. 37. 39. Chap. Chapter 4, p. 610. arXiv: arXiv:1011.1669v3.

Launiainen, S., G. G. Katul, A. Lauren, and P. Kolari (2015). "Coupling boreal forest CO2, H2O and energy flows by a vertically structured forest canopy – Soil model with separate bryophyte layer." In: *Ecol. Modell.* 312, pp. 385–405.

Lee, J and S Lee (2012). "PIV analysis of the bottom gap effect on the flow around a fir tree." In: *15th Int. Symp. Flow Vis.* 2010. Minsk, Belarus.

Lee, J.-P., E.-J. Lee, and S.-J. Lee (2014). "Shelter effect of a fir tree with different porosities." In: *J. Mech. Sci. Technol.* 28.2, pp. 565–572.

Lee, S. J. and H. B. Kim (1999). "Laboratory measurements of velocity and turbulence field behind porous fences." In: *J. Wind Eng. Ind. Aerodyn.* 80.3, pp. 311–326.

Letts, M. G., J. Rodríguez-Calcerrada, V. Rolo, and S. Rambal (2012). "Long-term physiological and morphological acclimation by the

evergreen shrub Buxus sempervirens L. to understory and canopy gap light intensities." In: *Trees* 26.2, pp. 479–491.

Leuning, R., F. M. Kelliher, D. G. G. de Pury, and E. D. Schulze (1995). "Leaf nitrogen, photosynthesis, conductance and transpiration: Scaling from leaves to canopies." In: *Plant, Cell Environ.* 18.10, pp. 1183–1200.

Leuning, R, F. X. Dunin, and Y. P. Wang (1998). "A two-leaf model for canopy conductance, photosynthesis and partioning of available energy. II. Comparison with measurements." In: *Agric. For. Meteorol.* 91, 113â€"125.

Leuzinger, S. and C. Körner (2007). "Tree species diversity affects canopy leaf temperatures in a mature temperate forest." In: *Agric. For. Meteorol.* 146.1-2, pp. 29–37.

Leuzinger, S., R. Vogt, and C. Körner (2010). "Tree surface temperature in an urban environment." In: *Agric. For. Meteorol.* 150.1, pp. 56–62.

Li, Z., J. D. Lin, and D. R. Miller (1990). "Air flow over and through a forest edge: A steady-state numerical simulation." In: *Boundary-Layer Meteorol.* 51.1-2, pp. 179–197.

Liang, L., L. Xiaofeng, L. Borong, and Z. Yingxin (2006). "Improved k–$\epsilon$ two-equation turbulence model for canopy flow." In: *Atmos. Environ.* 40.4, pp. 762–770.

Liu, C., Z. Zheng, H. Cheng, and X. Zou (2018). "Airflow around single and multiple plants." In: *Agric. For. Meteorol.* 252.December 2017, pp. 27–38.

Liu, J, J. M. Chen, T. a. Black, and M. D. Novak (1996). "E-$\epsilon$ modelling of turbulent air flow downwind of a model forest edge." In: *Boundary-Layer Meteorol.* 77.1, pp. 21–44.

Liu, X. (2012). "suGWFoam : An Open Source Saturated-Unsaturated GroundWater Flow Solver based on OpenFOAM." In: *Report* 01, pp. 1–54.

Lokys, H. L., J. Junk, and A. Krein (2015). "Future changes in human-biometeorological index classes in three regions of Luxembourg, Western-Central Europe." In: *Adv. Meteorol.* 2015, pp. 15–17.

Lopes, A., J. M.L. M. Palma, and J. V. Lopes (2013). "Improving a Two-Equation Turbulence Model for Canopy Flows Using Large-Eddy Simulation." In: *Boundary-Layer Meteorol.* 149.2, pp. 231–257.

Loughner, C. P., D. J. Allen, D.-L. Zhang, K. E. Pickering, R. R. Dickerson, and L. Landry (2012). "Roles of Urban Tree Canopy and

Buildings in Urban Heat Island Effects: Parameterization and Preliminary Results." In: *J. Appl. Meteorol. Climatol.* 51.10, pp. 1775–1793.

LUCOR, D., J. MEYERS, and P. SAGAUT (2007). "Sensitivity analysis of large-eddy simulations to subgrid-scale-model parametric uncertainty using polynomial chaos." In: *J. Fluid Mech.* 585, p. 255.

Maass, J., J. M. Vose, W. T. Swank, and A. Martínez-Yrízar (1995). "Seasonal changes of leaf area index (LAI) in a tropical deciduous forest in west Mexico." In: *For. Ecol. Manage.* 74.1-3, pp. 171–180. arXiv: 1612.00593v2.

Macdonald, E. and J. Hubert (2002). "A review of the effects of silviculture on timber quality of Sitka spruce." In: *Forestry* 75.2, pp. 107–138.

Majdoubi, H, T Boulard, H Fatnassi, and L Bouirden (2009). "Airflow and microclimate patterns in a one-hectare Canary type greenhouse: An experimental and CFD assisted study." In: *Agric. For. Meteorol.* 149.6, pp. 1050–1062.

Malys, L., M. Musy, and C. Inard (2014). "A hydrothermal model to assess the impact of green walls on urban microclimate and building energy consumption." In: *Build. Environ.* 73, pp. 187–197.

Manickathan, L., T. Defraeye, J. Allegrini, D. Derome, and J. Carmeliet (2018a). "Comparative study of flow field and drag coefficient of model and small natural trees in a wind tunnel." In: *Urban For. Urban Green.* 35.December 2017, pp. 230–239.

Manickathan, L., T. Defraeye, J. Allegrini, D. Derome, and J. Carmeliet (2018b). "Parametric study of the influence of environmental factors and tree properties on the transpirative cooling effect of trees." In: *Agric. For. Meteorol.* 248, pp. 259–274.

Manoli, G., S. Bonetti, J.-c. Domec, M. Putti, G. Katul, and M. Marani (2014a). "Tree root systems competin for soil moisture in a 3D soil-plant model." In: *Adv. Water Resour.* 66.3, pp. 32–42.

Manoli, G., S. Bonetti, J. C. Domec, M. Putti, G. Katul, and M. Marani (2014b). "Tree root systems competing for soil moisture in a 3D soil-plant model." In: *Adv. Water Resour.* 66, pp. 32–42.

Manzoni, S., G. Vico, G. Katul, P. A. Fay, W. Polley, S. Palmroth, and A. Porporato (2011). "Optimizing stomatal conductance for maximum carbon gain under water stress: A meta-analysis across plant functional types and climates." In: *Funct. Ecol.* 25.3, pp. 456–467.

Margheri, L., M. Meldi, M. Salvetti, and P. Sagaut (2014). "Epistemic uncertainties in RANS model free coefficients." In: *Comput. Fluids* 102, pp. 315–335.

Marshall, B. Y.J. M. (1987). "Glossary of terms for thermal physiology." In: *Pflugers Arch. Eur. J. Physiol.* 410.6, pp. 567–587.

Maruyama, T. (2008). "Large eddy simulation of turbulent flow around a windbreak." In: *J. Wind Eng. Ind. Aerodyn.* 96.10-11, pp. 1998–2006.

Matthews, T. K. R., R. L. Wilby, and C. Murphy (2017). "Communicating the deadly consequences of global warming for human heat stress." In: *Proc. Natl. Acad. Sci.* 114.15, pp. 3861–3866.

Matzarakis, A., H. Mayer, and M. G. Iziomon (1999). "Applications of a universal thermal index: Physiological equivalent temperature." In: *Int. J. Biometeorol.* 43.2, pp. 76–84.

Mayhead, G. J. (1973). "Some drag coefficients for british forest trees derived from wind tunnel studies." In: *Agric. Meteorol.* 12.C, pp. 123–130. arXiv: arXiv:1011.1669v3.

McClure, S., J. Kim, S. Lee, and W. Zhang (2017). "Shelter effects of porous multi-scale fractal fences." In: *J. Wind Eng. Ind. Aerodyn.* 163.January, pp. 6–14.

McVicar, T. R., M. L. Roderick, R. J. Donohue, L. T. Li, T. G. Van Niel, A. Thomas, J. Grieser, D. Jhajharia, Y. Himri, N. M. Mahowald, A. V. Mescherskaya, A. C. Kruger, S. Rehman, and Y. Dinpashoh (2012). "Global review and synthesis of trends in observed terrestrial near-surface wind speeds: Implications for evaporation." In: *J. Hydrol.* 416-417, pp. 182–205.

Medlyn, B. E., R. A. Duursma, D. Eamus, D. S. Ellsworth, I. C. Prentice, C. V. Barton, K. Y. Crous, P. De Angelis, M. Freeman, and L. Wingate (2011). "Reconciling the optimal and empirical approaches to modelling stomatal conductance." In: *Glob. Chang. Biol.* 17.6, pp. 2134–2144.

Melesse, A. M., A. Frank, V. Nangia, and J. Hanson (2008). "Analysis of energy fluxes and land surface parameters in a grassland ecosystem: a remote sensing perspective." In: *Int. J. Remote Sens.* 29.11, pp. 3325–3341.

Melesse, A. M., W. Abtew, and T. Dessalegne (2009). "Evaporation estimation of Rift Valley lakes: Comparison of models." In: *Sensors* 9.12, pp. 9603–9615.

Merlot, S., A.-C. Mustilli, B. Genty, H. North, V. Lefebvre, B. Sotta, A. Vavasseur, and J. Giraudat (2002). "Use of infrared thermal imaging to isolate Arabidopsis mutants defective in stomatal regulation." In: *Plant J.* 30, pp. 601–9.

Meroney, R. (1968). *Characteristics of Wind and Turbulence in and above Model Forests.pdf*.

Miri, A., D. Dragovich, and Z. Dong (2019). "Wind-borne sand mass flux in vegetated surfaces – Wind tunnel experiments with live plants." In: *CATENA* 172.December 2017, pp. 421–434.

Mitchell, D., C. Heaviside, S. Vardoulakis, C. Huntingford, G. Masato, B. P Guillod, P. Frumhoff, A. Bowery, D. Wallom, and M. Allen (2016). "Attributing human mortality during extreme heat waves to anthropogenic climate change." In: *Environ. Res. Lett.* 11.7, p. 074006.

Montero, J., A. Antón, P. Muñoz, and P. Lorenzo (2001). "Transpiration from geranium grown under high temperatures and low humidities in greenhouses." In: *Agric. For. Meteorol.* 107.4, pp. 323–332.

Moonen, P., C. Gromke, and V. Dorer (2013). "Performance assessment of Large Eddy Simulation (LES) for modeling dispersion in an urban street canyon with tree planting." In: *Atmos. Environ.* 75, pp. 66–76.

Morakinyo, T. E., L. Kong, K. K.-L. Lau, C. Yuan, and E. Ng (2017). "A study on the impact of shadow-cast and tree species on in-canyon and neighborhood's thermal comfort." In: *Build. Environ.* 115, pp. 1–17.

Najm, H. N. (2009). "Uncertainty Quantification and Polynomial Chaos Techniques in Computational Fluid Dynamics." In: *Annu. Rev. Fluid Mech.* 41.1, pp. 35–52.

Ng, E., L. Chen, Y. Wang, and C. Yuan (2012). "A study on the cooling effects of greening in a high-density city: An experience from Hong Kong." In: *Build. Environ.* 47.1, pp. 256–271.

Nobel, P. S. (2009). *Physicochemical and Environmental Plant Physiology*. Elsevier Science.

Nowak, D. J., D. E. Crane, and J. C. Stevens (2006). "Air pollution removal by urban trees and shrubs in the United States." In: *Urban For. Urban Green.* 4.3-4, pp. 115–123.

Oke, T. R. (1973). "City size and the urban heat island." In: *Atmos. Environ. Pergamon Pres* 7, pp. 769–779.

Oke, T. R., J. M. Crowther, K. G. McNaughton, J. L. Monteith, and B. Gardiner (1989). "The Micrometeorology of the Urban Forest [and Discussion]." In: *Philos. Trans. R. Soc. B Biol. Sci.* 324.1223, pp. 335–349.

Oke, T. R., G. Mills, A. Christen, and J. A. Voogt (2017). *Urban Climates*. Cambridge: Cambridge University Press, pp. 1–525.

Pachauri, R. K., M. R. Allen, V. R. Barros, J Broome, W Cramer, R Christ, J. A. Church, L Clarke, Q Dahe, P Dasgupta, and Others (2014). *Climate change 2014: synthesis Report. Contribution of working groups I, II and III to the fifth assessment report of the intergovernmental panel on climate change*. Vol. 403. 8. IPCC, p. 558. arXiv: 1307.3552.

Packwood, A. R. (2000). "Flow through porous fences in thick boundary layers: Comparisons between laboratory and numerical experiments." In: *J. Wind Eng. Ind. Aerodyn.* 88.1, pp. 75–90.

Parada, M., P. Vontobel, R. M. Rossi, D. Derome, and J. Carmeliet (2017). "Dynamic Wicking Process in Textiles." In: *Transp. Porous Media* 119.3, pp. 611–632.

Parlow, E., R. Vogt, and C. Feigenwinter (2014). "The urban heat island of Basel - Seen from different perspectives." In: *Erde* 145.1-2, pp. 96–110.

Patera, A., J. Van den Bulcke, M. N. Boone, D. Derome, and J. Carmeliet (2018). "Swelling interactions of earlywood and latewood across a growth ring: global and local deformations." In: *Wood Sci. Technol.* 52.1, pp. 91–114.

Penman, H. L. and R. K. Schofield (1951). "Some physical aspects of assimilation and transpiration." In: *Carbon Dioxide Fixat. Photosynth.* 5.

Perera, M. (1981). "Shelter behind two-dimensional solid and porous fences." In: *J. Wind Eng. Ind. Aerodyn.* 8.1-2, pp. 93–104.

Poggi, D., A. Porporato, L. Ridolfi, J. D. Albertson, and G. G. Katul (2004). "The effect of vegetation density on canopy sub-layer turbulence." In: *Boundary-Layer Meteorol.* 111.3, pp. 565–587.

Pope, S. B. (2000). *Turbulent Flows*. Cambridge: Cambridge University Press.

Raupach, M. R. and A. S. Thom (1981). "Turbulence in and above plant canopies." In: *Annu. Rev. Fluid Mech.* 13.1, pp. 97–129.

Richards, P. and R. Hoxey (1993). "Appropriate boundary conditions for computational wind engineering models using the k-$\epsilon$ turbulence model." In: *J. Wind Eng. Ind. Aerodyn.* 46-47, pp. 145–153.

Robitu, M., M. Musy, C. Inard, and D. Groleau (2006). "Modeling the influence of vegetation and water pond on urban microclimate." In: *Sol. Energy* 80.4, pp. 435–447.

Rodríguez-Calcerrada, J., M. Letts, V. Rolo, S. Roset, and S. Rambal (2013). "Multiyear impacts of partial throughfall exclusion on Buxus sempervirens in a Mediterranean forest." In: *For. Syst.* 22.2, p. 202.

Rosenfeld, M., G. Marom, and A. Bitan (2010). "Numerical Simulation of the Airflow Across Trees in a Windbreak." In: *Boundary-Layer Meteorol.* 135.1, pp. 89–107.

Rotach, M. W., R. Vogt, C. Bernhofer, E. Batchvarova, A. Christen, A. Clappier, B. Feddersen, S. E. Gryning, G. Martucci, H. Mayer, V. Mitev, T. R. Oke, E. Parlow, H. Richner, M. Roth, Y. A. Roulet, D. Ruffieux, J. A. Salmond, M. Schatzmann, and J. A. Voogt (2005). "BUBBLE - An urban boundary layer meteorology project." In: *Theor. Appl. Climatol.* 81.3-4, pp. 231–261.

Roy, J. (2011). *Dependence on Stomatal Resistance Model of CFD Simulation of Crop Evapotranspiration in Greenhouse*.

Rudnicki, M., S. J. Mitchell, and M. D. Novak (2004). "Wind tunnel measurements of crown streamlining and drag relationships for three conifer species." In: *Can. J. For. Res.* 34.3, pp. 666–676.

Ryder, J., J. Polcher, P. Peylin, C. Ottlé, Y. Chen, E. van Gorsel, V. Haverd, M. J. McGrath, K. Naudts, J. Otto, a. Valade, and S. Luyssaert (2014). "A multi-layer land surface energy budget model for implicit coupling with global atmospheric simulations." In: *Geosci. Model Dev. Discuss.* 7.6, pp. 8649–8701.

Sagaut, P. (2006). *Large Eddy Simulation for Incompressible Flows: An Introduction*. Scientific Computation. Berlin/Heidelberg: Springer-Verlag, p. 575.

Salim, M. H., K. H. Schlünzen, and D. Grawe (2015). "Including trees in the numerical simulations of the wind flow in urban areas: Should we care?" In: *J. Wind Eng. Ind. Aerodyn.* 144, pp. 84–95.

Salmond, J. A., M. Tadaki, S. Vardoulakis, K. Arbuthnott, A. Coutts, M. Demuzere, K. N. Dirks, C. Heaviside, S. Lim, H. Macintyre, R. N. McInnes, and B. W. Wheeler (2016). "Health and climate related ecosystem services provided by street trees in the urban environment." In: *Environ. Heal.* 15.S1, S36.

Saneinejad, S. (2013). "The influence of evaporative cooling on the micro-climate and thermal comfort in a street canyon." PhD thesis, p. 201.

Saneinejad, S., P. Moonen, and J. Carmeliet (2014). "Coupled CFD, radiation and porous media model for evaluating the micro-climate in an urban environment." In: *J. Wind Eng. Ind. Aerodyn.* 128, pp. 1–11.

Santamouris, M and D. N. Asimakopoulos (2001). *Energy and Climate in the Urban Built Environment*. BEST (Buildings Energy and Solar Technology) Series v. 1. James & James.

Santiago, J. L., F. Martín, a. Cuerva, N. Bezdenejnykh, and A. Sanz-Andrés (2007). "Experimental and numerical study of wind flow behind windbreaks." In: *Atmos. Environ.* 41.30, pp. 6406–6420.

Sanz, C. (2003). "A note on k-$\epsilon$ modeling of vegetation canopy air-flows." In: *Boundary-Layer Meteorol.* 108.1992, pp. 191–197.

Schindelin, J., I. Arganda-Carreras, E. Frise, V. Kaynig, M. Longair, T. Pietzsch, S. Preibisch, C. Rueden, S. Saalfeld, B. Schmid, J.-Y. Tinevez, D. J. White, V. Hartenstein, K. Eliceiri, P. Tomancak, and A. Cardona (2012). "Fiji: an open-source platform for biological-image analysis." In: *Nat. Methods* 9.7, pp. 676–682. arXiv: 1081-8693.

Schouveiler, L. and A. Boudaoud (2006). "The rolling up of sheets in a steady flow." In: *J. Fluid Mech.* 563.May, p. 71.

Schymanski, S. J. and D. Or (2016). "Wind increases leaf water use efficiency." In: *Plant. Cell Environ.* 39.7, pp. 1448–1459.

Sellers, P. J., D. A. Randall, G. J. Collatz, J. A. Berry, C. B. Field, D. A. Dazlich, C. Zhang, G. D. Collelo, and L. Bounoua (1996). *A revised land surface parameterization (SiB2) for atmospheric GCMs. Part I: Model formulation*.

Seto, K. C., B. Guneralp, and L. R. Hutyra (2012). "Global forecasts of urban expansion to 2030 and direct impacts on biodiversity and carbon pools." In: *Proc. Natl. Acad. Sci.* 109.40, pp. 16083–16088. arXiv: arXiv:1408.1149.

Shashua-Bar, L. and M. Hoffman (2000). "Vegetation as a climatic component in the design of an urban street." In: *Energy Build.* 31.3, pp. 221–235.

Shashua-Bar, L., D. Pearlmutter, and E. Erell (2009). "The cooling efficiency of urban landscape strategies in a hot dry climate." In: *Landsc. Urban Plan.* 92.3-4, pp. 179–186.

Shaw, R. H. R. and U. Schumann (1992). "Large-eddy simulation of turbulent flow above and within a forest." In: *Boundary-Layer Meteorol.* 61.1, pp. 47–64.

Shih, T.-H., W. W. Liou, A. Shabbir, Z. Yang, and J. Zhu (1995). "A new k-$\epsilon$ eddy viscosity model for high reynolds number turbulent flows." In: *Comput. Fluids* 24.3, pp. 227–238.

Shuttleworth, W. J. (1993). *Evaporation. Chapter 4 in Handbook of Hydrology*.

Shuttleworth, W. J. and J. S. Wallace (1985). "Evaporation from sparse crops-an energy combination theory." In: *Q. J. R. Meteorol. Soc.* 111.469, pp. 839–855.

Singh, A. K., H. Singh, S. P. Singh, and R. L. Sawhney (2002). "Numerical calculation of psychrometric properties on a calculator." In: *Build. Environ.* 37.4, pp. 415–419.

Sinoquet, H., X. Le Roux, B. Adam, T. Ameglio, and F. A. Daudet (2001). "RATP: A model for simulating the spatial distribution of radiation absorption, transpiration and photosynthesis within canopies: Application to an isolated tree crown." In: *Plant, Cell Environ.* 24.4, pp. 395–406.

Sławiński, C. and H. Sobczuk (2011). "Soil–Plant–Atmosphere Continuum." In: 1982, pp. 805–810.

Stacey, G. R., R. E. Belcher, C. J. Wood, and B. A. Gardiner (1994). "Wind flows and forces in a model spruce forest." In: *Boundary-Layer Meteorol.* 69.3, pp. 311–334.

Tadrist, L., M. Saudreau, and E. de Langre (2014). "Wind and gravity mechanical effects on leaf inclination angles." In: *J. Theor. Biol.* 341, pp. 9–16.

Taha, H., H. Akbari, and A. Rosenfeld (1991). "Heat Island and Oasis Effects." In: pp. 123–138.

Taha, H. (1997). "Urban climates and heat islands: albedo, evapotranspiration, and anthropogenic heat." In: *Energy Build.* 25.2, pp. 99–103.

Telewski, F. W. (1995). "Wind-induced physiological and developmental responses in trees." In: *Wind Trees*, pp. 237–263.

Thom, A. S., J. B. Stewart, H. R. Oliver, and J. H. Gash (1975). "Comparison of aerodynamic and energy budget estimates of fluxes over a pine forest." In: *Q. J. R. Meteorol. Soc.* 101.427, pp. 93–105.

Tominaga, Y., A. Mochida, R. Yoshie, H. Kataoka, T. Nozu, M. Yoshikawa, and T. Shirasawa (2008). "AIJ guidelines for practical applications

of CFD to pedestrian wind environment around buildings." In: *J. Wind Eng. Ind. Aerodyn.* 96.10-11, pp. 1749–1761.

Toparlar, Y., B. Blocken, B. Maiheu, and G. J. F. van Heijst (2018). "The effect of an urban park on the microclimate in its vicinity: a case study for Antwerp, Belgium." In: *Int. J. Climatol.* 38, e303–e322.

Tsalicoglou, C., J. Allegrini, and J. Carmeliet (2018). "Wind tunnel measurements of buoyancy-driven urban flows." In: *Proc. 18th Int. Symp. Flow Vis.*

Tuzet, a, a Perrier, and R Leuning (2003). "A coupled model of stomatal conductance , photosynthesis." In: *Plant, Cell Environ.* 26, pp. 1097–1116.

United Nations (2015). *World Urbanization Prospects: The 2014 Revision*. Tech. rep.

Van der Walt, S., J. L. Schönberger, J. Nunez-Iglesias, F. Boulogne, J. D. Warner, N. Yager, E. Gouillart, and T. Yu (2014). "scikit-image: image processing in Python." In: *PeerJ* 2, e453. arXiv: 1407.6245.

Verboven, P., D. Flick, B. M. Nicolaï, and G. Alvarez (2006). "Modelling transport phenomena in refrigerated food bulks, packages and stacks: basics and advances." In: *Int. J. Refrig.* 29.6, pp. 985–997.

Vogel, S (1989). "Drag and reconfiguration of broadleaves in high winds." In: *J. Exp. Bot.* 40.217, pp. 941–948.

Vogel, T., J. Votrubova, J. Dusek, and M. Dohnal (2016). "Mesoscopic aspects of root water uptake modeling - Hydraulic resistances and root geometry interpretations in plant transpiration analysis." In: *Adv. Water Resour.* 88, pp. 86–96.

Vollsinger, S., S. J. Mitchell, K. E. Byrne, M. D. Novak, and M. Rudnicki (2005). "Wind tunnel measurements of crown streamlining and drag relationships for several hardwood species." In: *Can. J. For. Res.* 35.5, pp. 1238–1249.

Volpe, V., M. Marani, J. D. Albertson, and G. Katul (2013). "Root controls on water redistribution and carbon uptake in the soil-plant system under current and future climate." In: *Adv. Water Resour.* 60, pp. 110–120.

Vrugt, J. A., M. T. Van Wijk, J. W. Hopmans, and J. Šimunek (2001). "One-, two-, and three-dimensional root water uptake functions for transient modeling." In: *Water Resour. Res.* 37.10, pp. 2457–2470.

Wang, Y. P. and P. G. Jarvis (1990). "Description and validation of an array model - MAESTRO." In: *Agric. For. Meteorol.* 51.3-4, pp. 257–280.

Watt, M. S., R. D'Ath, A. C. Leckie, P. W. Clinton, G. Coker, M. R. Davis, R. Simcock, R. L. Parfitt, J. Dando, and E. G. Mason (2008). "Modelling the influence of stand structural, edaphic and climatic influences on juvenile Pinus radiata fibre length." In: *For. Ecol. Manage.* 254.2, pp. 166–177.

Weitzman, J. S., L. C. Samuel, A. E. Craig, R. B. Zeller, S. G. Monismith, and J. R. Koseff (2014). "On the use of refractive-index-matched hydrogel for fluid velocity measurement within and around geometrically complex solid obstructions." In: *Exp. Fluids* 55.12.

Weller, H. G., G. Tabor, H. Jasak, and C. Fureby (1998). "A tensorial approach to computational continuum mechanics using object-oriented techniques." In: *Comput. Phys.* 12.6, p. 620.

Wieneke, B. (2017). "PIV Uncertainty Quantification and Beyond DOI." PhD thesis, p. 184.

Williams, M and E. Rastetter (1996). "Modelling the soil-plant-atmosphere continuum in a Quercus-Acer stand at Harvard Forest: the regulation of stomatal conductance by light, nitrogen and soil/plant hydraulics." In: *Plant, Cell Environ.* Pp. 911–927.

Wilson, J. D. (1985). "Numerical studies of flow through a windbreak." In: *J. Wind Eng. Ind. Aerodyn.* 21.2, pp. 119–154.

Wilson, N. R. and R. H. Shaw (1977). "A Higher Order Closure Model for Canopy Flow." In: *J. Appl. Meteorol.* 16.11, pp. 1197–1205.

Wong, N. H., Y. Chen, C. L. Ong, and A. Sia (2003). "Investigation of thermal benefits of rooftop garden in the tropical environment." In: *Build. Environ.* 38.2, pp. 261–270.

Woodrum, C. L., F. W. Ewers, and F. W. Telewski (2003). "Hydraulic, biomechanical, and anatomical interactions of xylem from five species of Acer (Aceraceae)." In: *Am. J. Bot.* 90.5, pp. 693–699.

Yoshida, S., R. Ooka, A. Mochida, S.Murakami, and Y. Tominaga (2006). *Development of Three Dimensional Plant Canopy Model for Numerical Simulation of Outdoor Thermal Environment*.

Yu, C. and W. N. Hien (2006). "Thermal benefits of city parks." In: *Energy Build.* 38.2, pp. 105–120.

Yuan, C., L. Norford, and E. Ng (2017). "A semi-empirical model for the effect of trees on the urban wind environment." In: *Landsc. Urban Plan.* 168.July, pp. 84–93.

Yue, W., C. Meneveau, M. B. Parlange, W. Zhu, H. S. Kang, and J. Katz (2008). "Turbulent kinetic energy budgets in a model canopy: comparisons between LES and wind-tunnel experiments." In: *Environ. Fluid Mech.* 8.1, pp. 73–95.

# CURRICULUM VITAE


## LENTO MANICKATHAN

| | |
|---|---|
| Date of birth | April 23, 1990 |
| Place of birth | Schaffhausen, Switzerland |
| Nationality | Indian |
| E-mail address | lento.manickathan@gmail.com |


## EDUCATION

| | |
|---|---|
| 2015 – 2019 | Doctor of Sciences<br>ETH Zurich, Switzerland |
| 2011 – 2014 | Master of Science in Aerospace Engineering<br>TU Delft, The Netherlands |
| 2008 – 2011 | Bachelor of Science in Aerospace Engineering<br>TU Delft, The Netherlands |

## ACADEMIC AND PROFESSIONAL EXPERIENCE

| | |
|---|---|
| 2015 – 2019 | Scientific Assistant at ETH Zurich<br>Zurich, Switzerland |
| 2012 | Research Intern at Shell Global Solutions<br>Rijswijk, The Netherlands |
| 2006 | Intern at Sulzer A.G.<br>Uster, Switzerland |

## PUBLICATIONS

### *Journal*

1. **Manickathan, L.**, Defraeye, T., Allegrini, J., Derome, D., & Carmeliet, J. (2018). Comparative study of flow field and drag coefficient of model and small natural trees in a wind tunnel. *Urban Forestry & Urban Greening*, 230–239. http://doi.org/10.1016/j.ufug.2018.09.011.

2. **Manickathan, L.**, Defraeye, T., Allegrini, J., Derome, D., & Carmeliet, J. (2018). Parametric study of the influence of environmental factors and tree properties on the transpirative cooling effect of trees. *Agricultural and Forest Meteorology*, 248, 259–274. http://doi.org/10.1016/j.agrformet.2017.10.014.

### *Conference*

1. **Manickathan, L.**, Kubilay, A., Defraeye, T., Allegrini, J., Derome, D., Carmeliet, J.: Integrated vegetation model for studying the cooling potential of trees in urban street canyons. *7th International Building Physics Conference*, Syracuse, NY, USA, September 23 - 26, 2018.

2. **Manickathan, L.**, Kubilay, A., Defraeye, T., Allegrini, J., Derome, D., Carmeliet, J.: Integrated CFD vegetation model with soil-plant-air water dynamics for studying the cooling potential of vegetation in an urban street canyon. *10th International Conference on Urban Climate/14th Symposium on the Urban Environment*, New York, NY, USA, 6 - 10 August 2018.

3. **Manickathan, L.**, Kubilay, A., Defraeye, T., Allegrini, J., Derome, D., Carmeliet, J.: Conjugate soil-vegetation-air-radiation model for studying the environmental impact of porous media such as vegetation. *Interpore 2018*, New Orleans, LA, USA, May 14 - 17, 2018.

4. **Manickathan, L.**, Kubilay, A., Defraeye, T., Allegrini, J., Derome D., Carmeliet, J.: Influence of vegetation on pedestrian thermal comfort in a street canyon. *1st International Conference on New*

*Horizons in Green Civil Engineering*, Victoria, BC, Canada, April 25 - 27, 2018.

5. **Manickathan, L.**, Defraeye, T., Allegrini, J., Derome, D., Carmeliet, J.: Transpirative cooling potential of vegetation in an urban environment using coupled CFD and leaf energy balance model. *15th Conference of the International Building Performance Simulation Association*, San Francisco, CA, USA, 2017.

6. **Manickathan, L.**, Defraeye, T., Allegrini, J., Derome, D., Carmeliet, J.: Conjugate Vegetation Model for Evaluating Evapotranspirative Cooling in Urban Environment. *97th AMS Annual Meeting*, Seattle, WA, USA, 2017.

7. **Manickathan, L.**, Defraeye, T., Allegrini, J., Derome, D., Carmeliet, J.: Aerodynamic characterization of model vegetation by wind tunnel experiments. *4th International Conference on Countermeasures to Urban Heat Island*, Singapore, 2016.

*Preprint*

1. **Manickathan, L.**, Defraeye, T., Carl, S., Richter, H., Allegrini, J., Derome, D., & Carmeliet, J. (2019). Unveiling dynamic changes in the diurnal microclimate of a Buxus sempervirens with non-intrusive imaging of flow field, leaf temperature, and plant microstructure. *Submitted to Agricultural and Forest Meteorology*. https://arxiv.org/abs/1903.02283.

2. Palha, A., **Manickathan, L.**, Ferreira, C.S., van Bussel, G. (2016): A hybrid Eulerian-Lagrangian flow solver. https://arxiv.org/abs/1505.03368v2.

## COLOPHON

This document was typeset in LaTeX using the typographical look-and-feel `classicthesis`. The bibliography is typeset using `biblatex` with `natbib`.